Scuola Normale Superiore



PhD Thesis

In Biophysical Sciences

# Nanoparticle-mediated enzyme replacement therapy and autophagy modulation in Krabbe disease


CANDIDATE:

Ambra Del Grosso

ADVISOR:

Marco Cecchini

SUPERVISOR:

Gianmichele Ratto


2019/2020

## List of Contents


**Chapter 1. Introduction ..... 1**

**Chapter 2: Krabbe disease ..... 5**

2.1 Scientific background ..... 5

*2.1.1 Lysosomal storage disorder: the case of Krabbe disease ..... 5*

*2.1.2 Molecular pathogenesis of Krabbe disease ..... 14*

*2.1.3 Therapeutics approaches for Krabbe disease: past, present and future ..... 20*

**Chapter 3: Nanomedicine for Lysosomal storage disorders ..... 28**

3.1 Scientific background ..... 28

*3.1.1 The issue of protein delivery ..... 28*

*3.1.2 Blood brain barrier and CNS drug delivery ..... 37*

*3.1.3 Blood nerve barrier and PNS drug delivery ..... 42*

3.2 Cross-Linked Enzyme Aggregates as Versatile Tool for Enzyme Delivery: Application to Polymeric Nanoparticles. ..... 45

*3.2.1 Introduction ..... 45*

*3.2.2 CLEA NPs synthesis and characterization ..... 46*

*3.2.3 Release profile of CLEA NPs ..... 52*

*3.2.4 In-vitro enzyme replacement therapy in PPT1 deficient cells ..... 56*

*2.3.5 Concluding remarks ..... 61*

*2.3.6 Material and methods ..... 62*

3.3 Targeted polymeric Nanoparticles promote enzyme replacement therapy in a mouse model of Krabbe disease: A breach through the BBB for enzyme replacement therapy. ..... 77

*3.3.1 Introduction ..... 77*

*3.3.2 Synthesis and characterization of targeted GALC CLEA NPs ..... 78*

*3.3.3 Intracellular delivery of targeted NPs ..... 81*

*3.3.4 NP-mediated enzymatic activity recovery in vitro ..... 84*

*3.3.5 NP-mediated enzymatic activity recovery in vivo ..... 89*

*3.3.5 Concluding remarks ..... 94*

*3.3.6 Material and methods ..... 103*

**Chapter 4: Autophagy in Lysosomal storage disorders ..... 114**

4.1 Scientific background ..... 114

*4.1.1 Autophagy machinery ..... 114*

*4.1.2 Autophagy in diseases ..... 118*

4.2 Lithium improves cell-viability in an immortalized cell model of Krabbe disease ..... 126
*4.2.1 Introduction ..... 126*
*4.2.2 Psychosine induces autophagy ..... 127*
*4.2.3 Li increases autophagy in psychosine-treated cells ..... 131*
*4.2.4 Psychosine content in PSY- and Li-treated cells ..... 134*
*4.2.5 Lithium improves viability of psychosine treated cells ..... 136*
*4.2.6 Improved viability does not correlate with reduced cytoplasmic oxidative stress ..... 139*
*4.2.7 Concluding remarks ..... 141*
*4.2.8 Material and methods ..... 146*
4.3 Dysregulated autophagy as a new aspect of the molecular pathogenesis of Krabbe disease ..... 155
*4.3.1 Introduction ..... 155*
*4.3.2 Autophagy is dysregulated in the TWI mouse central and peripheral nervous system ..... 156*
*4.3.3 P62 aggregates accumulate differently in distinct neural cell types ..... 159*
*4.3.4 Autophagosome-lysosome fusion and autophagosome-mediated p62 recycling are not impaired in TWI brains ..... 162*
*4.3.5 Autophagy is dysregulated in TWI primary cells ..... 163*
*4.3.6 RAP and not RESV-mediated autophagy induction partially restore autophagy markers levels. ..... 169*
*4.3.7 Concluding remarks ..... 171*
*4.3.8 Material and methods ..... 175*

**Chapter 5: From GALC deficiency to Krabbe disease pathogenesis: still an open issue ..... 184**
5.1 New methods applied to the case of Krabbe disease ..... 184
5.2 Quantitative Microproteomics Based Characterization of the Central and Peripheral Nervous System of a Mouse Model of Krabbe Disease ..... 185
*5.2.1 Introduction ..... 185*
*5.2.2 Tissue sampling and protein extraction ..... 188*
*5.2.3 Proteome profiling ..... 189*
*5.2.4 Proteome changes in the CNS and PNS of the Twitcher mouse . 191*
*5.2.5 Gene Ontology Enrichment Analysis ..... 195*
*5.2.6 Validation by western blot analysis ..... 198*
*5.2.7 Concluding remarks ..... 200*
*5.2.8 Material and methods ..... 207*

5.3 Capturing Metabolism-Dependent Solvent Dynamics in the Lumen of a Trafficking Lysosome ..... 216
*5.3.1 Introduction ..... 216*
*5.3.2 ACDAN Is a Stable Fluorescent Marker of the Lysosome Lumen 220*
*5.3.3 Feedback-Based 3D Orbital Tracking and Fluctuation Spectroscopy on Single Lysosomes: Validation Tests ..... 224*
*5.3.4 ACDAN GP Fluctuations in the Lumen of a Trafficking Lysosome ..... 230*
*5.3.5 ACDAN GP Fluctuations Depend on Ongoing Metabolic Activity 238*
*5.3.6 ACDAN GP Fluctuations Are Altered in a Cellular Model of LSD 240*
*5.3.7 Concluding remarks ..... 245*
*5.3.8 Material and methods ..... 248*

**Chapter 6: Conclusions and future perspectives ..... 260**

**List of abbreviations ..... 264**

**List of publications ..... 268**

**Bibliography ..... 269**

**Acknowledgements ..... 295**

# Chapter 1. Introduction

Krabbe disease (KD), also known as Globoid Cell Leukodystrophy (GLD), is a rare and hereditary neurodegenerative condition.[1] The cause of this disorder has been attributed to the deficiency of the lysosomal enzyme galactosylceramidase (GALC).[2] GALC loss of function leads to psychosine (PSY) accumulation in the central and peripheral nervous system (CNS and PNS), causing a series of cellular and tissue modifications.[2,3] However, the exact pathogenetic mechanisms that link GALC deficiency to cellular damage are still not completely understood, and no cure is currently available for KD, being treatment symptomatic and supportive only.[4,5] Classical enzyme replacement therapy (ERT), which is typically performed by intravenously administering the free recombinant enzyme, would be the most obvious therapeutic choice, but the presence of the blood brain barrier (BBB) restricts GALC translocation into the CNS.

Thus, owing to the lack of an effective cure and to the poor general understanding of KD physio-pathology, novel approaches to investigate these two fundamental aspects prove to be necessary and have been investigated in this thesis.

In particular:

Chapter 2 provides an overview of the existing literature on KD, starting from a brief description of lysosomal storage disorders (LSDs) in general. Then, a specific section describes the currently know features of the KD molecular pathogenesis. Finally, "past, present and future" therapeutics approaches for KD are discussed.

Chapter 3 first describes the problem of therapeutic proteins delivery across the BBB. Nanomedicine is then discussed as an innovative strategy to overcome this issue, and the results of two related researches obtained during my PhD are reported.

In the first work (Section 3.2), a new cross-linked-enzyme-aggregates(CLEAs)-based nanoparticles (NPs) approach is proposed for ERT in different LSDs, including KD. In the second work (Section 3.3), results of pre-clinical *in-vitro* (in primary murine and human KD cells) and *in-vivo* (in Twitcher mice) tests of this new CLEAs-NPs approach are reported.

Chapter 4 provides a detailed overview of the autophagy machinery in health and disease. Autophagy dysregulation is then described concerning neurodegenerative disorders and LSDs. Results of two works obtained during my PhD regarding autophagy in KD are then presented.

In the first one (Section 4.2), autophagy has been exploited in an immortalized KD cellular model, and Lithium has been investigated as a therapeutic strategy to improve cell viability activating autophagy in a m-TOR independent way. In the second one (Section 4.3), for the first time in literature autophagy has been studied in an animal model for KD, and the m-TOR dependent autophagy induction has been proposed as a therapeutic strategy to obtain PSY and/or protein aggregates clearance from cells.

Chapter 5 describes the results of two experiments I attended during my PhD, in which two innovative research strategies have been applied to the case of KD.

First (Section 5.2), a new quantitative microproteomics-based characterization of CNS and PNS of the Twitcher mice is presented. Later (Section 5.3), a 3D-orbital tracking method used to study metabolism-dependent solvent dynamics in the lumen of trafficking KD lysosomes is shown.

Finally, in Chapter 6 conclusions are drawn, and further studies and applications are proposed and discussed.

## *Aims of the thesis*

The **first aim** of this thesis regards KD therapy. Given the lack of an efficient ERT for KD, the goal is to develop a new nanomedicine-based ERT approach based on biocompatible nanoparticles to get into the CNS and release the missing enzyme. Our experimental hypothesis is that the brain-targeting peptides we use allow GALC-loaded nanoparticles to pass the BBB. This could be the first step for starting the study of an innovative ERT for KD based on this approach.

Moreover, given the fact that KD pathogenesis is still not completely known and that GALC-supplying therapeutic approaches (as gene therapy or bone marrow transplantation) are beneficial but not completely curative, we hypothesized that molecular mechanisms that have not yet been considered can be implicated in the pathogenesis of KD, and that consequentially they can be exploited as therapeutic target for single or combined therapies.

Given this scenario, we decided to focus on the study of the autophagy molecular mechanism, which has never been considered for KD, to discover something missing about KD pathogenesis. Thus, the **second aim** of this thesis is to study the autophagy machinery as a new pathogenetic mechanism for KD. This choice is based on the numerous dysfunctions of the autophagy process which has been found implicated in many others LSDs and Neurodegenerative disease, and on the evidence that in KD there is an accumulation of "waste material", such as PSY and α-synuclein. Moreover, the **second aim** aspires also to exploit autophagy as a possible therapeutic target, which could contribute to reinstate the "normal phenotype" helping in the clearance of undesirable cell products.

# Chapter 2: Krabbe disease

## 2.1 Scientific background

### 2.1.1 Lysosomal storage disorder: the case of Krabbe disease

Lysosomal storage disorders (LSDs) are a large group of over 70 clinically recognized metabolic disorders, which are individually rare but collectively common (1:5000 live births). For the most part, LSDs result from an enzyme deficiency within the lysosomes, which ultimately causes accumulation of undegraded substrates. This storage process leads to a broad spectrum of clinical manifestations depending on the specific substrate and site of accumulation.[6] Most LSDs show a widespread tissue and organ involvement, with brain, viscera, bone and connective tissues usually affected. Brain disease is particularly prevalent, involving two-thirds of all LSDs.[7] The most applied clinical treatments for LSDs involving neurological damage are essentially two: hematopoietic stem cell transplantation (HSCT) and enzyme replacement therapy (ERT). In addition, supportive cares are usually used (see Tab. 2.1 for an overview of LSDs with prominent neurologic findings).

**Features of lysosomal storage diseases with prominent neurologic findings**

| LSD | Defective protein | Presenting signs and symptoms | Treatment options |
|---|---|---|---|
| **GM1 gangliosidosis** | Acid β-galactosidase | IO: hypotoni, DD, coarse facial features, HM, CRS (±)<br>LO: DD, ataxia, dysarthria, PR, dystonia | SC, HSTC |

| | | | |
|---|---|---|---|
| **GM2 gangliosidosis, B variant, Tay-Sachs disease** | Hexosaminidase A | IO: hypotonia, hyperacusis, DD, CRS<br>LO: ataxia, dystonia, psychoses, PR | SC, HSTC |
| **GM2 gangliosidosis, O variant, Sandhoff disease** | Hexosaminidase A & B | Similar to Tay-Sachs disease | SC |
| **GM2 gangliosidosis, AB variant** | GM2 activator protein | Similar to Tay-Sachs disease | SC |
| **Fabry disease** | α-Galactosidase | Acroparesthesia, pain crises, corneal opacities, fatigue, angiokeratomas | SC, ERT, HSTC |
| **Gaucher disease, types 2 and 3** | β -Glucocerebrosidase | HSM, DD, strabism, Sz, myoclonus, horizontal supranuclear gaze palsy | SC, ERT, HSTC |
| **Niemann-Pick type A** | Sphingomyelinase | HSM, hypotonia, DD, CRS (±) | SC |
| **Niemann-Pick type C1** | NPC1 | Neonatal onset: jaundice, HSM, hypotonia<br>LO: emotional lability, ataxia, dystonia, HSM (±), VSO | SC, HSTC |
| **Niemann-Pick type C2** | NPC2 | Similar to Niemann-Pick type C1 | SC |
| **Metachromatic leukodistrophy** | Arilsulfatase A | Late IO: weakness, hypotonia, DD, genu recurvatum<br>JO: weakness, PR, ataxia, behavior changes<br>AO: pyramidal or cerebellar signs, behavior changes, psychoses, dementia. | SC, HSTC |
| **Krabbe disease** | Galactocerebrosidase | IO: spasticity, irritability, hypotonia, fisting, DD<br>LO: spastic paraparesis, weakness, burning paresthesia, ataxia, weakness, vision loss | SC, HSTC |
| **α-Mannosidosis** | α -Mannosidase | DD, hearing loss, midly coarse facial features (large jaw), mild DM | SC, HSTC |
| **β-Mannosidosis** | β-massonidase | DD, MR, hearing loss, mild facila coarsening, angiokeratomas | SC |
| **Sialidosis, Mucolipidosis I** | Sialidase | IO: NIFH, DD, coarse facial features, DM, HSM, PR, renal disease | SC |
| **Sialic acid storage disease, Salla disease** | Transport protein | IO: severe DD, fair hair and skin, HSM, coarse facial features | SC |

| | | | |
|---|---|---|---|
| | | LO: hypotonia, MR, ataxia, DD, speech delay, coarse facial features | |
| **Galactosialidosis** | Protective protein cathepsin A | Neonatal onset: NIFH, HSM, severe DD<br>IO and late IO: coarse facial features, HSM, kidney and heart defects, DD, DM, MR<br>LO: coare facial features, DM, cornela clouding, MR, ataxia, Sz, CRS (±) | SC |
| **Fucosidosis** | α-L-fucosidase | Spasticity, DD, coarse facial features, DM, MR, angiokeratomas | SC, HSTC |
| **MPS I (Hurler and Hurler-Scheie)** | α-L-iduronidase | Coarse facial features, DD, DM, MR, hearing loss, corneal clouding, hernias. | SC, HSCT, ERT |
| **MPS II (Hunter)** | Iduronate-2-sulfatase | DD, DM, hearing loss, coarse facial features, joint stiffness. | SC, HSTC, ERT |
| **MPS III A (Sanfilippo)** | Glucosamine-N-sulfatase | Aggressive behavior, DD, midly coarse facial features, hirsute, coarse hair, mild DM | SC, HSTC |
| **MPS III B** | α-N-Ac-glucosaminidase | Similar to MPS III A | SC |
| **MPS III C** | AcCoA: α-glucosaminide-N-acetyltrasnferase | Similar to MPS III A | SC |
| **MPS III D** | N-acetylglucosamine-6-sulfatase | Similar to MPS III A | SC |
| **MPS VII** | β-Glucorinidse | NIFH, DM, DD coarse facial features, HSM, MR | SC, HSTC, ERT |
| **Mucolipidosis II** | UDP-N-Ac-glucosaminylphosphotrasnferrase | Coarse facial features, DD, weakness, DM, gingival hyperplasia, macroglossia | SC, HSTC |
| **Mucolipidosis IV** | Mucolipin 1 | DD, corneal opacities, retinal degeneration, strabismus | SC |
| **Mulitple sulfatase deficiency** | Sulfatase modifier protein | DD, icthyosis, coarse facial features, deafness, mild DM, PR | SC |
| **Neuronal Ceroid Lipofuscinosis 1** | Palmitoyl-prtein thioesterase 1 | Vision loss, motor dysfunction, hypotonia, DD, MR | SC, HSTC |
| **Neuronal Ceroid Lipofuscinosis 2** | Tripeptidyl peptidase 1 | Sz, motor dysfuntion, DD, MR, ataxia, dementia | SC |
| **Saposin defect, MLD type** | Saposin B | Similar to JO MLD | SC |
| **Saposin defect Gaucher type** | Saposin C | Similar to Gaucher disease, type 3 | SC |

| | | | |
|---|---|---|---|
| **Saposin defect, generalized type** | Prosaposin | HSM, DD, motor abnormalities, axaggerated Moro reflex, MR | SC |
| **Asparylglucosaminuria** | Aspactylglucosaminidase | Delayed speech, motor clumsiness, mildly coarse facial features, behavioural problems | SC |
| **Farber disease** | Acid ceramidase | Painful and swollen joints, nodules, DD, hourse cry, hypotonia | SC, HSTC |
| **Wolman Diseas** | Acid lipase | HSM, vomiting, diarrhea, anemia, PR | SC, HSTC |
| **Schindler disease** | α-N-acetylgalactosaminidase | DD, blindness, Sz, spasticity, PR | SC |
| **Pompe disease** | α-Glucosidase | Hypotonia, DD, cardiac enlargement | SC, ERT |

**Table 2.1.** Features of lysosomal storage diseases with prominent neurologic findings. Abbreviations: AO: adult onset; CSF :cerebrospinal fluid; CRS :cherry-red spots; DD: developmental delay; DM: dystosis multiplex; ERT: enzyme replacement therapy; HSTC: hematopoietic stem cell transplantation; HM: hepatomegaly; HSM: hepatosplenomegaly; IO: infantile onset; JO: juvenile onset; LO: late onset; MLD: metachromatic leukodistrophy; MPS: mucopolysaccaridosis; MR: mental retardation; NIFH: nonimmune fatal hydrops; PR: psychomotor regression; Sz: seizures; SC: supportive care; VSO: vertical supranuclear opthalmoplegia.
*HSTC is not available for all patients with a given diagnosis, and ERT may be in use or only at the stage of preclinical trials. The use of these treatments in a few patients does not necessarily indicates successful outcome. Modified from *Wenger et al., 2003*. [8]

Krabbe disease (KD or Globoid cell leukodistrophy; OMIM #245200) is an autosomal recessive LSD caused by homozygous or compound heterozygous mutations in the galactosylceramidase gene (GALC; OMIM #606890; chromosome 14q31).[9,10,11] Based on the Human Gene Mutation Database (HGMD), more than 130 KD-associated mutations in the GALC gene have been identified, comprising deletions, frameshifts, and missense mutations.[12] Among the mutations, a 30-kb deletion that encodes nonfunctional protein is the most common.[13,14] In addition, most other GALC mutations associated with KD are missense mutations that cause catalytic inactivation, protein truncation, misfolding, mis-targeting and/or

degradation.[15] GALC gene, encodes for an 80-85 kDa precursor form consisting in a single-chain peptide of 669 amino acid residues.[11] The precursor is then processed into the active form, consisting of two subunits, a 50-52 kDa and a 30 kDa mature form, obtained by the action of proteases probably localized in lysosomes.[10,16] Furthermore, human GALC protein possesses four potential N-glycosylation sites[17], which play a role in the mannose-6-phosphate receptor (M6PR)-mediated targeting of GALC to lysosomes.[18] Lysosomal enzymes, in fact, are synthetized in the endoplasmic reticulum (ER) and transported to the Golgi apparatus, where they are modified by addition of sugar residues and/or phosphorylation. Certain enzyme-attached residues, such as mannose-6-phosphate (M6P), are recognized by the M6PR, which mediate intracellular trafficking to lysosomes. Lysosomal enzymes are also secreted to the extracellular milieu, where they can bind to M6PR on the cell surface of the same cell or a different cell. This mediates clathrin-mediated uptake and endocytic transport to lysosomes (see Fig. 2.1 for a schematic representation of lysosomal enzymes transport pathway). Importantly, this pathway constitutes the foundation for delivery of recombinant enzymes in replacement therapy protocols, as well as for hematopoietic stem cell and gene therapy approaches.[19]

GALC enzyme shows an optimal hydrolytically activity at acid pH (typical of the lysosomal environment) and its specific substrates are glycolipids with a terminal galactose moiety in the β-anomeric configuration. Recently, the crystal structures of GALC and the GALC-product complex were obtained, revealing novel domain architecture with a previously uncharacterized lectin-domain not observed in other hydrolases

(Fig. 2.2). Specifically, all three domains of GALC contribute to the substrate-binding pocket, and disease-causing mutations are widely distributed throughout the protein.[17] As shown in the scheme reported in figure 2.3, the enzyme acts during myelin turnover to catabolize the myelin lipids.[20,21] The major natural substrate of the enzyme is galactosylceramide (Gal-cer), which is a sphingolipid containing sphingosine, galactose and fatty acid, almost exclusively localized in the myelin sheath.

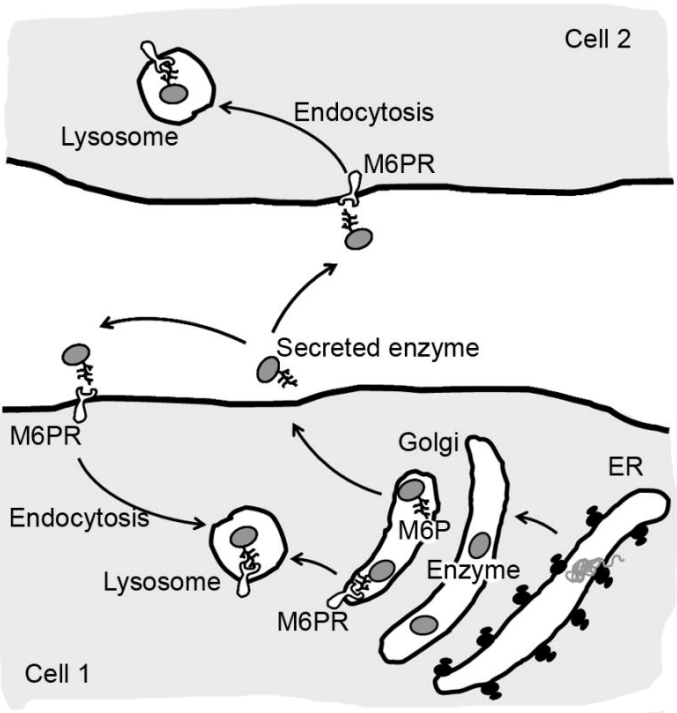


**Figure 2.1** Mechanism of lysosomal enzymes transport mediated by the mannose-6-phosphate receptor (M6PR). M6P: mannose-6-phosophate residue; ER: endoplasmic reticulum.[19].

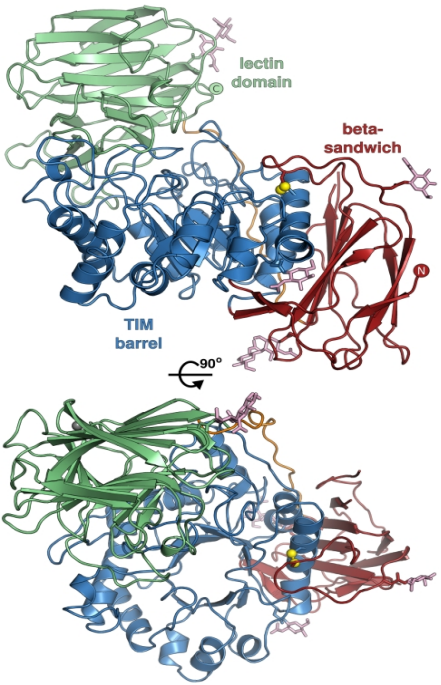


**Figure 2.2.** Structure of GALC. Ribbon diagram of GALC colored by domain: β-sandwich (red), TIM barrel (blue), linker (orange), and lectin domain (green). The disulfide bond (yellow spheres), calcium ion (gray sphere), and glycosylation moieties (violet sticks) are shown. The N and C termini are marked by labeled circles (*Top*). [17]

Other known natural substrates of GALC are galactosylsphingosine or psychosine (PSY), monogalactosyldiglyceride, and the precursor of seminolipid (1-alkyl, 2-acyl-3-galactosyl glycerol). In vivo degradation of the substrates requires an activator protein, saposin A, in addition to GALC. Mutation in the saposin A gene, in fact, causes an atypical form of KD (OMIM # 611722).

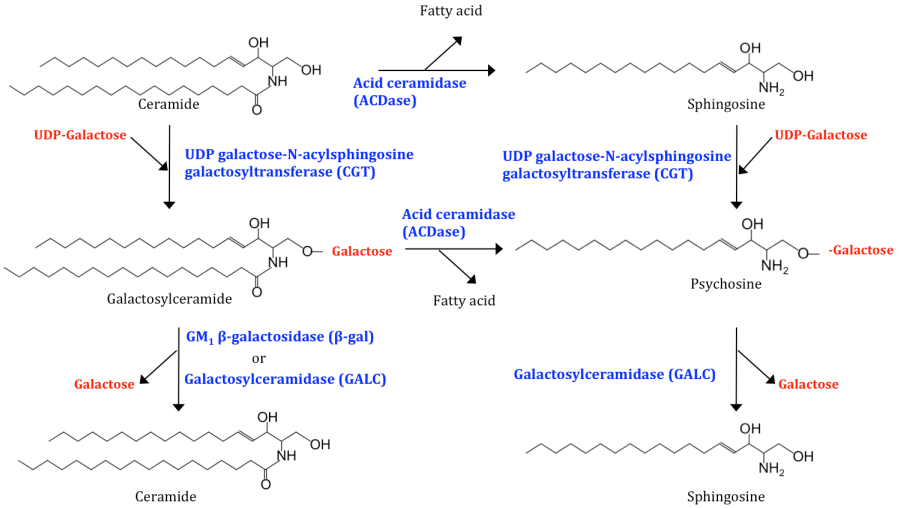


**Fig. 2.3.** Anabolic and catabolic pathways of psychosine and galactosylceramide. Galctosylceramide (Gal-cer) is one of major glycosphingolipids of myelin. It is synthesized by galactosylation of ceramide by the action of UDP-galactose ceramide galactosyl transferase (CGT; EC 2.4.1.47). Gal-cer is degraded to ceramide by degalactosylation by both $GM_1$ β-galactosidase (β-gal, EC 3.2.1.23) and galactosylceramidase (GALC; EC 3.2.1.46). Psychosine (PSY) is synthesized by galactosylation of sphingosine which is generated from deacylation of ceramide by Acid ceramidase (ACDase; E.C. 3.5.1.23). PSY can also be synthesized from galctosylceramide by the action of ACDase. PSY is a neurotoxic lysolipid and present at extremely low levels in the cells and tissues under normal conditions. However, under the GALC deficient conditions, PSY accumulates to high levels in tissues, especially in the brain. Unlike most other LSDs, the primary substrate of GALC (gal-cer) is not found at such high levels in KD tissues due to its alternative hydrolysis by $GM_1$ ganglioside β-galactosidase (EC) or ACDase. Updated from Won et al., 2016. [12]

## *Clinical manifestations*

KD in humans is typically a neurodegenerative disease of infancy, but there are examples in which KD has been diagnosed in older children and adults.[1,22] The first hallmarks, generally, are alteration of neuronal conduction and neurological dysfunctions. Four different clinical forms are usually described according to symptom onset: infantile, late infantile, juvenile and adult. The infantile phenotype (95% of known cases) has

usually onset within first 6 months of life and leads to death by age 2-4 years.[23,24] Hyperirritability, hypersensitivity to the external environment, stiffness of the limbs, and episodic fever of unknown origin are firstly reported. The psychomotor functions deteriorate quickly with marked hypertonicity, extended and crossed legs, flexed arms, and the backward-bent head. At the latest stage of the disease, the infants are in a decerebrate posture and become blind and unresponsive of their surroundings. The late infantile form, instead, has onset between 6 months to 3 years. Irritability, psychomotor regression, stiffness, ataxia, and loss of vision are frequent initial symptoms. The course is progressive and results in death approximately 2 or 3 years after the onset. The juvenile form presents onset between 3 and 8 years. Patients commonly develop loss of vision, hemiparesis, ataxia, and psychomotor regression.[25] Adult form, finally, whose onset is after 20 years, has a milder phenotype and a slower rate of progression, allowing sometimes a normal life span to patients. Some individuals remain stable for long periods of time while others show a steady decline in vegetative state and death [Debs et al., 2013].[25]

As described in Jacob et al., 1973[26] and Suzuki, 2003b[27], KD symptoms indicate central and peripheral nervous system (CNS and PNS) involvement, particularly of the cerebellum, which is responsible for control, refinement and execution of movements and co-ordination of muscle activity.[28] Disease progression is typically characterized by the loss of higher cerebral functions and, in the late stage of the disease, by a massive loss of oligodendrocyte and myelin.[27,3,22,1] Owing to cell death, there is an activation of the inflammatory cascade, which recruits macrophages and activates microglia, amplifying the production of cytotoxic molecules. The

inflammatory response to demyelination is then followed by astrocytic gliosis. In the areas of active demyelination, moreover, multinucleated macrophages, called globoid cells, are often clustered around blood vessels.[29,30] However, there are also evidence that inflammation can occours before major demyelination in KD (See *The microglial hypothesis* in the next paragraph).

### 2.1.2 Molecular pathogenesis of Krabbe disease

Sphingolipids are essential components of cellular membranes and defects in their synthesis or degradation cause severe human diseases.[31] The glycosphingolipid Gal-cer is the primary lipid component of the myelin sheath and is degraded by GALC.[17] However, as already mentioned, GALC is also responsible for the degradation of PSY, a glycolipid whose high accumulation is cytotoxic and which has been found accumulated in both KD CNS and PNS.[32,33,34]

These findings paved the basis for the formulation of the so called "*Psychosine hypothesis*" in 1972.[35] This proposed that GALC deficiency leads to PSY intracellular accumulation, which primarily kills oligodendrocytes in the CNS[29,36] and Schwann cells in the PNS[35]. KD, indeed, has traditionally been considered a white matter disease.[37]

In the most recent literature, however, new aspects of the molecular pathogenesis of KD have been discovered, as the involvement of endothelial cell dysfunction[38] and autophagy[39,40,41,42,43,] , the presence of neuronal degeneration[44,45,46] and defects in calcium signaling[47]. Very recently, moreover, Nicaise and colleagues, formulated an interesting new hypothesis, "the *microglial hypothesis*", which suggests that the pathophysiological effects of PSY could not only be limited to myelinating

cell death, but rather, PSY may impact primarily on microglia and astrocytes that, when activated, would become cytotoxic for oligodendrocytes. [48]

Despite many important experimental evidences and molecular hypothesis, the exact pathogenic mechanisms that lead from GALC deficiency to cell death is still not completely understood.

### *Psychosine*

PSY is a metabolic byproduct in the metabolism of sphingolipids, which accumulated under GALC-deficient conditions. As shown in figure 2.3, PSY can be generated by the anabolic galactosylation of sphingosine by UDP-galactose-N-acylsphingosine galactosyltrasnferase (CGT; E.C. 2.4.1.45) or by the catabolic deacylation of galactosylceramide by acid ceramidase (ACDase; E.C. 3.5.1.23). Two studies have directly[49] or indirectly[50] supported the anabolic pathway. The catabolic PSY generation, instead, has been only recently demonstrated from Li and colleagues.[51]

Under normal conditions, the cellular and tissue levels of PSY are extremely low (< than 10 pmol/mg protein). However, under GALC-deficient conditions PSY accumulates to high levels in tissues, especially in the brain (up to ~ 50% of total brain cerebrosides[2,27]). Similar to PSY, Gal-cer is synthesized by galactosylation of ceramide by CGT. Unlike most other LSDs, the primary substrate of GALC (Gal-Cer) is not found at such high levels in KD tissue because of its alternative hydrolysis by GM1 β-galactosidase (β-gal; EC 3.2.1.23; Fig. 2.3)[52] and ACDase[51].

CGT is highly expressed in oligodendrocytes and Schwann cells, whereas is expressed to a lower degree in neurons and astrocytes.[53,54,55,] Accordingly, CGT-expressing cells are the most vulnerable to the PSY-induced neurotoxicity under GALC-deficient conditions.[56,57,2] Moreover,

because oligodendrocytes accumulate PSY under GALC-deficient conditions[12], their spontaneous degeneration could cause PSY burden on neighboring cells (as astrocytes, microglia and neurons) and thus accelerate the progression of the pathology[36]

Due to the PSY detergent-like properties, PSY-induced changes in membrane architecture were initially believed to be the cause of oligodendrocytes apoptosis and subsequent demyelination in KD.[2] Furthermore, a study of 2009[58] showed that PSY accumulates preferentially in the lipid rafts of the CNS and PNS of KD patients and of the spontaneous KD model [the Twitcher (TWI) mouse]. They also showed that this PSY accumulation is accompanied by increase in cholesterol, changes in the distribution of the lipid raft markers flotillin-2 and caveolin-1 and alterations in the distribution of the PKC (Protein kinase C) signaling molecule, providing a model for PSY-induced KD pathogenesis (schematized in Fig. 2.4).

Subsequently, however, a very recent study from D'Auria and colleagues demonstrated that PSY-toxicity in KD involves deregulation of cell signaling not only by disruption of lipid rafts, but also by direct local destabilization and fragmentation of the membrane through microvesiculation[59].

Nevertheless, the mechanisms underlying PSY-induced apoptosis are not fully understood at present, and many studies have demonstrated the participation of multiple cell signaling pathways in PSY-induced toxicities (summarized in Tab. 2.2).

Interestingly, phospholipase A2 (PLA2) has been hypothesized to play a role in PSY induce cell death.[60] Very recently, moreover, Misslin and colleagues specifically demonstrated that non-selective inhibition of

cPLA2/sPLA2 and selective inhibition of cPLA2, but not sPLA2, attenuates PSY-induced cell death of human astrocytes, supporting the proposal that novel drugs for KD may require testing on astrocytes as well as oligodendrocytes.[61]

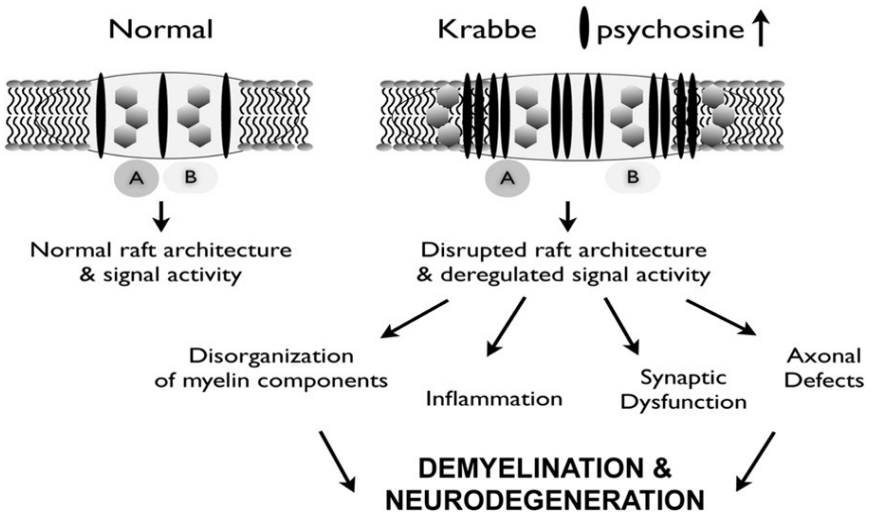


**Figure 2.4.** Proposed model of deregulation of various raft-modulated cell functions in KD. The illustration proposes a working model where the preferential accumulation of PSY in the raft domain leads to deregulation of raft-associated signals in KD. In this hypothetical model, under normal sphingolipid metabolism, two hypothetical partners (A, B) are spatially accommodated to provide functional interaction (normal signal activity). In KD, the raft domain increases in size because of the accumulation of PSY and other components of the raft, leading to the spatial separation of the two partner molecules, disrupting the function of the associated signal. The consequent deregulation in signal activity can influence different dependent cellular processes according to the cell type where this occurs (From White et al., 2009). [58]

Furthermore, from 2014, new evidences for possible defects in protein folding in KD have also been reported.[46] Neuronal inclusions consisting primarily of α-synuclein, in fact, have been found in both KD and TWI brain. Inclusions were more frequent with the advancement of the disease and

affected specific brain areas. [6244,] Further, PSY was found to facilitate α-synuclein fibrillization[62], and α-Synuclein was found to interact directly but reversibly with PSY[63] suggesting a link between PSY and α-synuclein inclusions.

Despite the effort of many research groups, thus, a solid conclusion regarding the exact pathogenetic mechanisms of PSY is still lacking.

**Mechanism Underlying PSY Toxicity**

| Pathways involved | Selected citations |
|---|---|
| **Membrane stability and functions :** | |
| Membrane disruption and altered lipid-raft function | White et al., 2009, 2011; Hawkins-Salsbury et al., 2013; D'auria et al., 2017; Zulueta Díaz et al., 2018; Abbandonato et al., 2019 [58,64,59,65,66] |
| **Stress and proapoptotic pathways :** | |
| Inhibition of cell survival signaling (e.g., Akt and ERK) | Hamanoue et al., 2004; Zaka et al., 2005; Won et al., 2013; Inamura et al., 2018 [67,68,69,36] |
| Activation of proapoptotic pathways (e.g., JNK, p53, caspases 3/9, and cytochrome C release) | Haq et al., 2003; Giri et al., 2006; Smith et al., 2011; Ribbens et al., 2014[70,60,71,43,] |
| Transcription factors (up- and downregulation of AP-1 and NF-jB) | Haq et al., 2003[70] |
| Increase of caspase-3, PTEN, Bad, and Cx43 expression and decrease of PI3K, pAKT and pBad expression. | Graziano et al., 2016[72] |
| **Immune and inflammatory responses** | |
| Cellular involvement in the CNS: | |
| Astrocytes | Kobayashi et al., 1986; Jesionek-Kupnicka et al., 1997; Mohri et al., 2006; Hawkins-Salsbury et al., 2012; Ransohoff and Brown, 2012; Snook et al., 2014; Misslin et al., 2017 |
| Microglia | Ohno et al., 1993; LeVine and Brown, 1997; Bashir and Haq, 2011; Ransohoff and Brown, 2012; Ijichi et al., 2013; Claycomb et al., 2014; Snook et al., 2014 |
| Peripheral immune cells (e.g., macrophages and lymphocytes) | Kobayashi et al., 1986; Ohno et al., 1993; Wu et al., 2000; Kondo et al., 2011[73,74,75,76, 61,73,77–85] |
| Pro- or anti-inflammatory mediators: | |
| Proinflammatory cytokines (e.g., IL-1b, IL-6, and TNF-a) | LeVine and Brown, 1997; Pedchenko and LeVine, 1999; Giri et al., 2002 |
| Chemokines (e.g., MCP-1, MIP-1a, and MIP-1b) | Wu et al., 2000; Wu et al., 2001 |

| | |
|---|---|
| Anti-inflammatory cytokine (e.g., IL-10 and LIF) | Wu et al., 2000; Potter et al., 2013 |
| MMP-3 expression and altered ECM composition | Ijichi et al., 2013; Claycomb et al., 2014 |
| Related transcriptional regulation; AP-1, C/EBP, and Oct-1 (no alteration in NF-jB) | Giri et al., 2002; Haq et al., 2003 |
| Innate immune responses; OL death induced TLR2 activation of microglia and macrophage | Snook et al., 2014 [12,70,77–79,81,84,86–88] |
| Systemic immune/inflammatory responses | |
| Functional impairment of hematopoietic stem/progenitor cell | Visigalli et al., 2010 |
| Thymic atrophy by autonomic denervation | Galbiati et al., 2007 |
| Increased apoptosis of peripheral blood lymphocytes and proinflammatory responses of peripheral blood mononuclear cells | Formichi et al., 2007 [89–91] |
| **Oxidative and nitrosative stress** | |
| Increased oxidative stress | Haq et al., 2003; Khan et al., 2005; Giri et al., 2008; Hawkins-Salsbury et al., 2012; Voccoli et al., 2014; Del Grosso et al., 2016 |
| Decreased levels of reduced glutathione | Khan et al., 2005; Hawkins-Salsbury et al., 2012 |
| Increased iNOS expression | Giri et al., 2002; Borda et al., 2008; Bashir and Haq, 2011; Ripoll et al., 2011; Hawkins-Salsbury et al., 2012 |
| Efficacy of antioxidant treatment (NAC) | Haq et al., 2003; Khan et al., 2005; Giri et al., 2008; Hawkins-Salsbury et al., 2012 [70,39,47,76,85,92–94] |
| **Cellular metabolic processes** | |
| Mitochondrial dysfunctions and decreased ATP levels | |
| Peroxysomal dysfunction | Khan et al., 2005; Haq et al., 2006 |
| Autophagy dysregulation | Ribbens et al., 2014; Del Grosso et al., 2016; Pellegrini et al., 2019; Del Grosso et al., 2019; Kose et al., 2019 |
| Lysosome alterations | Folts et al., 2016; Begarani et al., 2019 |
| Unfolded protein aggregation (α-Synuclein) | Irahara et al., 2018; Abdelkarim et al., 2018; Marshall et al., 2018; Marshall et al., 2016; Smith et al., 2014 [39–44,46,62,93,95–99] |
| **Abnormal lipid metabolism** | |
| Upregulated biosynthesis of cholesterol and free fatty acids | Giri et al., 2008 |
| $sPLA_2$ activation and increases in AA and LPC | Giri et al., 2006, 2008 |
| $sPLA_2$ activation and increases in AA and LPC | Giri et al., 2008 [60,92] |
| AMPK inactivation | |
| **Neuro- and axonopathies and neuromuscular dysfunctions** | |
| Axonal defects and neuronal death | Castelvetri et al., 2011; Lim et al., 2016 |
| Decrease peripheral nerve conduction and skeletal muscles atrophy | Dehkharghani et al., 1981; Marjanovic et al., 1996; Dolcetta et al., 2005 |
| Neuromuscular junctional abnormalities by dysregulations of caspases and Akt | Cantuti-Castelvetri et al., 2015 |
| α-Synuclein inclusion in neurons | Smith et al., 2014 |
| Neurofilament abnormality by deregulation of PP1 and PP2A and dysregulation of axonal transport by | Cantuti-Castelvetri et al., 2012; Cantuti Castelvetri et al., 2013 [44,100–106] |

| | |
|---|---|
| GSK3b activation | |
| **Endothelial and vascular dysfunction** | |
| Enlargement of perivascular space, dilated lumens, and altered endothelium and smooth muscle cell morphologies; increased brain vascular permeability, vessel fragmentation; decreased microvascular density and total vessel lengths | Kondo and Suzuki, 1993; Belleri et al., 2013; Giacomini et al., 2015 |
| Decreased endothelial proliferation and migration and thus decreased neovascularization | Belleri et al., 2013 |
| Actin cytoskeleton disruption and decreased tight junction protein | Belleri et al., 2013 [107–109] |

**Table 2.2.** Mechanisms underlying PSY toxicity. Updated from Won et al., 2016. [12]

### 2.1.3 Therapeutics approaches for Krabbe disease: past, present and future

No effective cure is currently available for KD, but important progresses have been made in the recent years. Therapeutics approaches can be divided into two main categories: the ones that aim to obtain a GALC activity replacement, and the ones that aim to correct or improve secondary symptoms of the disease. In this introduction we will focus mainly on the first category.

In the perspective of developing safe and effective enzymatic activity replacement for KD, three main needs must be considered:

- Early intervention: it is fundamental to modify disease course;
- Robust and long-lasting targeting of all the affected organs;
- Different levels of enzyme activity might be necessary to restore normal function in different cells/tissue and stages of the disease.

In this context, the most widely used mammalian model of KD is the already mentioned TWI mouse[110], which presents an autosomal recessive mutation in the GALC gene with no counterpart in humans[110]. Newborn TWI mice are indistinguishable from their unaffected littermates and at about postnatal day (PND) 21 signs of manifestations occurs. With the disease

progression animals experience severe tremors, paralysis of hind legs and neck muscles, important weight loss, and lifespan rarely extends beyond PND40.[110] Pathological changes are almost limited to the nervous system and closely recapitulate human pathology, although less severe early CNS demyelination and more extensive PNS pathology is observed.[111,112] See figure 2.5 for a schematic overview of the disease progression in the TWI mouse.

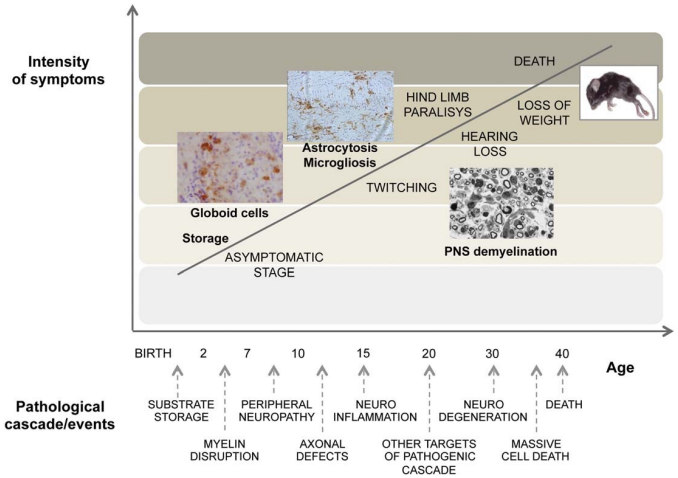


**Figure 2.5.** Representative diagram showing typical patterns of KD progression in the Twitcher mouse. The cascade of pathological events corresponds to different steps of symptomatic manifestations. Picture represents: lectin-positive cells (globoid cells), CD68-positive cells (activated microglia), and micrograph of sciatic nerve sections (adapted from Ricca and Gritti 2016).[113]

### *Hematopoietic stem cell transplantation*

HSCT is the current standard of care for KD. Unfortunately, it is not curative, and it has limited effect on patients with infantile KD. For the

adolescent, juvenile or adult onset forms, instead, it is instead more successful in slowing down the disease progression.[114]

HSCs can derive from bone marrow (BMT) or from umbilical cord blood (UCB). It is theorized that GALC-positive donor cells of hematopoietic origin can migrate to the CNS and provide sustained levels of GALC. GALC secreted by the donor cells can then be taken up by deficient cells in the CNS by the M6PR (see Section 2.1.1). Subsequently, GALC can be endocytosed and transported via the endosomal system to the lysosome, where it can exert its enzymatic activity.[115] This process, known as cross-correction, is theoretically able to supply GALC activity to neural cells of the CNS.

HSCT can provide some benefit to patients with infantile KD only if initiated before the onset of symptoms. It has been shown to decrease the severity of disease, including increased motor skills and language development.[114] If the transplant is tolerated, some cases have also reported circulating GALC activity levels similar to unaffected family members.[116] In 2005, Escolar and colleagues evaluated the efficacy of using UCB from unrelated donors. Asymptomatic newborns were transplanted with UCB with partial human leukocite antigen (HLA) mismatch. All patients that engrafted survived, and GALC activity levels in peripheral blood were at normal levels post transplantation. However, although there were significant improvements in motor-skill development compared to untreated patients, developmental delay remained apparent.[116] Furthermore, patients undergoing HSCT are at risk of developing severe graft versus host disease. While the risks associated with HSCT have decreased due to better HLA typing and the use of UCB, there are still significant risks. Some patients, indeed, still die shortly after HSCT.[117]

### *Enzyme replacement therapy*

Systemic ERT provides very low amounts of enzyme in the CNS of KD mice, resulting in negligible long-term therapeutic improvement.[118,119] Chimeric proteins have been investigated to promote enzyme transport across the BBB. For example, the protein transduction domain from HIV Tat protein fused with murine GALC (Tat-PTD) increased the secretion rate and M6PR-independent uptake of murine GALC *in vitro*.[120] Similar results have more recently been reported with the human GALC.[120] However, the efficacy of these approaches upon *in vivo* delivery remains to be tested.[113] Limited efficacy of ERT in TWI mice has been demonstrated also following intracerebral (IC) administration of the GALC enzyme.[121]

### *Substrate reduction therapy*

An alternative way to compensate for the low GALC activity is to inhibit the production of PSY. This approach is called substrate reduction therapy (SRT) and has shown promise in other LSDs.[122,115] L-cycloserine, for example, is an irreversible inhibitor of serine palmitoyltransferase, an upstream enzyme in the PSY synthesis pathway.[123] Treatment of pre-symptomatic TWI mice with L-cycloserine extended their life span by several days and decreased levels of astrocytosis.[124] However, no significant increase in myelination was observed.[124] Li and colleagues, instead, had very recently showed that pharmacological inhibition of the ACDase activity with carmofur significantly decreased PSY accumulation in cells from KD patients and prolonged the lifespan of the TWI mice. Compared to L-cycloserine, carmfour that directly inhibit ACDase may have a more

acceptable safety profile due to its mechanistic proximity to PSY biogenesis.[51]

### *Single and combined gene therapy strategies*

As already anticipated (see Section 2.1.1), also the efficacy of CNS-directed gene therapy (GT) relies on the principle of cross-correction. With the current technologies, in fact, only a relatively small proportion of cells can be transduced by a viral gene transfer vector. However, the transduced cells can then over-express GALC, which is secreted and correct adjacent cells.

Adeno-associated virus (AAV)-mediated gene therapy, in particular, allows for efficient delivery of GALC cDNA to enzyme-deficient cells, providing a persistent source of enzyme to GALC-deficient tissues. The majority of AAV capsid proteins used to pseudotype vectors for CNS applications (AAV1, 5, 9, rh10) have a strong tropism for neurons.[125] Therefore, the neurons will supply the majority of cross-corrective enzyme. Specifically, the results of the experiments using AAV in TWI mice showed prolonged life span, reduced PSY levels, increased body weight and better performance in behavioral tests. Mice, however, later die with signs similar to those of the untreated mice.[126,127,128] More recently, AAV2 genome construct expressing murine GALC was packaged in AAVrh10 capsid. Treated mice were active and symptom-free up to 8 months of age with slower symptom progression compared to untreated mice.[129] Lentiviral vectors (LVs) were also applied to transfer the functional GALC gene in the TWI CNS with proficient transduction of proliferating and post-mitotic oligodendroglia.[130] Likewhise, LV IC GT has been tested in KD affected rhesus macaques (non-human

primates, NHP).[130] This treatment protocol platform showed favorable safety profile and consistent pattern of LV transduction and enzyme biodistribution, leading to GALC activity levels in the CNS and cerebrospinal fluid (CSF) of KD NHPs close to those of non-affected animals.[130]

Very interestingly, in 2015, four different studies demonstrated that combining gene therapy with other approaches allow obtaining encouraging results in TWI mice. Specifically, Ricca and colleagues demonstrated that neonatal LV vector-mediated IC GT or transplantation of GALC-overexpressing neural stem cells (NSC) synergize with BMT, providing dramatic extension of lifespan and global clinical–pathological rescue in TWI mice.[131] Hawkins-Salsbury and co-workers simultaneously treated TWI mice with IC GT, SRT (L-cycloserine) and BMT. Treating multiple pathogenic targets at the same time resulted in an unprecedented increase in life span up to an average of 298.5 days (range of 160 – 454 days), with improved motor function, persistent GALC expression, nearly normal PSY levels, and decreased neuroinflammation.[132] Rafi and colleagues, instead, treated PND 10 TWI mice with single intravenous (IV) injection of AAVrh10-GALC 1 day after BMT. The mice show greatly extended lifespan and normal behavior with improved CNS and PNS findings.[133] Finally, in 2018 Marshall and colleagues reported a global adeno-associated virus (AAV)9-based GT protocol to deliver GALC. They demonstrated that, when globally administered via intrathecal (IT), IC, and IV injections to newborn TWI mice, this approach largely surpassed prior published benchmarks of survival and metabolic correction, showing long-term protection of demyelination, neuroinflammation and motor function. BMT performed in this protocol, moreover, without immunosuppressive preconditioning, added minimal

benefits to the AAV9 gene therapy. See figure 2.6 for an overview of the lifespan improvement obtained by treating TWI mice with different combination approach therapy involving GT.[133,132,131,134]

Despite the encouraging results obtained regarding phenotype correction on the TWI mice, however, with all tested protocols animals at a certain point suddenly die for uncertain complications. Thus, it seems that GALC activity restoring is not enough to completely correct the disease phenotype, suggesting that other secondary mechanisms could have a fundamental role in the pathophysiology of the disease.

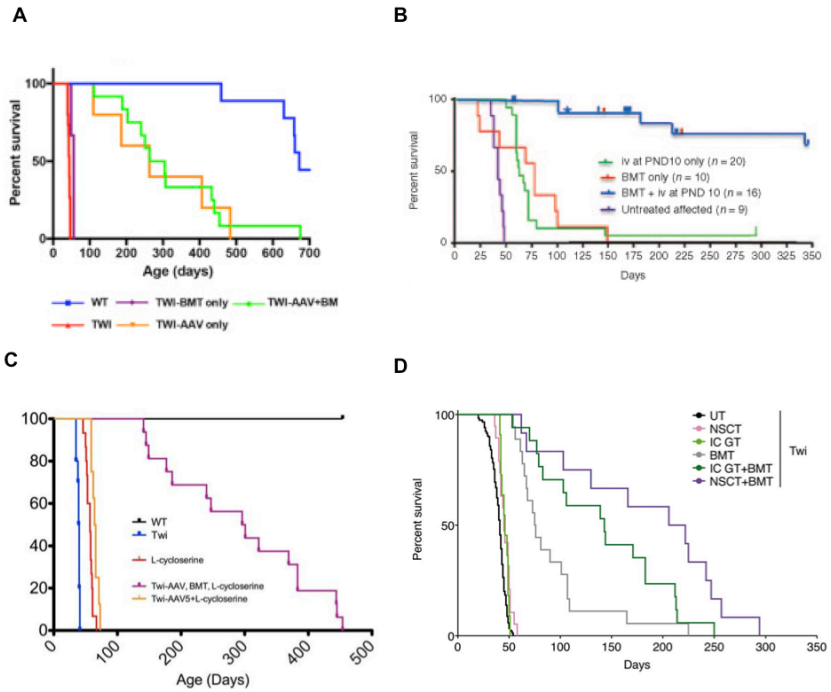


**Figure 2.6.** Kaplan-meier survival curves of Twitcher mice treated with different single or combined therapies. **(A)** Adapted from Marshall et al., 2018.[134] **(B)** Adapted from Rafi et al.,

2015.[133] **(C)** Adapted from Ricca et al., 2015.[131] **(D)** Adapted from Hawkins-Salsbury et al., 2015.[132]

### *Complementary therapeutic targets*

All events that occur downstream of the primary storage and contribute to KD pathophysiology represent potential complementary therapeutic targets.[135,136] For example, pharmacological modulators of relevant signaling pathways[92,105,69], antioxidant[76,47] and anti-inflammatory molecules[137,137] provide little clinical improvement when used as single treatments, but may represent interesting complementary approaches in combination strategies. They also might be beneficial to slow the progression of the disease, until enzymatic activity is effectively restored and the storage defects have been corrected.[113] In this perspective, pharmacological modulation of the ERK1/2, AKT, and/or GSK3b pathways, which are affected as a consequence of PSY accumulation and contribute to neuronal[105,138], oligodendroglial[68], and muscular[103] dysfunction in TWI mice may be considered as complementary therapies for KD.

Moreover, modulations of autophagy (see Chapter 4) and lysosomal trafficking are emerging as promising experimental therapeutic approaches for several LSD[113,122], aimed at enhancing storage clearance and/or implementing enzyme replacement[139,140,141].

# Chapter 3: Nanomedicine for Lysosomal storage disorders

## 3.1 Scientific background

### 3.1.1 The issue of protein delivery

In 1982 US-FDA approved the first therapeutic recombinant protein: recombinant insulin. It has been the major therapy for type 1 diabetes mellitus ever since.

In the following years, biopharmaceutical drugs based on recombinant therapeutic proteins have really transformed the pharmaceutical industry. In 2017, 293 therapeutic peptides and proteins have been approved by US-FDA, and over 900 are currently in development.[142] They target different type of diseases and represent approximately the 20% of the total number of drugs in the pipeline.[143]

Compared to small-molecules drugs, protein therapeutics are more specific and potent, serving complexes functions that cannot be mimicked by simple chemical compounds. Due to the intrinsically high specificity of proteins, moreover, there is often less possibility for them to interfere with normal biological processes and low adverse effects. Furthermore, for diseases in which a gene is mutated, protein therapeutics can provide effective replacement therapy without the need for GT.[144]

However, as the macromolecular nature of proteins provides the structural complexity required for specificity, it makes also them among the most challenging molecules to formulate and deliver. Loss of proteins activity during storage or in the body is one of the major issues regarding formulation technologies. Factors as temperature, moisture and buffer in

which proteins are dissolved can significantly affect proteins functionality. Regarding protein delivery, instead, the main challenges are due to high molecular mass of these types of drugs, which results in poor permeability across biological barriers such as skin, blood brain barrier (BBB), mucosal barrier and cell membranes.

Despite the mentioned disadvantages, many delivery strategies have been recently developed, enabling the commercialization of many of successful products[144] and suggesting that advantages of protein therapeutics exceed their limitations.

### *Systemic delivery*

The simplest way to administer protein therapeutics is by systemic delivery. However, therapeutics proteins (recombinant proteins, peptides or enzymes) are commonly bound by proteins of blood and removed by first pass liver clearance. Even molecules that can circulate in the blood are often degraded by proteases or accumulate in off-target districts. Nonetheless, therapeutic approaches based on the systemic delivery of recombinant proteins exist. It is the case, for example, of recombinant enzymes used to treat LSDs.

The first enzyme product to be licensed for this use was *alglucerase*. It was used for the treatment of Gaucher disease (GD), a chronic congenital disorder of lipid metabolism caused by a deficiency of the lysosomal enzyme β-glucocerebrosidase. GD is characterized by enlarged liver and spleen, increased skin pigmentation and painful bone lesions.[145,146] At first, β-glucocerebrosidase was purified from human placenta (*alglucerase*), which required purification of about 50000 placentas per patient per year,

obviously placing practical limits. A recombinant form of β-glucocerebrosidase was than developed (*Imiglucerase*). *Imiglucerase* is available in sufficient quantities to treat many more patients and also eliminated the risk of transmissible disease correlated with the purification from placentas.[147] At present, *Imiglucerase* is considered a highly effective treatment for GD, although it remains one of the most expensive drugs available on the market (annual cost for US patients of $200000).[148] In type 1 GD, intravenously administered enzyme is efficiently delivered to the target cells, the macrophages, and the response can be easily monitored by measuring organomegaly and hematological parameters, and by imaging bone and bone marrow. By *Imiglucerase* treatment, livers and spleens shrink, cytopenias improve, the bone marrow normalizes and, most importantly, patients feel much better.[149]

At the moment, five more ERTs have been approved for five other LSDs: Fabry disease (FD), Mucopolysaccharidosis (MPS) type I, II and VI, and glycogen storage disease (GSD) type II (Tab. 3.3). Unfortunately, none of these has the same efficacy as the treatment with *Imiglucerase*. This seems to be caused by the cell type affected in a given LSD.[150] In addition, an intravenously administered enzyme is completely excluded from some tissues, as the brain. *Imiglucerase*, in fact, has no effects on neuronopathic manifestations of type 2 and 3 GD, and ERT is contraindicated in patients with MPS I or II who have cognitive impairment as it will not change their ultimate prognosis.[151] In order to compensate the weaknesses of these therapies, large concentrations and frequently repeated administrations are used as short-term treatment options. Alternatively, approaches based on modified proteins and on nanovectors are currently under study.

| LSD | ERT product(s) and dosing | Endpoints in clinical trials | Efficacy in clinical practice | Unmet needs |
|---|---|---|---|---|
| **GD** | Imiglucerase 15-60 Units/kg every other week<br>Velaglucerase α 15-60 Units/kg every other week | Improvements in blood counts and in organomegaly<br>Improvements in blood counts, reductions in organomegaly | Resolution of symptoms and most signs of disease, improved quality of life<br>Little experience to date but likely to be similar to imiglucerase | Cannot treat neuronopathic disease. Effects on bone may not be optimal |
| **FD** | Agalsidase α 0.2 mg/kg every other week<br>Agalsidase β 1 mg/kg every other week | Improvements in pain scores and decreased use of analgesics. Stabilization of renal function. Reduction in left ventricular hypertrophy. Reduction in GL-3 in plasma, urine and tissue biopsies.<br>Clearance of GL-3 from endothelial cells, tissue and plasma. Stabilization of renal function. | Stabilize renal function and cardiac size, improve pain and quality of life. Some reduction in frequency of occurrence of established renal failure and cardiovascular events | Cannot reverse established disease and patients treated as adults continue to suffer significant morbidity and mortality. Not clear whether early treatment can prevent development of significant end-organ involvement |
| **MPS I** | Laronidase 100 Units/kg weekly | Improved respiratory function and walking ability. Reduction in hepatomegaly, left ventricular mass and urine GAG | Improvements in hepatomegaly, growth, joint mobility, breathing, and sleep apnea in patients with milder disease phenotypes | Bony disease persists. Not prevent cognitive decline |
| **MPS II** | Idursulfase 0.5 mg/kg weekly | Improved respiratory function and walking ability. Reduction in organomegaly, left ventricular mass and urine GAG | Reductions in hepatomegaly with some improvements in mobility and respiratory function | Bony disease persists. Not prevent cognitive decline |
| **MPS IV** | Galsulfase 1 mg/kg weekly | Improvements in walking and stair climbing. Reduction of urine GAG | Improved endurance and growth | Lack of effect on skeletal dysplasia and corneal clouding |
| **GSD II** | Alglucosidase α 20 mg/kg every other week | Infantile-onset form: Increased survival, decreased left ventricular mass. Late- | Infantile-onset form: cardiomyopathy resolves but skeletal muscle involvement | Infantile-onset form: preventing death from cardiac failure may simply leave babies immobile and |

| | | | |
|---|---|---|---|
| | onset form: Improved walking and stabilized pulmonary function | progresses. Once patients have been ventilated, they will remain ventilator-dependent. Late-onset form: some improvements in muscle strength in first year of treatment with subsequent stabilization. Improved wellbeing. | ventilator-dependent. Some responders who have gained motor milestones may show late, peripheral involvement. Late-onset form: very high doses needed to see effect on skeletal muscle |

**Table 3.3.** Enzyme replacement therapy for LSDs: agents available and their efficacy. Adapted from Lachmann et al., 2011.[149]

### *Modified proteins*

To enhance the capability of therapeutic proteins and enzymes to overcome circulation and reach the desired intracellular targets, specific modification of these molecules can be exploited. In this context, peptide-modified enzymes have been broadly tested to improve the delivery of lysosomal enzymes.

Efforts have been made to obtain endocytosis of lysosomal enzymes in a glycosylation-independent manner, by capitalizing on the insulin-like growth factor II (IGF-II) that binds to a different domain of the M6PR (Fig. 3.7). Based on this principle, a chimeric enzyme was created, containing recombinant β-glucuronidase (the deficient enzyme in MPS VII) fused to a peptide derived from IGF-II.[152] This fusion-enzyme efficiently targeted M6PR, followed by clathrin-mediated endocytosis and lysosomal delivery. Importantly, in skin fibroblasts from MPS VII patients and the MPS VII mouse model, binding of the fusion-enzyme to the M6PR was enhanced as compared to the enzyme lacking the targeting peptide. Yogalingam and colleagues, instead, developed an IGF-II-tagged alpha-N-

acetylglucosaminidase (the deficient enzyme in MPS III). Their results suggest that the fusion-enzyme has increased M6PR-mediated lysosomal targeting to neurons and astrocytes, two critical cell types in MPS III.[153]

Fusion-enzymes have been designed also to target endocytic receptors alternative to M6PR present on the cell surface. α-l-iduronidase or α-glucosidase, the lysosomal enzymes deficient in MPS I and Pompe disease, respectively, have been synthesized as recombinant proteins fused to a peptide derived from the receptor associated protein (RAP). RAP-derived chimeras of α-l-iduronidase or α-glucosidase showed a significant enhancement of uptake into skin fibroblasts isolated from patients, rat glioma cell cultures, and mouse myoblasts.[154]

In addition, fusion-enzymes containing protein transduction domains, such as peptides derived from the HIV transcription factor Tat, have been produced (Fig. 3.7). Although the mechanism of Tat internalization is still controversial, it is believed that charge-mediated electrostatic interactions of Tat with membrane phospholipids and polysaccharides can facilitate internalization of the enzyme within cells.[19] Several works have focused on gene and enzyme therapies using recombinant lysosomal enzymes fused to Tat peptides, including β-glucuronidase, gluco-cerebrosidase, and galactocerebrosidase for treatment of MPS VII, GD, and KD, respectively.[155,156,120,157]

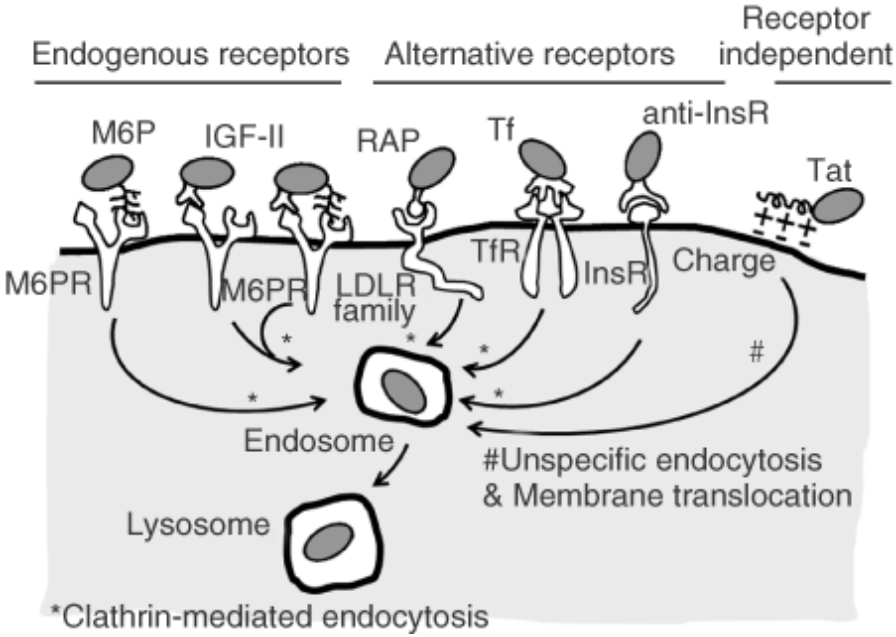


**Figure 3.7.** Fusion-lysosomal enzymes. To improve ERT for LSDs, recombinant enzymes constituted by the an enzymatic module fused to an affinity peptide were produced. Peptides can target natural receptors of lysosomal enzymes, as the mannose-6-phosphate receptor (M6PR), which can be targeted by M6P and insulin-like growth factor II (IGF-II). They can also target alternative receptors of endocytosis: the low-density lipoprotein receptor (LDLR; targeted by receptor-associated protein RAP), the transferrin receptor (TfR; targeted by transferrin, Tf), or the insulin receptor (InsR; targeted by a peptide derived from an antibody to InsR, anti-InsR). Fusion-enzymes can also be addressed to negatively charged domains of the plasma membrane, which can be targeted by Tat peptides. Fusion-enzymes targeted by the described peptides enter inside cells and traffic to lysosomes via clathrin-mediated endocytosis, instead those targeted by Tat use unspecific endocytosis. From Muro et al., 2010.[19]

Thus, it is evident that these fusion-enzymes display enhanced uptake by cells *in-vitro.* They also showed improved delivery to the organs of the reticuloendothelial system in animal models.[19] The CNS remains, however, a challenging target for this type of strategy.

### *Nanoparticles*

Nanoparticles (NPs), which can be composed of different materials such as lipids, polymers or dendrimers, have been much studied as carriers agents (Fig. 3.8).[158,159,] Several of them have already been commercialized, as pacilitaxel-containing albumin nanoparticles (*Abraxane*) for treatment of patient with breast cancer, or doxorubicin liposomes (*Doxil*) for the treatment of ovarian cancer and AIDS-associated sarcoma.

Despite NPs are typically studied for small-molecules deliveries, recent studies demonstrated their ability also in encapsulating and delivering bigger molecules as proteins. A promising example is the delivery of cytokines for tumor immunotherapy. Specifically, immunosuppressive factors associated with the tumor microenvironment, in particular the transforming growth factor-β (TGFβ) inhibitor and the immunostimulant interleukin-2 (IL-2), were encapsulated into a single liposomal polymeric nanoparticle. This method led to sustained local delivery, thereby reducing the toxicity of IL-2, and the combination therapy delayed tumor growth and increased survival in a mouse model of melanoma.[160] Among protein delivered through NPs-mediated approach, moreover, enzymes deserve special attention. Enzyme encapsulation, in fact, can protect the physicochemical characteristics of the molecule, eradicating some of the key limitations of ERT, including immunologic reactions and degradation.[161,162] It can also enhance the pharmacological response by improving pharmacokinetics and pharmacodynamics and allowing controlled release of the payload.[19] In 2015, for example, Tancini and colleagues demonstrated the ability of poly-(lactide-co-glycolide) (PLGA) NPs in deliver recombinant acid α-glucosidase (GAA) in GAA deficient Fibroblasts. Enzymatic activity

tests reported a more efficient cellular uptake of GAA loaded to NPs and a more significant stability of the enzyme (up to 7 days) *in vitro*, if compared with the same amount of GAA given as free enzyme.[163] Galliani and colleagues, instead, demonstrated that PLGA nanoparticles could be loaded with GALC, α and β-glucosidase and palmitoyl protein thioesterase 1 [PPT1; defective in Neuronal Ceroid Lipofuscinosis 1 (NCL1) disease]. This system allowed enzymes encapsulation with excellent activity retention and permitted the recovery of the full PPT1 enzymatic activity in human NCL1 cells (see Section 3.2).[164] Kelly et al., finally, demonstrated that Polyethylene glycol-b-poly(lactic acid) (PEGPLA) polymersomes loaded with recombinant β-galactosidase can deliver active β-galactosidase to an *in vitro* model of GM1 gangliosidosis.[165]

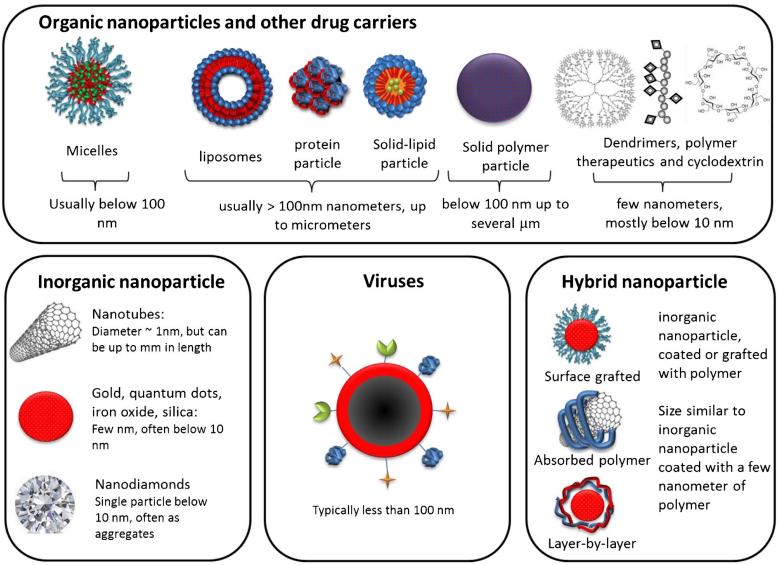


**Figure 3.8.** Different types of nanoparticles and relative sizes. From Young et al., 2016.[158]

### 3.1.2 Blood brain barrier and CNS drug delivery

#### *BBB anatomy and transport mechanism*

The blood–brain barrier (BBB) is a term used to describe the unique properties of the microvasculature of the CNS. CNS vessels are continuous and nonfenestrated, but also contain a series of additional properties that allow them to tightly regulate the movement of molecules, ions, and cells between the blood and the CNS.[166] From the anatomical point of view, BBB is composed from: endothelial cells connected by tight junctions (TJ), basal lamina, pericytes embedded in basal lamina and astrocytes that touch with the endfeet of their projections the abluminal side of brain vessels and neurons.[167] The normal function of endothelial cells is mainly dependent on the presence of the junctional complexes: TJ and adherens junctions (AJ). TJ, especially, are essential for BBB functioning, as they limit the passage of polar solutes by paracellular ways. AJ plays a role in sustaining the structure and tightness of the BBB.

The passage of molecules through the BBB is finely regulated by their physical and chemical characteristics, like affinity for a certain transference system and molecular weight. BBB absorption can occur by mean of three mechanisms: passive or active transport, and efflux (Fig. 3.9). Passive transport comprises the following non-energetic transportation pathways: a) paracellular diffusion, which allows the passage between endothelial cells of hydrophilic compounds; b) transcellular diffusion, which allows the passage through endothelial cells of small lipophilic compounds. Active transport, instead, enables the movements of substances (such as nutrients, ions and endogenous substance) into the CNS in an energy-dependent way.

This type of transport includes: a) carrier mediated transcytosis that is suitable for relatively small molecules; b) absorptive mediated transcytosis for positively-charged peptides; c) receptor-mediated transcytosis.

Receptor-mediated transcytosis is a specific process that uptakes macromolecules present on the luminal side of brain endothelial cells and transports them into the brain. It consists in specific receptors that bind conforming ligands activating internalization into cells. This type of transport is especially exploited by endogenous peptides, as insulin, Tf, IGF and nicotinic acetylcholine receptor.[168]

On the other hand, absorptive-mediated transcytosis does not require plasma membrane receptors. This transport, in fact, is triggered by the electrostatic interactions which occur between the negatively-charged surface of endothelia and the positively-charged blood proteins. Cationic therapeutic complex, thus, can take the absorptive mediated transcytosis to enter the CNS. Cationized albumin, for example, was used as a targeted drug delivery approach in investigational models of neurodegeneration.[169]

Again, carrier-mediated transport represents the path by which nutrients can be delivered into the brain by capillary endothelial luminal and abluminal membranes (membranes associated with the blood component or with the brain extracellular fluid, respectively) through specialized transporters.[170] For example, the glucose transporter (GLUT-1) facilitates the crossing of glucose to the brain, whereas valine, histidine, methionine and tyrosine are carried by the System-L transporter. L-DOPA (anti-parkinson) is a classic example of drug that enters the CNS by this mechanism, through the large amino acid transporter 1 (LAT-1).[171]

Finally, efflux mechanisms also exist. The most known is the P-glycoprotein mechanism, which is able to pump out undesirable complexes, as anticancer drugs and antibiotics.[172]

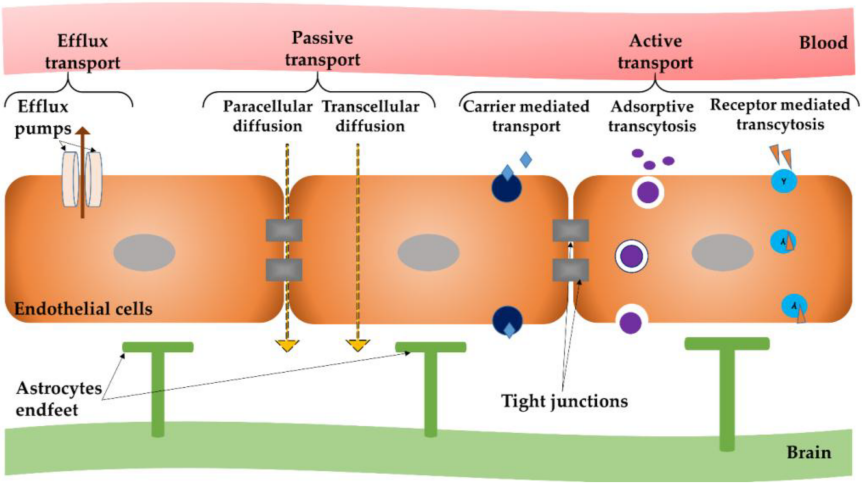


**Figure 3.9.** Transport mechanism across the BBB. From Teleanu et al., 2019.[173]

### *Drug delivery across BBB*

It has been estimated that more than 90 % of all small-molecules drugs and nearly 100 % of all larger therapeutics are not able to overcome the BBB.[170] Many research efforts, therefore, are directed to the development of new strategies capable to make drugs that can cross the BBB and reach the CNS.

Both invasive and non-invasive techniques for BBB-crossing are currently under study (Fig. 3.10). Regarding invasive techniques, an option is the BBB transient disruption with nonoxious agents, hyperosmotic

solutions or ultrasounds. Moreover, this approach is non-patient friendly and compromises the integrity and the physiological functions of the BBB.[174] Another investigated invasive technique is the direct intracerebroventricular or IT infusion of the drug. Currently, clinical trials are ongoing in humans to test the safety and tolerability of recombinant human heparan-N-sulfatase and idursulphase formulated for IT administration in MPS III and MPS II patients, respectively.[175,176] Although outcomes from these studies encourage further investigations, the clinical application of these approaches is considered challenging due to the short half-life of the enzymes. Frequent and high-dose injections, in fact, would be necessary to increase the chance for clinical success, increasing moreover also the possibilities for toxic effects and immunoreactions.

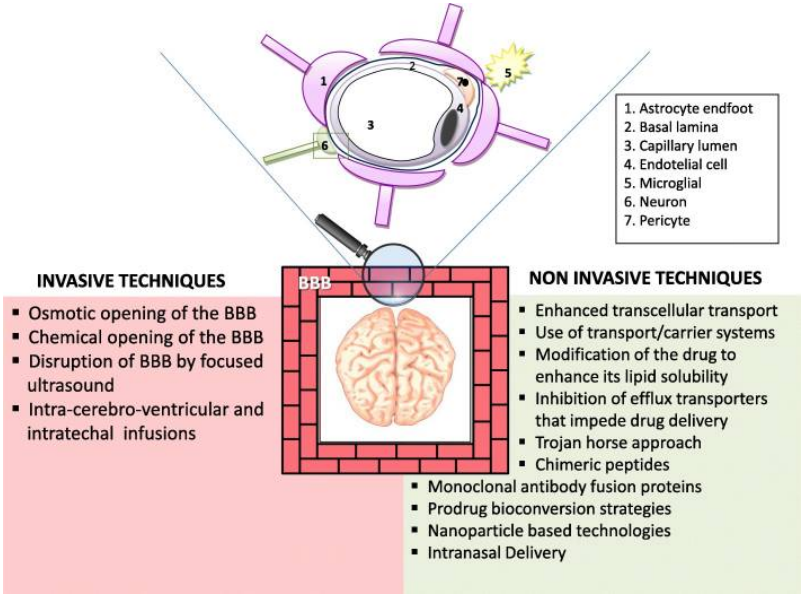


**Figure 3.10.** Techniques for brain delivery. From Bellettato and Scarpa; 2018.[174]

On the other hand, many non-invasive strategies consisting in modifying drugs to facilitate their transport across the BBB have been recently developed. Some possibilities are, for example, the modification of the specific drug to enhance its lipid solubility[177], the synthesis of peptides or antibody-fusion proteins[178], and the targeted NPs technologies. This latter approach, in particular, offers a promising method for successfully treating brain disease. NPs (see Section 3.1.1), in fact, can be functionalized with targeting agents (as peptides or aptamers) to allow the nanovector to get through the BBB.[179,180] Moreover, depending on the core material, it is possible to fine tune almost all the physical characteristics of the NPs including: size, shape, charge, binding capacity, and hydrophobicity/hydrophilicity. These factors correlate to the NP pharmacokinetic half-life, biodistribution, stability, and binding capacity for the therapeutic protein or enzyme.[181] Polymeric PLGA NPs, in particular, are a very attractive option, owing to the biocompatibility of this material, which has been already approved by the US-FDA for human use. Recently, *in-vivo* studies using PLGA NPs conjugated with the simil-opioid glycopeptide g7 demonstrated that these NPs are able to overcome the BBB after intraperitoneal, intranasal, and oral administrations.[182,183]

These results have supported the application of g7-NPs for delivering therapeutic enzymes across the BBB, as performed in two studies on MPS I and MPS II animal models.[183,184] First, Salvalaio and colleagues aimed at assessing the g7-PLGA NP brain delivery capacity using FITC-albumin, a model drug with a molecular weight similar to that of the lysosomal enzymes. Results demonstrated the g7-PLGA NPs ability to cross the BBB and to localize in all brain parenchyma.[183] Later, Rigon and colleagues

demonstrated the capability of g7-PLGA NPs to deliver iduronate 2-sulfatase (IDS) enzyme in the brain of MPS II mice. The 6-weeks treatment produced a significant reduction of GAG deposits in liver and brain tissues, as well as a reduction of some neurological and inflammatory markers.[184]

These data proved the applicability of targeted NPs for therapeutic delivery of high molecular weight molecules in the brain, encouraging especially their application for the delivery of therapeutic enzymes.[174]

### 3.1.3 Blood nerve barrier and PNS drug delivery

Delivery of therapeutic compounds to the PNS is difficult to achieve due to complicated nature of the blood-nerve barrier (BNB).

Endoneurial vasculature is lined by non-fenestrated endothelial cells linked by specialized tight junctions, forming a restrictive barrier that protects the endoneurial microenvironment and ensures that molecules and ions in the systemic circulation will not interfere with sensory and motor signal transduction.[185] Groups of axons and endoneurial blood vessels together form fascicles, which are further protected from the periphery by the perineurium, a component of the BNB composed of concentric layers of basement membrane and sheets of perineurial cells (Fig. 3.11). The entire nerve is surrounded by the collagenous epineurium, which provides tensile strength but does not contribute to the BNB. While the BNB is fundamental for normal function it hinders the transport of therapeutic compounds from the vasculature into the nerve. The sciatic nerve itself is impermeable to hydrophilic small molecules as well as larger biologics; only small, lipophilic molecules can easily access the endoneurium.[186]

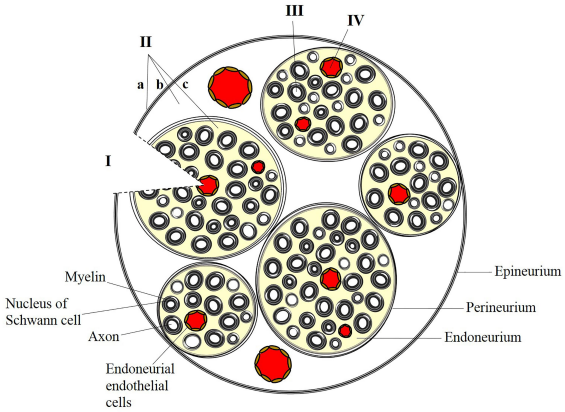


**Figure 3.11.** Strategies for targeted delivery to the peripheral nervous system. (I) Direct placement of a bioengineered nerve conduit in the presence of breached perineurial and blood-nerve (endoneurial) barriers. (II) Administration of anesthetic or analgesic by injection at or outside the epineurium (a), outside the perineurium (b), or within a fascicle (c). Administration of a peptide or protein requires localized, transient disruption of perineurial and blood-nerve barriers. (III) Presynaptic uptake and retrograde trafficking at peripheral nerve terminals results in delivery of cargo along individual axons within a fascicle. (IV) Endothelial targeting of systemically administered nanoparticles can preferentially target the endoneurial vasculature. From Langert and Brey, 2018.[186]

There are three main strategies that are currently investigated for the BNB drug-delivery (Fig. 3.11). Injury or traumatic damage to the nerve, for example, can breach the BNB. Here, biomaterials can be directly implanted into the peripheral nerve environment providing bypassing the BNBr.[187] Strategies based in gene therapy can also be exploited to target peripheral nerves in the presence of an intact barrier. Here, targeting can be conveyed by incorporating bacterial toxins that display natural neurotropism for ganglioside receptors that are enriched at presynaptic terminals. Retrograde transport can facilitate delivery of encapsulated cargo along the axon, to the dorsal root ganglia, or spinal cord. This approach has been investigated in models of regeneration, inherited neuropathies, and neuropathic pain.[186]

Finally, for systemically administered nanocarriers, the most promising strategy consists in incorporating PNS-specific modifications, such that the administered compounds will be: protected from degradation/phagocytosis/opsonization within the circulation, identify and recognize the targeted peripheral nerves, and be able to cross the BNB. Recently, a novel preparation of dioleoyl-phosphatidylcholine (DOPC) based liposomes could preferentially target peripheral neurons and Schwann cells when conferred with some key modifications that mimic properties of neural cell membranes has been studied.[188]

## 3.2 Cross-Linked Enzyme Aggregates as Versatile Tool for Enzyme Delivery: Application to Polymeric Nanoparticles.

*The experiments presented in this Section have been published after peer-reviewing in Bioconjugated Chemistry 29(7), 2225-2231. Co-authors of this work are: Galliani M, Santi M, Del Grosso A, Cecchettini A, Santorelli F M, Hofmann S L, Lu J Y, Angella L, Cecchini M and Signore G. Role of authors: study concept and design: MG, GS. Acquisition of data: All authors. Analysis and interpretation of data: All authors. Drafting of the manuscript: All authors. Statistical analysis: MG, GS. Obtained funding: GS, MC. Study supervision: GS.*

*I, in particular, set up the methods for the purification of the recombinant enzyme GALC, produced it for the subsequent encapsulation experiments, and contributed to the discussion and presentation of the obtained data.*

### 3.2.1 Introduction

As already explained in par. 3.1.1, protein delivery represents to date one of the most promising strategies for the treatment of diseases such as cancers, diabetes and rare diseases like LSDs.[144]

NP-based carriers (see par. 3.1.1 and 3.1.2) represent a promising platform for protein and enzyme delivery, as they can protect the payload from degradation and target specific areas even beyond the BBB. Thus, preparation of stable, efficient formulations of active proteins in nano-structured vectors is an actively researched topic. Liposomes and polymeric NPs have been extensively investigated, usually with heterogeneous results due to unpredictable encapsulation efficiency and activity retention.[189,190,191,192,193,194,195] Among the investigated materials for NP synthesis, PLGA has received special attention, being a biocompatible, nontoxic, and

FDA-approved polymer for intravenous administration in humans.[196] However, successful encapsulation of proteins and enzymes in PLGA NPs is still an open issue. Most studies on protein loading in PLGA NPs are based on double emulsion/solvent evaporation method that requires harsh conditions (such as halogenated solvents and sonication) which could easily denature proteins and enzymes.[197,163] Several efforts have been made to adapt other methods, such as nanoprecipitation, to protein loading, whereas recent work has investigated the use of either polycation-modified PLGA or copolymers of the analogous poly(lactic acid) and poly(ethylene glycol) (PLA– PEG).[198,199,200,201,202,165]

Although some of these strategies led to fairly good results, to date there is no reliable approach for efficient loading of enzymes with good encapsulation efficiency and activity retention. In the framework of our interest in drug delivery in LSDs, we demonstrate here a new encapsulation strategy that allows loading enzymes with excellent efficiency and activity retention.

### 3.2.2 CLEA NPs synthesis and characterization

We investigated the use of cross-linked enzyme aggregates (CLEAs). CLEAs were first described in the early 2000s, and are produced by precipitation of the enzyme into a water-miscible solvent together with cross-linking of the physical aggregates. CLEAs are usually stable in organic solvents and show unaltered and in some cases even enhanced enzymatic activity compared with the parent enzymes.[203,204,205] Our approach to the synthesis of CLEAs-loaded NPs (CLEA NPs) was based on a two-step process. In the first step, CLEAs were synthesized by adding the enzyme solution to acetone in the presence of glutaraldehyde, resulting in Schiff

base formation and subsequent cross-linking of the precipitated enzyme (Fig. 3.12 A).

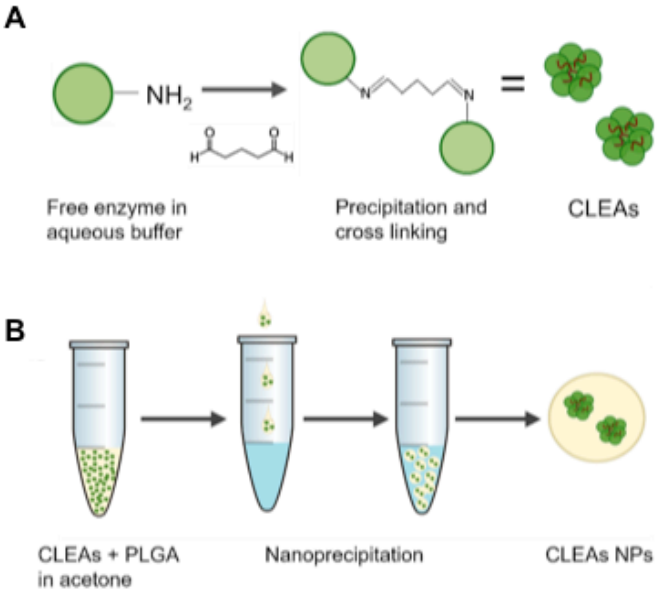


**Figure 3.12. (A)** Schematic illustration of CLEAs and **(B)** CLEAs NPs synthesis.

In the second step, CLEA NPs were produced by nanoprecipitation (Fig. 3.12 B). CLEAs and PLGA were mixed in acetone and added dropwise to an aqueous solution of sodium cholate. When transferred into water, PLGA precipitates and spontaneously encapsulates CLEAs in NPs that can be collected by centrifugation. To better understand the role of the cross-linker, we also prepared control enzyme aggregates-loaded NPs (EA NPs) by precipitating the enzyme in absence of cross-linker in the first step (leading to physical enzyme aggregates, EAs). Next, we evaluated physicochemical properties and encapsulation efficiency of CLEA NPs. CLEAs encapsulation

affects neither the size nor the surface charge of NPs compared to empty NPs produced with the same strategy (Tab. 3.4). We tested the strategy on four enzymes currently investigated for ERT: palmitoyl protein thioesterase 1 [PPT1; defective in Neuronal Ceroid Lipofuscinosis 1 (NCL1 disease)], α glucosidase (αGLU; defective in Pompe disease), β glucosidase (βGLU; defective in Gaucher's disease) and GALC (see Tab. 2.1).

| | **CLEAs NPs** | | **EAs NPs** | | **DE NPs** | |
|---|---|---|---|---|---|---|
| **Loaded enzyme** | *HD (nm) (SEM)* | *ZP (mV) (SEM)* | *HD (nm) (SEM)* | *ZP (mV) (SEM)* | *HD (nm) (SEM)* | *ZP (mV) (SEM)* |
| **PPT1** | 126 (3) | -32 (1) | 158 (5) | -36 (3) | 233 (79) | -33 (5) |
| **GALC** | 167 (5) | -37 (1) | 166 (2) | -37 (1) | 136 (1) | -36 (3) |
| **αGLU** | 206 (2) | -37 (2) | 169 (2) | -37 (2) | 228 (96) | -37 (2) |
| **βGLU** | 184 (1) | 33.4 (0.4) | 178 (4) | -38 (2) | 125 (10) | 37.0 (0.4) |

**Table 3.4.** Size and Zeta Potential of CLEAs NPs, EAs NPs and DE NPs. HD = hydrodynamic diameter. ZP = zeta potential. SEM = standard error of the mean of three independent experiments.

Indeed, all formulations show hydrodynamic diameter ranging from 130 to 200 nm and zeta potential around −35 mV, in keeping with values usually observed for PLGA NPs obtained by nanoprecipitation. Enzyme encapsulation efficiency in NPs was determined via ninhydrin assay after amino acid digestion, since other approaches based on the quantification of intact protein complexes afforded no reproducible results. In all cases encapsulation efficiency for CLEA NPs largely exceeds what was found for double emulsion NPs (DE NPs) and is far superior to what was observed for EAs in all cases except for αGLU (Tab. 3.5).

| | EE% (SEM) | | |
|---|---|---|---|
| **Loaded enzyme** | *CLEAs NPs* | *EAs NPs* | *DE NPs* |
| **PPT1** | 88 (11) | 0.9 (0.4) | 32 (7) |
| **GALC** | 47 (7) | 35 (3) | 26 (3) |
| **αGLU** | 13.8 (0.3) | 31 (3) | 9 (3) |
| **βGLU** | 69 (6) | n.d. | 40 (11) |

**Table 3.5.** Encapsulation efficiency (EE) of CLEAs NPs, EAs NPs and DE NPs loaded with PPT1, GALC, αGLU or βGLU. n.d. = no data, the obtained value is equal to or lower than the blank value for all batches. SEM = standard error of the mean of three independent experiments.

This behavior can be easily rationalized considering a different partitioning equilibrium between aqueous and organic phase of EAs, free enzyme, and CLEAs, whose surface lysine residues are derivatized and made hydrophobic by the cross-linker. This could lead to different water solubility, and hence lowered encapsulation efficiency for the more hydrophilic underivatized enzymes.

Next, we examined in more detail whether CLEAs are actually encapsulated in the inner part of the NPs or rather adhered to the surface. To this end, we labeled CLEAs with Atto488 (488-CLEAs) and encapsulated them into NPs tagged with Atto633-labeled PLGA (633-NPs). The internalization of 488-CLEAs into 633-NPs was first verified by confocal imaging and colocalization analysis. Confocal images of 488-CLEA 633-NPs (Fig. 3.13) revealed that all green labeled CLEAs are associated with red labeled NPs (Manders' coefficient: >0.7 in all formulations), while several empty 633-NPs are also present in the samples (Manders' coefficient ≤0.5 (Fig. 3.13).

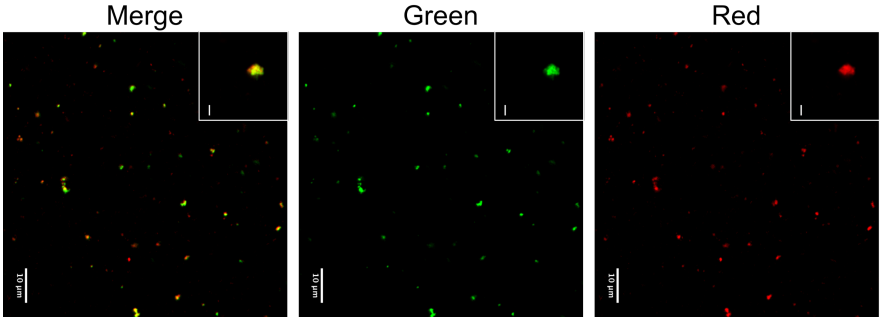


**Figure 3.13.** Representative confocal images of PPT1 488-CLEAs 633-NPs. Inset scale bar = 2 μm.

To confirm this result, we performed a KI quenching assay, which provides an evaluation of the interaction between a fluorophore and the water environment by exploiting the well-known fluorescence quenching effect of a KI solution. Stern–Volmer plot of 488-CLEAs quenching shows that, for all formulations, encapsulated 488-CLEAs have a lower Stern–Volmer quenching constant (KSV) with respect to 488-CLEAs outside NPs, reflected by a lower slope of the regression line (Fig. 3.14 and Tab. 3.6).

| Loaded enzyme | *488-CLEAs 633-NPs* | *488-CLEAs + 633-NPs* |
|---|---|---|
| **PPT1** | 8.7 | 30.6 |
| **GALC** | 16.3 | 44.2 |
| **aGLU** | 6.2 | 41.6 |
| **bGLU** | 9.1 | 40.6 |

**Table 3.6.** Stern-Volmer constant (KSV) from quenching of 488-CLEAs in 488-CLEAs 633-NPs and 488-CLEAs outside 633-NPs.

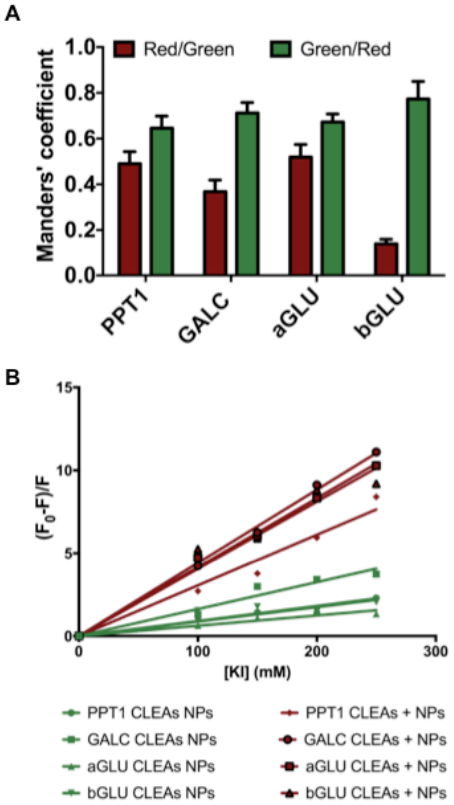


**Figure 3.14. (A)** Manders' coefficient resulting from colocalization analysis of 488-CLEAs 633-NPs formulated with PPT1, GALC, αGLU and βGLU. Error bars represent the standard error of the mean of 10 analysis. **(B)** Stern-Volmer plot resulting from quenching of 488-CLEAs in 488-CLEAs 633-NPs (green points) and 488-CLEAs outside 633-NPs (red points) with increasing concentrations of KI. $F_0$ and F are the fluorescence intensities in absence and in presence of the quencher, respectively.

This suggests that CLEAs are encapsulated in the inner part of the NP and effectively shielded from the solvent. Remarkably, the ability of NPs to decrease the quenching rate of embedded compounds is also reflected by the low KSV of 633-PLGA, that is screened by the NP itself (Fig. 3.15 and Tab. 3.7).

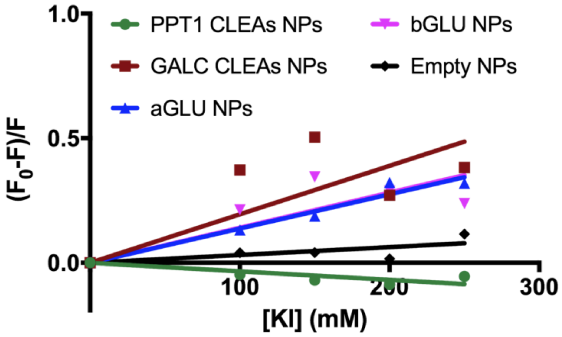


**Figure 3.15.** Stern-Volmer plot resulting from quenching of 633-NPs in 488-CLEA 633-NPs and empty 633-NPs with increasing concentrations of KI. $F_0$ and F are the fluorescence intensities in absence and in presence of the quencher, respectively.

| Loaded enzyme | *488-CLEAs 633-NPs* |
|---|---|
| **PPT1** | 0.3 |
| **GALC** | 1.9 |
| **αGLU** | 1.4 |
| **βGLU** | 1.4 |

**Table 3.7.** Stern-Volmer constant (KSV) from quenching of 633-NPs in 488-CLEAs 633-NPs and empty 633-NPs.

### 3.2.3 Release profile of CLEA NPs

We then evaluated the release profile of PPT1 488-CLEA 633-NPs in neutral and acidic environment at 37 °C (Fig. 3.16 A). In both cases, PPT1 release profiles are biphasic and typical of PLGA NPs, characterized by an initial burst release followed by a sustained release.[195,206]

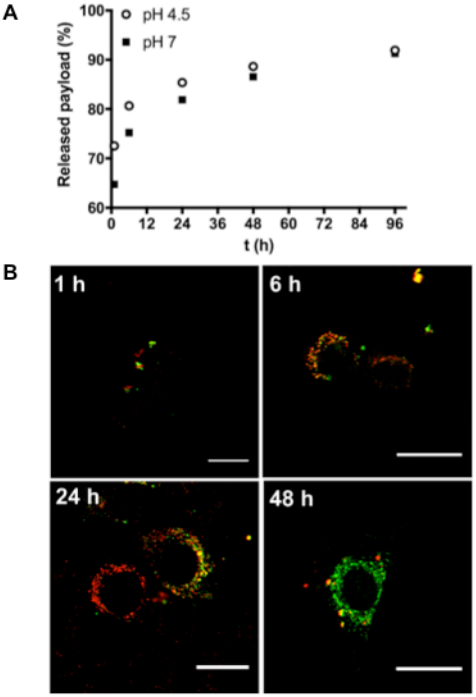


**Figure 3.16. (A)** Release profile of PPT1 488-CLEAs 633-NPs in acidic and neutral buffer at 37°C. **(B)** Confocal images of NIH-3T3 cells treated with PPT1 488-CLEAs 633-NPs 1, 6, 24 and 48 hours after administration. Figures display red/green (NPs/CLEAs) superimposed images. Scale bars = 25 μm.

Release profile is in line with what was previously reported on PLGA NPs in neutral and acidic media. The different behavior could be related to the predominance of PLGA erosion or acid-catalyzed hydrolysis at pH = 7.4 and 4.5, respectively.[207,208] The Stern–Volmer plot evidences that virtually no enzyme is present on the surface of the NP; thus, the observed burst release is likely due to the release of a fraction of enzyme located in proximity to the surface.

We then evaluated the loss of activity due to the process of cross-linking and encapsulation in NPs (Tab. 3.8). As expected, enzymatic activity of EAs is higher than in CLEAs, due to the structural modifications occurring to the protein upon cross- linking.

| | AY % (SEM) | | | | |
|---|---|---|---|---|---|
| **Loaded enzyme** | *CLEAs* | *CLEAs NPs* | *EAs* | *EAs NPs* | *DE NPs* |
| **PPT1** | 6 (2) | 64 (11) | 54 (2) | 27 (6) | 0.5 (0.2) |
| **GALC** | 28 (4) | 59 (6) | 27 (2) | 16 (2) | n.d. |
| **αGLU** | n.d. | n.d. | 35 (4) | 37 (3) | n.d. |
| **βGLU** | 25 (10) | 61 (13) | 2 (7) | n.d. | 0.1 (0.1) |

**Table 3.8.** Activity yield (AY) of CLEAs, CLEAs NPs, EAs, EAs NPs and DE NPs loaded with PPT1, GALC, aGLU or bGLU. n.d. = no data, the obtained value is equal to or lower than the blank value for all batches. SEM = standard error of the mean of three independent experiments.

This pattern is completely reversed when loaded NPs are considered. EAs usually experience a significant loss of activity upon encapsulation in PLGA, while CLEAs loaded in NPs show increased activity compared with CLEAs precursor, except for αGLU, which remains completely inactive. The apparently counterintuitive activity increase upon encapsulation could be rationalized by taking into account the well-known enhancement of catalytic activity of NP-immobilized enzymes, which in our case could apply to the immobilized CLEAs.[209,210]

Furthermore, the mildly acidic environment typical of PLGA might promote hydrolysis of imine bonds in the cross-linked CLEAs, thus restoring pristine activity.[211] To verify this hypothesis, we prepared a batch of reduced βGLU CLEAs (R-CLEAs), where the Schiff bases formed upon cross-

linking were converted into irreversible amine bonds via reductive amination and encapsulated into PLGA NPs (R-CLEA NPs).[210] We then evaluated activity recovery upon encapsulation compared with the precursor R-CLEAs. R-CLEAs show only 1.5-fold activity increase upon encapsulation in NPs, compared with the 2.3-fold increase shown by CLEAs (Fig. 3.17), thus evidencing that the presence of a reversible cross-linking between enzymes is a fundamental requirement for reestablishment of catalytic activity.

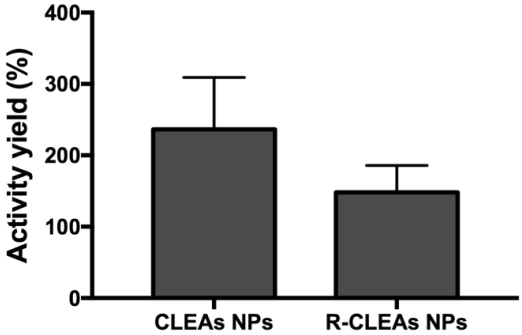


**Figure 3.17.** Activity yield of CLEA NPs and R-CLEA NPs formulated with βGLU. 100% = specific activity of CLEAs or R-CLEAs prior to NPs synthesis. Error bars represent the standard error of the mean of three independent experiments.

The slight activity increase observed in R-CLEA NPs can be due to the incomplete reduction of the imine bonds in a structurally complex matrix such as a protein aggregate. αGLU is the sole enzyme, among those tested, that is not suitable for CLEAs encapsulation, since it completely loses activity after CLEAs formation. Notably, activity is not restored after encapsulation in PLGA. Since no lysine residue is present at the catalytic site of αGLU, it is tempting to assume that irreversible conformational changes take place in proximity of the catalytic site as a result of the cross-linking

process.[212]

Note that enzymes loaded with the double emulsion method, despite a reasonably high encapsulation efficiency (usually between 25% and 42%, Tab. 3.5), show a nearly complete loss of activity (Tab. 3.8), thus confirming that double emulsion is not suitable for efficient encapsulation with maintained activity.

### 3.2.4 *In-vitro* enzyme replacement therapy in PPT1 deficient cells

Finally, we evaluated in vitro behavior of enzyme-loaded NPs. Preliminary to in vitro experiments, we evaluated cytotoxicity of PPT1 CLEA NPs (see Fig. 3.18), and we did not observe any toxic effect.

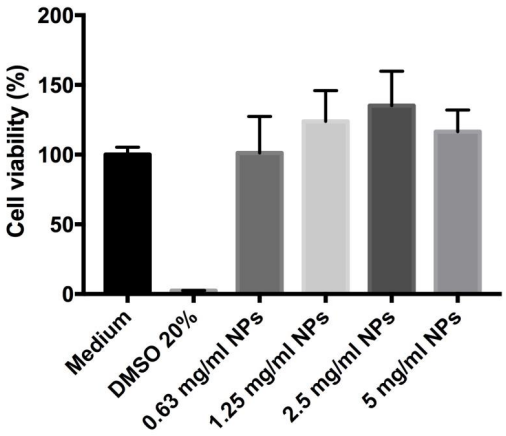


**Figure 3.18.** Cell viability upon incubation with increasing concentrations of PPT1 CLEA NPs. Error bars represent the standard error of the mean of three independent experiments.

First, we evaluated the release profile using fluorescently labeled PPT1 488-CLEA 633-NPs in NIH-3T3 cells by means of confocal microscopy at different time points (Fig. 3.16 B and 3.19).

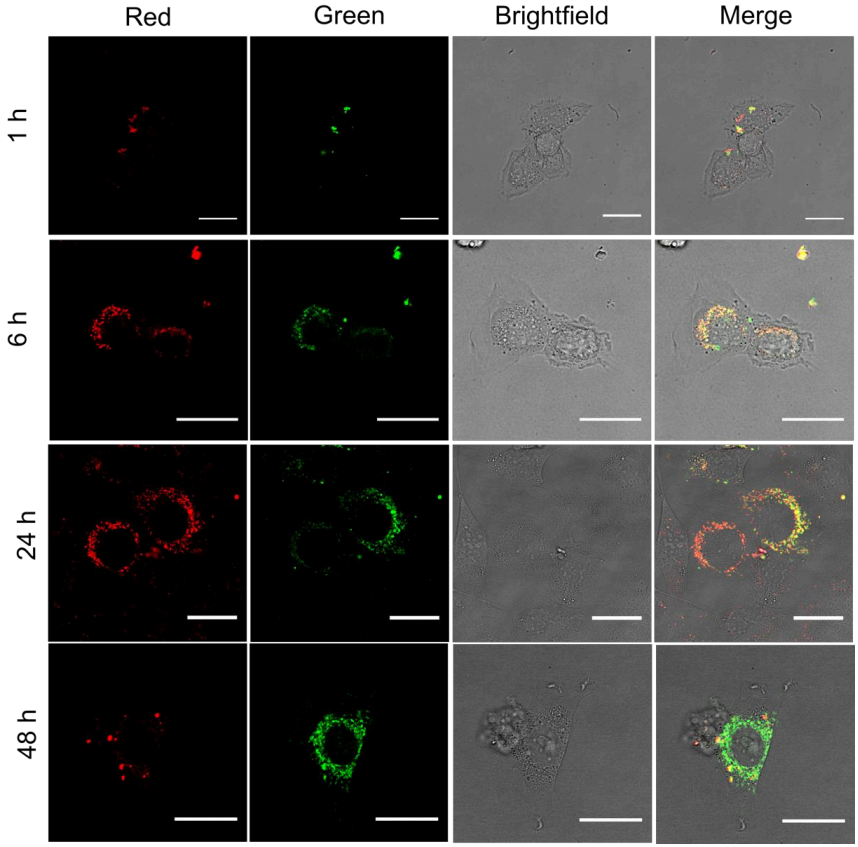


**Figure 3.19.** Red, green, brightfield channels and superimposed images of NIH-3T3 cells treated with PPT1 488-CLEA 633-NPs 1, 6, 24 and 48 hours after administration. Scale bars = 25 mm.

Imaging 1 hour after treatment shows extensive colocalization of CLEAs and NPs in discrete aggregates. After 6 h, CLEAs and NPs are still colocalized but distributed as vesicles inside cells, indicating compartmentalization at lysosomal level. After 24 hours, red labeled PLGA is present at vesicular level in most cells, while cells showing only green vesiculated PPT1 are also present. This suggests that PPT1 is being released and follows the expected

trafficking and secretion pathway typical of PPT1.[213] After 48 hours only a few cells show red vesicles, whereas most cells show green vesicles due to released and trafficked PPT1. Red fluorescence is mainly concentrated in big vesicles or aggregates either within or outside cells, suggesting that NPs are processed and by a more quantitative colocalization analysis (Fig. 3.20) that shows increasing red/green and decreasing green/red colocalization over time, in agreement with the spreading of enzyme and concomitant compartmentalization of PLGA residues. Notably, incubation with free enzyme highlights extensive endocytosis in short times, leading to a highly vesiculated signal.

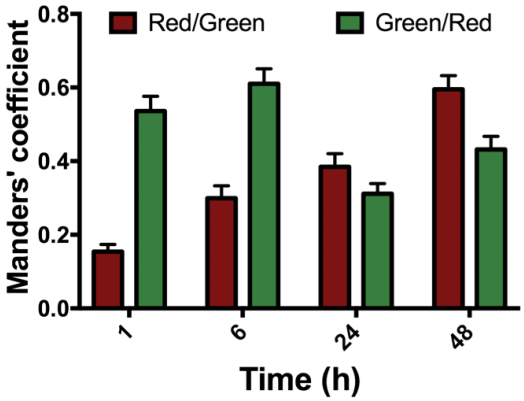


**Figure 3.20.** Manders' coefficient resulting from colocalization analysis of NIH-3T3 cells treated with PPT1 488-CLEA 633-NPs 1, 6, 24 and 48 hours after administration. Error bars represent the standard error of the mean of 10 analysis.

Colocalization with empty NPs coadministered to the cells evidence that the common fate of both species is in the lysosomal compartment after 6–24 hours. However, the enzyme mostly disappears after 24–48 hours, presumably owing to constitutive cell recycling (see Fig. 3.21).

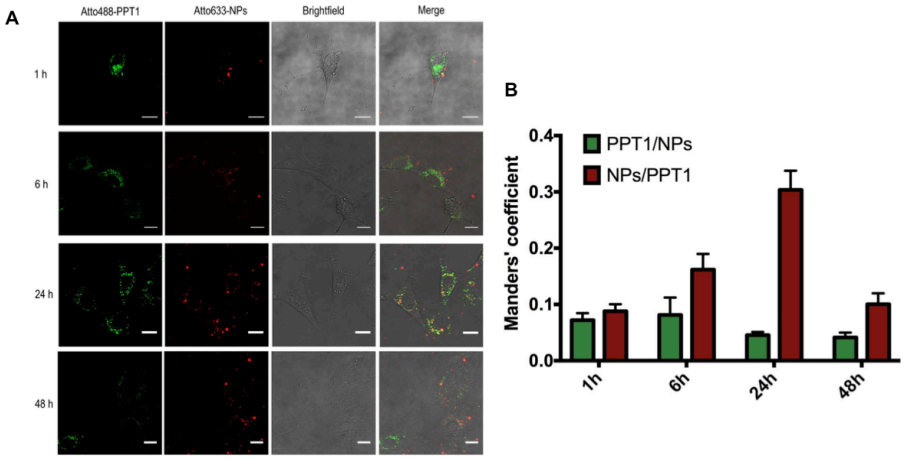


**Figure 3.21. (A)** Red, green, brightfield channels and superimposed images of NIH-3T3 cells treated with Atto 488- labeled PPT1 and empty Atto 633-labeled NPs 1, 6, 24 and 48 hours after administration. Scale bars = 15 mm. **(B)** Manders' coefficient resulting from colocalization analysis of NIH-3T3 cells treated with Atto 488-labeled PPT1 and empty Atto 633-labeled NPs 1, 6, 24 and 48 hours after administration. Error bars represent the standard error of the mean of 10 analysis.

Since this disappearance kinetics is markedly different from what observed using PPT1 CLEA NPs, it is tempting to assume that NPs are able to control the release and extend the half-life of the enzyme inside the cell.

Finally, we set up a proof of concept experiment to evaluate the ability of PPT1 CLEA NPs to restore enzymatic activity in vitro in a line of primary fibroblasts (cln1-pt9) harboring the homozygous R122W mutation in the PPT1 gene. To this end, we produced a targeted version of PLGA NPs using a mixture of plain and Tf2-derivatized PLGA. Peptide Tf2 was recently described, and recognizes holotransferrin without altering its binding capability, thus allowing indirect targeting of transferrin receptor (TfR).[214] Given the high density of TfR on the BBB, Tf2 decorated NPs could allow

delivery to the CNS. The presence of Tf2 on the NP surface did not affect the NPs properties in terms of size, zeta potential, encapsulation efficiency, and activity yield, apart from a minor decrease in encapsulation efficiency (Tab. 3.9).

| | *HD(nm) (SEM)* | *ZP(mV) (SEM)* | *EE% (SEM)* | *AY% (SEM)* |
|---|---|---|---|---|
| **PPT1 CLEAs Tf2 NPs** | 144 (4) | -31 (1) | 58 (5) | 66 (19) |

**Table 3.9.** Characterization of PPT1 CLEAs Tf2 NPs. HD = hydrodynamic diameter; ZP = zeta potential; EE = encapsulation efficiency; AY = activity yield; SEM = standard error of the mean of three independent experiments.

PPT1 CLEA NPs and PPT1 CLEA Tf2 NPs were administered to the cells, and after incubation, we assayed the cell enzymatic activity. As shown in figure 3.22, both targeted and untargeted NPs promote recovery of enzymatic activity, although with different efficiency. At low doses (<110 U) cell response is the same after treatment with either NPs or free enzyme, while at high doses (>110 U), enzymatic recovery obtained using free PPT1 reaches a plateau, likely reflecting saturation in the enzyme uptake mechanism. Note that enzymatic recovery is slightly higher for cells treated with Tf2-modified NPs respect to untargeted NPs, probably due to increased NPs uptake in the presence of Tf2, which can activate receptor mediated endocytosis.

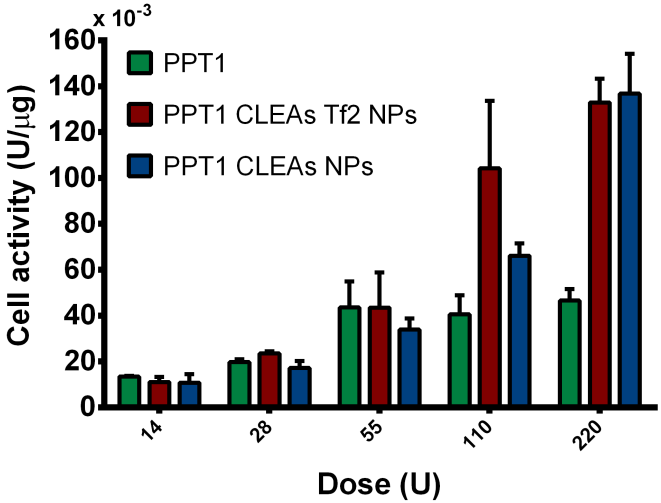


**Figure 3.22.** Enzymatic activity of fibroblasts from NLC1 patients after treatment with increasing doses of PPT1, PPT1 CLEAs Tf2 NPs and PPT1 CLEAs NPs. 1 unit (U) = amount of enzyme that catalyzes 1 nmol of substrate per hour. Error bars represent the standard error of the mean of 3 experiments.

### 2.3.5 Concluding remarks

In summary, we developed a simple and general approach for the encapsulation of enzymes in PLGA NPs based on the formation of CLEAs, that is easily adaptable to different proteins and polymeric NPs. Enzymes are encapsulated with excellent efficiency and activity retention, taking a significant step forward compared to traditional synthesis methods such as double emulsion/solvent evaporation. We also demonstrated that enzyme-loaded NPs can be administered to primary NCL1 skin fibroblasts, fully restoring enzymatic activity and paving the way to the development of more effective enzyme replacement therapies.

### 2.3.6 Material and methods

#### *Materials.*

Poly(D,L-lactide-co-glycolide) (PLGA; Resomer RG 503H and Resomer RG 752H) was purchased from Sigma Aldrich and used as received. Recombinant human PPT1 was produced according to a reported procedure.[215] Recombinant α-GLU from Bacillus stearothermophilus was purchased from Creative Enzymes (USA) and used as received. βGLU from almonds was purchased from Sigma-Aldrich and used as received. Atto 488 NHS-ester and Atto 633 amine were purchased by Atto-TEC GmbH (Germany) and used as 10 mg/mL stock solutions in dimethyl sulfoxide (DMSO). All other chemicals were purchased from Sigma-Aldrich unless otherwise specified. All chemicals were used as received. CLEAs Synthesis. 200 µL of 1 mg/mL enzyme solution in water was added dropwise to 600 µL of acetone simultaneously with 2 µL of 25% glutaraldehyde–water solution under stirring in an ice bath. The mixture was stirred overnight at 4 °C, and then 200 µL of acetone were added. The suspension was centrifuged (13,200 rpm, 4 °C, 30 min) and washed twice with 1 mL of acetone. CLEAs were suspended in 1 mL of acetone and stored at -20 °C until use. EAs were prepared according to the same procedure without addition of glutaraldehyde.

#### *CLEA NPs Synthesis.*

Generally, 200 µL of CLEAs were added to 200 µL of a solution composed of PLGA 752H (8 mg) and PLGA 503H (2 mg) in acetone. The mixture was added dropwise to 1200 µL of 2% (w/v) sodium cholate in water under stirring. The resulting NPs suspension was centrifuged (13,200

rpm, 4 °C, 20 min) and washed twice with 500 µL of water. Obtained CLEA NPs were suspended in 500 µL of 10 mg/mL trehalose aqueous solution and stored at −20 °C until use. EA NPs were produced following the same procedure by replacing CLEAs with EAs. TF2-modified NPs were produced by replacing PLGA 503H with PLGA-TF2. Fluorescently labeled NPs (488-CLEAs 633- NPs) were produced by replacing CLEAs with 488-CLEAs and by adding 0.1 mg of 633-PLGA to the organic mixture. Empty NPs were prepared with the same protocol by replacing CLEAs with the same volume of acetone.

*Encapsulation Efficiency Determination.*

The amount of enzyme in the samples was determined via ninhydrin assay as described by Starcher.[216] Ninhydrin reagent was prepared as follows: 200 mg of ninhydrin was dissolved in 7.5 mL of ethylene glycol, and then 2.5 mL of 4 N acetate buffer (pH 5.5) and 250 µL of 100 mg/mL stannous chloride solution in ethylene glycol were added. Samples and standards were first digested by adding 50 µL of 12 M HCl and 100 µL of 6 M HCl to 50 µL of sample. The mixture was incubated at 95 °C and then dried under vacuum. 50 µL of deionized water were added to the residue and 10 µL of this solution were added to 110 µL of ninhydrin reagent. The mixture was incubated at 95 °C for 15 minutes then 50 µL were transferred in a 96-well microplate. Absorbance was measured at 560 nm with a microplate reader (Promega GloMax discover Multimode microplate reader). Enzyme concentration was determined by interpolation from a calibration curve prepared with the corresponding enzyme subject to the same digestion and reaction procedures. NPs encapsulation efficiency (EE%) was determined as

follows:

$$EE\% = \frac{[Enzyme]_{NPs} \cdot 2.5}{[Enzyme]_{Inj}} \cdot 100$$

where $[Enzyme]_{NPs}$ is the enzyme concentration in NPs and $[Enzyme]_{Inj}$ is the enzyme concentration in CLEAs, EAs, or enzyme solution used for CLEAs NPs, EA NPs, or DE NPs synthesis, respectively. 2.5 is the dilution factor of the $[Enzyme]_{Inj}$ in the NPs synthesis process.

### *488-CLEAs 633-NPs Quenching.*

190 µL of potassium iodide (KI) solutions at increasing concentrations (0, 100, 150, 200, 250 mM) was transferred in each well of a 96-well microplate and 10 µL of sample was added. Fluorescence was measured with a microplate reader (Promega GloMax discover Multimode microplate reader) at the following excitation and emission wavelengths:

Excitation 475 nm – emission 500–550 nm for 488-CLEAs quenching

Excitation 627 nm – emission 660–720 nm for 633-PLGA quenching

The kinetics of the process was evaluated by applying the Stern–Volmer relationship:

$$\frac{F_0}{F} = 1 + k_q \tau_0 [KI]$$

where $F_0$ and F are the fluorescence intensities in the absence and in the presence of the quencher, respectively, $k_q$ is the quencher rate coefficient, $\tau_0$ is the lifetime of the emissive excited state of the fluorophore, and [KI] is the quencher concentration.

### *PPT1 CLEAs Release in Cuvette.*

200 µL of PPT1 488-CLEA 633-NPs were transferred into a Spectra Por dialysis membrane (Biotech Cellulose Ester, molecular weight cut off 100

kDa, Spectrum Laboratories) and placed in 25 mL of PBS (pH 7.4) or citrate buffer (pH 4.5) at 37 °C under stirring. At different time points (1, 6, 24, 48, 96, 168, and 336 h) the external buffer was collected and replaced with 25 mL of fresh buffer. Fluorescence was measured on the external buffer aliquots with Cary Eclypse fluorometer (excitation filter 485 nm, emission filter 490–600 nm).

### *Activity Yield Determination.*

Enzymatic activity of CLEAs, EAs, CLEA NPs, EA NPs, and DE NPs was determined via fluorescence-based assays by employing a specific fluorogenic substrate for each enzyme involved in this study.

Activity yield (AY%) of CLEAs, EAs, CLEA NPs, EA NPs, and DE NPs was calculated as the ratio between the specific activity of the sample ($SA_S$) and the specific activity of the unaltered enzyme ($SA_{ctr}$):

$$AY\% = \frac{SA_s}{SA_{ctr}} \cdot 100$$

where the specific activities are defined as unit of enzyme (U) per microgram of enzyme ($\mu g_e$):

$$SA = \frac{U}{\mu g_e}$$

1 unit of enzyme (U) corresponds to 1 nmol of substrate ($nmol_{sub}$) hydrolyzed in 1 h:

$$U = \frac{nmol_{sub}}{h}$$

Activity expressed as U was calculated by interpolation from a calibration curve of 4-methylumbelliferone.

*Cell Culture.*

Mouse embryonic fibroblast cells (NIH-3T3) were purchased from the American Type Culture Collection (ATCC). Cells were maintained in Dulbecco's modified Eagle medium (DMEM) from Invitrogen (Carlsbad, CA). Growth medium was supplemented with 10% fetal bovine serum (FBS), 4 mM L-glutamine, 1 mM sodium pyruvate, 100 U/mL penicillin, and 100 mg/mL streptomycin (Invitrogen). Cells were maintained at 37 °C in a humidified 5% $CO_2$ atm.

*Confocal Imaging*.

NIH-3T3 cells were seeded 24 hours before the experiments into a glass-bottom Petri dish (WillCo-dish GWSt-3522) to reach 80–90% confluence. Incubation with PPT1 488-CLEA 633-NPs was performed for 1 hour at 37 °C, 5% $CO_2$ in DMEM with 10% FBS at a final NPs concentration of 1.25 mg/mL in a total volume of 200 µL. After incubation, cells were washed three times with PBS and fresh medium was added. The samples were analyzed by confocal microscopy at different time points after treatment (1, 6, 24, and 48 hours). Cells were imaged using a Leica TCS SP5 SMD inverted confocal microscope (Leica Microsystems AG) interfaced with Ar and HeNe laser for excitation at 488 and 633 nm, respectively. Cells were mounted in a thermostated chamber at 37 °C (Leica Microsystems) and viewed with a 40× 1.5 NA oil immersion objective (Leica Microsystems). The pinhole aperture was set to 1.0 Airy. All images were analyzed using ImageJ software v 1.51 and colocalization was evaluated using JACoP plugin. The final value of Manders' coefficient is an average obtained from the analysis of 10 images taken with the same magnification for each experiment.

### *Enzymatic Activity Recovery in NCL1 Cells.*

NCL1 primary cells were seeded 24 hours before experiments into 96-well microplates to reach 80–90% confluence. Incubation with increasing doses of PPT1 CLEA NPs, PPT1 CLEA Tf2 NPs, or PPT1 was performed for 1 hour at 37 °C, 5% $CO_2$ in DMEM with 10% FBS in a total volume of 100 µL. After incubation, cells were maintained on ice and washed three times with cold PBS. Cellular lysates were obtained by adding 30 µL of radioimmunoprecipitation assay (RIPA) buffer (Thermo Fisher Scientific). To evaluate enzyme activity, 15 µL of cellular lysate were added to 20 µL of substrate solution specific for PPT1 and incubated 2 hours at 37 °C. After incubation, 150 µL of stop solution were added to each sample and fluorescence was measured with a microplate reader in a 96 well plate (Promega GloMax discover Multimode microplate reader) with excitation filter 365 nm and emission filter 415–445 nm.

Total amount of protein in cellular lysate was determined via Bradford assay. Absorbance was measured at 575 nm with Promega GloMax discover Multimode microplate reader.

### *Recombinant murine galactosylceramidase (GALC) production*

HEK 293T cells stably expressing and secreting His6-tagged murine wild-type GALC (kindly provided by J.E. Deane, University of Cambridge, United Kingdom) were maintained in 400 µg/ml zeocin selection medium and expanded in 1450 $cm^2$ inner surface roller bottles (37°C, 5% $CO_2$, 0.7 rpm).[17] The enzyme was routinely purified from the extracellular medium using nickel-affinity chromatography (Ni Sepharose excel histidine-tagged protein purification resin; 17-3712-03 GE Healthcare Life Sciences), buffer

exchanged with 10 kDa molecular mass cut-off concentrator and stored at -20°C.

### *Fluorescently labelled PLGA (PLGA-Atto633) synthesis*

PLGA activation I: PLGA-NHS synthesis PLGA 503H was activated by means of NHS-EDC chemistry. Briefly, 0.05 mmol of PLGA 503H were dissolved in 5 ml of anhydrous DCM under nitrogen atmosphere and 0.5 mmol of solid NHS were added, followed by 0.5 mmol of EDC-HCl and 0.6 mmol of triethylamine (TEA). The mixture was stirred for 18 hours at room temperature (RT). Methanol was added to precipitate the polymer. PLGA-NHS was collected by centrifugation and washed twice by re-dissolution in DCM and precipitation with methanol followed by centrifugation. The final product was characterized by 1H-NMR in CDCl3, dried and stored at -20°C until use. Polymer characterization: 1H NMR (Bruker AVANCE 300 spectrometer, 300 MHz, $CDCl_3$). δPLGA-NHS: 5.2 (-$OCH(CH_3)COO$-), 4.8 (-$OCH_2COO$-), 2.9 (-$COCH_2CH_2COON$-), 1.6 (- $OCH(CH_3)CO$-) ppm. PLGA-Atto633 synthesis 0.22 mmol of PLGA-NHS were dissolved in dimethyl sulphoxide (DMSO) and 0.24 mmol of Atto633-amine were added. The mixture was stirred for 18 hours at RT. Methanol was added to precipitate the product and the mixture was centrifuged and washed twice by re-dissolution in methylene chloride (DCM) and precipitation with methanol followed by centrifugation. The final product was dried and stored at -20°C until use. Excitation and emission spectra of PLGA-Atto633 (633- PLGA) were measured in acetone with a Cary Eclypse fluorometer and are shown in figure 3.21 A.

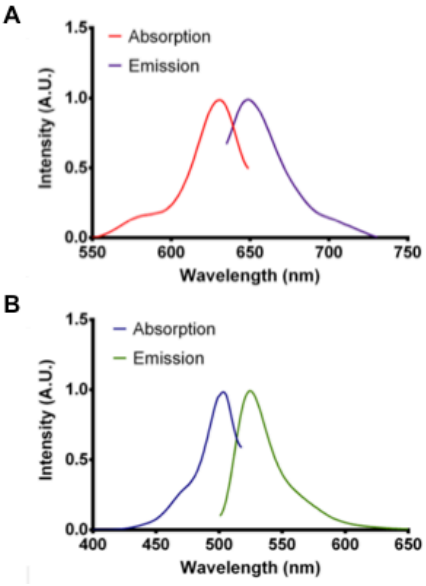


**Figure 3.21.** Absorption and emission spectra of **(A)** 633-PLGA and **(B)** 488-PPT1 CLEAs.

## *CLEAs modification*

### *CLEAs labelling with Atto488*

Typically, a precise amount of Atto488-NHS solution in DMSO (10 mg/ml) was added to 1 ml of CLEAs with 1:20 CLEAs:Atto488-NHS molar ratio. The mixture was stirred for 4 hours at RT then centrifuged (13,200 rpm, 30 minutes) and washed twice with 1 ml of acetone. Resulting 488-CLEAs were suspended in 1 ml of acetone. Excitation and emission spectra of 488-CLEAs were measured in acetone with a Cary Eclypse fluorometer and are shown in figure 3.21 B.

### *R-CLEAs synthesis*

To avoid reaction of the reducing agent with acetone, CLEAs were transferred into ethanol. To do this, 2 ml of βGLU CLEAs were centrifuged (13,200 rpm, 4°C, 30 minutes) and resuspended in 2 ml of ethanol. 1.5 mg of solid sodium cyanoborohydride ($NaCNBH_3$) were added to 2 ml of βGLU CLEAs under stirring. The mixture was stirred 4 hours at 4°C then centrifuged and washed once with 2 ml of ethanol and once with 2 ml of acetone. Resulting R-CLEAs were suspended in 2 ml of acetone.

### *Double emulsion (DE) NPs synthesis*

90 ml of 1 mg/ml enzyme solution were added to 450 ml of PLGA solution in DCM (20 mg/ml) and emulsified with a probe sonicator (Bandelin Sonoplus, Germany) at 80W for 45 seconds. The resulting emulsion was transferred into 1,45 ml of 2% (w/v) sodium cholate aqueous solution and emulsified again at 80W for 45 seconds. The mixture was stirred at RT for 1 hour to evaporate DCM then centrifuged (13,200 rpm, 4°C, 20 minutes) and washed twice with 500 ml of deionized water. Resulting DE NPs were suspended in 500 ml of 10 mg/ml trehalose aqueous solution and stored at -20°C until use. Empty DE NPs were prepared with the same protocol by replacing the enzyme solution with deionized water.

### *NPs size and zeta potential*

The hydrodynamic diameter and surface charge (zeta potential) of NPs were determined with a ZetaSizer NanoZS (Malvern Instruments Inc., UK) by means of dynamic light scattering (DLS). Samples were diluted 100-fold in deionized water and transferred into polypropylene cuvettes and

measurements were performed at RT. The mean hydrodynamic diameter was calculated from the autocorrelation function of the intensity of scattered light from the NPs by DTS Nano software. For zeta potential measurement, samples were diluted 100-fold in deionized water and transferred into electrophoretic cells and measurements were performed at RT. Electrophoretic mobility was measured and converted into surface zeta potential by DTS Nano software.

### *CLEA NPs confocal imaging*

Samples were prepared by adding 20 ml of CLEA NPs to 60 ml of 1% agar in PBS and then transferred into a glass-bottom Petri dish (WillCo-dish GWSt-3522). NPs were imaged using a Leica TCS SP5 SMD inverted confocal microscope (Leica Microsystems AG) interfaced with Ar and HeNe laser for excitation at 488 and 633 nm, respectively. NPs were viewed with a 40X 1.5 NA water immersion objective (Leica Microsystems) and the pinhole aperture was set to 1.0 Airy. All images were analysed using ImageJ software version 1.51 and colocalization was evaluated using JACoP plugin by calculating the Manders' coefficient for red/green and green/red overlap. The final value of Manders' coefficient is the average obtained from the analysis of 10 images taken with the same magnification for each experiment.

### *Enzymatic activity assays*

Enzymatic activity of CLEAs, EAs, CLEA NPs, EA NPs and DE NPs was determined via fluorescence-based assays by employing a specific fluorogenic substrate for each enzyme involved in this study.

*PPT1 activity assay*

PPT1 activity assay was performed as described by van Diggelen et al.[217] The following reagents were necessary for substrate preparation:

a. C/M: chloroform:methanol 2:1
b. Triton 5%: Triton X-100 5% (w/v) in C/M
c. Pi/Ci buffer: 0.4 M $Na_2HPO_4$, 0.2 M citric acid, 0.2% sodium azide, pH 4.0
d. β-glu: β-glucosidase from almonds 18.9 mg/ml in water
e. DTT/BSA: 33 mM dithiothreitol (DTT), 0.2% bovine serum albumin (BSA) prepared as follows: 125 µg/ml BSA aqueous solution (40 ml) at pH 10 was incubated at 50°C for 4 hours, then pH was adjusted to 7 with 1 M HCl and volume was adjusted to 50 ml with water. The mixture was centrifuged (10 min, 3000 rpm) and pellet was discarded. Sodium azide was added to a 0.02% final concentration. The resulting 10% BSA solution was stored at -20°C until use and diluted 50-fold in 33 mM DTT to obtain DTT/BSA reagent.
f. Stop buffer: 0.5 M $NaHCO_3$, 0.5 M $Na_2CO_3$, 0.025% Triton-X100, pH 10.7.

Fluorogenic substrate for PPT1 (4-methylumbelliferyl-6-thio-palmitate-β-D-glucopyranoside) was purchased by Santa Cruz Biotechnology and dissolved in C/M at 2 mg/ml concentration. 150 µl of this solution were added to 60 µl of Triton 5% and solvent was evaporated at 30°C. 400 µl of Pi/Ci buffer were added and the mixture was sonicated for 10 seconds. 360 µl of DTT/BSA and 40 µl of β-glu were added and the final solution was stored at -80°C until use. For activity determination 30 ml of substrate solution were added to 20 ml of sample (free PPT1, PPT1 CLEAs or PPT1 CLEA NPs), and

incubated for 1 hour at 37°C. The amount of enzyme reacting with the substrate was always adjusted to be included within the linear range of the enzymatic activity curve (Fig. 3.24 A); typically, 1-4 ng of free enzyme were used in each assay. 20 ml of this mixture were transferred in a 96-well microplate and 100 ml of stop solution were added. Fluorescence was measured with a microplate reader (Promega GloMax discover Multimode microplate reader) with excitation filter 365 nm and emission filter 415-445 nm.

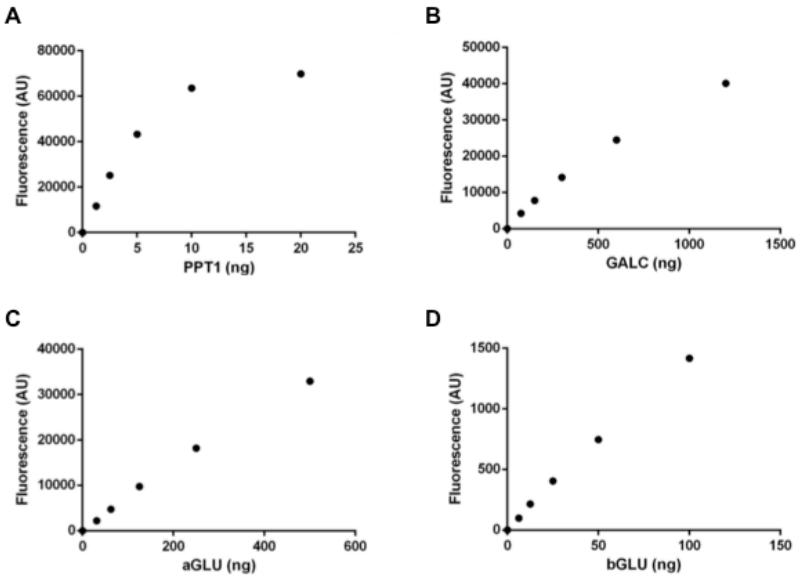


**Figure 3.24.** Enzymatic activity curves of **(A)** PPT1, **(B)** GALC, **(C)** αGLU and **(D)** βGLU.

### *GALC activity assay*

Fluorogenic substrate for GALC (4-methylumbelliferyl-β-D-galactopyranoside) was dissolved in dimethylsulphoxide (DMSO) at 10 mM concentration then diluted to 1 mM in buffer consisting of 50 mM sodium

citrate, 125 mM sodium chloride and 0.5% Triton-X100 (pH 4.5). 50 ml of sample were added to 50 ml of 1 mM substrate and incubated for 20 minutes at 37°C. The amount of enzyme added to the substrate was always adjusted to be included within the linear range of the enzymatic activity curve (Fig. 3.24 B). 40 ml of this mixture were transferred into a 96-well microplate and 40 ml of stop solution consisting of 0.5 M glycine and 0.5 M sodium hydroxide (pH 10) were added. Fluorescence was measured with a microplate reader (Promega GloMax discover Multimode microplate reader) with excitation filter 365 nm and emission filter 415-445 nm.

*αGLU activity assay*

Fluorogenic substrate for αGLU (4-methylumbelliferyl-a-D-glucopyranoside) was dissolved in dimethylsulphoxide (DMSO) at 10 mM concentration then diluted to 1 mM in buffer consisting of 0.4 M disodium hydrogen phosphate and 0.2 M citric acid (pH 6.5). 50 ml of sample were added to 50 ml of 1 mM substrate and incubated for 20 minutes at 37°C. The amount of enzyme added to the substrate was always adjusted to be included within the linear range of the enzymatic activity curve (Fig. 3.24 C) 40 ml of this mixture were transferred into a 96-well microplate and 80 ml of stop solution consisting of 0.1 M sodium carbonate were added. Fluorescence was measured with a microplate reader (Promega GloMax discover Multimode microplate reader) with excitation filter 365 nm and emission filter 415-445 nm.

*βGLU activity assay*

Fluorogenic substrate for βGLU (4-methylumbelliferyl-b-D-glucopyranoside) was dissolved in dimethylsulphoxide (DMSO) at 10 mM concentration then diluted to 1 mM in buffer consisting of 0.4 M disodium

hydrogen phosphate and 0.2 M citric acid (pH 6.5). 50 ml of sample were added to 50 ml of 1 mM substrate and incubated for 20 minutes at 37°C. The amount of enzyme added to the substrate was always adjusted to be included within the linear range of the enzymatic activity curve (Fig. 3.24 D). 40 ml of this mixture were transferred into a 96-well microplate and 80 ml of stop solution consisting of 0.1 M sodium carbonate were added. Fluorescence was measured with a microplate reader (Promega GloMax discover Multimode microplate reader) with excitation filter 365 nm and emission filter 415-445 nm.

### *Cell viability assay*

NIH 3T3 cells were seeded 24 hours before experiments into 96-well microplates to reach 80-90% confluence. Incubation with increasing doses of PPT1 CLEA NPs was performed for 4 hour at 37°C, 5% $CO_2$ in DMEM with 10% FBS in a total volume of 100 ml. After incubation, cells were washed to remove non-internalized NPs and maintained in fresh medium for 24 hours. Cell viability was measured with Cell Counting Kit-8 and absorbance was measured at 450 nm with a microplate reader (Promega GloMax discover Multimode microplate reader).

### *Targeted PLGA synthesis*

PLGA activation II: PLGA-Mal synthesis 0.05 mmol of PLGA-NHS were dissolved in DCM. 0.1 mmol of N-(2-aminoethyl) maleimide trifluoroacetate and 0.11 mmol of TEA were added and the mixture was stirred for 2 hours at RT. Methanol was added to precipitate the obtained polymer. PLGA-Mal was collected by centrifugation and washed twice by re-dissolution in DCM

and precipitation with methanol followed by centrifugation. The final product was characterized by 1H-NMR in $CDCl_3$, dried and stored at -20°C until use. Polymer characterization: 1H NMR (Bruker AVANCE 300 spectrometer, 300 MHz, CDCl3). δPLGA-Mal: 6.7 (-HC=CH-), 5.2 (-$OCH(CH_3)COO$-), 4.8 (-$OCH_2COO$-), 1.6 (-$OCH(CH_3)CO$-) ppm. PLGA-TF2 synthesis TF2 peptide was synthesized by solid phase peptide synthesis as described elsewhere4. 2.25 mmol of TF2 peptide were added to 2.05 mmol of PLGA-Mal in DMF and the mixture was stirred at RT for 48 hours. Methanol was added to precipitate the product and the mixture was centrifuged and washed twice by re-dissolution in DCM and precipitation with methanol followed by centrifugation. The reaction was monitored by 1H-NMR in CDCl3 (Bruker AVANCE 300, 300 MHz) until absence of the maleimide group multiplet (δ 6.7 ppm), indicating complete conversion. The final product was dried and stored at -20°C until use.

## 3.3 Targeted polymeric Nanoparticles promote enzyme replacement therapy in a mouse model of Krabbe disease: A breach through the BBB for enzyme replacement therapy.

*The experiments presented in this Section are accepted for publication in Science Advances. Co-authors of the work are: Del Grosso A, Galliani M, Angella L, Santi M, Tonazzini I, Parlanti G, Signore G and Cecchini M. Role of authors: study concept and design: ADG, MG. Acquisition of data: All authors. Analysis and interpretation of data: All authors. Drafting of the manuscript: ADG, MG, GS, MC. Statistical analysis: MG, ADG, GS, MC. Obtained funding: MC. Study supervision: GS, MC. I, in particular, produced recombinant murine GALC, performed in-vitro and in-vivo experiments, performed statistical analysis, and drafted the manuscript.*

### 3.3.1 Introduction

In recent years, lot of interest arose from the development of enzyme-loaded nanosystems which may enhance the efficacy of ERT and minimize side effects using innovative and biocompatible nanomaterials. Enzyme encapsulation in biodegradable micelles, liposomes, and polymer- and lipid-based NPs can protect enzyme integrity and activity, eradicating some of the key limitations of ERT, including immunologic reactions and degradation.[161] It can also enhance the pharmacological response by improving pharmacokinetics and pharmacodynamics and allowing for a controlled release of the payload.[19] Moreover, the possibility to decorate the surface of the nanocarrier with targeting molecules (peptides, aptamers and antibodies) promotes passage through biological barriers such as the BBB and blood-ocular-barrier (BOB).[218]

In the previous Section (Section 3.2)[164] we demonstrated a new encapsulation strategy that allows loading enzymes with excellent efficiency and activity retention. In particular, we reported a synthesis method for a new enzyme delivery platform based on CLEAs encapsulation into PLGA NPs. We demonstrated that this system allows encapsulation of different enzymes (PPT1, GALC and glucosidase) with excellent activity retention. Delivery efficiency and enzyme activity recovery were validated *in vitro* using NCL1 primary fibroblasts.

In the present work we focused on GALC for testing *in vivo* enzyme delivery into the brain. To this end, we synthetized and fully characterized three new formulations of GALC CLEA-loaded PLGA NPs. These NPs were functionalized with targeting peptides [Angiopep-2 (Ang2)[219], g7[220] or transferrin binding (Tf2) peptides[214]], aimed to allow NPs to pass the BBB. At first, we studied NP cell uptake and trafficking, and their capability to reinstate enzymatic activity in murine model cells and in fibroblasts from KD patients. Then, we tested our nanosystem *in-vivo*, in the TWI mouse (Section 2.1.3).

We evaluated enzymatic activity recovery 4 hours after NP intraperitoneal injection in different organs of the CNS (brain) and PNS (sciatic nerve and spinal cord), as well as in typical accumulation organs (liver and kidneys). Moreover, we assessed the presence of targeted NPs in extracted brains and livers by means of confocal fluorescence microscopy.

### 3.3.2 Synthesis and characterization of targeted GALC CLEA NPs

For these experiments, three targeted versions of GALC-loaded CLEA NPs were synthesized, each decorated with a different peptide for CNS targeting (Fig. 3.25 A).

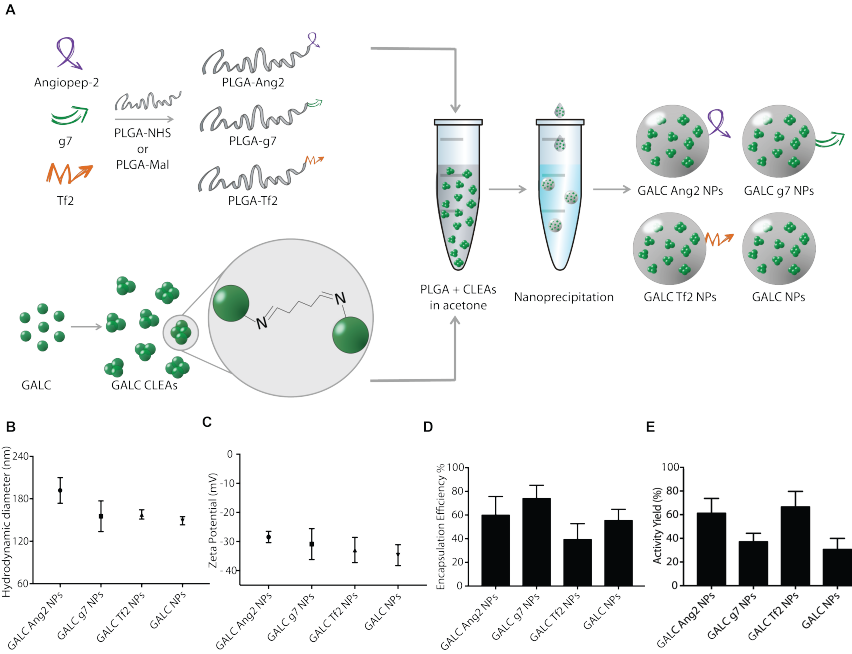


**Figure 3.25.** Targeted GALC CLEA NP synthesis and characterization. **(A)** *Graphical summary of the experiment.* Peptide-modified PLGA was produced by covalent linking of each peptide to a previously activated form of PLGA. GALC CLEAs were obtained by precipitation of GALC in acetone in presence of glutaraldehyde, resulting in Schiff base formation between enzyme molecules. Lastly, targeted GALC CLEA NPs were obtained by nanoprecipitation. **(B)** *Hydrodynamic Diameter of GALC CLEA NPs.* Error bars represent the standard error of the mean of 4 independently synthesized NP batches. **(C)** *Zeta Potential of GALC CLEA NPs*. Error bars represent the standard error of the mean of 4 independently synthesized NP batches. **(D)** *Encapsulation efficiency of GALC CLEA NPs*. Encapsulation efficiency is expressed as % of encapsulated GALC respect to the amount of enzyme employed in each synthesis. Error bars represent the standard error of the mean of 4 independently synthesized NP batches. **(E)** *Activity Yield of GALC CLEA NPs.* Activity yield is expressed as % of specific activity (nmol substrate hydrolyzed in 1 hour by 1 µg of enzyme) with respect to the free unaltered enzyme. Error bars represent the standard error of the mean of 4 independently synthesized NP batches.

GALC CLEA NPs were produced with a two-step protocol previously developed by our group and functionalized with the targeting peptides Ang2, g7 or Tf2 with a pre-formulation approach including a peptide-

modified PLGA in the formulation. First, Ang2, g7 and Tf2 peptides were synthesized by solid phase synthesis. Then, each peptide was covalently attached to PLGA exploiting the terminal carboxylic acid on the polymer.[221] Precisely, cysteine-terminated Ang2 and Tf2 were linked to maleimide-activated PLGA, whereas amine-terminated g7 was attached to n-hydroxysuccinimide-activated PLGA. Next, GALC CLEAs were first produced by precipitation of the enzyme in acetone in presence of glutaraldehyde, resulting in Schiff base formation and subsequent crosslinking of the precipitated enzyme. Then, GALC CLEAs were encapsulated into targeted PLGA NPs by nanoprecipitation. To this end, GALC CLEAs, PLGA and peptide-modified PLGA were mixed in acetone and added dropwise to an aqueous solution of sodium cholate. In this process, PLGA spontaneously precipitated as acetone diffused into water, encapsulating CLEAs into NPs that could be collected by centrifugation. Control non-targeted GALC CLEA-loaded NPs were produced by encapsulation of CLEAs in non-modified PLGA NPs.

The main features of GALC CLEA NPs are reported in figure 3.25 B-E. All the produced NPs showed a hydrodynamic diameter below 200 nm with small differences among the NP types, with GALC Ang2 NPs and non-targeted NPs displaying the largest (191±18 nm) and the smallest (149±6 nm) diameters, respectively. On the contrary, the surface zeta potential was rather uniform among all NP types (around -30 mV). GALC CLEAs were successfully encapsulated by all the NP formulations, with encapsulation efficiencies ranging from 40 to 75%. The NP formulation showing the best encapsulation efficiency was GALC g7 NPs, whereas GALC Tf2 NPs led to the greatest enzyme loss during synthesis. The activity yield also varied among

the batches, with GALC Ang2 and GALC Tf2 NPs being the formulations with highest GALC activity preservation.

### 3.3.3 Intracellular delivery of targeted NPs

Before testing the efficacy of GALC CLEA NP-mediated ERT, we explored their cellular uptake and intracellular trafficking in primary fibroblasts extracted from TWI and wild type (WT) mice by means of confocal microscopy and colocalization analysis. In particular, we investigated whether GALC CLEA NPs could be endocytosed by cells and reach the right intracellular target of GALC, that is the lysosome.[16,98] To this end, we produced a dual fluorescently labelled version of each NP formulation used in this study (Ang2-, g7- or Tf2-targeted NPs as well as non-targeted NPs) by encapsulating Atto 488-labelled GALC CLEAs into Atto 633-tagged PLGA NPs. We then incubated either TWI or WT fibroblasts with NPs for 4 hours. Cells were subsequently washed and incubated in fresh medium; after 24 hours cells were fixed and stained for lysosomes and nuclei. 4-color confocal fluorescence microscopy was finally carried out to assess the intracellular localization of both NPs and GALC independently (Fig. 3.26 A).

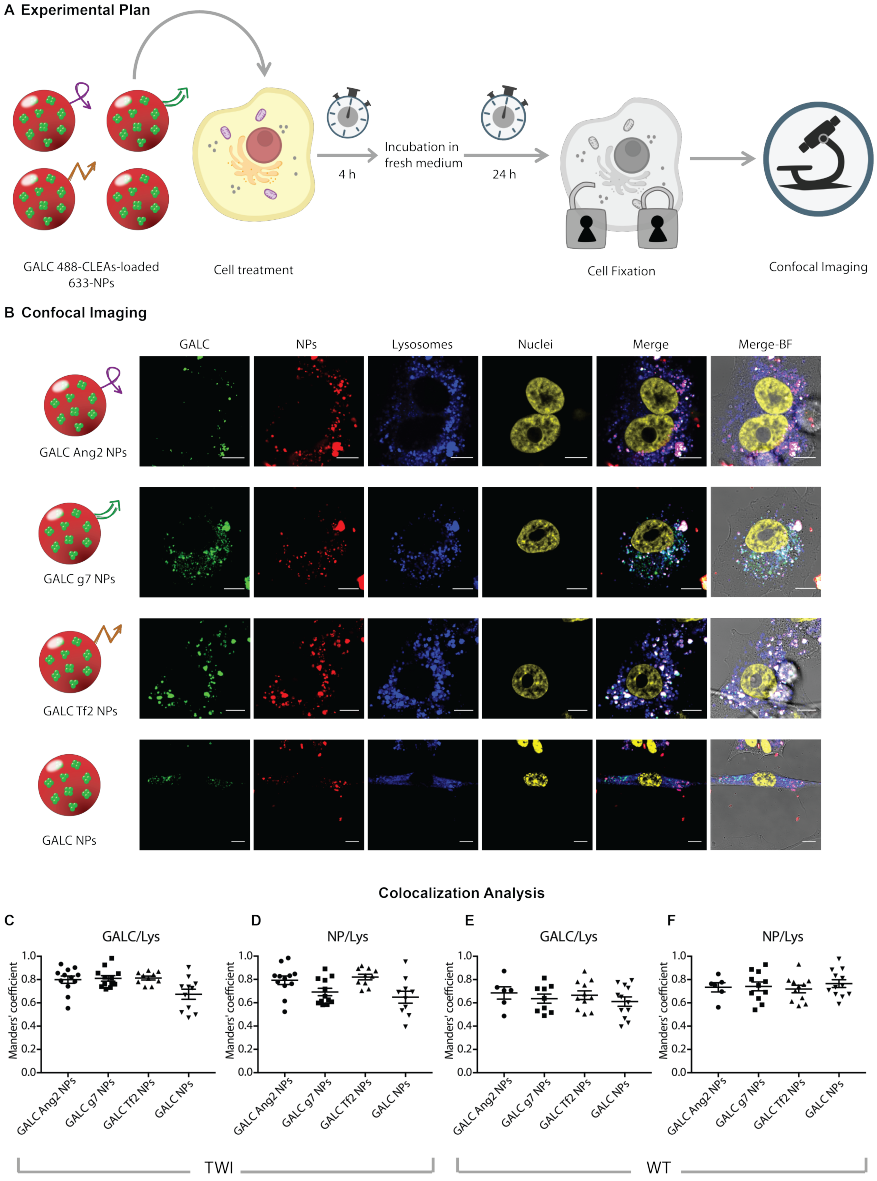


**Figure 3.26.** Intracellular localization of targeted GALC CLEA NPs. **(A)** *Graphical summary of the experiment.* TWI or WT primary fibroblasts were incubated with fluorescently labelled

GALC CLEA NPs for 4 hours, then washed and added with fresh medium. After 24 h, cell lysosomes were stained and cells were fixed and imaged with a confocal microscope. **(B)** *Confocal imaging*. Representative confocal images of TWI fibroblasts treated with fluorescently labelled GALC Ang2 NPs, GALC g7 NPs, GALC Tf2 NPs or GALC NPs. From the left to the right column: GALC (green, stained with Atto-488), NPs (red, stained with Atto-633), lysosomes (blue, stained with Lysotracker red DND-99), nuclei (yellow, stained with DAPI), superimposition of GALC, NPs, lysosomes and nuclei fluorescence and superimposition of all channels with brightfield images. Scale bars: 10 μm. **(C-D)** *Colocalization analysis.* Manders' coefficient of GALC/lysosomes and NPs/lysosomes overlap in TWI cells treated with GALC CLEA NPs. **(E-F)** Manders' coefficient of GALC/lysosomes and NPs/lysosomes overlap in WT cells treated with GALC CLEA NPs.

A first visual image analysis clearly showed that both GALC and NPs extensively colocalized in lysosomes of both TWI (Fig. 3.26 B) and WT (Fig. 3.27) fibroblasts.

Moreover, the enzyme was found in lysosomes independently from the presence and the identity of the targeting ligand, in TWI and WT cells as well. These qualitative results were confirmed by a quantitative colocalization analysis that we performed by calculating the Manders' coefficient for GALC/Lysosomes and NP/Lysosomes. As shown in figure 3.26 C, this coefficient was around 0.8 both for GALC/lysosomes and PLGA/lysosomes overlap, proving that the enzyme and NPs are highly colocalized with the lysosomes.

Overall, these data demonstrate that GALC CLEA NPs are effectively endocytosed by GALC-deficient cells into lysosomes, the desired cell compartment allowing for optimal GALC action.

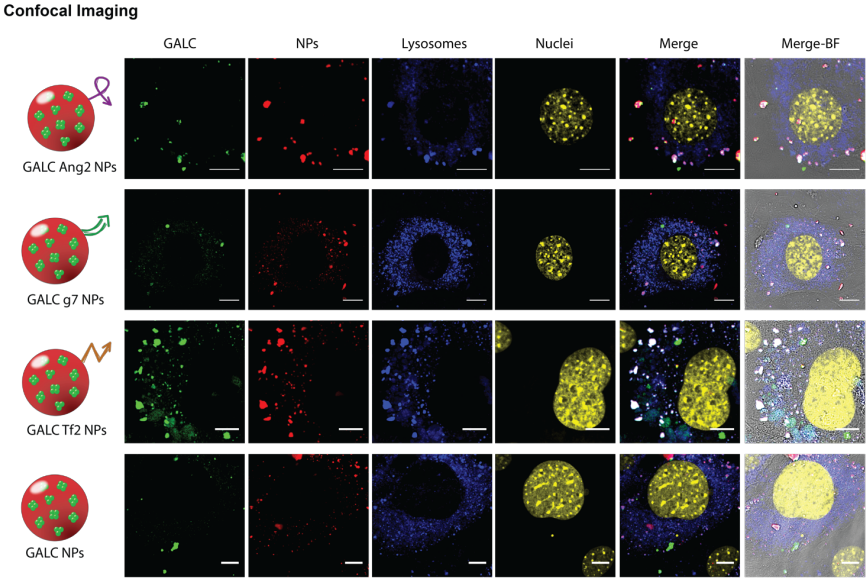


**Figure 3.27.** Intracellular localization of targeted GALC CLEA NPs in WT cells. Confocal imaging. Representative confocal images of WT fibroblasts treated with fluorescently labelled GALC Ang2 NPs, GALC g7 NPs, GALC Tf2 NPs or GALC NPs. From the left to the right column: GALC (green, stained with Atto-488), NPs (red, stained with Atto-633), lysosomes (blue, stained with Lysotracker Red DND-99), nuclei (yellow, stained with DAPI), superimposition of GALC, NPs, lysosomes and nuclei fluorescence and superimposition of all channels with brightfield image. Scale bars: 10 µm.

### 3.3.4 NP-mediated enzymatic activity recovery in vitro

After the demonstration of the capability of GALC CLEA NPs to reach cell lysosomes, we tested if they could restore GALC enzymatic activity in deficient cells *in vitro*. In order to pursue this aim we used murine TWI and WT cells and fibroblasts from KD patients and healthy donors (see material and methods for details, paragraph *cell culture and treatments*).

First, we performed a dose-response enzymatic recovery experiment in GALC-deficient (TWI) murine cells to find a useful dose-range to approximately reach the GALC enzymatic activity of healthy cells. WT cells

were used as healthy control. Specifically, we treated TWI cells with increasing doses of targeted or non-targeted GALC CLEA NPs, which corresponded to the following doses of enzyme: 0.75, 1.5, 3.0 and 6.0 U. Intracellular GALC activity was tested 4 hours after treatments. Control TWI cells were also treated with equivalent doses of free recombinant murine GALC (rm-GALC). See figure 3.28 A for an overview of the experimental plan.

The first important observation was that the administration of enzyme-loaded NPs led to significant GALC activity (> 25% with respect to WT cells) within TWI cells regardless the tested formulation/dose. More specifically, the enzymatic activity increased with the dose in all cases (Fig. 3.28 B). Focusing on targeted formulations, the trend was quite similar for Ang2- and g7- NPs. In both cases only the 0.75U dose returned a GALC intracellular activity significantly different from that of WT (taken as 100%) cells. With the dose of 1.5U of NPs, instead, GALC activity was approximately 50% of the WT conditions, and by administrating 3U the activity reached that of WT cells. At the maximal dose (6U) the WT activity was even exceeded. Tf2 NPs behaved similarly to Ang2- and g7 NPs at the lowest and the highest doses, whereas intermediate doses yielded similar recovery to the lowest dose. Unsurprisingly, non-targeted NPs were internalized with efficiency comparable to targeted NPs, being significantly different from the WT conditions for the two lowest doses. The third dose recovered the WT activity and the last one over-exceeded it.

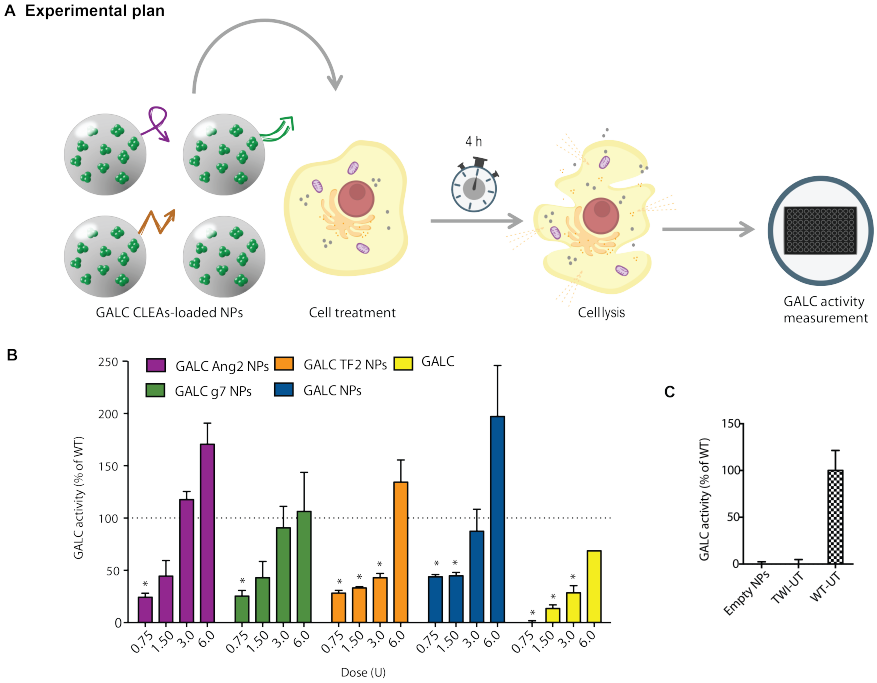


**Figure 3.28.** *In vitro* enzyme replacement therapy: dose-response experiment. **(A)** *Graphical summary of the experiment.* GALC-deficient primary fibroblasts (derived from TWI mice) were treated with GALC CLEA NPs. After 4 hours GALC activity was measured on cellular lysates by HMU-βGal assay. **(B)** *Dose response experiment results.* Cells were treated with targeted GALC CLEA NPs (GALC Ang2 NPs, GALC g7 NPs or GALC Tf2 NPs), with non-targeted NPs (GALC CLEA NPs) or with the free rm-GALC (GALC). For every treatment 4 doses were tested: 0.75, 1.50, 3.0 and 6.0 U [Unit (U) = amount of enzyme that catalyzes 1 nmol of substrate per hour]. Results are expressed in U/μg and reported in % of the activity of the WT cells [(U/ μg) = Unit of enzyme per microgram of cell lysate]. * = $P < 0.05$ specific treatment *vs.* WT; one-way ANOVA (Dunnett's multiple-comparisons test); mean ± SEM; N = 3. **(C)** *Controls.* For control, NPs non-loaded with GALC CLEAs (Empty NPs) were also administered to the cells. WT and TWI untreated cells activity is also showed. Mean ± SEM; N = 3.

Cells treated with free GALC showed increased activity upon treatment, but this effect was less pronounced than in the case of NPs. NPs not loaded with GALC CLEAs (Empty NPs in Fig. 3.28 C) did not yield any detectable enzymatic activity. Basal GALC activity of TWI fibroblasts (TWI-

UT in Fig. 3.28 C) was approximately indistinguishable from the background level of the experimental setting, as already reported.[222]

Given that the 3U dose of NPs demonstrated the ability to successfully recover the WT activity in the majority of the formulations without over-exceeding the WT level, it was selected for the subsequent time-response experiments. In this case, both murine and human cells were treated with targeted- and non-targeted NPs or with free rm-GALC. After 4 hours cells were washed and added with fresh medium. GALC enzymatic activity was then assayed 24 or 96 hours after treatments (see the experimental plan in Fig. 3.29 A).

Murine cells treated with targeted or non-targeted NPs successfully maintained approximately the WT enzymatic activity for 24 and 96 hours, except for non-targeted NPs at the time point of 96 hours. Moreover, activity promoted by g7- and Tf2-targeted NPs significantly went beyond the WT levels. The rm-GALC treated cells, instead, reached the WT activity only after 96 hours and only in this case we measured a significant difference between 24 and 96 hours within the same treatment.

The same experiments were carried out with KD patient fibroblasts having the common 30kb deletion in the GALC gene (30kbΔ in Fig. 3.29 D). Cells treated with targeted or non-targeted NPs showed similar activity to that of cells from healthy donors (HD), except for those treated with g7- and Tf2-targeted NPs after both 24 and 96 hours, whose activities were significantly higher than the HD level.

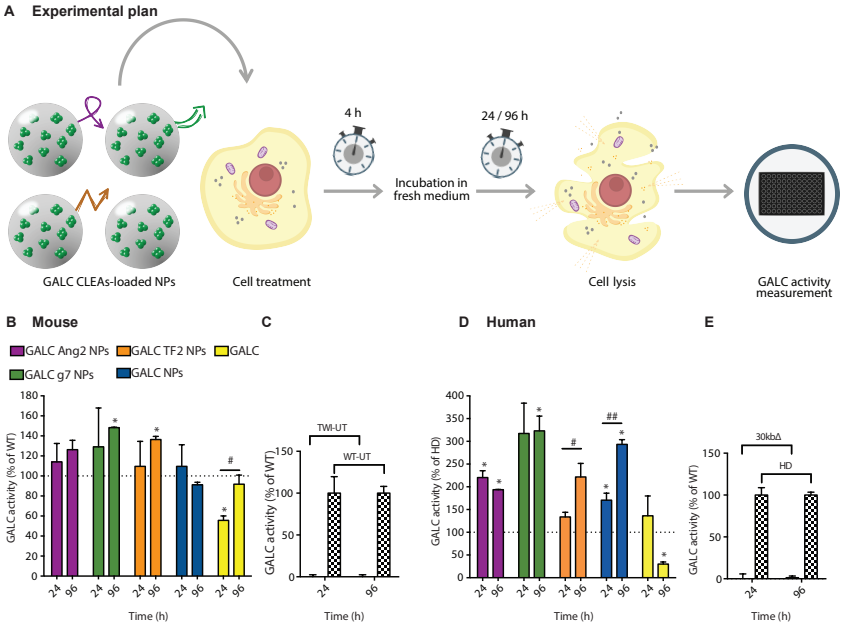


**Figure 3.29.** *In vitro*: enzyme replacement therapy time-response experiment. **(A)** *Graphical summary of the experiment.* GALC-deficient primary murine (from TWI mice) and human (from KD patients with GALC 30kbΔ) fibroblasts were treated with a single dose [3.0 U; Unit (U) = amount of enzyme that catalyzes 1 nmol of substrate per hour] of targeted GALC CLEA NPs (GALC Ang2 NPs, GALC g7 NPs or GALC Tf2 NPs), non-targeted NPs (GALC CLEA NPs) or with the free rm-GALC (GALC). 4 hours later cells were incubated with fresh medium. GALC activity was measured in the cell lysates 24 or 96 hours later by HMU-βGal assay. **(B)** *NPs mediated ERT in GALC deficient mouse cells*. Results are expressed in U/μg and reported as % of the activity of the WT cells [(U/ μg) = Unit of enzyme per microgram of cell lysate]. * = $P < 0.05$ specific treatment *vs.* WT; one-way ANOVA (Dunnett's multiple-comparisons test). # = $P < 0.05$ GALC 96 h *vs.* GALC 24 h; student t-test; mean ± SEM; N = 3. **(C)** *Controls.* WT and TWI untreated cells activity at 24 and 96 h. Mean ± SEM; N = 3. **(D)** *NPs mediated ERT in GALC deficient human cells*. Results are expressed in U/μg and reported in % of the activity of the healthy (HD = human donor) cells [(U/ μg) = Unit of enzyme per microgram of cell lysate]. * = $P < 0.05$ specific treatment *vs.* WT; one-way ANOVA (Dunnett's multiple-comparisons test). # = $P < 0.05$ GALC Tf2 NPs 96 h *vs.* GALC Tf2 NPs 24 h; ## = $P < 0.01$ GALC NPs 96 h *vs.* GALC NPs 24 h; student t-test; mean ± SEM; N = 3. **(E)** *Controls.* HD and 30kbΔ untreated cells activity at 24 and 96 h. Mean ± SEM; N = 3.

In the case of Tf2-targeted and non-targeted NPs, the activity resulted significantly higher after 96 hours compared to the 24 hours time point. Free rm-GALC-treated cells reached HD levels after 24 hours, but activity decreased with time, resulting in an opposite trend with respect to what reported for the murine cells. The GALC activity of TWI and 30kbΔ cells was not discernable from the background at both time points. (Fig. 3.29 C and E). Altogether, these data demonstrate that GALC CLEA NPs maintain enzymatic activity upon cellular uptake, and that they can completely reinstate GALC activity in TWI and KD patient cells as well.

### 3.3.5 NP-mediated enzymatic activity recovery *in vivo*

The next step was to test GALC CLEA NPs as therapeutic agents for enzymatic activity recovery in the brain of the TWI mouse. Prior to these experiments, the stability of the encapsulated enzyme in presence of serum proteins was evaluated. To this end, in order to mimic a biological fluid, we incubated all kinds of NPs employed in the study in a medium containing 50% FBS[223] (similar to serum concentration in blood), and studied the kinetics of drug release. At specific time points we measured the GALC activity both in the medium (due to the released enzyme) and within the NP (due to the enzyme not released yet). The release kinetics of GALC CLEAs was only slightly affected by the presence of serum proteins. Specifically, in the presence of proteins, around 50% of the payload was released within the first 24 hours (Fig. 3.30 A), whereas in serum-free medium NPs could retain 60% of the enzyme in the same time window (Fig. 3.30 B).

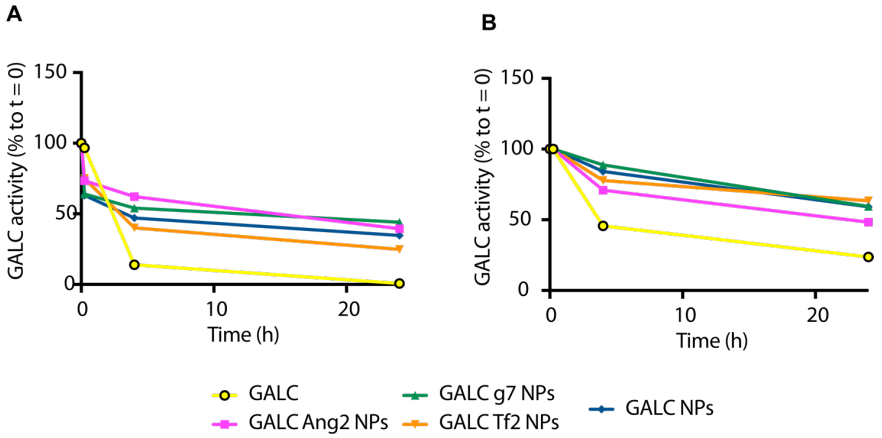


**Figure 3.30.** GALC-loaded NPs activity over time in presence and in absence of serum proteins. **(A)** GALC activity over time upon incubation of free GALC, GALC Ang2 NPs, GALC g7 NPs, GALC Tf2 NPs and GALC NPs in medium containing 50% fetal bovine serum at 37°C and at final GALC concentration 100 U/ml. **(B)** GALC activity over time upon incubation of free GALC, GALC Ang2 NPs, GALC g7 NPs, GALC Tf2 NPs and GALC NPs in serum protein-free medium (PBS) at 37°C and at final GALC concentration 100 U/ml. Activity is expressed as percentage respect to the activity same sample (free GALC or GALC-loaded NPs) at the same concentration in PBS prior incubation.

Remarkably, one should also note that the incubation of free non-encapsulated GALC in the presence of serum proteins lead to a dramatic loss of activity already after few hours. This confirms that although the protein corona had an influence on the release kinetics of the payload, as expected[224], the encapsulation into NPs is a fundamental requirement not only to allow the right targeting, but also to enable the enzyme to reach the desired target in its active form. Then, to finally demonstrate the delivery of active enzyme to the brain *in vivo*, the mice were administered with the NPs, and the presence of active GALC in key CNS and PNS organs was evaluated by means of enzymatic activity measurement and confocal fluorescence microscopy. This experiment was carried out in young mice (PND19-PND21), before symptom onset.[225]

Thus, we first synthesized targeted and non-targeted GALC CLEA NPs labeled with the fluorophore Atto-633 to allow visualization of NPs in extracted tissues (see the experimental plan in Fig. 3.31 A and material and methods for further details). Then, TWI mice were treated with NPs or with free rm-GALC via a single IP injection. After 4 hours mice were sacrificed by transcardial PBS-perfusion to thoroughly wash blood vessels, and organs were extracted for characterization. In particular, we investigated GALC activity in representative organs of the CNS and PNS (brain and spinal cord, and sciatic nerves, respectively) and in typical accumulation organs (liver and kidneys). GALC activity was assayed and compared with the activity of the same organs extracted from control mice [non-treated WT mice (WT-UT), non-treated TWI mice (TWI-UT) and non-treated HET mice (HET-UT) mice; see the legend in Fig. 3.31 B]. The presence of NPs was then investigated by fluorescence confocal imaging in PFA fixed tissues. Mice were divided in five experimental groups (see again legend in Fig. 3.31 B): WT-UT, HET-UT, TWI-UT, TWI treated with targeted NPs (TWI Targ-NPs) and TWI treated with non-targeted NPs or with rm-GALC (TWI Controls). To further assess the reproducibility of results, we tested two independently synthesized NP batches for each NP type (lot a and lot b; Fig. 3.31 B).

As reported in figure 5 C, GALC activity raised up to the 42±4% of the activity measured for WT-UT in the brains of TWI mice treated with targeted NPs. This value was significantly higher with respect to the approximately undetectable activity of the TWI-UT and, more importantly, reached the value of the HET-UT (45±8%), which represents a condition for which the disease does not manifest. TWI Controls, instead, reported a

lower median value, not significantly different from the TWI-UT, indicating that GALC could not be transported into the brain.

We detected a significantly higher activity in the liver in both TWI Targ-NPs and TWI Control mice (Fig. 3.31 D) with respect to the TWI-UT. This activity had likewise a higher median value for TWI Controls with respect to TWI Targ-NPs, indicating greater liver accumulation in the case of non-targeted NPs and of rm-GALC.

Kidneys showed a similar trend as the liver, but values of TWI Targ-NPs and TWI Controls mice remained lower compared to the liver, not reaching the HET-UT and not being significantly different from the TWI-UT (Fig. 3.31 E). Concerning sciatic nerve and spinal cord, instead, we did not observe any significantly detectable GALC activity neither in TWI Targ-NPs nor in TWI Controls (Fig. 3.31 F and G).

Finally, we visualized the presence of NPs in brain and liver by fluorescence confocal microscopy. As shown in figure 3.31 H we could detect the presence of fluorescently-labelled NPs in the brain of mice treated with the three differently targeted GALC CLEA NPs. On the contrary, we could not find any NP fluorescence signal for mice treated with non-functionalized NPs. Livers were taken as positive controls, and, as expected, presented a clear NP fluorescence both in the case of mice treated with targeted and non-targeted NPs.

Taken together, these data demonstrate that targeted GALC CLEAs NPs can induce GALC enzymatic activity via systemic administration in TWI brains up to the level required for the disease not to manifest. As expected, the presence of NPs was detected also in accumulation organs, while the spinal cord and sciatic nerves were not effectively treated.

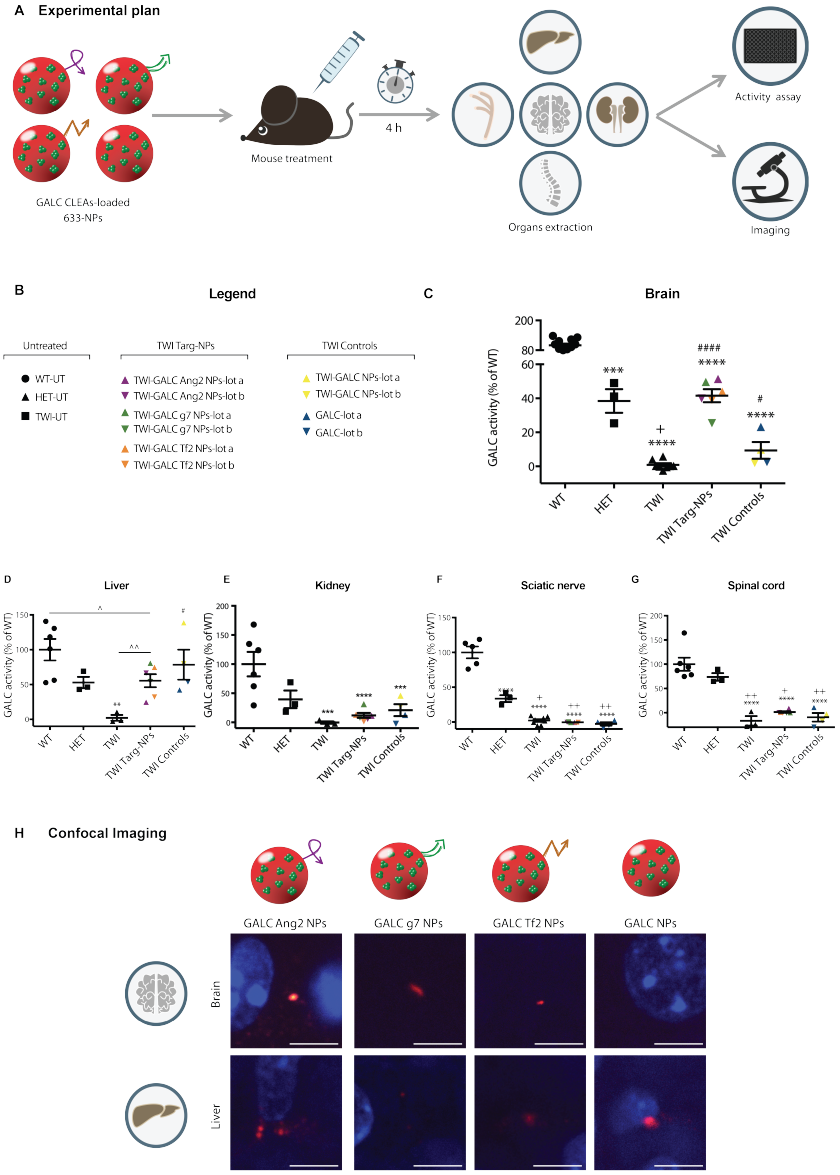


**Figure 3.31.** *In-vivo* NP mediated ERT in the TWI mice. **(A)** *Graphical summary of the experiment.* TWI mice were treated with targeted GALC CLEA 633 NPs (GALC Ang2 NPs, GALC

g7 NPs or GALC Tf2 NPs), non-targeted GALC CLEA 633 NPs (GALC CLEA NPs) or with the free rm-GALC (GALC). 4 hours later mice were sacrificed and GALC activity was assayed in extracted brain, sciatic nerves, spinal cord, kidneys and liver by HMU-βGal assay. **(B)** *Legend.* Untreated: wild type (WT-UT); heterozygous (HET-UT) and Twitcher (TWI-UT). GALC CLEA 633 targeted NPs (TWI Targ-NPs): TWI-GALC Ang2 NPs (lot a and b); TWI-GALC g7 NPs (lot a and b) and TWI-GALC Tf2 NPs (lot a and b). Control treatments (TWI Controls): GALC CLEA 633 NPs (TWI-GALC NPs lot a and b) and free rm-GALC (GALC-lot a and b). **(C)** *Brain GALC activity.* *** = P < 0.001 HET *vs.* WT; **** = P < 0.0001 TWI, TWI Targ-NPs and TWI Controls *vs.* WT; + = P < 0.05 TWI *vs.* HET; # = P < 0.05 TWI Controls *vs.* TWI; #### = P < 0.0001 TWI Targ-NPs *vs.* TWI one-way ANOVA (Tukey's test). Mean ± SEM; N = 3-12 / groups. **(D)** *Liver GALC activity.* ** = P < 0.01 TWI *vs.* WT; # = P < 0.05 TWI Controls *vs.* TWI; one-way ANOVA (Tukey's test). ^ = P < 0.05 TWI Targ-NPs *vs.* WT; ^^ = P < 0.01 TWI Targ-NPs *vs.* TWI; Student t-test. Mean ± SEM; N = 3-6 / groups. **(E)** *Kidney GALC activity.* *** = P < 0.001 TWI and TWI Controls *vs.* WT; **** = P < 0.0001 TWI Targ-NPs *vs.* WT; one-way ANOVA (Tukey's test). Mean ± SEM; N = 3-6 / groups. **(F)** *Sciatic nerve GALC activity.* Results are expressed in U/. est). Mean ± SEMroups. Targ-NPs s. . Control treatments (TWI Controls): GALC CLEA 633 NPs (TWI-GALC NPs < 0.0001 all groups *vs.* WT; + = P < 0.05 TWI *vs.* HET; ++ = P < 0.01 WT; TWI Targ-NPs and TWI Controls *vs.* HET; one-way ANOVA (Tukey's test). Mean ± SEM; N = 3-8 / groups. **(G)** *Spinal cord GALC activity.* **** = P < 0.0001 HET, TWI Targ-NPs and TWI Controls *vs.* WT; + = P < 0.05 TWI Targ-NPs *vs.* HET; ++ = P < 0.01 TWI and TWI Controls *vs.* HET; one-way ANOVA (Tukey's test). Mean ± SEM; N = 3-7 / groups. **(C-D-E-F-G)** Results are expressed in U/μg and reported in % of the WT activity [(U/ μg) = Unit of enzyme per microgram of cell lysate]. **(H)** Confocal imaging. Representative confocal images of brains and livers of the treated TWI mice. NPs are shown in red in the brains of the mice administered with the functionalized targeted GALC CLEA 633 NPs (GALC Ang2 NPs, GALC g7 NPs or GALC Tf2 NPs), while are not present in the brain of the mice treated with the non-targeted GALC CLEA 633 NPs (GALC CLEA NPs). All livers present NPs. Scale bar 5 μm.

### 3.3.5 Concluding remarks

In this study, we aimed as investigating for the first time the efficacy of CNS-targeted GALC-loaded biodegradable NPs as ERT agents for KD both *in vitro* and *in vivo*. The final objective of this work was to determine whether the targeted versions of our drug delivery system could reach the CNS and the PNS of the mouse model for KD and promote enzymatic activity recovery in these regions.

We tested 3 different peptides with potential as CNS targeting agents, namely, Ang2, g7, and Tf2. Ang2 is a 19-amino acid peptide that promotes brain targeting as it binds the low-density lipoprotein receptor-

related protein 1 (LRP-1).[219] The efficacy of this peptide as CNS targeting agent has been extensively demonstrated with the Ang2-paclitaxel conjugate ANG1005, currently in preparation for the Phase III clinical trial[226], but also in Ang2-modified nanostructures, including NPs[227]. The g7 peptide is a glycosylated 7-amino acid-long peptide derived from the synthetic opioid peptide MMP-2200. Polymeric NPs bearing g7 peptide on the surface have been shown to cross the BBB with a mechanism that is still unclear, probably involving membrane-membrane interactions and micropinocytosis-related processes. Recently described peptide Tf2 allows indirect targeting of the transferrin receptor by recognizing transferrin and has the potential to target the CNS, given the high density of the transferrin receptor on the BBB[227].

We modified our previously developed NP formulation (Section 3.2)[164] based on CLEAs formation and encapsulation into PLGA NPs, with each one of these 3 peptide ligands. The presence of targeting ligands on the NP surface led to an increase of the NP hydrodynamic diameter, in particular for NPs functionalized with the Ang2 peptide.

Although all the formulations could successfully encapsulate GALC, encapsulation efficiency varied among the NP compositions. Ang2- and Tf2-functionalized NPs showed a lower encapsulation efficiency compared to g7-targeted NPs (60%, 39%, and 74%, respectively). Further evaluations are required to rationalize this observation, but it is worth noting that both Ang2 and Tf2, that show lower encapsulation efficiency, are also positively charged at neutral pH and have a higher isoelectric point (9.33 and 9.08, respectively, vs. 5.98 of g7). It is possible that unfavorable electrostatic interactions take place during the enzyme encapsulation process, leading to

poorer outcome. However, Ang2- and Tf2 NPs consented a higher activity yield of GALC CLEAs (61% and 67% respectively) compared to GALC g7 NPs (37%). Even in this case the different peptide environment could lead to different exposure of the enzyme to the outer medium or cause undesired interactions between the targeting peptide and the enzyme. All in all, despite small differences in terms of encapsulation efficiency and activity yield, the presence of targeting ligands did not represent an obstacle in the encapsulation of active GALC CLEAs in NPs of suitable size[228]..

Before testing the potential of the NP formulations as ERT candidates, we verified that all NP types could enter cells and reach the intracellular target of GALC, which is represented by lysosomes, a key point to be investigated since endocytic route and signaling can be severely altered in most LSDs.[98] onfocal images and colocalization analysis confirmed that all the NPs employed in this study were taken up by cells and were localized into lysosomes 24 hours upon treatment. This was independent of the type of ligand and also of the type of cell since similar results were obtained in TWI and WT fibroblasts. This means that while the targeting peptides should address NPs to a certain region in the organism, at the cellular level they do not affect the expected fate of NPs, which in this case leads to the endo-lysosomal route.[229] Taken together, our results indicate that GALC CLEA NPs can successfully transport the enzyme inside cells and accumulate in the lysosomes, where GALC is supposed to perform its physiological activity, and that the preferred localization of delivered GALC in the lysosomes is not affected by the presence of targeting ligands on the carrier's surface.

Thus, we proceeded with testing the ability of all NPs formulations to deliver enzymatically active GALC in cells. A dose-response experiment revealed that all formulations could promote enzymatic activity in primary murine GALC-deficient cells in a dose-dependent manner. Interestingly, the recombinant enzyme administered alone provided cells with an activity that was always lower than the one resulting from the corresponding NP dose. Indeed, NP doses of 3 and 6 U allowed performing efficient ERT *in vitro*, bringing enzymatic cell activity equal or even higher than the physiological activity of healthy cells, while not even the highest dose of free rm-GALC could induce WT activity. These data prove the effectiveness of our NPs to deliver GALC inside cells in an active form, and in a more efficient way if compared to the non-encapsulated enzyme. This behavior can be probably attributed to the known ability of polymeric NPs to protect the enzyme before it reaches the lysosomes[165] and to the capability of controlling the release of their cargo at the lysosomal acidic pH[230] However, to definitely prove the capability of our GALC loaded NPs of properly acting on their physiological substrate, experiments on cells that naturally accumulate PSY are mandatory. To this end, PSY quantification experiments on TWI oligodendrocytes[36] are currently ongoing in our laboratory.

Moreover, a time-response experiment showed that targeted NPs can maintain constant GALC activity (equal or higher than WT) between 24 and 96 hours after treatment. Non-targeted NPs, instead, were affected by an activity decrease at t = 96 hours. These results suggest that targeting agents could enhance NPs persistence inside cells.[231] Free rm-GALC, rather, yielded less than 50% of WT activity after 24 hours and reached the WT level only after 96 hours. These *in vitro* data add important information to

the very little knowledge present in the literature about the suitability of polymeric NPs for ERT. To date, only a few works have investigated the capability of PLGA NPs to deliver functional enzymes, and only *in vitro*.[164,165] In this context, our results confirm the potential of NPs made of this material for enzyme delivery *in vitro*.

Given the very promising *in vitro* data, we proceeded with the testing of our NP formulations *in vivo* in the TWI mouse. We treated TWI mice intraperitoneally with single NP injection, to later assay the GALC activity inside different organs (of CNS or PNS and in accumulation organs). We preliminarily carefully evaluated different routes of drug administration, and we decided to use IP injection given that is the predominantly used method for systemic drugs administration in small species for which intravenous access is challenging and that allows administering large volumes of fluid safely. [232] As expected, we found substantial GALC activity in the examined accumulation organs.[19,233] Both targeted (Ang2, g7 or Tf2) GALC CLEA NPs and controls (non-targeted NPs and rm-GALC) accumulated in a similar amount in the liver and kidneys 4 hours after injection. These generally high liver accumulations confirm the effectiveness of IP injection. IP injected drugs, indeed, are primarily absorbed by mesenteric vessels, which drain into the portal vein, pass through the liver, and finally reach the systemic circulation.[232] Regarding the brain, instead, we found that mice treated with targeted NPs displayed a GALC activity that was approximately equal to the activity of the HET-UT mice (heterozygous mice for GALC mutation). This is a key finding if considered that heterozygous mice are characterized by a completely healthy phenotype. The same is valid for human carriers of GALC mutations. This result is even more appealing

considering that brains of mice treated with non-targeted NPs or with the free enzyme, instead, did not show any significative GALC activity increase. The fact that GALC activity was not found in the brains of mice treated with non-targeted NPs, but was instead present in their livers, confirms that, after reaching systemic circulation, BBB passage can be attributed to the mechanism of the specific targeting peptides, which have been already extensively investigated by us and others[214,219,220]. Although some studies demonstrated the ability of different types of NPs to reach the brain, this is the first time that a nanovector is shown to deliver a functional enzyme into the brain of a LSD model. Several efforts have been made to exploit certain cell receptors to allow a free native or modified enzyme to pass the BBB, but with not very promising results.[233,234] Even if the enzyme could reach the brain, in fact, it would be rapidly metabolized by cells, causing the need for very frequent injections in the perspectives of clinical treatment. Indeed, despite ERT with free recombinant enzymes is the most widely applied clinical method to treat non-CNS involved LSDs, it requires long-term and frequent treatments, resulting in expensive therapies that are not free from side effects, including immunoreactions.[235] In this context, the possibility to perform ERT with the enzyme encapsulated in a safe nanovector is definitely appealing, as it could protect and slowly release the enzyme, thus minimizing some of the classical-ERT disadvantages. To this end, a systematic pharmacodynamic study of our new drug is required, in order to determine the time evolution of GALC activity in the TWI nervous system. In this way, the time after injection at which GALC activity decreases under the heterozygous level can be found, and this interval can be used to determine the time needed between subsequent injections.

Concerning the other analyzed tissues of the nervous system (the spinal cord and sciatic nerve), neither enzyme-loaded NPs nor the recombinant enzyme could induce a significant GALC activity increase. This is actually not surprising. It is known, indeed, that efficient drug delivery of therapeutic doses to these components can be difficult to achieve owing to neuroanatomy issues and the restrictiveness of the blood-nerve barrier.[186] Blood flow tended to be higher for brain and brain stem than for spinal cord or sciatic nerve.[236] Furthermore, in TWI mice it can be further reduced due to the typical TWI nerve edema. In other edematous neuropathies, in fact, has been been demonstrated the presence of a reduced nerve blood flow, wich appear due to increased intercapillary distances.[237] Thus, a time longer than 4 hours would be likely necessary to appreciate an elevation of the enzyme activity also in these areas

There is also the possibility that different targeting strategies may be required. All the three tested peptides, in fact, have been demonstrated efficient in promote the delivery of cargo across the BBB, but may be not suitable for the delivery across the BNB. Targeting ICAM-1 receptor, highly expressed in the endoneurial endothelial cells during inflammation, may be a promising strategy to investigate for BNB targeting (see Section 3.1.3).

In any case, specific studies to address this point will be necessary, being the involvement of PNS a foundamental feature of KD and many other LSDs.

Two other important aspects that deserve to be underlined concern inter-batch reproducibility and the effect of cell sex on uptake of NPs. Regarding the first one, all the *in vivo* experiments of this work were carried with two different NP batches, each one independently synthetized (i.e. in

different days) with different lots of recombinant enzyme. Results were perfectly consistent among the two batches. This observation gives an adjunctive strength to our approach, demonstrating the reproducibility also among different batches of the produced drug. Inter-batch reproducibility is indeed a very critical point regarding NPs in general. For this reason, for example, many efforts have been recently made to construct chips capable to automatically synthetize polymeric NPs in a very reproducible way.[238] Cell sex, instead, is an interesting overlooked factor, which can affect NP uptake by cells. Recently, in fact, Serpooshan and co-workers demonstrated that cell sex leads to differences in quantum-dot uptake between male and female human amniotic stem cells (hAMSCs) and primary fibroblasts.[239]

These findings pave the basis on the fact that variations existing in the production of paracrine factors (as proteins or hormones) by male and female cells may have the capacity to modify the protein corona of NPs, potentially affecting NP cell interactions. However, mice treated with our targeted NPs formulations did not report significant different outcomes between male and female animals. Targeting peptides, thus, seem to promote BBB translocation in a sex-independent manner, in accordance with the fact that also enzyme release from our targeted NPs is not dramatically affected by the presence of the protein corona. Nevertheless, given the difference in cell-secreted molecules that can occur between organisms with different sexes during life, a longitudinal study of this aspect would be desirable in the perspective of an effective treatment.

Lastly, in order to underline the potential of clinical translatability of this drug delivery system, we also performed a test in human cells derived from KD patients carrying the 30kb-deletion in the GALC gene, one

of the most common mutations causing KD.[240] NPs revealed to be able to carry enzymatically active GALC very efficiently also into human cells, providing them with a GALC enzymatic activity that was much higher than the one of healthy cells up to 96 hours after the treatment. For comparison, free rm-GALC could even not provide 50% of the activity of healthy cells. This confirms the potential of GALC CLEA NPs for ERT also in a human KD physiological environment.

In view of a clinical translation, a possible technical limitation that is also common to other ERT approaches for other rare diseases might be the availability of a large amount of drug allowing treating the patient for all lifetime. Producing recombinant enzymes from eukaryotic cells, in fact, remains a quite expensive process.[149] If this was the case, NP-mediated ERT could be decisive if used as a sort of "*buffer therapy*", to be promptly applied to the child immediately after birth for a limited period of time, in combination with other therapeutic approaches. In this way, a physiological enzyme activity would avoid nervous system damage before the "*long-term therapy*" (most likely gene therapy) can engraft and provide its therapeutic effect.[241] Finally, we should stress that developing a therapy preventing all neural damages is a dramatically challenging task in KD. It is indeed very rapidly progressing, with a median age of symptom onset of 4 months, and median time to diagnosis after onset of 3 months. Therefore, in order to have a chance of success, it is imperative that therapy must guarantee GALC activity in the CNS and PNS as soon as possible. Consequently, also a deeper understanding of disease progression in early-onset KD is critical for developing treatments, designing clinical trials, and evaluating outcomes.

In conclusion, with this study we demonstrated for the first time the capability of targeted polymeric NPs to perform delivery of a protein into the brain of a murine model of LSD, overcoming the BBB and delivering functional enzyme in therapeutically relevant amount. This effective approach opens new exciting therapeutic opportunities for all CNS-involved LSDs with no cure available to date, but also for all disorders which could benefit from the passage of specific proteins through the BBB to reach CNS.

Regarding KD, however, next points which are mandatory to be investigated in the TWI mice will be, at first, to check if the NPs can reduce PSY amount inside TWI CNS and PNS, and, consequentially, if they can ameliorate overall mouse health (as lifespan and motor/cognitive abilities). Only after the assessment of these two fundamental aspects, a systematic pre-clinical testing of the developed drug in the TWI mice will be carried out.

### 3.3.6 Material and methods

#### Materials

Poly (D,L-lactide-co-glycolide) (PLGA; Resomer RG 503H and Resomer RG 752H) was purchased from Sigma-Aldrich and used as received. Atto 488-NHS ester and Atto 633 amine were purchased from Atto-TEC GmbH (Germany) and used as 10 mg/ml stock solutions in DMSO. All other chemicals were purchased from Sigma-Aldrich unless otherwise specified. All chemicals were used as received.

#### Methods

#### PLGA-NHS synthesis

PLGA was activated via n-hydroxysuccinimide (NHS) 1-Ethyl-3-(3-dimethylaminopropyl)-carbodiimide (EDC) chemistry. 0.05 mmol of PLGA were dissolved in 5 ml of anhydrous DCM under nitrogen atmosphere and 0.5 mmol of NHS were added. Then, 0.5 mmol of EDC-HCl and 0.6 mmol of triethylamine (TEA) were added. The reaction mix was stirred for 18 hours at RT, then product was precipitated with methanol and collected by centrifugation. The final product was washed twice with methanol, then characterized by 1H-NMR in $CDCl_3$ and stored at -20°C until use. Characterization: $^1$H-NMR (Bruker AVANCE 300 spectrometer, 300 MHz, $CDCl_3$). $\delta$PLGA-NHS: 5.2 ppm (-OCH($CH_3$)COO-), 4.8 ppm (-O$CH_2$COO-), 2.9 ppm (-CO$CH_2CH_2$COON-), 1.6 ppm (-OCH($CH_3$)CO-).

## PLGA-Mal synthesis

PLGA-NHS was further modified with a maleimide group to allow the reaction with cysteine-terminated peptides. 0.05 mmol of PLGA-NHS were dissolved in DCM and 0.1 mmol of N-(2-aminoethyl) maleimide trifluoroacetate were added together with 0.11 mmol of TEA. The reaction mix was stirred for 2 hours at RT, then the product was precipitated with methanol and collected by centrifugation. The final product was washed twice with methanol and characterized by $^1$H-NMR (Bruker AVANCE 300 spectrometer, 300 MHz, $CDCl_3$). $\delta$PLGA-Mal: 6.7 ppm (-HC=CH-), 5.2 ppm (-OCH($CH_3$)COO-), 1.6 ppm (-OCH($CH_3$)CO-).

## Peptide-modified PLGA synthesis

All peptides employed in this study were synthesized via solid phase peptide synthesis as described elsewhere.[17,164]

The peptide sequences are the following:

Ang2: TFFYGGSRGKRNNFKTEEYGC

g7: GF(D-)TGFLS(O-β-D-glucose)

Tf2: CGGGHKYLRW

2.25 mmol of peptide were added to 2.05 mmol of PLGA-NHS (for g7-PLGA synthesis) or PLGA-Mal (for Ang2-PLGA and Tf2-PLGA synthesis) in DMF. The mixture was stirred at RT for 18 hours (g7-PLGA) or 48 hours (Ang2-PLGA and Tf2-PLGA). The final product was precipitated with methanol and collected by centrifugation and washed twice with methanol. The reactions were monitored via $^{1}$H-NMR in $CDCl_3$ (Bruker AVANCE 300, 300 MHz) until absence of the NHS or the maleimide group $\delta$, indicating complete conversion. The final products were dried and stored at -20°C until use.

## Fluorophore-tagged PLGA synthesis

0.24 mmol of Atto633-amine were added to 0.22 mmol of PLGA-NHS in DMSO. The mixture was stirred for 18 hours at RT, then the final product was precipitated with methanol and collected by centrifugation. The obtained labelled PLGA was washed twice with methanol, then dried and stored at -20°C until use.

## Recombinant murine GALC production

HEK 293T cells stably expressing and secreting His6-tagged murine wild-type GALC (kindly provided by Prof. Deane of the Cambridge University)[17] were maintained in 400 μM zeocin selection medium and expanded in 1450 $cm^2$ inner surface roller bottles (37°C, 5% $CO_2$, 0.7 rpm). The enzyme was routinely purified from extracellular medium by nickel-affinity chromatography (Ni Sepharose excel histidine-tagged protein purification resin; 17-3712-03 GE Healthcare Life Sciences) as in Galliani et

al., 2018[164]. The purified enzyme was finally buffer exchanged with 10 kDa molecular mass cut-off concentrator and stored at - 20°C until use.

### CLEAs synthesis

To produce GALC CLEAs, typically 200 µl of GALC solution (750 µg/ml in 10 mM mannitol, 5 mM glycine, 140 mM NaCl, 3.7 mM sodium phosphate buffer, Tween 80 0.05%, pH 5.5) were added to 600 µl of acetone simultaneously with 2 µl of 25% glutaraldehyde under stirring. The mixture was then stirred overnight at 4°C. The formed CLEAs were centrifuged (30 min, 4°C, 13,200 rpm) and washed twice with 1 ml of acetone. The final GALC CLEAs were suspended in 1 ml of acetone and stored at -20°C until use. To produce fluorescently labelled GALC CLEAs, Atto 488-NHS solution in DMSO (10 mg/ml) was added to 1 ml of GALC CLEAs with 1:20 CLEAs:Atto488-NHS molar ratio. The mixture was stirred for 4 hours at RT then centrifuged (30 minutes, 13,200 rpm) and washed twice with 1 ml of acetone. Resulting Atto488-tagged CLEAs were suspended in 1 ml of acetone and stored at -20°C until use.

### CLEA NPs synthesis

For targeted NP synthesis, 200 µl of GALC CLEAs were added to 200 µl of a solution containing 8 mg of PLGA 752H and 2 mg of peptide-modified PLGA in acetone. This mixture was then added dropwise to 1200 µl of 2% sodium cholate in water under stirring. The formed NP suspension was centrifuged (20 min, 4°C, 13,200 rpm) and washed twice with 500 µl of water. The final NP pellet was suspended in 50 µl of 100 mg/ml D-(+)-trehalose and stored at -20°C until use.

To produce non-targeted NPs, peptide-modified PLGA was replaced with the same amount of PLGA 503H. Fluorescently labelled NPs were obtained adding 0.1 mg of Atto633-tagged PLGA and replacing GALC CLEAs with Atto488-tagged GALC CLEAs. Empty NPs were produced replacing GALC CLEAs with the same volume of acetone.

### Hydrodynamic diameter and Zeta potential

Hydrodynamic diameter and Zeta potential of NPs were measured with a ZetaSizer NanoZS (Malvern Instruments Inc. UK) by means of dynamic light scattering. Samples were diluted 1:1000 in deionized water before measurement. Samples were transferred into polypropylene cuvettes for hydrodynamic diameter measurement or into appropriate electrophoretic cells for zeta potential determination. Measurements were performed at RT. Mean hydrodynamic diameter resulted from the autocorrelation function of the intensity of scattered light calculated by DTS Nano software. Electrophoretic mobility was determined and converted into zeta potential by DTS Nano software.

### Protein quantitation

GALC concentration in NP samples was determined via ninhydrin assay. Briefly, 5 µl of NPs were digested overnight at 95°C in 200 µl of 6 M HCl, then vacuum dried. The residue was suspended in deionized water, then 10 µl of each sample was added to 110 µl of ninhydrin reagent (20 mg/ml ninhydrin, 2 mg/ml stannous chloride in 75% ethylene glycol in 4N acetate buffer, pH 5.5). The reaction mixture was heated at 95°C for 20 minutes then samples were plated into a 96-well microplate. Absorbance was measured at 560 nm. Protein concentration was calculated by interpolation from a

calibration curve prepared with GALC subject to the same digestion and reaction protocols. NP encapsulation efficiency was determined as follows:

$$EE\% = \frac{GALC(\mu g)_{NPs}}{GALC(\mu g)_{INJ}} \cdot 100$$

Where $GALC(\mu g)_{NPS}$ is the amount of GALC encapsulated in NPs and $\text{GALC}(\mu\text{g})_{\text{INJ}}$ is the amount of GALC employed in each synthesis.

### GALC activity measurement in NPs

To determine GALC activity in NP samples, 2 µl of NPs were added to 50 µl of assay buffer (50 mM sodium citrate, 125 mM NaCl, 0.5% Triton X100, pH 4.5). Then, 50 µl of 1 mM 4-methylumbelliferyl-β-D-galactopyranoside in assay buffer were added. Samples were incubated at 37°C for 20 minutes, then 200 µl of stop solution (0.5 M glycine, 0.3 M NaOH) were added. Samples were plated into a 96-well multiplate for fluorescence and fluorescence was measured with Promega GloMax discover Multimode microplate reader with excitation filter 365 nm and emission filter 415-485 nm. Activity yield (AY%) of NPs was calculated as the ratio between the specific activity of the sample ($SA_{NPs}\text{SA}_{\text{NPs}}$) and the specific activity of the unaltered GALC ($SA_{GALC}\text{SA}_{\text{NPs}}$) $\text{SA}_{\text{GALC}}$) as follows:

$$AY\% = \frac{SA_{NPs}}{SA_{GALC}} \cdot 100$$

Where the specific activities are defined as unit of enzyme ($U\text{U}$) per microgram of enzyme ($\mu g_{GALC}\mu\text{g}_{\text{GALC}}$):

$$SA = \frac{U}{\mu g_{GALC}}$$

1 Unit of enzyme ($U\text{U}$) is defined as 1 nmol of substrate ($nmol_{SUB}\text{nmol}_{\text{SUB}}$) hydrolyzed in 1 hour:

$$1U = \frac{1\ nmol_{SUB}}{h}$$

## Primary human and murine cell cultures and treatments

Adult mouse fibroblast cultures were obtained from WT and TWI ears, according to the protocol established in the laboratory of Dr. Evan Eichler (University of Washington, https://genome.ucsc.edu/ENCODE/protocols/cell/mouse/Fibroblast_Stam_protocol.pdf) with minor modifications. Briefly, after anaesthesia, mouse ears were extracted, washed with sterile water and cut into small pieces. All pieces were then collected in a tube and added with collagenase XI (C7657-100 mg; Sigma Aldrich) diluted in high glucose DMEM (approximately 2.5 mg of collagenase -320 CDU- for 1 mouse). After 2 hours of incubation at 37 °C the Eppendorf tube was centrifuged for 5 minutes at 200 g, the supernatant was discarded and the pellet was washed with 2 ml of PBS and centrifuged again discarding the supernatant. Trypsin-EDTA 0.05% (59418C-100ML; Thermo Fisher Scientific) was then added to the tube and left 45 minutes at 37 °C. The tube was then centrifuged and the pellet was resuspended in the complete DMEM [high glucose DMEM supplemented with 10% of heat-inactivated fetal calf serum (FCS), 4 mM L-glutamine, and 1% penicillin/streptomycin; all products were from GIBCO-Life Technologies)]. Obtained cells were thus dissociated pipetting up and down with a 10 ml syringe (with a G21 needle), plated in a 60 mm cell petri dish and incubated at 37 °C in a humidified atmosphere containing 5% $CO_2$. The day after, cells were washed and medium was replaced. After reaching confluence (approximately 3-4 days), cells (p0) were washed with 1 ml of PBS and split with a ratio of 1:2. Human fibroblasts [from a healthy donor

(HD; C0045C; Life Technologies) and from a patient with the large common Caucasian 30 kDa deletion in the GALC gene, c.1161+6532_polyA+9kbdel (30kbΔ; F0461990, Gaslini institute Biobank)][240] were kindly donated by Dr. Gritti (San Raffaele Telethon Institute for Gene Therapy, Milan, Italy) and maintained under the just mentioned culture conditions. For experiments, WT, TWI, 30kbΔ and HD fibroblast cells were plated in standard 96 well cell plates (12500 cell per well). 24 hours later medium was replaced with fresh medium containing NPs at different concentrations. After 4 hours of NPs incubation medium was removed and cells were washed 3 times with 100 µl of PBS. Then, cells were lysed for the enzymatic assay or fresh medium was added and cells were lysed after 24 or 96 hours. For every NP experiment: male and female strains were used for experiments with mice cells; a female strain were used for experiments with human cells. WT and TWI cells were used at passage 4, 30kbΔ and HD cells at passage 8.[242]

### GALC enzymatic activity assay in cell and tissues

GALC enzymatic activity assay was carried out both in murine/human fibroblasts and mouse tissues (brain, liver, kidney, sciatic nerve and spinal cord). Both primary cells and tissues were lysed on ice with RIPA buffer (Sigma Aldrich) containing a protease and phosphatase inhibitors cocktail (cOmplete and PhosSTOP; Roche Diagnostics). Cell lysates were sonicated (for 4 sec at 12 µm of intensity) whereas tissues were homogenized in 1.5 ml eppendorf tube with appropriate micro-pestles. Then, after centrifugation (15000 g for 25 min, 4 °C), the supernatants were collected and tested for protein concentration by micro-BCA protein assay kit (Thermo Scientific Pierce). In order to measure GALC activity, we used 6-hexadecanoylamino-4-methylumbelliferyl-beta-D-galactopyranoside (HMU-

βGal), the fluorescent substrate currently used for the clinical diagnosis of Krabbe disease[243]: 10 µl of lysates was added to 20 µl of 50 µM HMU-betaGal substrate solution, incubated for 17 hours at 37°C; the reaction was then stopped and the fluorescent product (4-MU) was read by using a microplate GloMax fluorescence reader. GALC activity (reported as nmol/mg protein extract in 17 hours of incubation) was calculated by comparison with a standard curve previously obtained by measuring the fluorescence of different concentration of 4-MU.

## Animal procedures

Twitcher heterozygous mice (TWI+/− C57BL6 mice; Jackson Labs), kindly donated by Dr. A. Biffi (San Raffaele Telethon Institute for Gene Therapy, Milan, Italy), were used as breeder pairs to generate homozygous TWI mice (TWI−/−, elsewhere abbreviated as TWI for simplicity). Animals were maintained under standard housing conditions and used according to the protocols and ethical guidelines approved by the Ministry of Health (Permit Number: Codice 535/2018-PR; official starting date: 9/7/2018). For genotyping purpose, mice genomic DNA was extracted from clipped tails of mice at PND 10-15 (EUROGOLD Tissue-DNA Mini Kit, Euroclone), as previously done by us[41]. The genetic status of each mouse was later determined from the genome analysis of the TWI mutation, as reported from Sakai and coworkers[244]. TWI, WT and HET animals (PND 19-21) were used for experiments. TWI animals were intraperitoneally injected with NPs (1600 mg/kg) or with free GALC (100 mg/kg) diluted in 1 ml of physiological solution.[119,245] After 4 hours mice were deeply anesthetized with a urethane solution (Sigma Aldrich, 0.8 ml/hg) and sacrificed by transcardial perfusion with PBS, so as to remove the blood from vessels.

Subsequently, brain and liver were extracted from each mouse and one brain hemisphere or liver lobe was placed in a paraformaldehyde (PFA) 4% solution and the other hemisphere or liver lobe in RIPA lysis buffer (R0278-50ML; Sigma Aldrich) containing a protease and phosphatase inhibitors cocktail [cOmplete (4693116001) and PhosSTOP (4906845001); Roche Diagnostics]. Spinal cord, sciatic nerve and kidneys were also extracted and stored in the complete RIPA buffer just described. Finally, organs placed in the PFA solution were stored at 4 °C for at minimum 3 days before vibratome cutting, whereas organs put in the lysis buffer were immediately processed to perform the GALC enzymatic assay. Regarding mice sex, experiments were done as follow: 5 WT male, 7 WT female, 4 TWI male, 3 TWI female, 1 HET male and 2 HET female were used for the untreated conditions; 3 TWI male and 3 TWI female were used for the targeted-GALC loaded NPs injections (1 male and 1 female for each targeting peptide: g7, ANG2 or Tf2); 2 TWI male and 2 TWI female were used for the control conditions (1 male and 1 female for non targeted-GALC loaded NPs and for the free GALC). All procedures were made with the maximal efforts to minimize mice suffering.

### Cells and tissues confocal imaging

TWI or WT fibroblasts were seeded 24 hours before experiments into a glass-bottom Petri dish (WillCo dish GWst-3522) to reach 80-90% confluence. Incubation with targeted- or non-targeted GALC-loaded NPs was performed at 37°C, 5% $CO_2$ in DMEM with 10% FCS at final NP concentration 1.5 mg/ml. After 4 hours, cells were washed twice with PBS and incubated with fresh medium for 20 h. Then, cells were incubated with 0.1 µM Lysotracker Red DND-99 (Thermo Fisher). After 15 minutes, cells

were washed with PBS and stained with 4% PFA before imaging. For tissue imaging brain and liver samples were processed as described in the *animal procedure* paragraph. Samples were cut with a vibratome (Leica VT1000 S) at a final slice thickness of 60 µm. In particular, consecutive coronal brain sections were cut at 0.5-2.10 mm from bregma. All samples were mounted with Fluoroshield Mounting Medium with DAPI. Samples were imaged with a Leica TCS SP5 SMD inverted confocal microscope (Leica Microsystems AG) interfaced with Ar, DPSS and HeNe lasers for excitation at 488, 560 and 633 nm, respectively, and with an external pulse diod laser for excitation at 405 nm. Samples were viewed with a 40x 1.5 NA oil immersion objective (Leica Microsystems) with pinhole aperture set at 1.0 Airy. All images were analyzed with FiJi software and colocalization was determined with JACoP plugin.

## Statistical analysis

If not differently specified, data are reported as mean ± SEM obtained from at least three independent experiments (in figure legends, "N" indicates the number of experiments performed). Data were statistically analyzed by using Prism 6.00 (GraphPad Software, San Diego, CA; RRID:SCR_002798). For parametric data, Student's t-test (unpaired, two-tailed) or one-way ANOVA (Tukey's or Dunnett's multiple-comparisons test) was used; the mean values obtained in each repeated experiment were assumed to be normally distributed about the true mean. Statistical significance refers to results for which $P < 0.05$ was obtained.

# Chapter 4: Autophagy in Lysosomal storage disorders

## 4.1 Scientific background

### 4.1.1 Autophagy machinery

Autophagy is a dynamic degradation pathway by which cytosolic material, including damaged organelles, proteins, carbohydrates, lipids and pathogens, are delivered to the lysosome for degradation. The autophagy process initiates by the formation of isolated membranes in the cytoplasm called phagophores. The membrane sources of phagophores arise from the ER, plasma membrane, mitochondria and ER–mitochondria contact sites.[246,247,248,249] The phagophores engulf cytoplasmic cargo during their elongation to form double-membraned vesicles called autophagosomes. Autophagosomes fuse with late endosomes to form single-membrane-bound hybrid organelles called amphisomes.[250] Amphisomes then fuse with the lysosomes to form acidic autolysosomes where the cargo is degraded.

Several autophagy-related (Atg) proteins orchestrate the advancement of the pathway, which is evolutionary conserved from yeast to mammals.[251,] Specifically, two ubiquitin-like conjugation systems participate in the initiation of autophagy (Fig. 4.1). The first reaction involves Atg5–Atg12 conjugation, in which Atg7 (E1 ubiquitin-activating enzyme-like) activates the ubiquitin-like protein Atg12, which is then transferred to Atg10 (E2 ubiquitin-conjugating enzyme-like), and is ultimately linked covalently to Atg5. The Atg12–Atg5 conjugate forms a large complex with Atg16L1 that is essential for the elongation of phagophores, but dissociates after autophagosome formation. The second system involves the conjugation of

microtubule-associated protein 1 LC3 (light chain 3) (mammalian homologue of yeast Atg8) to PE (phosphatidylethanolamine). LC3 undergoes post-translational C-terminal cleavage by the protease Atg4B, resulting in the cytosolic LC3-I form, which is then conjugated to PE in a reaction involving Atg7 (E1-like) and Atg3 (E2-like) to generate the autophagosome-associated LC3-II form. LC3-II mediates membrane tethering and hemifusion essential for the expansion and closure of phagophores to form autophagosomes where it remains associated throughout their lifespan.[252] LC3-II residing on the autophagosomal inner membrane is degraded within the autolysosomes, whereas those on the cytoplasmic surface of autolysosomes are delipidated by Atg4 and recycled.[253]

Distinct classes of PI3K (phosphoinositide 3-kinase) regulate autophagy in mammalian cells. The activity of the PI3KC3 (class III PI3K) member hVps34 (mammalian vacuolar protein sorting 34 homologue) is essential for autophagosome biogenesis, whereas inhibition of PI3KC1a (class Ia PI3K) activity stimulates autophagy by the mTOR (mammalian target of rapamycin) pathway (Fig. 4.1).[254] The lipid kinase hVps34 phosphorylates phosphatidylinositol to form PtdIns3*P*, which possibly functions in autophagosome synthesis.[255] hVps34 is part of the autophagy-initiating macromolecular complex (PI3KC3) consisting of Beclin-1/Atg6, Atg14L and hVps15.[256,257,258] The activity of hVps34 is enhanced by its interaction with Beclin-1, which has several binding partners governing autophagosome formation.[259] Beclin-1 interactors that positively regulate autophagy are Atg14L, Ambra1 (activating molecule in Beclin-1-regulated autophagy), UVRAG (UV irradiation resistance-associated gene) and Bif-1 (endophilin

B1). The small GTPase Rab5 also binds to and activates hVps34 to induce autophagy (Fig. 4.1).[260]

Autophagosome biogenesis is also regulated by the ULK1 (UNC-51-like kinase 1)–Atg13–FIP200 (focal adhesion kinase family-interacting protein of 200 kDa) macromolecular complex.[261]

Newly generated autophagosomes move bidirectionally along the microtubules with a bias towards the microtubule-organizing center where the lysosomes are enriched.[262,263] Subsequent fusion events (autophagosome/late endosome and emphisome/lysosome) are mediated by Rab7, ESCRTs (endosomal sorting complexes required for transport), SNAREs (*N*-ethylmaleimide-sensitive factor- attachment protein receptors) and the class C Vps proteins (Fig. 4.1). During the formation of amphisomes, tethering between vesicular membranes is mediated by the small GTPase Rab7 and its effector/activator HOPS (homotypic fusion and vacuole protein sorting) complex.[264]

Functional multivesicular bodies (MVBs) are also essential for the maturation of autophagosome since perturbations in MVB formation, such as with mutations in the ESCRT proteins, block the autophagic flux.[265266,267]

The syntaxin-5 SNARE complex regulates ER–Golgi transport through the secretory pathway that is essential for the activity of lysosomal proteases such as cathepsins for autophagic degradation.[268]

Regarding degradation of the autophagic cargo, whereas it can be non-selective during nutrient deprivation, it can also be cargo-specific, as shown for p62 (sequestosome-1), mutant huntingtin, NBR1 (neighbor of *BRCA1* gene 1) and certain pathogens.[269,252] The P62 protein, in fact, is a fundamental adaptor protein with an LC3-binding motif that enables

specific cargo recognition and degradation.[270] Furthermore, autophagy regulates metabolism of lipids (lipophagy) including cholesterol[271], and also acts in organelle quality control by regulating their turnover. For example, excess or damaged mitochondria are removed by autophagy (mitophagy).[272]

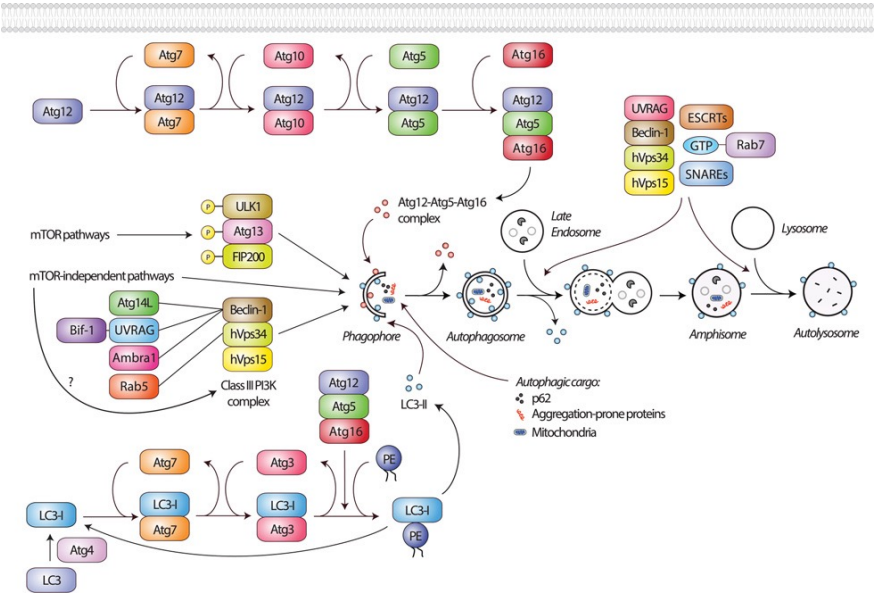


**Figure 4.1.** The mammalian autophagy pathway and its regulatory machinery Autophagy is initiated by the formation of phagophores in the cytoplasm, which engulf cytoplasmic cargo to form autophagosomes. Autophagosomes fuse with the late endosomes forming amphisomes that then fuse with the lysosomes to form autolysosomes where the autophagic cargo is degraded. Autophagy is controlled by mTOR-dependent and mTOR-independent pathways. The ULK1–Atg13–FIP200 and the PI3KC3 complexes regulates autophagosome synthesis downstream of the mTOR signalling pathways. Several Beclin-1 interactors positively modulate this process. Two ubiquitin-like conjugation systems involving Atg proteins function in the elongation of phagophores. The Atg5–Atg12 conjugation involves Atg7 (E1-like) and Atg10 (E2-like), whereas the LC3–PE conjugation involves Atg7 (E1-like) and Atg3 (E2-like). The Atg5–Atg12 conjugate forms a complex with Atg16, Atg5–Atg12·Atg16, which has E3-like activity towards LC3–PE conjugation (LC3-II). Autophagosome maturation involving fusions with late endosomes and lysosomes are mediated by Rab7, ESCRT proteins, SNARE proteins and the UVRAG–Beclin-1–hVps34–hVps15 complex. Autophagic cargo consisting of non-specific or

specific substrates such as p62, aggregation-prone proteins or mitochondria, are degraded in the autolysosomes.[251]

### 4.1.2 Autophagy in diseases

Autophagy regulates many fundamental biological processes during development, normal physiology, and in response to a wide variety of stresses, being consequently involved in extremely different types of diseases and conditions.

It is not surprising that many attempts to manipulate autophagy therapeutically are currently ongoing. For example, there are dozens of clinical trials where anti-cancer drugs are being combined with autophagy inhibitors.[273] Conversely, stimulation of the autophagy pathway has been proposed as a strategy to extend healthy aging.[274] Stimulation of autophagy is also widely accepted as cytoprotective mechanism against neurodegenerative disorders (NDs), and a variety of clinical interventions are moving forward to increase autophagy as a therapeutic intervention for NDs.[275] More recently, in addition, modulation of autophagy has been proposed for LSDs, especially for them involving neural damage.

The next two paragraphs provide an overview of the autophagy involvement in NDs and LSDs. Related therapeutic strategies are also discussed.

#### *Autophagy in neurodegenerative disorders*

NDs, such as Alzheimer's disease (AD), Parkinson's disease (PD), amyotrophic lateral sclerosis (ALS), Huntington's disease (HD), spinobulbar muscular atrophy (SBMA), dentatorubral pallidoluysian atrophy (DRPLA) and a number of SCAs spinocerebellar ataxias (SCAs) belong to the class of

the protein conformational disorders (PCD) associated with progressive neurodegeneration and cognitive decline.[276,277] PCD are principally characterized by the presence of intraneuronal ubiquitylated mutant protein aggregates (also called inclusions), but also extracellular amyloid plaques such as in AD. The conformational change attributed to the mutant proteins is generally believed to promote the disease by a toxic gain-of-function, but the nature of the toxic species is not yet clear.[251,278] Different studies demonstrated the involvement of the polyubiquitin-binding protein p62 in control the biogenesis and degradation of protein aggregates in NDs. P62, in fact, is commonly found in inclusion bodies, such as Lewy bodies in PD, neurofibrillary tangles in AD and huntingtin aggregates in HD.[278,279,280] It acts as a scaffold to facilitate aggregation of ubiquitylated mutant proteins. Loss of p62, indeed, suppresses inclusion body formation in neurons. Additionally, p62 is a specific autophagy substrate that targets the mutant proteins for autophagic degradation.[281,269] Also sequestration of ubiquitylated mutant proteins into autophagosomes is mediated by p62.[269]

In general, cytoplasmic aggregation-prone proteins causing neurodegeneration [such as A53T and A30P mutants of α-synuclein (familial PD), various polyQ-expanded proteins such as mutant huntingtin (HD), ataxin-1 (SCA1) and ataxin-3 (SCA3), mutant SOD1 (copper/zinc superoxide dismutase 1; familial ALS) and tau (AD)] are good autophagy substrates; thus, up-regulation of autophagy is considered a potential therapeutic strategy for several neurodegenerative diseases.[282,283,284] The beneficial effects of autophagy up-regulation in neurodegenerative diseases first came with the mTORC1 inhibitor Rapamycin (RAP), which ameliorated the disease phenotype in transgenic HD mice.[285] Subsequently, RAP has

shown to be protective in various cellular and animal neurodegenerative models.[286,287,288] Later, lots of autophagy enhancers have been discovered and tested. Resveratrol (RESV), for example, can induce autophagy via an mTOR dependent pathway and was found to promote remyelination in a model of multiple sclerosis.[289]

The discovery of mTOR-independent autophagy enhancers, as Lithium (Li), a drug that has been used for decades to treat people chronically with affective disorders, also provides an alternative way to stimulate autophagy. Li, similarly to RAP, is an attractive drug to consider, as both can pass the BBB.[290,291,292] Li induces mTOR-independent autophagy by inhibiting inositol monophosphatase (IMPase) and reducing inositol and IP3 levels. It has been also shown that glycogen synthase kinase-3b (GSK-3b), another enzyme inhibited by Li, has opposite effects on autophagy.[293] Thus, interestingly, with the rationale to counteract the autophagy inhibitory effects of mTOR activation resulting from Li treatment, Sarkar and colleagues used the mTOR inhibitor RAP in combination with Li in models of HD, showing that the combination therapy exerts additive protective effect against neurodegeneration in a HD Drosophila model. [293]

### *Autophagy in lysosomal storage disorders*

As expected, LSDs, characterized by accumulation of undigested macromolecules within the cell, generally show impaired autophagy features. Considering the highly integrated function of lysosomes and autophagosomes, in fact, is reasonable to expect that abnormal lysosomal storage would have an impact upon the autophagy machinery.[294]

In 2000, Tanaka and colleagues[295] defined lysosome associated membrane protein-2 (LAMP-2) as a critical protein for autophagy. LAMP-2 is an important component of lysosomal membranes and its deficiency causes Danon disease, an LSD characterized by autophagosome accumulation and cardiomyopathy. The cause of this disorder is considered one of the first evidences of the autophagic involvement in LSDs. The accumulation of autophagosomes was likewise described[296] in murine models of NCLs and a disruption of autophagy was later suggested.[297] In 2006, Jennings and coworkers[298] pointed that MPS IV and other LSDs display mitochondrial alterations that could be reproduced administering healthy cells with autophagy inhibitors. In the same period, Fukuda and collaborators[299] reported a disruption of endocytic and autophagic pathways, along with a consequent increase in autophagic activity in Pompe disease, while in the following year, Pacheco and colleagues[113] described an enhanced autophagy in Niemann Pick type C and Sandhoff diseases and indicated Beclin-1 as a possible key molecule in this process. The activation of autophagy and the enhancement in Beclin-1 levels were also described by Takamura and co-authors in GM1-gangliosidosis[300] along with mitochondrial dysfunction, whereas a deficitary autophagy was found instead in multiple sulphatase deficiency (MSD) and MPS IIIA by Settembre and colleagues.[301]

Hence, some LSDs display an increase in autophagic activity, while others show an autophagic deficit. In order to find a common denominator between blocked and induced autophagy, a unifying hypothesis was presented by Settembre and colleagues[302] and was later proposed again by Ballabio and Gieselmann[303] and subsequently by Lieberman and

collaborators[294] together with the idea that LSDs can be considered as "autophagy disorders". According to this theory (see Fig. 4.2), lysosomal storage interferes with the fusion of autophagosomes with lysososmes, causing a partial block of the autophagic flux, a consequent accumulation of autophagosomes and the increase in factors involved in autophagosome formation by compensatory feedback.

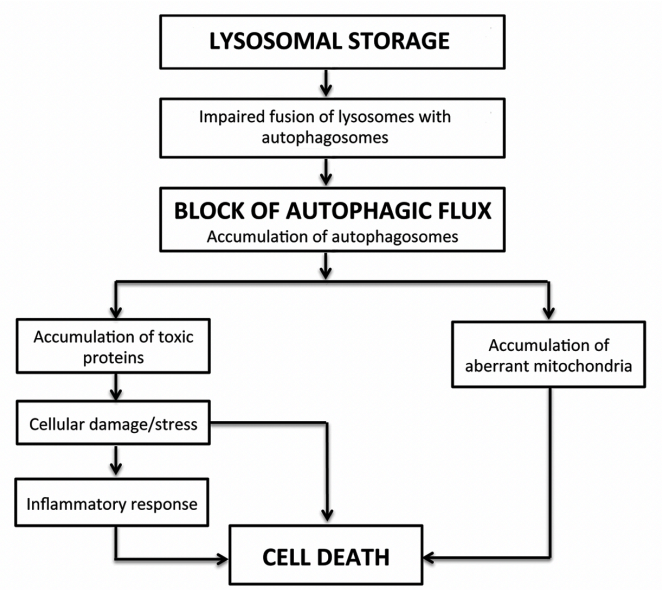


**Figure 4.2.** Hypothesis for autophagy involvement in LSDs pathogenesis.[294]

This may therefore cause an accumulation of polyubiquitinilated proteins, p62, aberrant mitochondria and toxic proteins, which would be physiologically degraded in case of normal autophagic activity. The accumulation of these autophagic substrates may then lead to cellular damage, increased stress with consequent activation of the inflammatory response and finally to cell death. The role of autophagy in LSDs, however,

remains an open issue, which probably cannot be solved with a global "autophagy-LSDs-theory", but should be investigated for every specific disorder.

Multiple lines of evidence suggest that autophagy could be targeted in LSDs as a treatment strategy (Tab. 4.1).[294,304] The most suitable disease contexts for this approach are likely to be LSDs where the lysosomal hydrolytic function is not overtly compromised (e.g., by direct mutation of an enzyme) so that the accumulated autophagic cargo can still be digested efficiently if autophagic flux is stimulated. However, in this case, a promising approach consists in combining ERT with autophagy induction. Recent data, for example, demonstrated that combination strategies that include induction of autophagy might be more effective in Pompe disease and similar LSDs than ERT alone, in this case possibly by stimulating clearance of the accumulating glycogen and facilitating GAA maturation.[305] Indeed, experiments with a Pompe mouse model *in vivo* demonstrated that treatment with RAP alongside ERT for the GAA enzyme reduced muscle glycogen levels compared with either treatment alone.[306] These emerging data highlight the potential benefits of combinatorial treatment strategies in the LSDs.

**Beneficial effects of the chemical inducers of autophagy in models of lysosomal storage disorders**

| **Autophagy inducers** | Mechanism of autophagy induction | LSD | Beneficial effects in LSD models |
|---|---|---|---|
| **mTOR-dependent autophagy inducers** | | | |
| **Ramapycin (Bloomaart et al., 1995)**[307] | Inibition of mTORC1 (Bloomaart et al., 1995)[307] | NPC1 | Rescue of autophagic flux and improvement in cell viability in mutant *Npc1* MEFs (Sarkar et al., 2013), mouse neurons with *Npc1* knockdown (Sarkar et al., 2013) and NPC1 patient iPSC-derived neuronal and |

| | | | |
|---|---|---|---|
| | | | hepatic cells (Maetzel et al., 2014)[251,308] |
| | | NPB | Reduction in mitochondrial ROS and lipid droplets, and induction of lysosomal exocytosis in NPB patient B lymphocytes (Canonico et al., 2016)[309292] |
| | | PD | Reduction in muscle glycogen in *Gaa*-deficient mice when treated together with recombinant human GAA (Ashe et al., 2010); Improved autophagic flux and GAA maturation in Pompe disease patient myotubes (Nascimbeni et al., 2012)[306,310] |
| | | GD | Improvement in lifespan and locomotor activity in GD *Drosophila* model (Kinghorn et al., 2016)[311] |
| **mTOR-idependent autophagy inducer** | | | |
| **Trehalose (Sarkar et al., 2007)**[312] | Inhibition of SLC2A glucose transporters (DeBosch et al., 2016)[313]; Activation of TFEB by Akt inhibition (Palmieri et al., 2017)[314] | NPC1 | Rescue of autophagic flux and improvement in cell viability in NPC1 patient iPSC-derived neurons (Matzel et al., 2014)[315] |
| | | CLN3 | Clearance of ceroid lipopigment deposits in CLN3 patient fibroblasts, and attenuation of neuropathology and extension of lifespan in *Cln3*-deficient mice (Palmieri et al., 2017)[314] |
| **Carbamazepine (Sarkar et al., 2005)**[316] | Reduction in inositol and IP3 levels (Sarkar et al., 2005)[316] | NPC1 | Rescue of autophagic flux and improvement in cell viability in NPC1 patient iPSC-derived neurons and hepatic cells (Maetzel et al., 2014)[315] |
| **Lithium (Sarkar et al., 2005)**[316] | Inhibition of IMPase and reduction in inositol and IP3 levels (Sarkar et al., 2005)[316] | NPC1 | Rescue of autophagic flux in mutant *Npc1* MEFs (Sarkar et al., 2013)[252] |
| | | CLN3 | Rescue of autophagic flux and improvement in cell viability in mutant *Cln3* cerebellar cells (Chang et al., 2011)[317] |
| **L-690,330 (Sarkar** | Inhibition of IMPase and | CLN3 | Rescue of autophagic flux and |

| | | | |
|---|---|---|---|
| **et al., 2005**) [316] | reduction in inositol and $IP_3$ levels (Sarkar et al., 2005)[316] | | improvement in cell viability in mutant *Cln3* cerebellar cells (Chang et al., 2011)[317] |
| **Verapamil (Williams et al., 2008**)[318] | Inhibition of L-type $Ca^{2+}$ channel and reduction in cytosolic $Ca^{2+}$ (Williams et al., 2008)[318] | NPC1 | Rescue of autophagic flux and improvement in cell viability in NPC1 patient iPSC-derived neurons (Maetzel et al., 2014) [315] |
| **BRD2716, BRD5631, BRD34009** (**Kuo et al., 2015**)[319] | | NPC1 | Rescue of autophagic flux and improvement in cell viability in NPC1 patient iPSC-derived neurons (Kuo et al., 2015)[319] |

**Table 4.1.** Beneficial effects of the chemical inducers of autophagy in models of LSDs. From Seranova et al., 2017.[305]

## 4.2 Lithium improves cell-viability in an immortalized cell model of Krabbe disease

*The experiments presented in this Section have been published after peer-reviewing in Journal of neuroscience research 94(11), 1246-1260. Co-authors of the work are: Del Grosso A, Antonini S, Angella L, Tonazzini I, Signore G and Cecchini M. Role of authors: study concept and design: ADG, MC. Acquisition of data: ADG, LA, SA, GS, IT. Analysis and interpretation of data: All authors. Drafting of the manuscript: All authors. Statistical analysis: ADG, IT, MC. Obtained funding: MC. Study supervision: MC. I, in particular, maintained cell culture, performed viability experiments, western blots, confocal imaging, ROS quantification, and statistical analysis and drafted the manuscript.*

### 4.2.1 Introduction

As already extensively reported in Section 4.1.2, studies on LSDs suggest that defective autophagy might be a general feature of this group of diseases. However, before the present work, autophagy had never been analyzed in KD except for a study performed by Ribbens et al. (2014).[43] They presented a new GALC-deficient murine oligodendrocyte line, which showed LC3-enhanced lysosomal localization and increased expression under treatment with PSY with respect to WT cells.

Here we report on autophagy in the human oligodendrocyte cell line MO3.13 treated with PSY and exploited Li as an autophagy modulator. Li was administered to MO3.13 cells treated with PSY, and autophagy activation was evaluated. We studied LC3 localization by LC3-YFP and LC3-RFP-GFP transfection and confocal fluorescence microscopy and p62 and LC3-I/-II expression by Western blotting. The effects of Li on PSY accumulation (by high-pressure liquid chromatography/ tandem mass

spectrometry [HPLC/MS] methods), ROS production (by fluorescence staining and flow cytometry), and PSY-induced apoptosis (by flow cytometry and microplate fluorimetry) were finally measured.

### 4.2.2 Psychosine induces autophagy

To monitor the effects of PSY on the autophagic pathway, human oligodendrocyte MO3.13 cells were treated with PSY 10 μM for 24 hours, and LC3-I/-II and p62 protein expression levels and LC3 localization were investigated. First, we monitored LC3 cell localization by LC3-YFP transfection and confocal fluorescence microscopy. This method allowed us to evaluate autophagosome formation in living cells by visualizing and quantifying the presence of LC3-YFP-positive puncta. At the beginning of autophagosome formation, in fact, LC3 is converted into a cleaved form (LC3-II) and inserted into autophagosome membranes, becoming less diffuse and becoming concentrated in so-called puncta.[320,321] LC3-YFP-based assessment of autophagosome has been reported to be both more sensitive and specific compared with other techniques, including electron microscopy.[322] As shown in figure 4.3 A, control cells are characterized by a diffused fluorescent signal and a low number of autophagosomes (2.4 ± 0.3 autophagosomes/cell). Conversely, PSY-treated cells revealed increased LC3 aggregation (5.3 ± 0.3 autophagosomes/cell), thus indicating autophagy activation ($P < 0.01$ PSY vs. control, Student's t-test).

Then, the expression of the two isoforms of LC3, LC3-I an LC3-II, was assayed by Western blotting. The conversion (cleavage) of LC3-I (17 kDa, a cytoplasmic form) into LC3-II (15 kDa, a cleavage form) is correlated with autophagic activity. Representative blots and their quantification are given in figure 4.3 B. We found a significant increase of LC3-II levels in PSY-treated

cells with respect to the control condition and a further increase in cells treated with PSY together with BAF ($P < 0.05$ PSY vs. control and vs. PSY + BAF, Dunnett's test). BAF is a drug that blocks the fusion between lysosomes and autophagosomes, and it is typically used to prevent LC3-II degradation. This control condition is needed to preclude that the measured LC3-II increase induced by PSY can stem from impaired autophagosome-lysosome fusion instead of augmented autophagy.[323,324]

Together with LC3, p62 is an autophagic activity marker that was examined by Western blotting. p62 is a ubiquitin-binding protein that can link ubiquitinated proteins to the autophagic machinery, making their degradation possible within the lysosome. As shown in figure 4.3 B, the levels of p62 were significantly increased in cells treated with PSY and BAF compared with those measured for cells treated only with PSY ($P < 0.05$ PSY+BAF vs. PSY, Student's t-test).

To verify directly that PSY does not impair autolysosome formation, we measured the lysosomally driven GFP quenching after transfection with the LC3-RFP-GFP construct. GFP is a stably folded protein, relatively resistant to lysosomal protease. However, the low pH inside the lysosomes quenches the fluorescent signal of GFP, making it difficult to trace the delivery of LC3-GFP into lysosomes.[177,325] In contrast, RFP exhibits a more stable fluorescence in acidic compartments, allowing LC3-RFP-GFP constructs to label autophagosomes as GFP-positive and RFP-positive (GFP+/RFP+) puncta, and autolysosomes as GFP-negative and RFP-positive (GFP–/RFP+) puncta.[261] As shown by the representative confocal fluorescence images in figure 4.3 C, a quite evident increase in both autophagosomes and autolysosomes was detected in PSY-treated cells with respect to the control condition,

whereas we found an increase of autophagosomes only in PSY+BAF-treated cells caused by the blockage of autophagosome maturation. The number of autolysosomes under the different conditions was finally quantified as the number of GFP–/RFP+ puncta, confirming the significant increase of autolysosome formation following PSY administration (Fig. 4.3 C; $P < 0.01$ PSY vs. control and $P < 0.05$ PSY+BAF vs. PSY, Tukey's test). Taken together, these data indicate an activation of the autophagic machinery following PSY administration in MO3.13 cells.

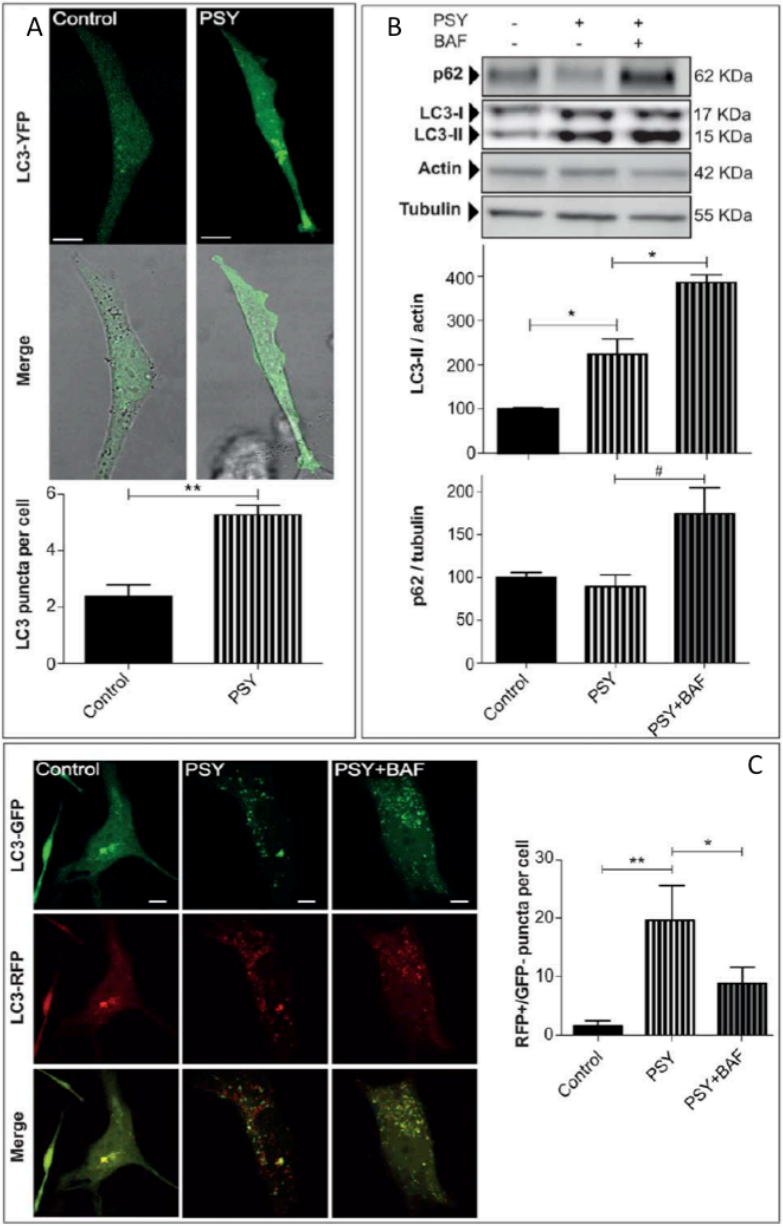
A
Control
PSY
LC3-YFP
Merge
LC3 puncta per cell
**
Control
PSY
B
PSY
BAF
p62
62 KDa
LC3-I
LC3-II
17 KDa
15 KDa
Actin
42 KDa
Tubulin
55 KDa
LC3-II / actin
*
*
p62 / tubulin
#
Control
PSY
PSY+BAF
C
Control
PSY
PSY+BAF
LC3-GFP
LC3-RFP
Merge
RFP+/GFP- puncta per cell
**
*
Control
PSY
PSY+BAF

**Figure 4.3.** Psychosine induces autophagy. **(A)** MO3.13 cells were transiently transfected with LC3-YFP, treated with 0.2% FBS medium alone (control) or PSY 10 μM (PSY) and imaged after 24 hours by live-cell confocal microscopy. The number of autophagosomes was quantified as the amount of LC3 puncta per cell in each condition; ** = P < 0.01 PSY vs. control, Student's t-test; At least 15 cells for each condition were quantified per experiment. **(B)** To monitor the induction of autophagy activity, the LC3-I/-II and p62 protein expression levels were quantified in MO3.13 cells differently treated as follow: Control and PSY (10 μM), in the presence or not of Bafilomycin 200 nM (PSY+BAF). Results were normalized to the actin or tubulin content and averaged the control condition within each experiment; for LC3-II: * = P < 0.05, PSY vs. control and vs. PSY+BAF, Dunnett's test (N =3); for p62: # = P < 0,05, PSY+BAF vs. PSY, Student's t-test. **(C)** To detect the autolysosomes formation MO3.13 cells were transfected with LC3-RFP-GFP, treated with 0.2% FBS medium alone (control), PSY, PSY+BAF and imaged after 24 hours by live-cell confocal microscopy. The number of autolysosomes was quantified as the amount of the LC3-RFP-positive/LC3-GFP-negative puncta per cell; ** = P < 0.01 PSY vs. control and * = P < 0.05 PSY+BAF vs. PSY Tukey's test (N =3); At least 12 cells for each condition were quantified per experiment. Scale bars = 10 μm.

### 4.2.3 Li increases autophagy in psychosine-treated cells

To investigate which Li concentration could be tolerated by MO3.13 cells, a dose–response vitality curve was obtained in the presence of increasing concentrations of Li (Fig. 4.4 A). To this end, cells were stained with annexin V/PI and analyzed by flow cytometry. A decreasing trend in cell survival was found by increasing concentration from 10 to 100 mM (P < 0.05 Li 100 mM vs. control, Dunnett's test). Given these results and that Li is therapeutically used at serum concentrations between 0.2 and 2 mM in humans[326,327], 1 mM and 2 mM were chosen for all our experiments. These values are are typically used also for in vitro studies.[328]

MO3.13 cells were thus pretreated with Li 1 mM or 2 mM and then given PSY 10 μM for 24 hours (Li1+PSY, Li2+PSY). To investigate the effect of Li on autophagy in PSY-treated cells, LC3-I/-II and p62 protein expression levels and LC3 localization were evaluated by confocal imaging and Western blotting, as for PSY alone. We found that LC3-positive puncta in Li1+PSY (13±2 autophagosomes/cell)- and Li2+PSY (15.9±8 autophagosomes/cell)-

treated cells were significantly more abundant than in cells treated with PSY alone ($P < 0.01$ PSY vs. Li1+PSY and $P < 0.001$ PSY vs. Li2+PSY, Dunnett's test), indicating an upregulation of the autophagosome formation machinery (Fig. 4.4 B). We next investigated the levels of LC3-I/-II by Western blotting (Fig. 4.4 C). Li1+PSY and Li2+PSY treatments did not lead to statistically significant LC3-II variations with respect to the control condition (PSY treatment alone). Nonetheless, addition of BAF to Li1+PSY- and Li2+PSY-treated cultures could increase the LC3-II expression markedly ($P < 0.01$ Li1+PSY vs. Li1+PSY+BAF and $P < 0.05$, Li2+PSY vs. Li2+PSY+BAF, Tukey's test), demonstrating that the autophagy flux is not blocked by Li. A comparable trend was found for p62 (Fig. 4.4 C). In this case also, Li1+PSY and Li2+PSY treatments compared with PSY alone led to similar p62 levels, and BAF administration together with Li led to enhanced p62 expression, although this did not reach statistical significance. Overall, these data demonstrate that cells given Li and PSY tend to produce more LC3-positive autophagosomes without impairment of the autophagy flux with respect to cells treated with PSY alone, in agreement with the hypothesis that Li can stimulate autophagy in the presence of an excess of exogenous PSY in MO3.13 human oligodendrocytes.

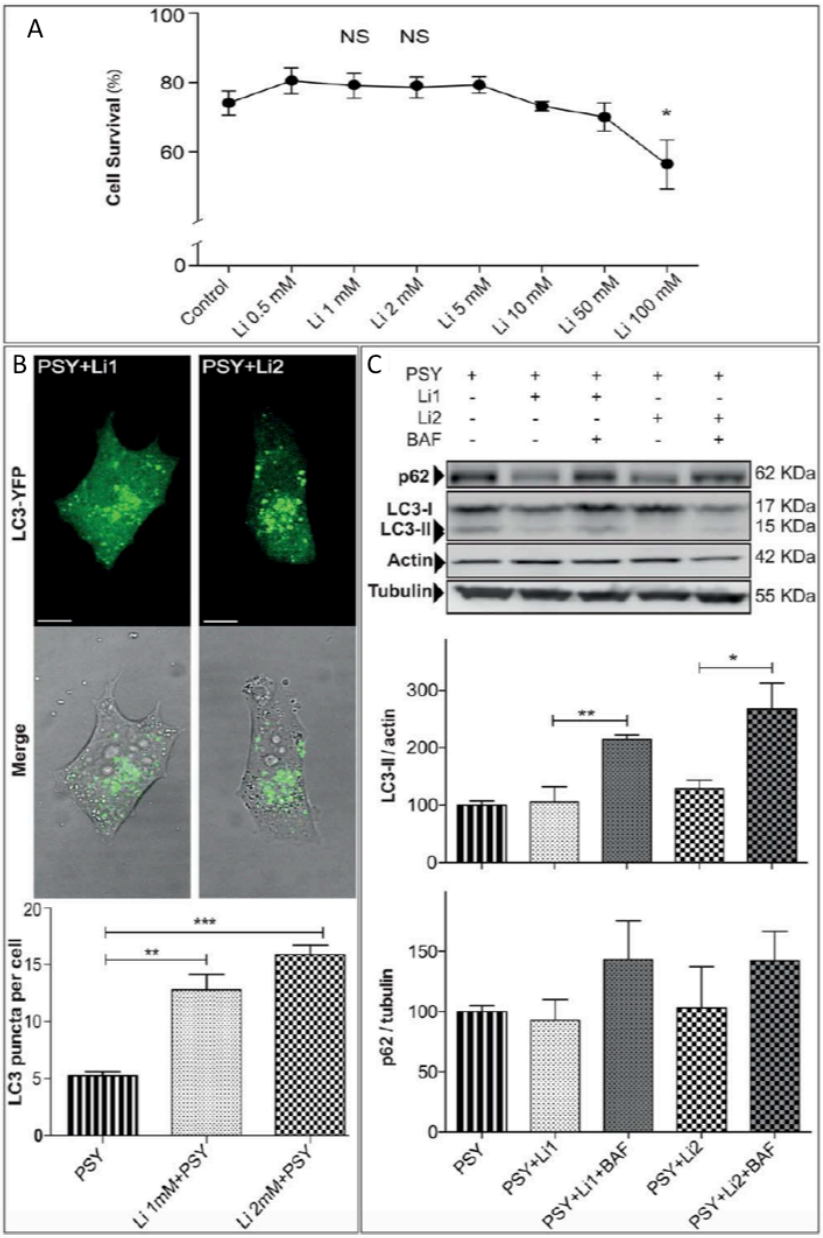
A
Cell Survival (%)
100
80
60
0
NS
NS
*
Control
Li 0.5 mM
Li 1 mM
Li 2 mM
Li 5 mM
Li 10 mM
Li 50 mM
Li 100 mM
B
PSY+Li1
PSY+Li2
LC3-YFP
Merge
LC3 puncta per cell
20
15
10
5
0
**
***
PSY
Li 1mM+PSY
Li 2mM+PSY
C
PSY
Li1
Li2
BAF
p62
62 KDa
LC3-I
LC3-II
17 KDa
15 KDa
Actin
42 KDa
Tubulin
55 KDa
LC3-II / actin
300
200
100
0
**
*
p62 / tubulin
150
100
50
0
PSY
PSY+Li1
PSY+Li1+BAF
PSY+Li2
PSY+Li2+BAF

**Figure 4.4.** Li increases autophagy in psychosine-treated cells. **(A)** Li dose–response viability curve obtained by annexin V/PI staining and flow cytometry; * = P < 0.05, Li 100 mM vs. control, Dunnett's test (N =4). **(B)** MO3.13 cells were transiently transfected with LC3-YFP, treated with PSY 10 µM (PSY), PSY and Li 1 mM (Li1+PSY), or Li 2 mM (Li2+PSY) and imaged after 24 hours by live-cell confocal microscopy. The number of autophagosomes was quantified as the amount of LC3 puncta per cell in each condition; ** = P < 0.01 Li1+PSY vs. PSY and *** = P < 0.001 Li2+PSY vs. PSY, Dunnett's test (N =3). At least 15 cells for each condition were quantified per experiment. **(C)** To investigate the autophagy activation in PSY-treated MO3.13 cells after Li treatments further, LC3-II and p62 levels were quantified in cells treated with Li1+PSY, Li2+PSY, in the presence or not of Bafilomycin 200 nM (Li1+PSY+BAF, and Li2+PSY+BAF). Results were normalized to the actin or tubulin content and averaged for each repetition toward the PSY condition; for LC3-II: ** = P < 0.01 Li1+PSY+BAF vs. Li1+PSY and * = P < 0.05 Li2+PSY+BAF vs. Li2+PSY, Tukey's test; for p62: * = P < 0.05 Li1+PSY+BAF vs. Li1+PSY, Dunnett's test (N =3). Insets: Representative blot panels. Scale bars = 10 µm.

### 4.2.4 Psychosine content in PSY- and Li-treated cells

To investigate whether stimulation of autophagy by Li could led to a clearance of the PSY content in oligodendrocytes, PSY levels were quantified in MO3.13 treated cells (PSY, Li1+PSY and Li2+PSY) by HPLC/MS analysis; untreated MO3.13 cells were used as negative control.

This measure turned out to be rather difficult because of signals originating from residual non-cellular PSY present in the lipid extract (for a detailed description of the sample preparation for HPLC/MS analysis see Section 5.2.8). For this reason, to gain a better comparison of different experiments, we normalized data within each experiment to the positive control (PSY-treated cells). As the representative mass spectrometry time/count plot of figure 4.5 A shows, our analytical method allowed us clearly to detect and quantify the PSY signals in our positive control (cell treated with PSY only); as expected, no PSY peak was present in our negative control (data not shown).

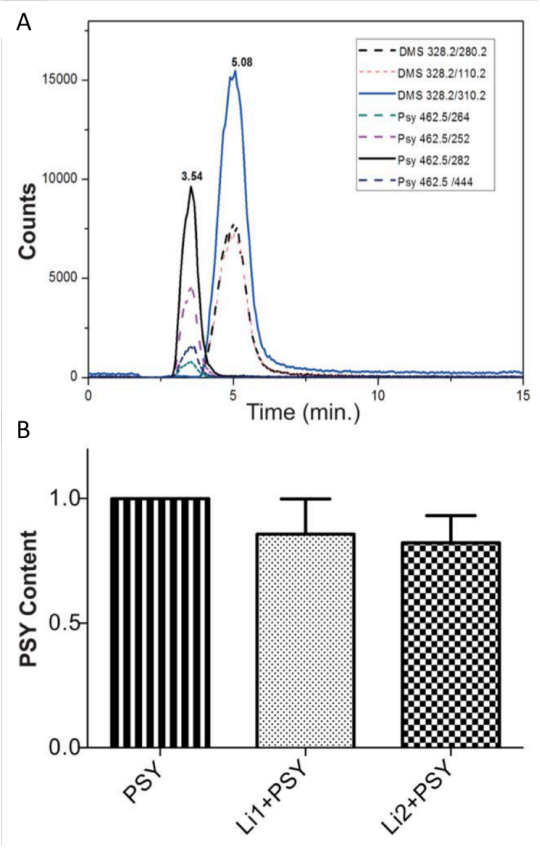


**Figure 4.5.** Evaluation of PSY content in PSY-treated MO3.13 cells after Li administration. **(A)** Representative time/count plot of the monitored transition for HPLC-MS quantification of PSY in PSY-treated MO3.13 cell lysates. The monitored transitions are shown at top right; the selected transitions for quantitative purpose are: transitions 328.2/310.2 for N,N-dimethylsphingosine and transition 462.5/282 for PSY. **(B)** PSY content in PSY-treated MO3.13 cells after Li administration (Li1+PSY, Li2+PSY); values are normalized to the PSY condition within each experiment (N =7).

The quantification of seven independent experiments is summarized by the graph in figure 4.5 B, in which cells pretreated with Li revealed a

reduction of PSY average levels compared with cells treated with PSY alone. In particular, PSY mean values decreased by about 25% and 20% in cells pretreated with Li 1 mM and Li 2 mM, respectively. Although the above mentioned noise did not allow us to reach statistical significance, the measured decreasing tendency of the PSY content in cells given Li suggests that the autophagic activity induced by Li can succeed in removing some of the exogenously introduced PSY.

### 4.2.5 Lithium improves viability of psychosine treated cells

MO3.13 cells were treated with PSY 10 μM for 24 hours, and viability measured by annexin V/PI staining and flow cytometry. An increased mortality rate (Fig. 4.6 B, C; P < 0,001 PSY vs. control, Student's t-test) was measured, as we previously reported.[47] Next, we investigated the effect of Li on PSY-treated cell viability. Representative FACS scatterplots are shown in figure 4.6 A for the PSY, Li1+PSY, and Li2+PSY conditions and for the untreated control. Already from these plots it is possible to notice qualitatively that Li can reduce the number of dots present in R3 quadrants with respect to that measured for cells treated only with PSY, indicating a reduction of secondary necrosis with the following recovery of viability.

The quantification of this experiment is given in figure 4.6 B, C; the administration of Li significantly increased the percentage of viable cells (P < 0.05 Li1+PSY vs. PSY and P < 0.01 Li2+PSY vs. PSY, Dunnett's test; Fig. 4.6 B) and decreased secondary necrosis (P < 0.01 Li1+PSY vs. PSY and P < 0.001 Li2+PSY vs. PSY, Dunnett's test; Fig. 4.6 C) compared with cells treated with PSY alone.

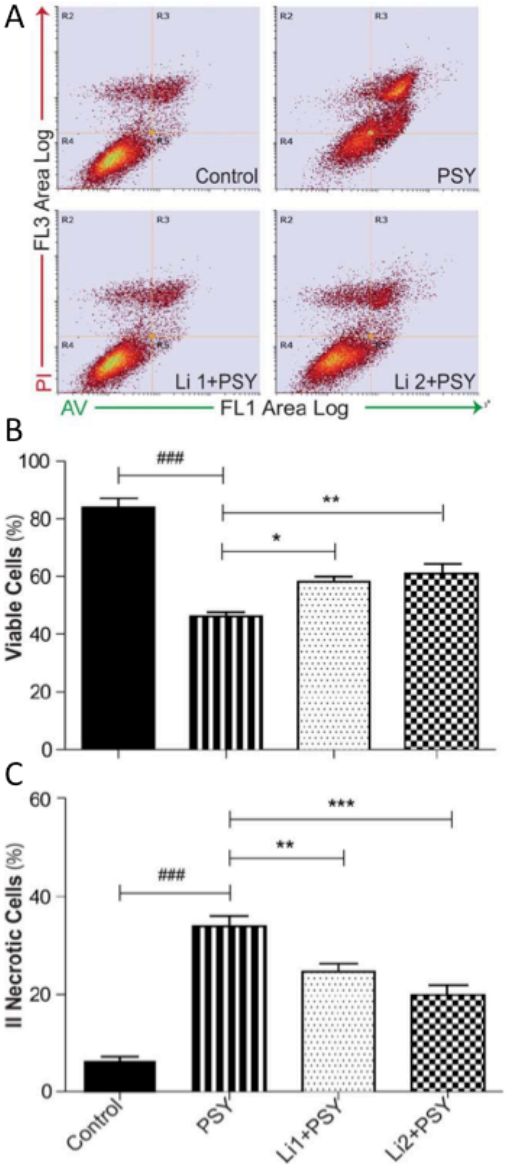


**Figure 4.6.** Li treatment improves cell viability in PSY-treated MO3.13 cells. **(A)** Representative dot-plots of MO3.13 cells stained with annexin V/PI and analyzed by flow cytometry: R4, R5, R3

and R2 quadrants define, respectively, the healthy, apoptotic, secondary necrotic, and necrotic populations. **(B)** The number of viable cells is reported in percentage of the total cell number. ### = P < 0.001 PSY vs. control, Student's t-test; * = P < 0.05 Li1+PSY vs. PSY and ** = P < 0.01 Li2+PSY vs. PSY, Dunnett's test (N =4). **(c)** The number of II necrotic cells is reported in percentage of the total cell number; ### = P < 0.001 PSY vs. control, Student's t-test; ** = P < 0.01 Li1+PSY vs. PSY and *** = P < 0.001 Li2+PSY vs. PSY (N =4).

To investigate further whether the improved viability could be caused by Li-induced activation of autophagy, MO3.13 cells were treated with PEI. PEI is an inhibitor of the autophagy pathway that, by elevating intracellular levels of IP3[290], has an effect opposite that of Li[316]. First, to test which PEI concentrations could be tolerated by MO3.13 (Fig. 4.7 A), a dose–response curve was obtained with increasing PEI concentrations. Only concentrations greater than 100 μM were toxic (P < 0.05 PEI 100 μM vs. control and P < 0.001 PEI 250 μM vs. control, Dunnett's test). Given these results and according to the literature[316], a concentration of 25 μM was chosen for the experiments. As shown in figure 4.7 B, C, cells given both PSY and PEI showed significantly less viability than cells exposed only to PSY (P < 0.05 PEI+PSY vs. PSY, Dunnett's test). We note that this cannot be ascribed to an additive cytotoxic effect of PEI because the PEI concentration was chosen to be fully tolerated by the cells. Therefore, downregulation of the autophagic pathway activated by Li makes MO3.13 cells less tolerant to PSY, in agreement with the viability rescue that we obtained with Li. These experiments demonstrate that Li pretreatment can reduce the cytotoxicity of PSY in MO3.13 cells. However, the viability rescue obtained in the presence of PSY can be ascribed to Li-driven autophagy activation.

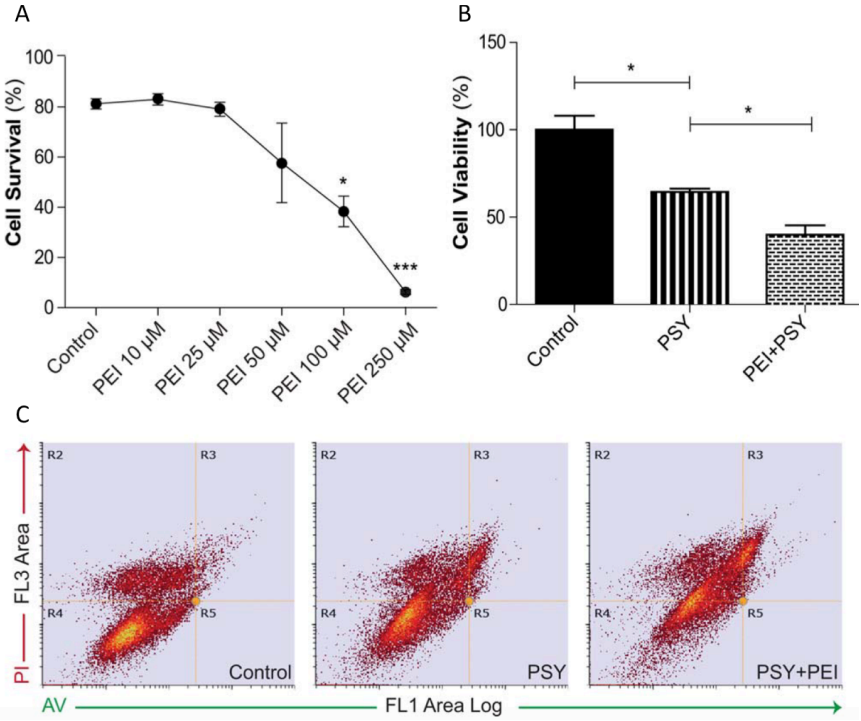


**Figure 4.7.** PEI decreases cell viability of PSY-treated MO3.13 cells. **(A)** Representative dot plots of MO3.13 cells treated with 0.2% FBS medium alone (control), PSY 10 µM (PSY), or PSY followed by PEI 25 µM (PEI + PSY); cells were stained with annexin V/PI and analyzed by flow cytometry: the R4 quadrant defines the viable cells and it was set on control condition. **(B)** PEI dose–response viability curve.

### 4.2.6 Improved viability does not correlate with reduced cytoplasmic oxidative stress

Finally, it is known that PSY-induced cell death is associated with increased ROS production[47,76], so ROS levels were investigated under our experimental conditions by $H_2$-DCFDA staining and flow cytometry. As expected, MO3.13 cells treated with PSY revealed an augmented cytoplasmic ROS with respect to control conditions (Fig. 4.8). Interestingly, the additional administration

of Li, both 1 and 2 mM, did not ameliorate the oxidative stress ($P > 0.01$ Li1+PSY and Li2+PSY vs. PSY, Dunnett's test), though leading to better cell viability (see above). To avoid possible stress originating from cell detachment before flow cytometry, we performed another set of experiments in which the dye fluorescence was read from adhered cells by microplate fluorimetry (for details see Section 5.2.8). The result of these measurements is summarized in figure 4.8 C, confirming what we obtained by flow cytometry. These final experiments show that Li protection from PSY cannot be ascribed to a nonspecific reduction of cytosolic oxidative stress.

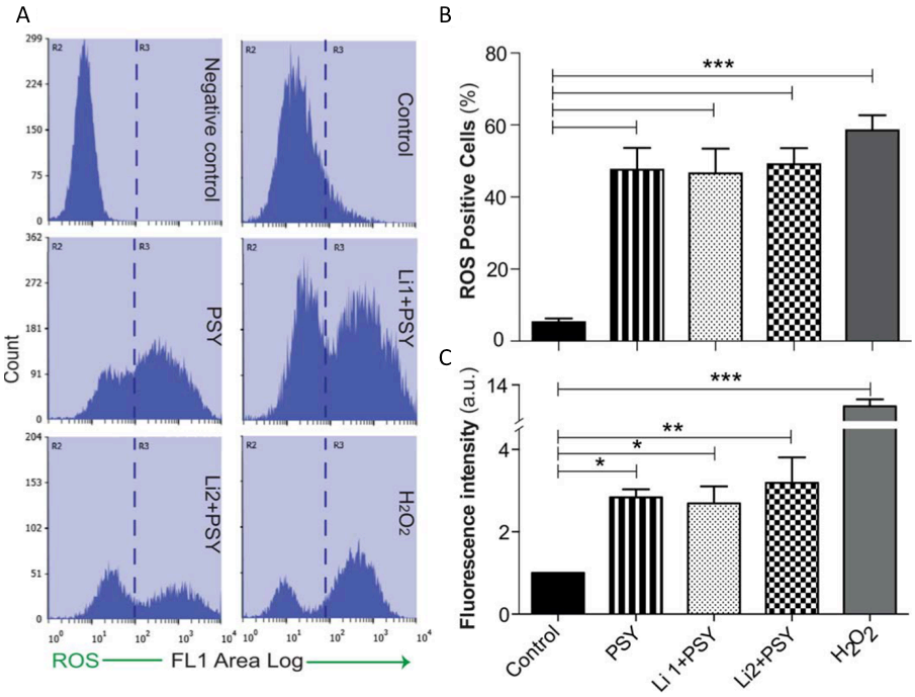


**Figure 4.8.** ROS detection in PSY- and Li-treated MO3.13 cells. **(A)** Representative histogram plots of MO3.13 cells treated with 0.2% FBS medium alone (control), PSY 10 μM (PSY), PSY and

Li 1 mM (Li1+PSY), or Li 2 mM (Li2+PSY); $H_2O_2$ 100 mM was used as positive control. Cells were stained with carboxyl-H2DCFDA and analyzed by flow cytometry. The R3 region was set by the histogram plot obtained for the unstained samples (negative control). **(B)** Cytoplasmic ROS levels increase after PSY administration and remain constant after additional Li treatments; *** = P < 0.001 PSY, Li1+PSY, Li2+PSY, and $H_2O_2$ vs. control, Dunnett's test (N =4). **(C)** DCF fluorescence from adhered cells measured by microplate fluorimetry. Cells treated with PSY revealed an increased amount of cytoplasmic ROS with respect to the control condition; * = P < 0.05 PSY and PSY+Li1 vs. control, *** = P < 0.001 PSY+Li2 vs. control, Dunnett's test (N =3). For each condition, the mean fluorescence intensity was normalized to the correspondent cell number and to the control condition within each experiment.

### 4.2.7 Concluding remarks

Our study addresses for the first time autophagy in KD with the aim of understanding whether this could be a possible therapeutic target with combined therapies. Remarkably, for medical purposes, drugs for inducing or inhibiting autophagy are already available for clinical practice.[283]

For our experiments we decided to use an accepted model of KD in vitro for testing against PSY excess, which consists in a human model of oligodendrocytes, the MO3.13 cell line, cultured in an excess of exogenous PSY. This model, although somewhat simplified, has already successfully allowed unravelling novel molecular mechanisms affected by the presence of PSY.[329,60,92] By using a 10 μM PSY concentration in previous work, we quantitatively demonstrated apoptotic cell death in the same model by annexinn V/PI staining and flow cytometry.[47] These data gave us the basic information for trying to rescue viability by acting on autophagy. Given the results obtained by Ribbens et al. (2014)[43], which suggested an upregulation of autophagosomes formation induced by PSY, we hypothesized that by helping this degradation pathway we would be able to help cells in PSY clearance and improve their tolerance to PSY, with a consequent increase in cell viability.

First, we characterized the autophagic pathway in the presence of PSY. To this end, LC3-I/-II and p62 expression were measured by Western blotting, and autophagosome/autolysosome formation was imaged by LC3-GFP/LC3-RFP-GFP transfection and confocal microscopy. Consistently with the results cited above, exogenous PSY administration could stimulate autophagy also in MO3.13 cells. LC3-positive vesicle formation was indeed significantly augmented with respect to the case of non-treated cells (Fig. 4.3 A), indicating an enhanced production of autophagosomes. At the molecular level, although we did not found a clear trend for p62, LC3-II expression was upregulated. The amount of LC3-II is indeed closely correlated with the number of autophagosomes, serving as a good indicator of autophagosome formation. However, because LC3-II itself is degraded by autophagy, LC3 immunoblotting is sometimes interpreted inappropriately: an LC3-II increase upon treatment might in fact also indicate a blockage of the autophagic degradation. As suggested by Mizushima et al. (2007)[323], we repeated the experiment in the presence of BAF, an inhibitor of auto-phagosome–lysosome fusion, to block LC3-II degradation. LC3-II expression was in this case further increased, indicating that autophagy was not blocked at the level of autophagosome/lysosome fusion. p62 Can bind LC3, thus serving as a selective substrate of autophagy, and for this reason it would be expected to follow LC3 levels. Actually, the expression level of p62 can also change independently of autophagy[330,331,332], making data interpretation difficult. In our case, although we did not find a variation induced by PSY, the treatment showed an increasing trend consistent with what we measured for LC3-II. To show that the autophagic machinery is active to its final stage, we imaged the delivery of LC3-RFP-GFP to the

lysosomes by confocal imaging in living cells. An important increase in the number of autolysosomes was detected in cells treated with PSY that, as expected, did not occur in the presence of BAF (Fig. 4.3 C). Therefore, we can conclude that exogenous PSY did not block autophagy in our experimental model, which instead showed quite an evident autophagy activation.

To stimulate autophagy further, we chose to use Li, which is clinically accepted for the treatment of bipolar disorders and whose neurotrophic and neuroprotective properties are known [see Section 4.1.2]. Pretreatment with Li was effective in regulating autophagy in various neuropsychiatric diseases such as Huntington's disease, Alzheimer's disease, Parkinson's disease, prion disease, and amyotrophic lateral sclerosis.[326] Interestingly, autophagy was not always upregulated. Conversely, it was reported that in a mouse model of cerebral ischemia and Alzheimer's disease Li can instead lead to downregulation. We thus repeated the analysis described above in cells pretreated with Li and exposed to PSY. We decided to pretreat cells with Li instead of co-treat or post-treat them, in order to obtain the best possible recovery on PSY-induced damages. Is expectable, in fact, to obtain weaker or slower results if the PSY-induced pathogenetic cascade is already started in the cell.

As shown in figure 4.4 B, autophagosome formation was clearly stimulated by Li. The molecular analysis of LC3-I/-II and p62 was instead less straightforward. Nonetheless, the increasing trend of both these proteins upon blocking of autophagic degradation by BAF is consistent with the measured augmented number of autophagosomes and with autophagic flux upregulation.

Therefore, the cytotoxic effect of PSY was essayed upon Li pretreatment and was diminished. The cell culture was indeed less sensitive to PSY, and cell death was reduced with a corresponding improvement in cell viability (see Fig. 4.6). To test our hypothesis in which this therapeutic effect originates from a more efficient PSY degradation, PSY accumulation in cells was quantified. Although a decreasing trend was found in PSY intracellular content, this variation was not large enough to reach statistical significance with our experimental pool. For this reason, we must suppose that other mechanisms not related to PSY clearance might contribute to the observed cell viability rescue. For example, cytotoxic molecules other than PSY, yet accumulating in KD, might be better digested by Li-stimulated autophagy. Smith et al. (2014)[44] indeed identified the presence of misfolded protein aggregates in both human and murine KD brains, consisting primarily of aggregated α-synuclein, and demonstrated that administration of PSY facilitates α-synuclein aggregation *in vitro*. In light of this, and given that autophagy stimulation has been successfully targeted to ameliorate some α-synucleinopathies[333,334,335], we can speculate about a connection between the clearance of some aggregate-prone protein and improved cell viability. Interestingly, cytosolic ROS production was not affected by Li (Fig. 4.8). Oxidative stress has been one of the first targets tested for counteracting PSY cytotoxicity. Administration of the antioxidant N-acetylcysteine (NAC) in cell cultures exposed to exogenous PSY gave good results for ameliorating cell viability, but, unfortunately, almost no effect was seen with its administration in TWI mice as dietary supplement.[76] As in our case, Li did not exert its protective effect by reducing ROS production; other mechanisms related to PSY or other cytotoxic protein reduction could come

into play. Altered autophagy and accumulation of lipids, especially cholesterol and glycosphingolipids, have been reported for a wide range of LSDs, including those without primary defects in glycosphingolipid or cholesterol degradation.[301,302] These lipids are the principal constituents of lipid rafts, specialized membrane microdomains rich in signaling molecules and that influence membrane fluidity.[336] Remarkably, lipid rafts were reported to be disrupted in KD, and this was demonstrated to be caused by PSY accumulation in lipid rafts.[58,64] Lipid rafts are present not only in the plasma membrane but also in other parts of the cell such as the endoplasmic reticulum, mitochondria-associated membranes, Golgi, mitochondria, and lysosomes[337,338] and are involved in many signaling cascades, including autophagy. It is possible that the abnormal accumulation of PSY affects the physiology of lysosomal membranes, making the autophagy pathway a good target for counteracting some of the PSY effects. Intriguingly, also amyloidogenic proteins, that, as previously mentioned, rapidly fibrillate in the presence of PSY, have been demonstrated to interacts with raft glycosphingolipids[339]. Finally, also inflammation, a neglected part of KD, could come into play. It is known that the inflammasome, a molecular platform activated by stress that regulates the activity of caspases and cytokines, colocalizes with the autophagosome and that a blocking of autophagy potentiates inflammasome activity, whereas stimulating autophagy limits it.[340] Recently it has been demonstrated that PSY-treated oligodendrocytes show activation of TLR2 signaling, with consequent innate immune system activation[84]; indeed, it is possible that autophagy activation cold help the cell in attenuating the inflammation response. Although additional studies are required to elucidate the molecular mechanism

correlated with the Li improvement in cell viability in PSY-treated oligodendrocytes, these data give a strong rationale to investigate further the modulation of the autophagic pathway in KD. Importantly, the proposed mechanism needs to be investigated in a GALC deficient condition. GALC deficency, in fact, can ultimatelly change the lysosomal environment (as the lysosomal pH), affecting the proper functioning of the autophagy machinery.[99]

### 4.2.8 Material and methods

#### *Cell Culture and Treatments*

Human oligodendrocyte MO3.13 cells (Tebu Bio, Le-Perray-en-Yvelines, France; catalog No. CLU301-P) were maintained at 37 °C in a humidified atmosphere containing 5% $CO_2$ in high glucose DMEM supplemented with 2mM L-glutamine, 1% penicillin/streptomycin, and 10% heat-inactivated FBS; all products were from GIBCO-Life Technologies (Carlsbad, CA). MO3.13 cells were seeded at 50000 cells/$cm^2$, 24 hours after plating cells were washed twice with PBS and then cultured in 0.2% FBS medium (DMEM supplemented with 0.2% FBS, 2 mM L-glutamine, 1% penicillin/streptomycin). For experiments, MO3.13 cells were cultured in 0.2% FBS medium (control) and treated with PSY 10 μM or pretreated with Li acetate (Li) 1 mM or 2 mM (for 30 min) and then with PSY (Li1+PSY and Li2+PSY, respectively), for 24 hours. For selected experiments, cells were also treated with prolyl endopeptidase inhibitor 2 (PEI) 10–250 μM for 30 minutes before PSY administration (PEI+PSY), Li 0.5– 100 mM in 0.2% FBS medium for 24 hours, or bafilomycin (BAF) 200 nM (4 hours before cell lysis) after PSY or Li1+PSY treatments. PSY (Sigma Aldrich; St. Louis, MO),

PEI (Santa Cruz Biotechnology, Dallas, TX), and BAF (Sigma Aldrich) were dissolved in DMSO, whereas Li was diluted in Milli-Q water; control cultures received the same quantity of vehicle (DMSO or/and Milli-Q water), which never exceeded 0.6% v/v.

### *Transfections*

For autophagosome and autolysosome formation analysis, cells were plated into 35-mm IBIDI microdishes (Ibidi, Martinsried, Germany) and 12 hours later transfected with LC3-YFP or LC3-RFP-GFP, respectively. LC3-YFP construct contains the LC3 gene fused to the yellow fluorescent protein (YFP) gene (kindly supplied by Dr. Mario Costa)[341], whereas the LC3-RFP-GFP (ptfLC3) tandem construct contains the LC3 gene fused to both red and green fluorescent proteins (RFP and GFP; ptfLC3 was a gift from Tamotsu Yoshimori; Addgene plasmid No. 21074). The constructs were transformed in Dh5-Alpha competent cells (Thermo-Fisher; Waltham, MA), grown overnight in Luria Bertani (LB) broth, and extracted with a Qiagen Plasmid Kit (Qiagen, Hilden, Germany), according to kit instructions. Plasmid DNA concentration and purity were measured with a biophotometer, followed by storage at −20°C. For each sample dish, the transfection solution was prepared by adding 1 µg plasmid DNA and 2 µl Lipofectamine 2000 (Life Technologies) in 100 µl Optimem medium (Life Technologies). After 20 minutes of incubation at RT (for liposome reaction) the transfection solution was added to the cells. 24 hours after transfection, MO3.13 cells were treated as previously reported (control, PSY, Li1+PSY, and Li2+PSY for the LC3-YFP transfected cells; control, PSY, and PSY+BAF for the LC3-RFP-

GFP transfected ones) and finally imaged by fluorescence confocal microscopy.

### *Confocal Imaging and Autophagosome/ Autolysosome Analysis*

24 hours after treatments, MO3.13 cells were tested for LC3-YFP or LC3-RFP-GFP puncta formation by live-cell confocal imaging. Confocal images were acquired with a laser scanning confocal microscope TCS SP2 (Leica Microsystems, Hilden, Germany) equipped with a cell incubator (37°C and 5% $CO_2$), a 633 oil objective, and an argon (488 and 514 nm) laser. Each reported confocal image was obtained from a z-series (stack depth was within 10 μm; steps 0.5–1 μm; each image was averaged three times). The resulting z-stack was processed in ImageJ (NIH; RRID:SCR_003070) into a single image by using "z-project" and "Max intensity" options. For a quantitative analysis of autophagosome and autolysosome formation, every image has been thresholded using "threshold"; after this, binary images were inverted, and the number of particles was analyzed by the "Analyze Particles" plugin, by setting "size ($pixel^2$)" 5 from 2 to infinity, and "circularity" 5 from 0.00 to 1.00. A region of interest (ROI) for every analyzed cell was made in brightfield images, and the particles were then analyzed for every single cell (ROI).

### *Western Blotting*

For Western blotting experiments, MO3.13 cells were cultured on standard 60-mm dishes, treated as previously described, and then lysed on ice with RIPA buffer (Sigma-Aldrich) containing protease and phosphatase inhibitors cocktail (cOmplete and PhosSTOP; Roche Diagnostics, Basel, Switzer- land). Cell lysates were sonicated (for 4 sec at 12 μm of intensity)

and after centrifugation (15000 g for 25 min, 4°C) tested for protein concentration by micro-BCA protein assay kit (Thermo Scientific Pierce). The samples were boiled in Laemli buffer containing b-mercaptoethanol (5% final concentration) for 5 minutes and centrifuged at RT, and the supernatants were finally used for gel electrophoresis (SDS-PAGE) or kept at –80°C until use. Samples (40 µg) were resolved by SDS-PAGE using Gel Criterion XT-Precasted polyacrylamide gel 4–12% Bis-Tris (Bio-Rad, Hercules, CA) and subsequently transferred to nitrocellulose membranes, as was done by Tonazzini et al. (2016).[342] Immunodetection was performed with the following antibodies against: LC3B (Abcam Cambridge, United Kingdom; catalog No. ab48394; RRID:AB_881433); p62 (Abcam; catalog No. ab56416; RRID:AB_945626), actin (Sigma-Aldrich; catalog No. A-3853; RRID:AB_262137), and tubulin (Sigma-Aldrich; catalog No. T6074; RRID:AB_477582. On the following day, blots were incubated with the corresponding peroxidase-linked secondary antibodies (goat anti-rabbit or mouse IgG-HRP conjugate; Bio-Rad, catalog No. 170-6516; RRID:AB_11125547; and catalog No. 170-6515; RRID:AB_11125142; dilution 1:2,500), and after incubation membranes were developed with Clarity enhanced chemiluminescent substrates (Bio-Rad). The chemiluminescent signal was acquired with an ImageQUANT LAS400 scanner (GE Healthcare Life Sciences, Uppsala, Sweden), and the density of immunoreactive bands was quantified in ImageJ. The results were normalized to the actin (LC3) or tubulin (p62) content and averaged for each repetition toward the control or PSY conditions. The signals of LC3 and P62 were detected in different blots to avoid artifacts.

### Antibody Characterization

The LC3B antibody recognized the expected full-length and cleaved forms of LC3-II protein (15 and 17 kDa, respectively), and the p62 antibody recognized a 62-kDa band, identical to that from previous reports.[343,344] To avoid artifacts from different transfer rates at different heights of the polyacrylamide gel, LC3 and p62 band intensities have been normalized to different control proteins, actin (LC3) and a-tubulin (p62). Actin and a-tubulin antibody detected 42- and a 55-kDa bands, respectively.[345,346]

### *Lipid Extraction*

For lipid extraction, MO3.13 cells were plated on standard 24-well plates, treated as previously reported, washed with cold PBS, and lysed on ice with 80 µl/well of RIPA (Sigma-Aldrich), containing a protease and phosphatase inhibitors cocktail. Each condition was used in triplicate, and a control well (without cells) was prepared for each treatment. For each sample, a 150-µl mixture was prepared combining 75 µl of the cell lysate, 12µl N,N-dimethylsphingosine, 1,250 µM (N,N-DMS, the selected internal standard for HPLC/MS-MS; Sigma-Aldrich), and 63 µl MilliQ water. Then the mixture was divided into three parts (50 µl each), and 500 µl of chloroform/methanol solution (2:1) was added to each part. Samples were vortexed, left at RT for 10 min, and supplemented with 100 µl NaCl 0.9% p/v in Milli-Q water. The biphasic mixture was centrifuged at 800 g for 30 min, and the lower layer was collected and evaporated to dryness under vacuum at 30°C. The residue was dissolved in 50 µl methanol/formic acid 100/0.1 and processed for high-performance liquid chromatography and tandem mass spectrometry (HPLC/MS).

### *HPLC-MS Analysis*

HPLC-MS quantitation was performed on a Shimadzu Nexera UHPLC chromatograph interfaced with an AbSciex 3200 QTRAP mass spectrometer (AB SCIEX, Toronto, Ontario, Canada). HPLC analyses were performed on a Vydac C4 1 X 250 mm (particle size 4 µm), using water/methanol/iso-propanol/formic acid 40/55/5/0.1 (A) and methanol/isopropanol/formic acid 95/5/0.1 (B) as mobile phases at 0.1ml/min flow. Runs were performed under a 45-min linear gradient from 0 to 100% of solvent B, followed by a 5-min purge step at 100% of B and by a 10-min re-equilibration step to the starting conditions.

MRM analyses were performed under the following conditions: ion spray voltage: 5000V, source temperature 350C, declustering potential 50 V, collision energy variable (see value in parentheses), ion source gas 20 liters/min, curtain gas: 25 liters/min. The following transitions were monitored (acquisition time 150 msec/transition): N,N-dimethylsphingosine (Q1/Q3, m/z, CE in parenthesis): 328.2/310.2 (26V); 328.2/280.2 (32 V); 328.2/110.2 (42 V). PSY (Q1/Q3, m/z, CE in parenthesis): 462.5/444 (25 V); 462.5/282 (30 V);462.5/264 (27 V); 462.5/252 (39 V). Transitions 328.2/310.2 (N,N-dimethylsphingosine) and 462.5/282 (PSY) were used for quantitation purposes.

### *Annexin V/Propidium Iodide Cell Death Assay*

For annexin V/propidium iodide (PI) cell death assay, MO3.13 cells were plated on standard 24-well plates and, after treatments, processed as described by Voccoli et al. (2014).[47] Briefly, cells were harvested and centrifuged for 5 minutes at 330 g, and the pellets obtained were washed

with PBS, centrifuged again; resuspended in binding buffer (10 mmol/liter HEPES, 135 mmol/liter NaCl, 5 mmol/liter $CaCl_2$) containing annexin V-FITC conjugate 1 μM (Invitrogen-Life Technologies, Carls-bad, CA) and PI 100 nM (Sigma-Aldrich); and incubated in ice for 30 min. Flow cytometry was performed by using an S3 flow cytometer (Bio-Rad) equipped with 488- and 561-nm diode-pumped solid-state lasers. Annexin V-FITC was excited with the 488-nm laser, and the emitted fluorescence was collected through a 586/25-nm bandpass filter; PI was excited with the 561-nm laser, and its fluorescence was collected through a 615/ 25-nm bandpass filter. Data were analyzed in ProSort (Bio-Rad) by dividing the scatterplot of annexin V vs. PI into four quadrants representing four clearly distinguishable populations of cells, viable cells (R4 quadrant), apoptotic cells (R5), necrotic cells (R3), and secondary necrotic cells (R2). The four quadrants were set on control conditions, and the cellular debris was excluded from the quantification by gating cells on a forward-scatter/side-scatter (FSC/SSC) graph; at least 25000 gated events were acquired for each sample.

### *ROS Detection by Flow Cytometry and Microplate Fluorimetry*

For ROS detection, cells were plated in standard 24-well plates and exposed to the treatments previously described, washed with 500 μl/well of prewarmed PBS with calcium and magnesium, and then stained with carboxyl-$H_2$-DCFDA ($H_2$-DCFDA; Life Technologies) for 30 minutes at 37°C. DCFA was diluted in DMSO to obtain a 10 μM working solution, and it was used at 2.5 μM final concentration (diluted in prewarmed PBS with calcium and magnesium). Negative (PBS with no staining solution) and positive (treated with 100 mM $H_2O_2$ diluted in 0.2% FBS medium for 1 hours)

control wells were also prepared. For flow cytometry, the staining cells were treated with 200 µl trypsin for 5 minutes at 37°C, harvested in 500 µl complete medium, centrifuged, resuspended in 500 µl prewarmed PBS with calcium and magnesium, and filtered in polypropylene Greiner round-bottomed tubes (Sigma Aldrich). To detect ROS production, the S3 flow cytometer previously described was used. The oxidation product of carboxyl-H2DCFDA was excited with the 488-nm laser, and the emitted fluorescence was collected through a 525/30-nm bandpass filter. More specifically, the dedicated ProSort software was used to create a protocol in which plot types, a region gate to exclude debris, and regions to estimate the percentage of cells with different characteristics were defined. Histograms were plotted as cell counts vs. emitted fluorescence intensity area. Background fluorescence was eliminated by setting a threshold gate on the histogram of the negative control (dashed line in Fig. 4.8 A, top left). Only cells with fluorescence greater than the value of the gate were considered positive for enhanced ROS production. For each sample at least 20000 gated cells were acquired.

To avoid artifacts from possible oxidative stress originating from cell detachment, we also evaluated ROS production by reading DCF fluorescence from adhered cells by using a microplate fluorescence reader (GloMax Multimode Readers; Promega, Madison, WI). For this measure, immediately after the 30 minutes staining, the working solution was discarded and the treatment medium (previously collected from each well and put aside in a new 24-well plate) was placed back to allow a sort of recovery for the cells (as suggested by Eruslanov and Kusmartsev, 2010)[347]. The oxidation product of carboxyl-H2DCFDA was excited at 475 nm and the emission

intensity was measured at 500–550 nm. After the measurement, cells were treated with 200 µl of trypsin for 5 minutes at 37°C, harvested in 500 µl complete medium, centrifuged, resuspended in 1 ml complete medium, stained with trypan blue, and counted by means of a Countess automated cell counter (Invitrogen). The mean fluorescence intensity coming from each well was finally normalized to the corresponding cell number and averaged for each repetition (N =3 independent experiments, each performed in triplicate) and finally normalized to the control condition. The signal coming from the control condition was consistent with that of the unstained sample (data not shown).

### *Statistical Analysis*

Data are reported as mean ± SEM obtained from at least three independent experiments (in figure legends, "N" indicates the number of experiments performed). Data were statistically analyzed in Prism 6.00 (GraphPad Software, San Diego, CA; RRID:SCR_002798). For parametric data, Student's t-test (unpaired, two-tailed) or one-way ANOVA (Tukey's or Dunnett's multiple-comparisons test) was used; the mean values obtained in each repeated experiment were assumed to be normally distributed about the true mean. Statistical significance refers to results for which $P < 0.05$ was obtained.

## 4.3 Dysregulated autophagy as a new aspect of the molecular pathogenesis of Krabbe disease

*The experiments presented in this Section have been published after peer-reviewing on Neurobiology of disease 129, 195-207. Co-authors of the work are: Del Grosso A, Angella L, Tonazzini I, Moscardini A, Giordano N, Caleo M, Rocchiaccioli S, and Cecchini M. Role of authors: study concept and design: ADG, MC. Acquisition of data: ADG, LA, AM, SR, NG. Analysis and interpretation of data: All authors. Drafting of the manuscript: All authors. Statistical analysis: ADG, LA, MC. Obtained funding: MC. Study supervision: MC. I, in particular, established and maintained primary cell cultures, performed western blots, immunohistochemistry and immunocytochemistry experiments, performed statistical analysis, and drafted the manuscript.*

### 4.3.1 Introduction

Autophagy, before the present work, had never been analysed in the TWI mouse, except for a very recent study performed by Abdelkarim and collaborators.[95] They demonstrated that PSY and α-synuclein colocalize in the lysosomal pathway in the TWI brain, and that TWI brains also show an elevated basal level of both LAMP-1 and LC3-I markers. α-synuclein is generally linked to the pathogenesis PD, but has just been recently found accumulated also in KD human and mouse brains.[95,44,46]

In this work, we investigate the expression of some fundamental autophagy markers, LC3, p62 and Beclin-1, in the TWI mouse, by immunohistochemistry and Western blot techniques. We also show the autophagy molecular process in primary fibroblasts from TWI and WT mice, with and without PSY treatment. By HPLC/MS, we investigate whether the changes in autophagy marker levels that we found in TWI cells could be

considered PSY-driven. Finally, in view of possible new therapeutic approaches to treat KD, we show the capability of two mTOR-dependent autophagy modulators (RAP and RESV) to rescue in vitro the WT phenotype.

### 4.3.2 Autophagy is dysregulated in the TWI mouse central and peripheral nervous system.

Forasmuch as KD has a strong neurological component, we extensively characterized autophagy in the nervous system of the TWI mouse; in particular, the brain and sciatic nerve were chosen as representative components of the CNS and PNS, respectively. As markers of autophagy, we focused on p62, LC3 and Beclin-1.

#### *Brain*

Immunohistochemistry experiments revealed a markedly increased presence of p62 aggregates (green in Fig. 4.9 A) in both PND 20 and 30 TWI brains compared to the age matched WT ones. Quantitative analysis of confocal images, indeed, showed an increase in both their number (Fig. 4.9 D) and area (Fig. 4.9 E) in TWI brains. A representative high-magnification image of p62 brain aggregates is also shown in Fig. 4.9 G. In agreement with these data, western blots reported augmented levels of p62 total expression in TWI brains compared to that measured for WT brains, for PND 20 and PND 30 mice (Fig. 4.9 H). Taken together, these experiments demonstrate for the first time a general upregulation of the autophagy marker p62 in TWI mice at the early (PND 20) and late stage (PND 30) of the disease. Total LC3 levels, instead, were rather similarly expressed in TWI and WT mice.

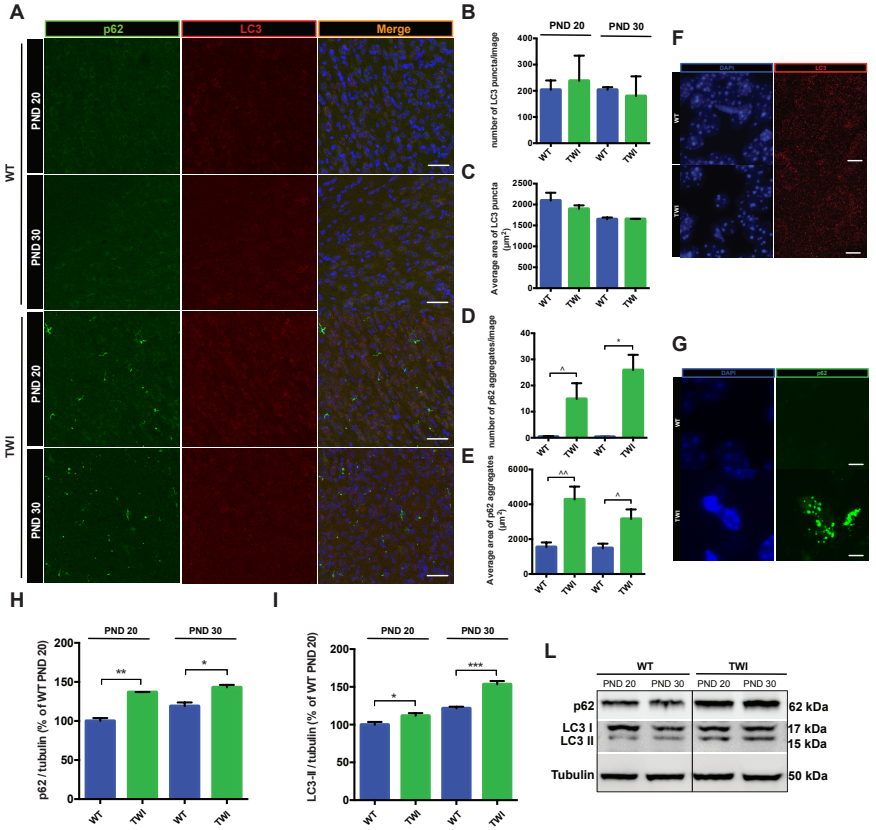


**Figure 4.9.** Autophagy is dysregulated in the TWI brain. **(A)** Immunohistochemistry staining of WT and TWI brains with anti-p62 (in green) and anti-LC3 (in red) antibodies, nuclei are stained with DAPI (in blue). Scale bar: 37 μm. **(B-E)** Analysis of the number and average area of LC3 puncta and p62 aggregates per field. **(D)** p62 aggregates: ^ = P < 0.15 TWI-PND20 vs. WT-PND 20; * = P < 0.05 TWI-PND 30 vs. WT-PND 30. **(E)** Average area of p62 aggregates: ^^ = P < 0.10 TWI-PND 20 vs. WT- PND 20 and ^ = P < 0.15 TWI-PND 30 vs. WT-PND 30; Student's t-test. Data are shown as mean ± SEM; N = 4 WT and N = 4 TWI. **(F)** High-magnification image of LC3 puncta in WT and TWI brain. Scale bar: 7.5 μm. **(G)** High-magnification images of p62 aggregates in WT and TWI brain. Scale bar: 7.5 μm. **(H)** Western blot analysis of the total p62 and LC3-II content in whole brain lysates. **(I)** p62: ** = P < 0.01 TWI-PND 20 vs. WT-PND 20; * = P < 0.05 TWI-PND 30 vs. WT-PND 30. **(L)** LC3: * = P < 0.05 TWI-PND 20 vs. WT-PND 20; *** = P < 0.001 TWI-PND 30 vs. WT-PND 30. Student's t-test. Data are reported as mean ± SEM, N ≥ 3. **(H)** Representative western blot bands.

Figure 4.9 A reports representative confocal fluorescence images of total LC3 in TWI and WT brains, for PND 20 and PND 30 mice. No evident differences can be observed by a visual analysis of these images. Quantification of autophagosomes as LC3 positive puncta was then carried out on magnified fluorescence images (Fig. 4.9 F), and showed no significant variations between TWI and WT mice in both their number and area, in PND 20 and PND 30 brains as well (Fig. 4.9 B, C). Nevertheless, Western blot data instead highlighted an increased expression of the phosphatidylethanolaminate form of LC3 (LC3-II; Fig. 4.9 I) in TWI mice with respect to the age matched WT mice, supporting the hypothesis of up-regulation of the autophagy flux. Finally, Beclin-1 total levels were mainly stable among the experimental groups, apart for a slight increase in PND 30 WT brains (Fig. 4.14 A), indicating that the initial phase of the autophagy process may not be altered in the TWI brain.

### *Sciatic nerve*

In agreement with the results obtained for the brain, Western blots performed on entire sciatic nerve lysates revealed a very important p62 increase of expression in TWI mice (at both PND 20 and PND 30) compared to the expression found in WT nerves. It was indeed about 3.5 times greater than that of aged matched WT nerves (Fig. 4.10 A). Similarly, we found upregulation of LC3-II in PND 20 and PND 30 TWI nerves (Fig. 4.10 B) and, as in the brain, this increase was more evident for late affected mice (PND 30). Moreover, in contrast to the brain, we reported an increased amount of Beclin-1 in TWI nerves in respect to the WT ones (Fig. 4.14 B).

Overall, these experiments demonstrate a widespread up-regulation of the autophagy machinery in the TWI nervous system, which resulted more pronounced in the case of PNS.

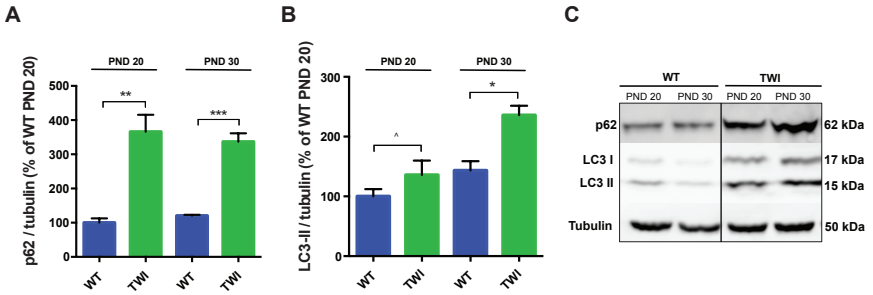


**Figure 4.10.** Autophagy is dysregulated in the TWI sciatic nerve. **(A, B)** Western blot analysis of the total p62 and LC3-II content in whole sciatic nerve lysates. **(A)** p62: ** = P < 0.01 TWI-PND 20 vs. WT PND 20; *** = P < 0.001 TWI-PND 30 vs. WT-PND 30. **(B)** LC3: ^ = P = 0.18 TWI-PND 20 vs. WT- PND 20; * = P < 0.05 TWI-PND 30 vs. WT- PND 30; Student's t-test. Data are shown as mean ± SEM, N ≥ 3. **(C)** Representative western blot bands.

### 4.3.3 P62 aggregates accumulate differently in distinct neural cell types

In order to investigate the localization of the p62 aggregates we performed a double immunostaining of TWI and WT brain slices with the anti-p62 antibody (red in Fig. 4.11) together with antibodies specific for different brain cell types (neurons: anti-NeuN, astrocytes: anti- GFAP, oligodendrocytes: anti-MBP; green in Fig. 4.11). Similarly to what has been previously shown (Fig. 4.9 A, D), also in this case the WT brain did not highlight significant p62 aggregates; they were instead present in the TWI brain, as expected (Fig. 4.11 A, B, C). Colocalization was found with the neuronal protein NeuN (Fig. 4.11 A), a widely used neuronal marker commonly localized in nuclei and perinuclear cytoplasm of most of the neurons in the CNS of mammals.[348] Conversely, the glial fibrillary acidic protein (GFAP) did not show colocalization with p62 aggregates (Fig. 4.11

B). The visual analysis of high magnification images and confocal z-stacks on several GFAP-positive cells, in fact, could not reveal colocalization either in cell nuclei, or in cell protrusions. Thus, astrocytes do not seem to be directly involved in the brain accumulations of p62. Finally, figure 4.11 C indicates that colocalization of p62 with oligodendrocytes, marked as MBP-positive cells[349] also might not occur. However, this is, in our opinion, a more intricate question. As expected, TWI brains presented extended demyelination (Fig. 4.11 C).[177,12] TWI oligodendrocytes differentiation and survival, in fact, are known to be intrinsically defective. These defects are associated with aberrant accumulation of endogenous PSY and reduced activation of the Erk1/2 and Akt/mTOR pathways before apoptotic cell death.[36] Consequently, the scattered and mild fluorescence signal deriving from oligodendrocytes staining made not straightforward the interpretation of colocalization images, and thus assessing the presence of p62 aggregates in oligodendrocytes.

Taken together, these data suggest that p62 accumulation is not homogeneously distributed among different TWI neural cell types. More specifically, while the widespread degeneration of TWI oligodendrocytes made difficult data interpretation for this type of cells, p62 aggregates were clearly found in neurons, but not in astrocytes.

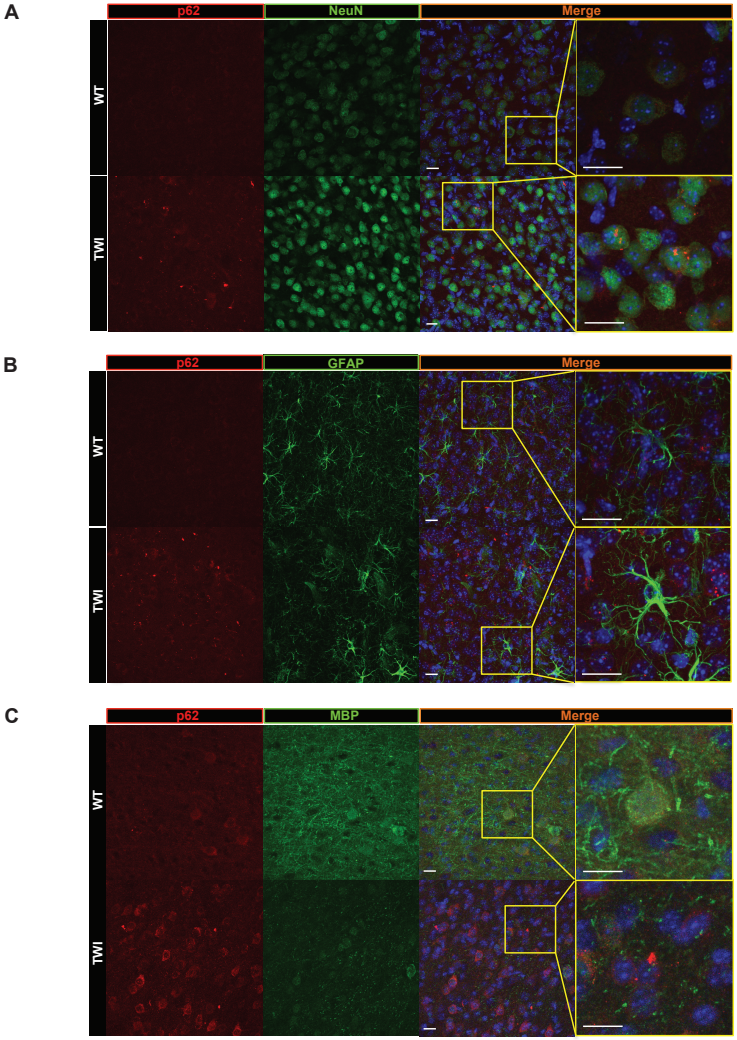


**Figure 4.11.** p62 accumulation in different CNS cell types. Immunohistochemistry staining of WT and TWI brains with anti-p62 antibody (in red) and antibodies for different neuronal cell types (in green): **(A)** neurons (anti-NeuN), **(B)** astrocytes (anti-GFAP) and **(C)** oligodendrocytes (anti-MBP). For every panel **(A, B and C)** merged images with DAPI (in blue) at normal and 3 X zooms are shown on the right side of the panel. Mice were sacrificed at PND 20. Scale bar: 20 µm.

### 4.3.4 Autophagosome-lysosome fusion and autophagosome-mediated p62 recycling are not impaired in TWI brains

We wondered if the p62 accumulations that we found in the TWI brain could be a consequence of an impaired autophagic flux or only the result of an augmented rate of ubiquitinated cell products tagged with p62. To discriminate which of the two hypotheses was correct we per- formed different double immunostainings to verify the correct progression of some crucial steps of the autophagy pathway.

First, we demonstrated that the autophagy flux correctly reaches its final stage, the fusion of the autophagosome with the lysosome. Colocalization of the autophagosome's marker LC3 with the lysosome's marker LAMP-1[301], in fact, occurred in both WT and TWI brains (Fig. 4.12 A). Mander's colocalization coefficient analysis (LC3/ LAMP-1) also revealed higher and less dispersed values for TWI mice with respect to WT mice (Fig. 4.12 D), suggesting a higher rate of autolysosome formation in the TWI CNS and consequently an increased autophagic activity. We also assayed the colocalization of the p62 aggregates with both autophagosome and lysosome markers, finding that it occurs for both p62 and LAMP-1 (Fig. 4.12 B, E) and p62 and LC3 (Fig. 4.12 C, F), in TWI and WT mice as well.

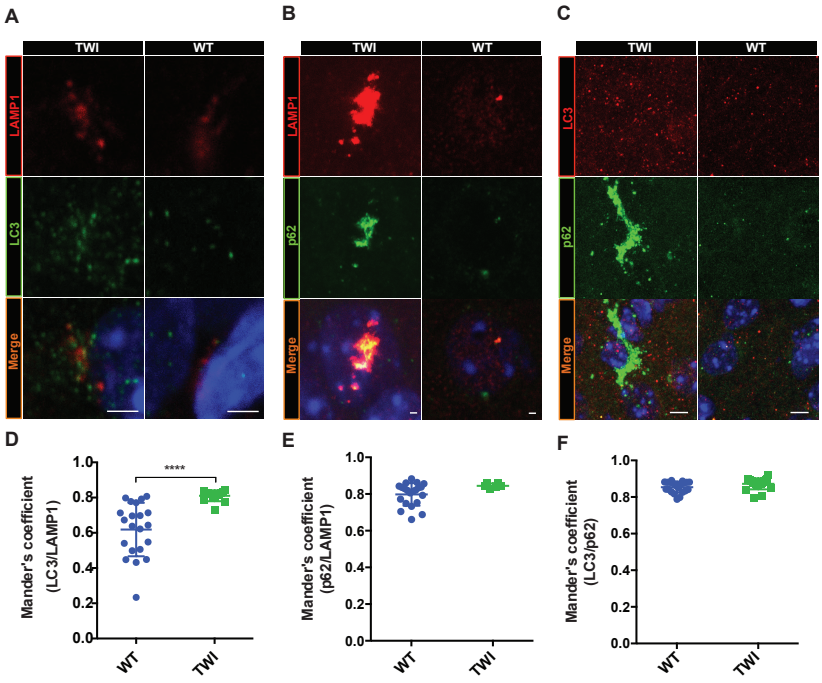


**Figure 4.12.** p62 colocalization with autophagosomes and lysosomes in the TWI brain.

### 4.3.5 Autophagy is dysregulated in TWI primary cells

In order to better understand if autophagy dysregulation could be determined by the cytotoxic catabolite, PSY, we investigated autophagy in primary fibroblasts from WT and TWI mice, with or without exogenous PSY administration.

For this treatment, we chose the minimum PSY concentration (100 µM) that could diminish cell viability of at least 50% after 24 hours from the administration (data not shown). Immunostaining was performed for p62 and LC3, and cells were imaged by confocal fluorescence microscopy (see a representative image in Fig. 4.13 A). An augmented number of p62

intracellular aggregates was reported in TWI untreated cells and in PSY-treated WT and TWI cells with respect to that measured in WT cells (Fig. 4.13 C). LC3 puncta, instead, increased only upon PSY treatment, in TWI and WT cells as well; no significant difference was measured between untreated TWI and WT cells (Fig. 4.13 B). These data agree with what we already observed in a PSY-treated oligodendrocyte cell line (MO3.13).[39]

As we did for whole organs extracts, we analysed the total p62 and LC3-II amount in the different conditions by Western blot (Fig. 4.13 D, E). Total p62 and LC3-II amounts significantly increased in PSY treated cells compared to the untreated ones, both for TWI and for WT cells. We also found higher levels of total p62 for untreated TWI cells with respect to the WT ones. Moreover, to exclude that the measured p62 and LC3-II increase induced by PSY could stem from impaired autophagosome-lysosome fusion rather than from an augmented autophagy activity, we also treated cells with BAF. BAF is a drug that blocks the fusion between lysosomes and autophagosomes and which is typically used to prevent LC3-II and consequently p62 degradation.[39,324,350,261] LC3-II, indeed, is itself degraded by autophagy. By blocking the fusion between autophagosomes and lysosomes, BAF was indeed expected to determine an overall increase of LC3-II in case of functional autophagy.

The administration of BAF induced a further increase of LC3-II and p62 total levels both in presence and absence of GALC activity, proving that enzyme deficiency does not interfere with autophagolysosome formation in our PSY treated cell model (WT+PSY and TWI+PSY). Moreover, the efficacy of BAF has been validated also for untreated WT and TWI cells (WT-UT and TWI-UT; Fig. 4.15).

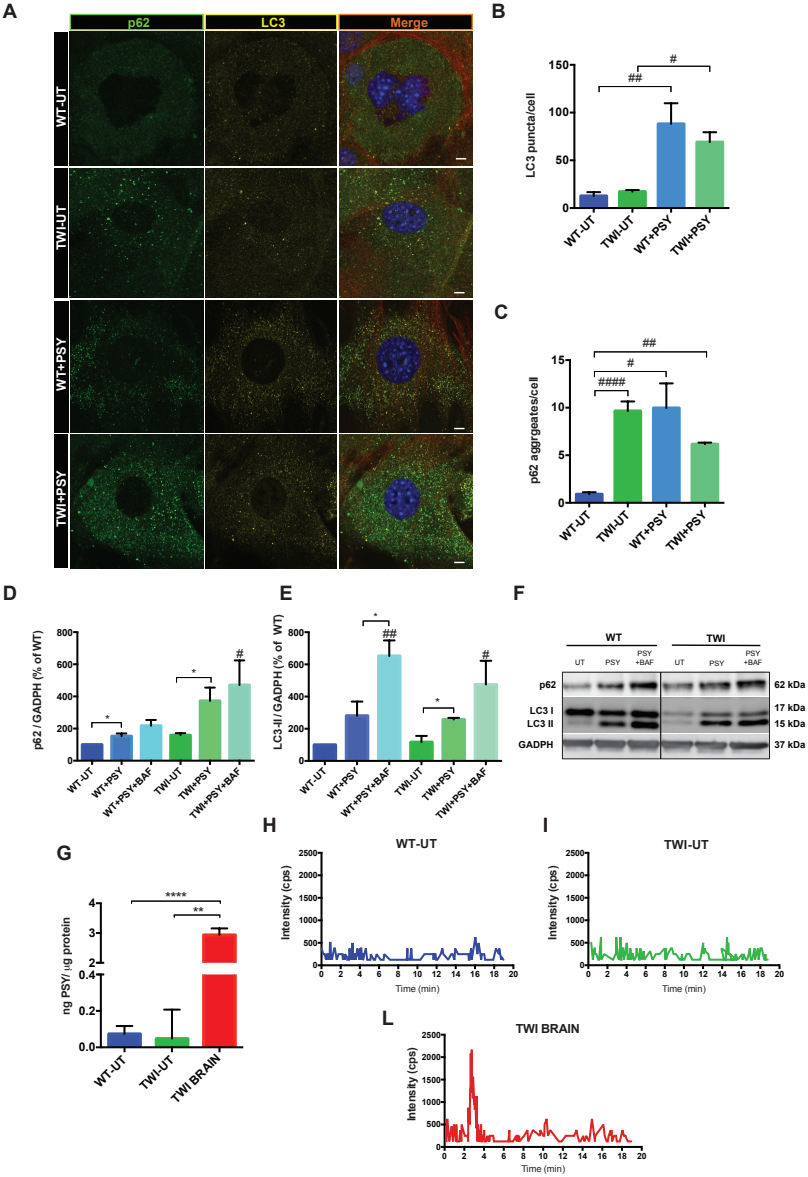


**Figure 4.13.** Autophagy in TWI primary cells. **(A)** Representative confocal imaging of WT and

TWI primary fibroblasts treated or not with PSY and immunostained for p62 (in green) and LC3 (in yellow); nuclei are stained with DAPI (in blue) and actin fibers with phalloidin (in red); scale bar: 10 µm. **(B, C)** Quantification of LC3 and p62 positive puncta. **(B)** LC3: ## = P < 0.01 WT + PSY vs. WT-UT, # = P < 0.05 TWI + PSY vs. TWI-UT; One-way ANOVA, Dunnett's test. **(C)** p62: #### = P < 0.0001 TWI-UT vs. WT-UT; # = P < 0.05 WT + PSY vs. WT-UT; ## = P < 0.01 TWI + PSY vs. WT-UT; One-way ANOVA, Dunnett's test. Data are shown as mean ± SEM; N =3. **(D, E)** Western blot analysis of the total p62 and LC3-II content in whole cell lysates. (d) p62: * = P < 0.05 WT + PSY and TWI + PSY vs. WT-UT and TWI-UT; Student's t-test. # = P < 0.05 TWI+PSY+BAF vs. WT-UT; One-way ANOVA, Dunnett's test. **(E)** LC3: * = P < 0.05 WT+PSY+BAF and TWI+PSY vs. WT+PSY and TWI-UT; Student's t-test. # = P < 0.05 TWI + PSY + BAF vs. WT-UT and ## = P < 0.01 WT + PSY + BAF vs. WT-UT; One-way ANOVA, Dunnett's test. Data are shown as mean ± SEM; N =3. **(F)** Representative western blot bands. **(G)** HPLC/MS quantification of PSY in WT and TWI primary fibroblast lysates and in a TWI brain (PND 20, used as positive control). **(H-L)** Representative chromatograms with the PSY monitored transition for quantitative purpose (462.5/282).

We also investigated Beclin-1 expression and found that its main band at 55 kDa[351] was not statistically different between the distinct WT and TWI conditions, although an increasing trend can be seen in figure 4.14 D, F Bands with lower molecular weight appear instead quite different between WT and TWI conditions, showing that the cleavage of the Beclin-1 complex did not occur in the same way in TWI and WT cells (Fig. 4.14 E, G).

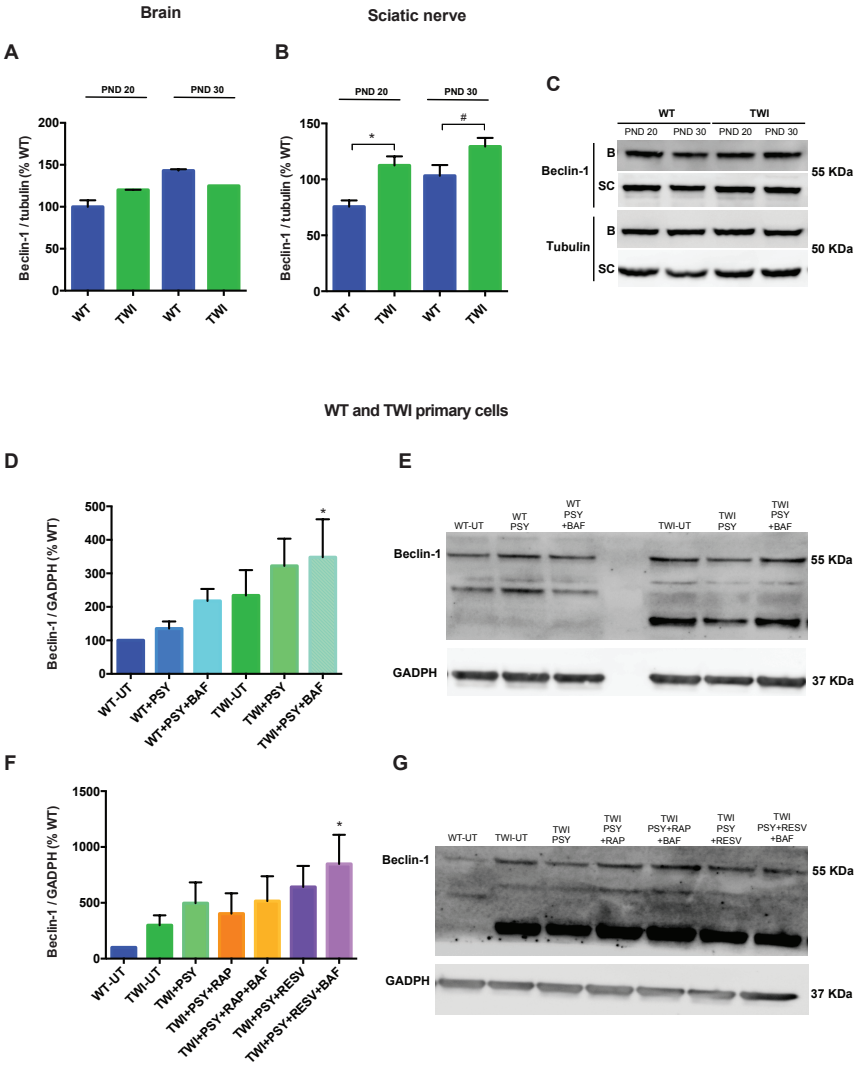


**Figure 4.14.** Western blot analysis of Beclin-1 content in the whole brain and sciatic nerve lysates of WT and TWI mice at PND 20 and 30. **(A, B)** Sciatic nerves: * = P < 0.05 TWI PND 20 *vs.* WT-PND 20, ^ = P = 0,08 TWI-PND 30 *vs.* WT PND 30; Student's t-test. Data are shown as mean±SEM; N≥3. **(C)** Representative western blot bands (abbreviations: B = brain; SC = sciatic nerve). **(D, F)** Beclin-1 content in whole cell lysates. # = P < 0.05 TWI+PSY+BAF *vs.* WT-UT and

TWI+PSY+RESV+BAF *vs.* WT-UT. One-way ANOVA, Dunnett's test. Data are shown as mean±SEM; N=3. **(E, G)** Representative western blot bands.

Finally, in order to assess if the autophagy activation suggested by the increase of p62 expression and number of aggregates per cell in untreated TWI-cells could be attributed to a PSY intracellular accumulation, we quantified the endogenous PSY amount by HPLC/MS in TWI and WT cells. As shown in figure 4.13 G, TWI untreated fibroblasts did not report a significant level of PSY, which was at the limit of detection of our set-up and almost undistinguishable to that measured for WT cells. As a positive control we performed the same measurement in TWI brain lysates. In this case, as expected, PSY resulted well detectable and significantly higher than in WT and TWI fibroblasts. Representative PSY chromatographic peaks are reported in figure 4.13 H, I, L for comparison.

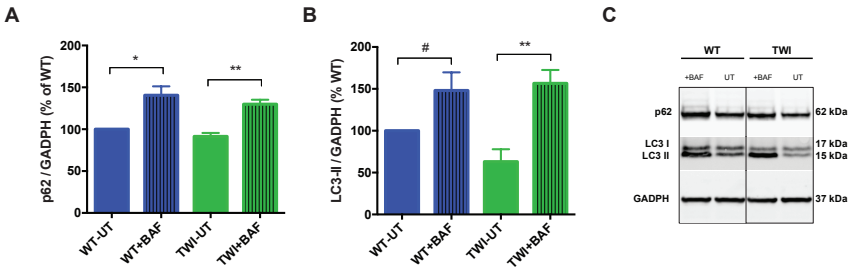


**Figure 4.15. (A, B)** Western blot analysis of the total p62 and LC3-II content in whole cell lysates. **(A)** p62: * = P < 0.05 WT+BAF vs. WT-UT; ** = P < 0.01 TWI+BAF vs. TWI-UT. **(B)** # = P < 0.06 WT+BAF vs. WT-UT; ** = P < 0.01 TWI+BAF vs. TWI-UT. Student's t-test; N=3. **(C)** Representative western blot bands.

### 4.3.6 RAP and not RESV-mediated autophagy induction partially restore autophagy markers levels.

Given the presence of augmented p62 intracellular aggregates found in vivo and in vitro in the missing GALC conditions, we decided to test the capability of autophagy inducers to stimulate the clearance of p62-aggregates from cells. We tested two well-known autophagy inducers, RAP and RESV, in TWI cells treated with PSY, so to exacerbate the KD phenotype. The Western blot experiments reported in figure 4.16 A demonstrated that a pre-treatment with RAP before PSY administration can restore the p62 level approximately to that of the wild type. RESV, instead, did not induce relevant changes in the p62 amount in PSY treated cells. LC3-II levels, as expected, increased with the addition of RAP or RESV. In both cases, moreover, p62 and LC3-II levels increased with the addition of BAF, confirming that both RAP and RESV did not impair autolysosome formation in our conditions (Fig. 4.12 A). Beclin-1, instead, resulted significantly upregulated only in RESV+BAF treated cells (Fig. 4.14 F), and, as previously mentioned, TWI and WT cells presented differences in the bands with molecular weights lower than the principal one (55 kDa).

Subsequently we focused on RAP, and studied the number of p62 aggregates and LC3-marked autophagosomes in TWI + PSY cells pre-treated with RAP by immunostaining and confocal fluorescence microscopy (representative images are shown in Fig. 4.16 D). This experiment confirmed the results obtained with the Western blot analysis, demonstrating that the pre-treatment with RAP can significantly decrease the number of p62 aggregates per cell, bringing back the number of aggregates at an intermediate value between the WT-UT control and the TWI-UT condition (Fig. 4.16 F). The number of autophagosomes (yellow

marked puncta), instead, could not be rescued by RAP pre-treatment (Fig. 4.16 E).

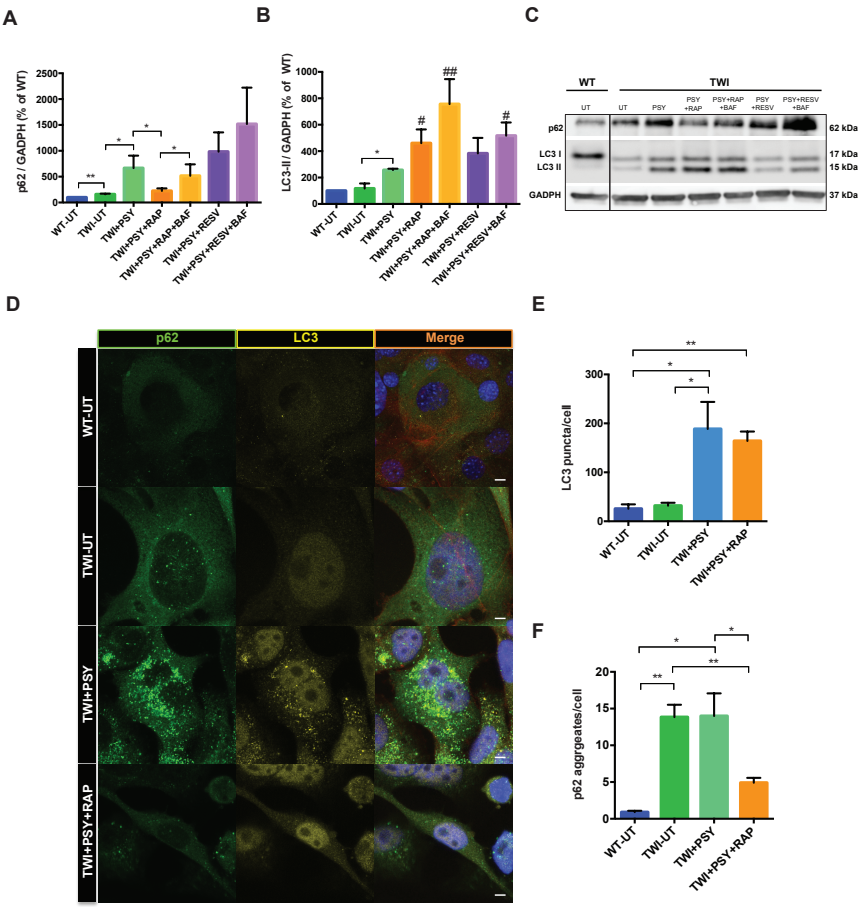


**Figure 4.16.** Autophagy induction in PSY treated primary cells. **(A. B)** Western blot analysis of the total p62 and LC3-II content in whole cell lysates. **(A)** p62: * = P < 0.05 TWI + PSY vs. TWI-UT, TWI + PSY + RAP vs. TWI + PSY, TWI + PSY + RAP+BAF vs. TWI + PSY + RAP; ** = P < 0.01 TWI-UT vs. WT-UT. Student's t-test. **(B)** LC3: * = P < 0.05 TWI+PSY vs. TWI-UT; Student's t-test. # = P 0< .05 TWI+PSY+RESV+BAF and TWI+PSY+RAP vs. WT-UT and ## = P < 0.01 TWI+PSY+RAP +BAF vs. WT-UT; One-way ANOVA, Dunnett's test. Data are shown as mean ±

SEM; N =3. **(C)** Representative western blot bands. **(D)** Immunocytochemistry staining of WT and TWI primary fibroblasts treated or not with PSY and RAP, immunostained for LC3 (in yellow) and p62 (in green); nuclei are stained with DAPI (in blue) and actin fibers with phalloidin (in red); scale bar: 10 μm. **(E, F)** Quantification of LC3 puncta and p62 aggregates. **(E)** LC3: * = P < 0.05 TWI + PSY vs. WT-UT and TWI-UT; ** = P < 0.01TWI+PSY+RAPvs.WT-UT. **(F)** p62: ** = P < 0.01TWI-UT vs. WT-UT and TWI+PSY+RAP vs. TWI-UT; * = P < 0.05TWI+PSY vs. WT-UT and TWI + PSY + RAP vs. TWI + PSY. Student's t-test. Data are shown as mean ± SEM; N =3.

### 4.3.7 Concluding remarks

The exact pathogenic mechanism that leads from the enzyme deficiency to cell death in KD is still not completely understood and no cure is currently available for KD, being treatment symptomatic and supportive only (See Section 2). A novelty that could bring freshness to the current therapeutic attempts came with the work of Folts and colleagues. Basically they showed that PSY induces multiple lysosomal dysfunctions (altered lysosomal pH, endolysosomal trafficking, lipid degradation and cathepsin activation), providing for the first time a direct link between enzymatic mutations and lysosomal abnormalities.[99] Since cellular waste material, such as proteins or lipids, has to reach lysosomes for degradation in the context of the autophagy pathway, is indeed reasonable to expect autophagy dysfunction to be implicated in the KD pathogenesis. Coupled with the fact that abnormal protein aggregates (e.g. α-synuclein and ubiquitinated proteins) have been foundin KD brains[44,46,63], the connection between the autophagy pathway and KD is especially supported. Hence, recent studies focus on the attractive possibility that acting on the autophagic pathway could lead to new promising therapeutic approaches. An example of treatment based on this concept is the idea of restoring physiological lysosomal pH to enhance normal autophagy mediated protein degradation.[352] In our previous work (Section 4.2), we started investigating

autophagy in KD. We demonstrated that autophagy is up-regulated in an oligodendrocyte cell culture upon PSY treatment, and that the further autophagy induction with Li is able to ameliorate cell viability after PSY administration.

Here, we focused on the TWI mouse. We characterized the expression and localization of some fundamental autophagy markers (p62, LC3 and Beclin-1) in TWI and WT CNS and PNS. We found that the basal levels of autophagy activation are higher in TWI brain and sciatic nerves with respect to the WT ones. At both PND 20 (symptoms onset) and 30 (late stage of the dis-ease), in fact, TWI tissues presented higher levels of LC3-II and p62 and showed increasing trend in Beclin-1 levels especially in the sciatic nerve. Regarding LC3-II, its augmentation positively correlates with increased autophagic activity; at the beginning of autophagosome formation, in fact, LC3 is converted into a cleaved form (LC3-II) and inserted into autophagosome membranes.[353] Increased brain LC3-II levels have already been found for others LSDs as Niemman Pick, Sandhoffand GM1 gangliosidosisdisease.[354] For KD, rather, only increased LC3-I ex-pression in the TWI brain has been recently demonstrated.[63] p62 aggregates, instead, were not yet reported in literature for KD, but found in many other neurodegenerative and lysosomal disorders models characterized by dysregulated autophagy machinery.[355,356] Furthermore, we also found that they are clearly present in neurons instead of astrocytes. Thus, accordingly with previous studies indicating that the pathologic process associated with autophagic deficiency is cell-type specific[281,44], these data suggest that there could be a failure in the autophagy process, leading to the accumulation of p62-tagged proteins, which acts differently depending on the cell type.

Moreover, these findings suggest that neurodegeneration, classically viewed in KD as a secondary consequence of demyelination, could be reinterpreted as an independent process, that occurs following the accumulation of undigested material, as typically happen in many neurodegenerative disorders.[357] Furthermore, reasonably, neurons remain particularly vulnerable to accumulated waste material; given their post-mitotic status, in fact, the possibility of diluting accumulated aggregates is unlikely. Thus, to understand if the accumulation of ubiquitinated undigested material could stem from a defect in the final step of the autophagy pathway, we tested the colocalization of the autophagosomes with the lysosomes, finding that in both WT and TWI brains. Moreover, also p62 colocalizes with both autophagosomes and lysosomes. This indicates that p62 follows the correct steps of the autophagy flux, being first embedded into the autophagosome and subsequently into the lysosome, where predictably is metabolized by lysosomal enzymes. These pieces of evidence suggest that autophagy is dysregulated but not impaired in the TWI brain, thanks to the fact that p62-mediated delivery to the autolysosomes would occur. However, other *in vivo* imaging experiments could be necessary to assess if the amount of autolysosomes is different between healthy and affected mice. Hence, we can speculate that the protein accumulations found in the TWI tissues could be the outcome of a saturated autophagic flux. Specifically, GALC deficiency could lead to a lysosomal dysfunction, partially blocking and, consequently, saturating the autophagy flux. This, in turn, could prevent the degradation of all the p62-tagged material, culminating in aggregations.[99]

At this point, we decided to move *in vitro*, where a modulation of the autophagy pathway could be easily implemented. Firstly, we characterized

the same autophagy markers also in primary fibroblasts derived from both WT and TWI mice, treated or not with PSY. We demonstrated that PSY administration increased the expression of the autophagy markers LC3-II and p62 in both WT and TWI cells. Beclin-1, instead, appeared to be differently cleaved between WT and TWI cells, indicating a diverse regulation of the early steps of the autophagy machinery. Interestingly, by immunocytochemistry, we also highlighted a higher number of p62 tagged aggregates in the TWI untreated cells with respect to the WT. These data suggest a higher basal level of autophagy activation in the missing GALC condition, that is further stimulated in the presence of PSY. At this point, in order to asses if this difference could be due to the accumulation of endogenous PSY, we quantified it by HPLC/MS. Given the lack of PSY content in both WT and TWI cells, we hypothesized that, probably, some other molecular mechanism, not directly linked with PSY accumulation, should be considered. A hydrolase deficiency, in fact, as commonly happens in LSDs, cause a general imbalance in the lysosome homeostasis, preventing the development of an optimal environment for the correct recycling of all the waste material. Besides the already demonstrated PSY-induced autophagy activation (Section 5.2)[39], thus, also the GALC deficiency would be responsible for the increased autophagic flux in an at least partially PSY-independent manner. Subsequently, aiming to promote the clearance of the p62 tagged aggregates and thus rescue the WT phenotype, we tested in vitro two well-known autophagy inducers (RAP and RESV). Both the modulators, as expected, activated the autophagy flow in our cellular model. Furthermore, while RESV did not reduce the p62 intracellular levels, RAP rescued the WT levels of the total p62 expression in cells disturbed by the

presence of PSY. Moreover, the number of aggregates showed a significant reduction, partially restoring the WT condition. Given the presence of a wide recent literature showing the positive effect of autophagy induction on the clearance of accumulated cell aggregates in vitro[358,359,360], our results concerning the reduction of aggregates after the RAP-mediated autophagy induction is not surprising. Thus, our data strongly give the rationale to test autophagy induction in the TWI mouse to remove protein aggregates from the nervous system. Moreover, since RAP is already available as pharmaceutical preparations, in case of positive *in vivo* results, this therapy could also be readily applicable to humans for clinical testing.

Although additional studies are required to fully characterize the autophagy machinery in the TWI mice, this paper suggests autophagy dysregulation as a new aspect involved in the molecular pathogenesis of KD. This could at least partially explain the failure of the main therapeutic attempts in completely curing this LSD. Despite important advances made in the last years in research, in fact, the principally studied therapies (as BMT, gene/cell therapy and their combination) can increase life expectancy of the treated TWI mice, which, however, later suddenly die for unclear complications.[361,361] This late death may be due to additional pathological processes that proceed despite the GALC provision.

### 4.3.8 Material and methods

#### *Animals*

TWI heterozygous mice (TWI+/− C57BL6 mice; Jackson Labs), kindly donated by Dr. A. Biffi (San Raffaele Telethon Institute for Gene Therapy,

Milan, Italy), were used as breeder pairs to generate homozygous TWI mice (TWI−/−, elsewhere abbreviated as TWI for simplicity). Animals were maintained under standard housing conditions and used according to the protocols and ethical guidelines approved by the Ministry of Health (Permit Number: CBS-not. 0517; approved the 4/ 1/2018). For genotyping purpose, mice genomic DNA was extracted from clipped tails by Proteinase K digestion and subsequent genomic DNA extraction (EUROGOLD Tissue-DNA Mini Kit, Euroclone), as previously done by us[30,362]. The genetic status of each mouse was later determined from the genome analysis of the TWI mutation, as reported from Sakai and coworkers.[244] Both PND 20 and 30 TWI and WT animals were used for experiments, while the heterozygous littermates were retained for the colony maintenance. For immunohistochemistry experiments, 4 TWI and 4 WT mice were used (2 PND 20 and 2 PND 30 for each group). Surgical procedures for fresh organs extraction and for fixation were performed under urethane anaesthesia (Sigma Aldrich, 0.8 ml/hg), and all efforts were made to minimize mice suffering.

### *Immunohistochemistry*

TWI and WT deeply anesthetized mice were sacrificed by transcardial perfusion with PBS and subsequently with PFA 4%. After perfusion, the brains were stored at 4°C in a 4% PFA solution for at minimum 2 days. Consecutive coronal brain sections, 50 µm thick, were cut with a microtome (VT 1000 S, Leica BIOSYSTEM) at 0.50–2.10mm from bregma. Sections were maintained at 4°C in PBS until use. For the immunohistochemistry staining, sections were transferred in a 24 well cell culture plate (maximum of 3 sections per well) and incubated with blocking solution (3% bovine serum

albumin, 0.3% TritonX-100 in PBS; 1 ml per well) for 1 hour at RT. Then, the blocking solution was removed and the primary antibody mix (1% BSA, 0.3% TritonX-100, antibody at the optimal dilution and PBS to reach 1 ml) was added to the well and left overnight at 4° under gentle shaking. We used the following antibodies: anti-p62 (ab56416 Abcam, 1:100), anti-LC3 (ab48394 Abcam, 1:200), anti-NeuN (ab104225 Abcam, 1:1000), anti-GFAP (ab7260 Abcam, 1:1000), anti-MBP (ab980 Merck Millipore, 1:500), anti-LAMP-1 (sc-20,011 Santa Cruz, 1:200) and anti-LAMP-1 (21997–1-AP Proteintech, 1:200). These primary antibodies have been validated in previous studies.[39,363,364,365,366] Next morning, primary antibody solution was removed and 3 washes with 1ml of PBS were made (10 minutes each). Then, secondary antibody solution was added (BSA 1%, TritonX-100 0,3%, anti-mouse or anti-rabbit Alexa 647 1:1000, anti-mouse or anti-rabbit Alexa 488 1:000 and PBS to reach 1ml to- tal volume). After 2 hours of incubation at RT other 3 washes with PBS were made. Sections were then stained with a Hoechst solution for 1 minutes and then mounted on SUPERFROST Microscope Slides (Thermo Scientific) with Vectashield Antifade Mounting Medium (VECTOR LABORATORIES). Finally, slides were sealed and stored at 4 °C until confocal imaging.

### *Cell culture and treatments*

Adult mouse fibroblast cultures were obtained from WT and TWI ears, according to the protocol established in the laboratory of Dr. Evan Eichler (University of Washington, https://genome.ucsc.edu/ENCODE/protocols/cell/mouse/Fibroblast_Stam_protocol.pdf) from mice that were less than six months old. Briefly, after anaesthesia, mouse ears were extracted, washed with sterile water and cut into small pieces. All pieces

were than collected in an Eppendorf tube and added with collagenase XI (C7657–100mg; Sigma Aldrich) diluted in high glucose DMEM (approximately 2.5 mg of collagenase –320 CDU- for 1 mouse). After 2 hours of incubation at 37°C the Eppendorf tube was centrifuged for 5 minutes at 200 g, the supernatant was discarded and the pellet was washed with 2 ml of PBS and centrifuged again discarding the supernatant. Trypsin-EDTA 0.05% (59418C-100ML; Thermo Fisher Scientific) was then added to the tube and left 45 minutes at 37°C. The tube was than centrifuged and the pellet was resuspended in the complete DMEM [high glucose DMEM supplemented with 10% of heat-inactivated FCS, 4 mM l-glutamine, 1% MEM Nonessential Amino Acids and 1% penicillin/streptomycin; all products were from GIBCO-Life Technologies)]. Obtained cells were thus divided pipetting up and down with a syringe, plated in a 60 mm cell petri and incubated at 37°C in a humidified atmosphere containing 5% $CO_2$. The day after, cells were washed and medium was replaced. After reaching confluence (approximately 3–4 days), cells (p0) were washed with 1 ml of PBS and split with a ratio of 1:2. Cells were cultured and used for experiments within the 10th passage in vitro. For treatments, WT and TWI fibroblast primary cells were plated in standard 6 well cell plates (300000 cell per well, for the western blot experiments), in 60 mm cell plates (800000 cell, for PSY quantification experiments) or in 12 mm WillCo dishes (70000 cell, for immunocytochemistry). After 24 hours, depending on the treatment, cells were pretreated with RAP 100 nM (tlrl-rap 5 mg; InvivoGen) or RESV 100 μM (tlrl-resv 100mg; InvivoGen) for 1 hour and then administered with PSY 100 μM (P9256-1MG; Sigma Aldrich). For selected experiments, cells were also treated with bafilomycin (BAF; B1793-

2UG; Sigma Aldrich) 200 nM for 4 hours before cell lysis. PSY, RAP, BAF, and RESV were dissolved in DMSO. Control cultures received the same quantity of DMSO, which never exceeded 0.6% v/v.

### *Immunocytochemistry*

WT and TWI fibroblasts were grown and fixed for 20 minutes with 4% formaldehyde/4% sucrose in PBS at RT. Then, fixed cells were washed 3 times with PBS (10 minutes for each wash). After washes, cells were incubated with primary antibodies (anti-LC3 and anti-p62, see par. Immuno- histochemistry) diluted in the GDB buffer (0.2% BSA, 0.5%Triton, 0.8 M NaCl, Phosphate buffer 30 mM with pH 7.4).[177] After an overnight incubation at 4 °C in a humid chamber, samples plates were washed 3 times in PBS and the secondary antibodies mix was added [anti-rabbit alexa 555, anti-mouse alexa 488 and alexa Fluor Phalloidin 647 (A-31572, A-11029, A-22287; Thermo Fisher Scientific), diluted, respectively, 1:1000, 1:1000 and 1:40 in the GDB buffer]. After 1,5 hour of incubation at RT, 3 washes with PBS and 1 with water (to remove salt) were performed. After drying, Vectashield mounting medium with DAPI (F6057-20ML; Sigma Aldrich) was added and plates were stored at 4 °C until usage.

### *Confocal microscopy and images analysis*

Immunostained cells and brain sections were imaged with a laser scanning confocal microscope TCS SP2 (Leica Microsystems) equipped with a 63× oil objective and interfaced with UV, Ar, HeNe and He lasers for excitation at 405, 488, 561 and 633nm, respectively. Each reported confocal image was obtained from a z-series (stack depth was maximum 10 μm with steps of 0.5–1 μm for cells and maximum 20–30 μm with steps of 2 μm for brain

sections). The resulting z-stack was processed in ImageJ (NIH; RRID:SCR_003070) into a single image by using "z-project" and "Max intensity" options. The processed z-stack was than merged using the "Merge channel options". For the quantitative analysis of the p62 aggregates and autophagosomes, every image was thresholded using the "threshold" tool (with a threshold of 100 for the p62 aggregates and 180 for the autophagosomes); subsequently, binary images were inverted, and the number of particles was analysed by the "Analyze Particles" plugin, by setting "size (micron$^2$)"=from 1 to infinity, and "circularity"=from 0.00 to 1.00. For the brain, particles were analysed on images randomly acquired on whole slices (see the par. Immunohistochemistry for details). For cell experiments, particles were analysed for every single cell: the area covered by each cell analysed was manually selected as a ROI on bright-field images (merged with the DAPI signal for tissues and with both the DAPI and the phalloidin signals for cells) and then the ROI was applied to the correspondent p62 positive binary image for the particles analysis. Colocalization was evaluated calculating Mander's coefficient with the JACoP plugin in ImageJ as previously done.[164] For each graph, images were taken with the same magnification. The confocal settings were kept the same, with pinhole aperture set at 1.0 Airy level and 1024 × 1024 pixels image format for all the experiments.

### *Western Blotting*

Western blot was carried out with cultured cells and mouse tissues. For *in vitro* experiments, cells were cultured on standard 6 well plates, treated as previously described, and then lysed on ice with RIPA buffer (R0278-50ML; Sigma Aldrich) containing a protease and phosphatase inhibitors cocktail

[cOmplete (4693116001) and PhosSTOP (4906845001); Roche Diagnostics]. Cell lysates were sonicated (for 4 s at 12 μm of intensity) and after centrifugation (15000 g for 25 min, 4°C) tested for protein concentration by the micro-BCA protein assay kit (23225; Thermo Scientific Pierce). The samples were boiled in Laemli buffer containing β-mercaptoethanol (5% final concentration) for 5 min, centrifuged at RT and the supernatants were finally used for gel electrophoresis (SDS-PAGE) or kept at −80°C until use. For mouse tissues the extracted whole brains and sciatic nerves were lysed on ice with the already mentioned complete RIPA buffer, and homogenized with pestels in 1.5ml microcentrifuge tubes. Homogenized tissues were then centrifuged (15000 g for 30 min, at 4°C) and the recovered supernatants were tested for protein content and processed as described above for cell lysates. Samples (6 μg for cell lysates and 30 μg for tissue lysates) were resolved by SDS-PAGE using Gel Criterion XT-Precast polyacrylamide gel 4–12% Bis-Tris (3,450,123; Bio-Rad) and subsequently transferred to nitrocellulose membranes, as previously described.[39] Immunodetection was performed with the following antibodies: anti-LC3 (1:1000), anti-p62 (1:800; see above for the codes) and anti-Beclin-1 (ab114071; Abcam, 1:1000). On the following day, blots were incubated with the corresponding peroxidase-linked secondary antibodies (goat anti-rabbit or mouse IgG-HRP conjugate; 170-6516 and 170-6515; Biorad, 1:2.500), and after incubation membranes were developed with Clarity enhanced chemiluminescent substrates (1,705,061; Bio-Rad). The chemiluminescent signal was acquired with an Image-QUANT LAS400 scanner (GE Healthcare Life Science), and the density of immunoreactive bands was quantified in ImageJ. Membranes were than incubated with a

stripping buffer containing β-mercaptoethanol and re-incubated as above with the anti-tubulin (T6074; Sigma Aldrich; 1:3000) or anti-GADPH (G8795; Sigma Aldrich, 1:3000) for 1 hour and then with the corresponding secondary antibodies. Secondary antibody incubation was thus made and images were acquired as described for the primary antibodies. LC3, p62 and Beclin-1 results were normalized to the tubulin content for brain lysates and to GADPH content for fibroblasts, and reported as % of the WT-PND 20 or WT untreated condition respectively.

### *PSY quantification*

For lipid extraction, WT and TWI cells were plated on standard 60 mm plates. After 48 hours of incubation, cells were washed with cold PBS and lysed on ice with 300 µl/well of RIPA buffer containing a protease and phosphatase inhibitors cocktail (as above). For each sample, a mixture was prepared combining the cell lysate, N,N-dimethylsphingosine 1.250 µM (N,N-DMS, the selected internal standard for HPLC/MS-MS; SML0311-5MG; Sigma-Aldrich)[367], and MilliQ water. Then a chloroform/methanol solution (2:1) was added. Samples were vortexed, left at RT for 10 min, and supplemented with NaCl 0.9% w/v in Milli-Q water. The biphasic mixture was centrifuged at 800 g for 30 min, and the lower layer was collected and evaporated to dryness under vacuum at 30°C. The residue was dissolved in 50 µl of methanol/formic acid 100/0.1 and processed for HPLC/MS. HPLC/MS quantitation was performed on a Shimadzu Nexera UHPLC chromatograph interfaced with a 5500 QTRAP mass spectrometer (AB SCIEX). HPLC analyses were performed on a Phenomenex Kinetex C8 3× 150mm column (particle size 4 µm), using water/methanol/isopropanol/formic acid 40/55/5/0.1 (A) and

methanol/isopropanol/formic acid 95/5/0.1 (B) as mobile phases at 0.4ml/min flow (column temperature=45°C). Runs were performed under a 10 minutes linear gradient from 65 to 100% of solvent B, followed by a 5 minutes purge step at 100% of B and by a 5 minutes re-equilibration step to the starting conditions. MRM analyses were performed under the following conditions: ion spray voltage: 5000V, source temperature 350°C, declustering potential 50V, collision energy variable (see value in parentheses), ion source gas 20 l/min, curtain gas: 25l/min. The following transitions were monitored (acquisition time 150msec/transition): i) N,N-dimethylsphingosine (Q1/ Q3, m/z, CE in parenthesis): 328.2/310.2 (26V); 328.2/280.2 (32V); 328.2/110.2 (42V); ii) PSY (Q1/Q3, m/z, CE in parenthesis): 462.5/ 444 (25 V); 462.5/282 (30 V);462.5/264 (27 V); 462.5/252 (39 V). Transitions 328.2/310.2 (N,N- dimethylsphingosine) and 462.5/282 (PSY) were used for quantitation purposes.

### *Statistical analysis*

If not differently specified, data are reported as mean±SEM obtained from at least three independent experiments (in figure legends, "N" indicates the number of experiments performed). Data were statistically analysed by using Prism 6.00 (GraphPad Software, San Diego, CA; RRID:SCR_002798). For parametric data, Student's t-test (unpaired, two-tailed) or one-way ANOVA (Tukey's or Dunnett's multiple-comparisons test) was used; the mean values obtained in each repeated experiment were assumed to be normally distributed about the true mean. Statistical significance refers to results for which $P < 0.05$ was obtained.

# Chapter 5: From GALC deficiency to Krabbe disease pathogenesis: still an open issue

## 5.1 New methods applied to the case of Krabbe disease

KD pathogenesis is still an open question, being the link between GALC deficiency, demyelination and neurodegeneration not fully understood yet. Thus, contribution of innovative strategies and advanced multidisciplinary technologies in this field are auspicable. In this Chapter, I present two studies in which I collaborated, coordinated by the group of Dr. McDonnel of the Fondazione Pisana per la Scienza Onlus (FPS) and Prof. Cardarelli of our institute. In section 5.2 a quantitative microproteomics based characterization of the CNS and PNS of the TWI mice is presented. In section 5.3 I report on an advanced 3D orbital tracking method used to capture metabolism-dependent solvent dynamics in the lumen of trafficking KD lysosomes.

## 5.2 Quantitative Microproteomics Based Characterization of the Central and Peripheral Nervous System of a Mouse Model of Krabbe Disease

*The experiments presented in this Section have been published after peer-reviewing on the journal Molecular & Cellular Proteomics 18(6), 1227-1241. Co-authors of the work are: Pellegrini D, Del Grosso A, Angella L, Giordano N, Dilillo, M, Tonazzini I, Caleo M, Cecchini M, McDonnell, LA. Role of authors: study concept and design: DP, ADG, LMD, MC. Acquisition of data: All authors. Analysis and interpretation of data: All authors. Drafting of the manuscript: All authors. Statistical analysis: DP, ADG, LMD, MC. Obtained funding: LMD, MC. Study supervision: LMD.*

*I, in particular, provided mice brain and sciatic nerves for microproteomics experiments, performed western blots and contributed to the discussion of the data and to the drafting of the Material and Methods Section.*

### 5.2.1 Introduction

Metabolic profiling of the TWI mouse has identified metabolic pathways influenced by KD, revealing decreased levels of long chain fatty acids, increased levels of short chain fatty acids and alteration of several metabolites involved in mitochondrial fuel selection, energy production, inflammation, neurotransmitter metabolism and osmotic regulation.[368,369,370,371] However, the proteome changes associated with KD and the pathogenic mechanisms are still not well understood. Mass-spectrometry based proteomics has become an indispensable tool for molecular biology and clinical research because of its ability to identify and quantify thousands of proteins.[372,373,374,] When combined with laser capture microdissection (LCM), MS-based proteomics may be used to investigate disease-associated changes in the proteome of specific tissue regions or cell

populations. Such specificity is essential because different anatomical regions in the brain have distinct and diverse functions, and may behave differently under pathological conditions.[375] Strict anatomical/cellular specification usually yields micrograms or submicrograms amounts of proteins[376,377] , and thus ultrasensitive microproteomics protocols are required to analyze these small sample amounts while maintaining high proteome coverage.[378,379,380] MS-based proteomics has been used to study several LSDs, including Niemann-Pick type C disease[381,382,383], Gaucher disease[384,385] and Fabry disease[386,387]. Mass spectrometry has been extensively used to quantify PSY in several tissues and cells used to study KD, including the TWI mouse brain[58], spinal cord[388], serum[367], newborn dried blood spots from infants[389] and a cell model of KD derived from the TWI mouse.[43] However, to date an in-depth proteome characterization of the CNS and PNS during KD progression is lacking. Here we report the first in-depth characterization of the CNS and PNS of the TWI mouse. 10-plex Tandem Mass Tags (TMT) based experiments were used to compare the proteomes of the corpus callosum, motor cortex and sciatic nerves of littermate homozygous TWI and WT mice. The corpus callosum represents one of the main regions of the brain showing extensive demyelination in KD patients[390,390,391,392] and in the TWI mouse[104]. The motor cortex was selected because in humans and rodents KD leads to muscle weakness, spasticity and paralysis[353]. In order to investigate the effects of KD on the PNS we chose the sciatic nerves as they show marked demyelination, decreased number of axons and axonopathy in the TWI mouse[393,394]. Figure 5.1 shows an overview of the experimental approach.

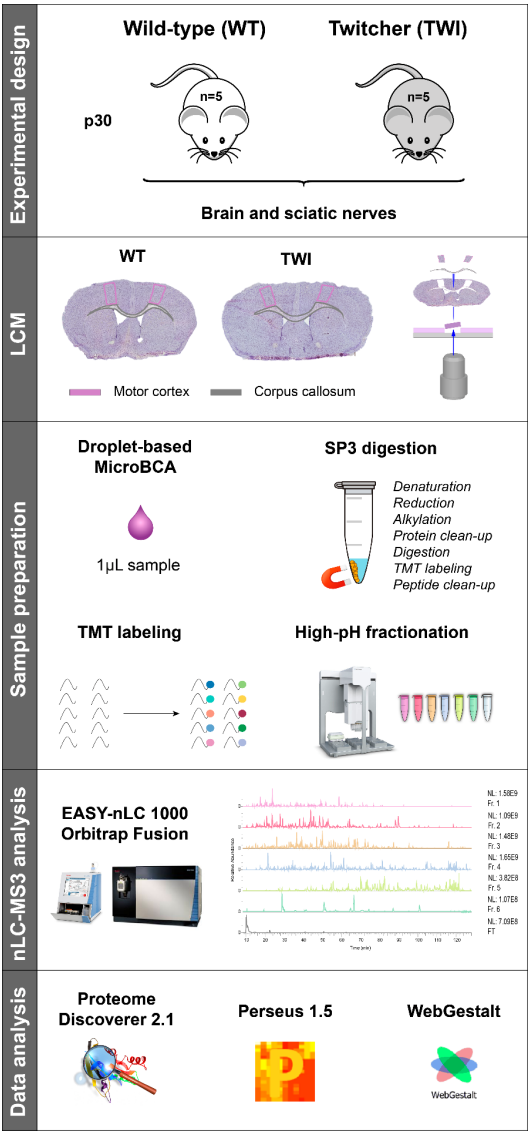


**Figure 5.1.** Ultrasensitive microproteomic workflow for the characterization of CNS and PNS of the TWI mouse. The brains and sciatic nerves were collected from five TWI and five WT mice at PND 30. Laser capture microdissection was used to isolate ROIs from the corpus callosum and

motor cortex. Proteins were extracted from the corpus callosum, motor cortex and sciatic nerves, quantified with microBCA assay and digested with the SP3 protocol. Peptides from each dataset were pooled and labeled with TMT 10-plex reagents. Labeled peptides were purified and fractionated on a RPS cartridge. MS3 spectra were acquired on an Orbitrap Fusion mass spectrometer and proteins were identified with Proteome Discoverer 2.1. Data and statistical analysis were performed with Perseus and WebGestalt softwares. The proteomic data were validated by western blot analysis on the sciatic nerves extracts.

### 5.2.2 Tissue sampling and protein extraction

Laser capture microdissection (LCM) was used to isolate and excise small ROIs from the corpus callosum and the motor cortex of the mouse brains. The brain morphology was found to be different between WT and TWI mice (Fig. 5.2). The corpus callosum of TWI mice exhibited a greater cell density and reduced white matter compared to WT mice. This morphological feature, due to demyelination of the corpus callosum, is consistent with the known histopathology of the TWI mouse brain.[104]

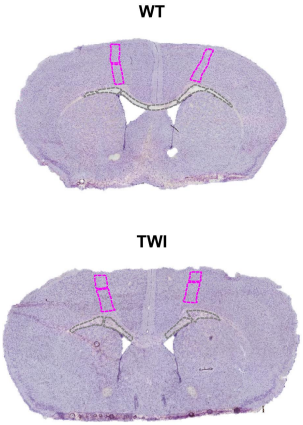


**Figure 5.2.** Representative coronal brain sections stained with hematoxylin of a WT and TWI mouse. Violet dashed lines indicate ROIs isolated from the motor cortex, grey dashed lines indicate ROIs isolated from the corpus callosum.

The motor cortex did not show any gross morphological difference between TWI and WT mice. For each mouse the small, localized regions of

the corpus callosum and motor cortex were isolated from sequential tissue sections to ensure approximately 2 µg of protein was available from each region of each mouse. The corpus callosum ROI was isolated from 4-8 brain sections per animal (total area of 2.6-3.6 $mm^2$) and the motor cortex ROI was isolated from 5-10 sections (total area of 2.5-4.2 $mm^2$). The protein amount extracted from each sample was estimated using a modified microBCA assay performed on a 1 µL aliquot.[378] This assay allowed us to quantify the protein content of each sample using only 5% of its total volume. We extracted 1.5-2.4 µg of proteins from the corpus callosum samples and 2.5-4.2 µg from the motor cortex samples. Table 5.1 summarizes the number of tissue sections, ROI areas and protein amounts extracted from the corpus callosum and motor cortex.

| Brain regions | # sections | ROIs area / $mm^2$ | µg proteins |
|---|---|---|---|
| **Corpus callosum** | 4 - 8 | 2.6 - 3.6 | 1.5 - 2.4 |
| **Motor cortex** | 5 - 10 | 3.3 - 5.1 | 2.5 - 4.2 |

**Table 5.1**. Summary of the number of tissue sections, ROIs areas and protein amounts extracted from the corpus callosum and motor cortex microdissected samples.

### 5.2.3 Proteome profiling

The quantitative microproteomics workflow combined SP3 protein digestion[378,379], in-solution TMT labeling and high-pH fractionation followed by LC-MS3. The corpus callosum and motor cortex analyses used the maximum protein amount available from all mice for each microdissected region (1.5 µg for the corpus callosum and 2.5 µg for the motor cortex). The analysis of the sciatic nerve was performed on 3 µg aliquots of the tissue extracts.

We assessed TMT labeling efficiency on the three datasets in terms of the percentage of PSMs with the TMT modification at lysine and N-termini residues (Fig. 5.3 A). The labeling efficiency was greater than 96% for all the datasets for both lysine and N-terminal residues. We also assessed the over labeling rate (TMT labeling of serine, threonine, histidine and tyrosine), figure 5.3 B shows a bar graph indicating the percentage of PSMs with a TMT modification at serine, threonine, histidine and tyrosine residues. The total over labeling rate was less than 5% for all datasets. The MS3 analyses of the high-pH fractionated TMT-labeled samples resulted in the identification of 3699, 4394 and 3388 protein groups from the corpus callosum, motor cortex and sciatic nerve isolates, respectively. Figure 5.2 C summarizes the number of identified protein groups, peptides PSMs and MS/MS spectra.

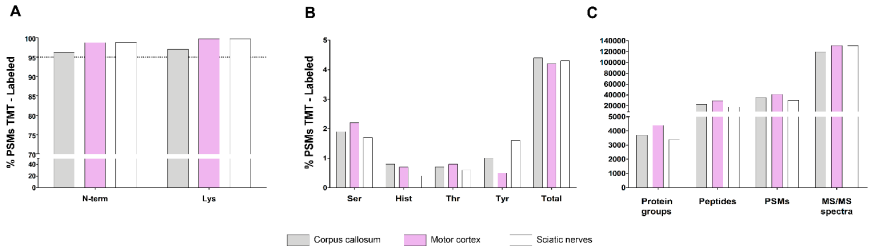


**Figure 5.3. (A)** TMT labeling efficiency expressed as the percentage of PSMs with the TMT modification at N-termini and lysine residues. **(B)** Over-labeling rate expressed as the percentage of PSMS with the TMT modification at serine, histidine, threonine and tyrosine residues. **(C)** Protein identification metrics: number of identified protein groups, peptides, PSMs and acquired MS/MS spectra. Grey, violet and white bars refer to the corpus callosum, motor cortex and sciatic nerves datasets.

For the determination of group-wise relative protein quantification the datasets were filtered such that each protein needed to be quantified in at least four TWI and four WT mice. This filtering reduced the number of

protein groups to 2607, 3579 and 2350 for the corpus callosum, motor cortex and sciatic nerve, respectively. A histogram of the mass errors of the identified peptides can be found in figure 5.4, which demonstrates that > 95% of all peptide identifications were within 2 ppm, and that > 99.9% were within 5 ppm.

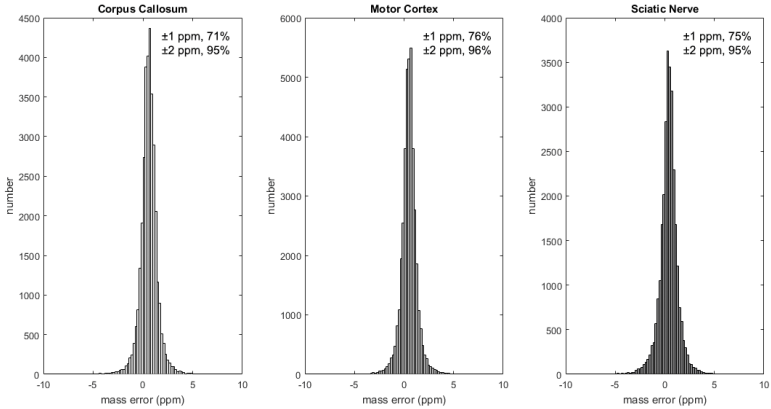


**Figure 5.4.** Histograms of mass errors (ppm) for the peptides identified from the extracts of the corpus callosum, motor cortex, and sciatic nerve datasets, demonstrating that >95% of the identifications are within 2 ppm.

### 5.2.4 Proteome changes in the CNS and PNS of the Twitcher mouse

Principal Component Analysis (PCA) was performed on the filtered, quantitative data matrices to summarize differences in protein expression between TWI and WT mice. The PCA score plot revealed that one mouse, originally considered a TWI mouse, fell into the cluster of WT mice for each tissue region (Fig. 5.5). The incorrect assignment of this mouse was further indicated by a GALC enzymatic activity assay performed on the sciatic nerve extract, which showed a GALC activity comparable to that of WT mice. The

initial genotyping of the littermate mice is shown in figure 5.6 A, which clearly indicates the homozygous TWI and WT mice selected for the experiment. These results indicated a labeling error with one of the TWI mice selected for the experiment; a subsequent genotyping of the suspect TWI-annotated mouse confirmed its status as a WT mouse (Fig. 5.6). Thus, this mouse was considered as a WT in the subsequent statistical analysis. In the PCA score plots of the corpus callosum and the sciatic nerve datasets (Fig. 5.5 A, C) the same WT mouse was well separated by PC1 (thus maximum variance in the data) from both the TWI and WT clusters.

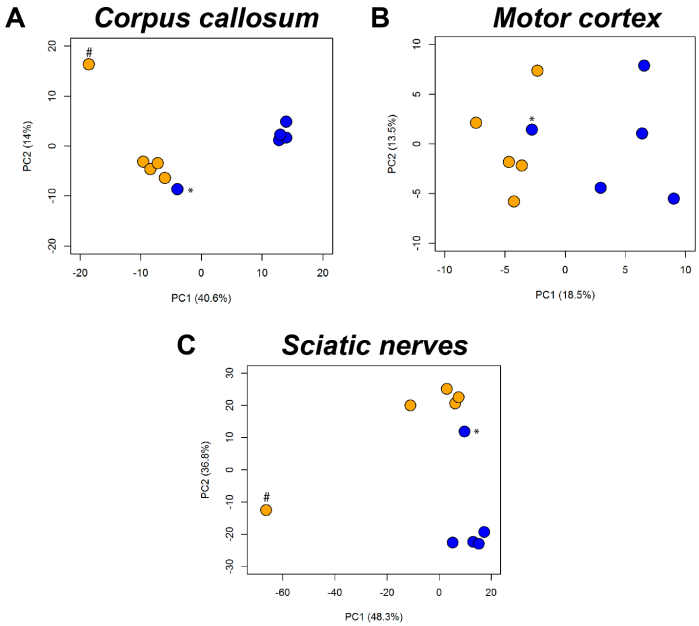


**Figure 5.6.** Principal Component Analysis performed on the protein expression values, using all the samples for the corpus callosum **(A)**, motor cortex **(B)** and sciatic nerve **(C)** datasets. Blue circles indicate TWI mice, orange circles indicate WT mice. * indicates the mouse originally designated as TWI, # indicates the WT mouse considered as an outlier in the corpus callosum and motor cortex dataset.

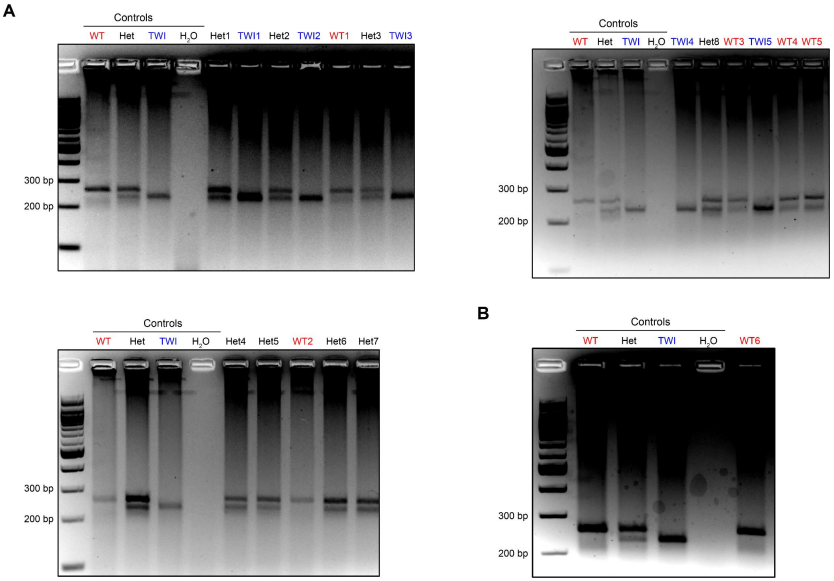


**Figure 5.6.** Genotyping of the Galc mutation. **(A)** Gel electrophoresis of the littermate mice, indicating the five homozygous WT and five homozygous TWI mice selected for proteomics analysis. Heterozygous animals were not included in the experimental design. **(B)** Gel electrophoresis of the WT mouse mislabeled as TWI, clearly confirming its WT genotype. The genotype was determined by PCR amplification of a genomic DNA fragment in intron 16 of the GALC gene using forward and reverse primers, 5'-CCACTCCCATCCTTTCTCC-3' and 5'-GGCCATCACATTCGTCAGA-3' respectively.

We repeated the TMT experiment on another aliquot of the sciatic nerve extracts, from the same cohort of mice, and the same mouse remained an outlier and was thus excluded from subsequent statistical analysis. Once the outlier was removed the TWI and WT mice were well separated as two distinct clusters, separated by PC1, for all tissue regions (Fig. 5.7 A-C). The percentage of variation explained by PC1 was 42.3%, 18.5%, and 68% for the corpus callosum, motor cortex, and sciatic nerve datasets, respectively.

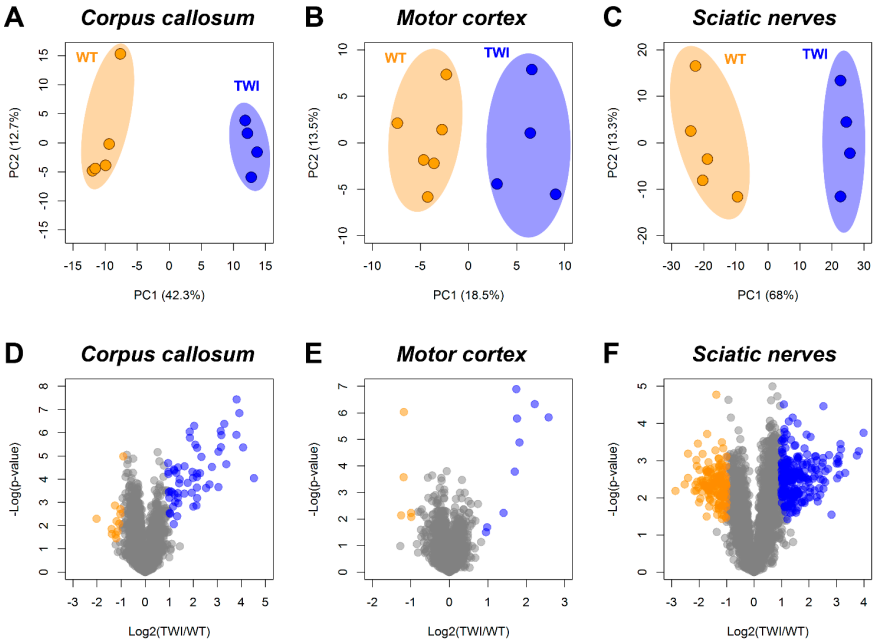


**Figure 5.7.** Principal Component Analysis performed on the filtered protein groups expression values for the corpus callosum **(A)**, motor cortex **(B)**, and sciatic nerves **(C)** datasets. Blue circles indicate TWI mice, orange circles indicate WT mice. Volcano plots for the corpus callosu motor cortex **(D, E)**, and sciatic nerves **(F)** datasets. Grey circles indicate non significant protein groups (log2(fold change) < 1 and >-1, FDR > 0.01). Blue circles indicate protein groups significantly up-regulated in the TWI mice (log2(fold change) >1, FDR < 0.01). Orange circles indicate protein groups significantly down-regulated in the TWI mice (log2(fold change) < -1, FDR < 0.01).

Significantly different protein levels between TWI and WT mice for the three datasets were calculated using a two-sided Student's *t*-test with FDR correction for multiple testing. Figure 5.7 D-F show the volcano plots for the datasets from the three tissue regions. We found 75, 14 and 387 protein groups differentially expressed in the corpus callosum, motor cortex and sciatic nerves of TWI mice, respectively. Specifically, in the corpus callosum

63 protein groups were significantly up-regulated and 12 down-regulated in TWI mice. In the motor cortex 9 protein groups were significantly up-regulated and 5 down-regulated in TWI mice. The sciatic nerve dataset exhibited the largest difference in protein expression, with 16% of the total number of quantified protein groups being differentially expressed (244 protein groups significantly up-regulated in TWI mice and 143 down-regulated).

Table 5.2 summarizes the number of protein groups identified, quantified and significantly different between TWI and WT mice for the three datasets. The total number of deregulated protein groups was 75, 14 and 386 for the corpus callosum, motor cortex and sciatic nerve datasets, respectively.

| # Protein groups | Corpus callosum | Motor cortex | Sciatic nerve |
|---|---|---|---|
| **Identified** | 3699 | 4394 | 3388 |
| **Quantified** | 2607 | 3579 | 2350 |
| **Up-regulated in TWI** | 63 | 9 | 243 |
| **Down-regulated in TWI** | 12 | 5 | 143 |

**Table 5.2.** Summary of the number of protein groups identified, quantified, up-regulated and down-regulated in TWI mice for the corpus callous, motor cortex and sciatic nerves datasets.

### 5.2.5 Gene Ontology Enrichment Analysis

Gene Ontology (GO) analysis was performed to understand which $G_O$ terms are represented in the differentially expressed proteins. We performed an Overrepresentation Enrichment Analysis (ORA) using WebGestalt on the corpus callosum and sciatic nerve datasets (the small number of differentially expressed proteins in the motor cortex dataset was

insufficient for the analysis). Figure 5.8 shows the enriched $G_0$ terms for both datasets, in which the bubble graphs show the number of differentially expressed proteins contributing to the terms and the FDR value.

Most of the enriched biological processes in the TWI mice are related to inflammatory and defense response. In the sciatic nerve dataset we also found down regulation of processes consistent with axon demyelination (reduced axon development, reduced neuron ensheathment, and reduced peripheral nervous system development) as well as reduced microtubule cytoskeleton organization. KEGG pathways upregulated in the TWI mice included those related to inflammatory response (e.g. antigen processing and presentation, leukocyte transendothelial migration, and complement pathway) and to phagocytosis and lysosomes. The glycosaminoglycan degradation pathway, a subclass of the lysosome pathway, was also found to be up-regulated in the TWI mice.

A cellular component ontology analysis was performed to investigate the subcellular localization of the deregulated proteins because Golgi apparatus, endosomes and lysosomes have previously been demonstrated to play critical roles in LSD's.[383,135,252] Figure 5.9 demonstrates that a significant number of the differentially regulated proteins in TWI mice were linked to these organelles.

**A**

***Corpus callosum***
***Biological processes***

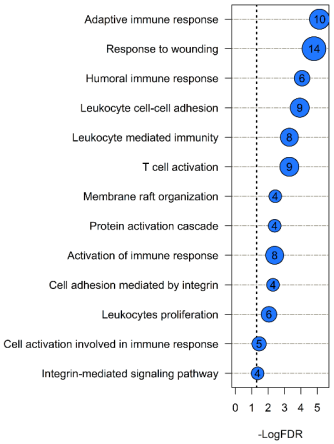


**B**

***Corpus callosum***
***KEGG Pathways***

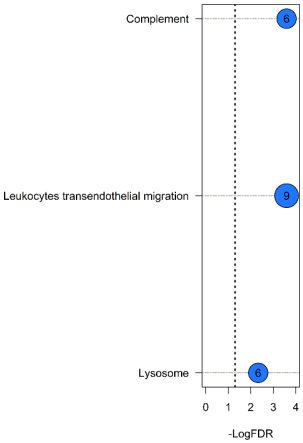


**C**

***Sciatic nerve***
***Biological processes***

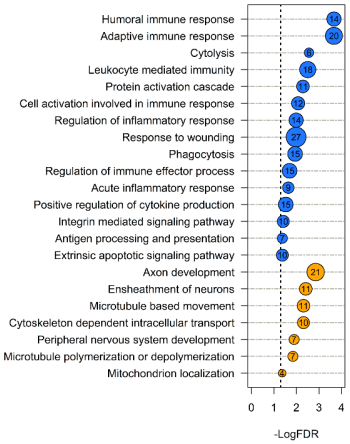


**D**

***Sciatic nerve***
***KEGG Pathways***

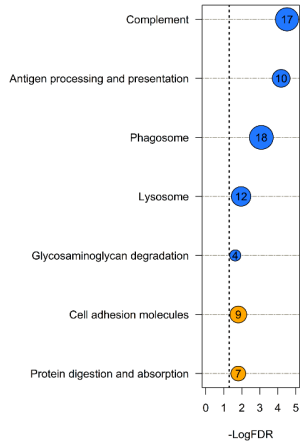

**Figure 5.8.** Gene ontology Overrepresentation Enrichment Analysis (ORA) performed on the protein groups that are significantly up- or down-regulated between TWI and WT mice for the corpus callosum and sciatic nerves datasets. **(A)** Biological processes enriched in the corpus callosum dataset, **(B)** KEGG pathways enriched in the corpus callosum dataset, **(C)** biological processes enriched in the sciatic nerves dataset, **(D)** KEGG pathways enriched in the sciatic nerves dataset. The number in the bubble indicates the number of protein groups in the experimental dataset that matched with the corresponding $G_0$ term. Blue and orange bubbles indicate biological processes/pathways enriched in the protein groups that are significantly up- and down-regulated in TWI mice, respectively.

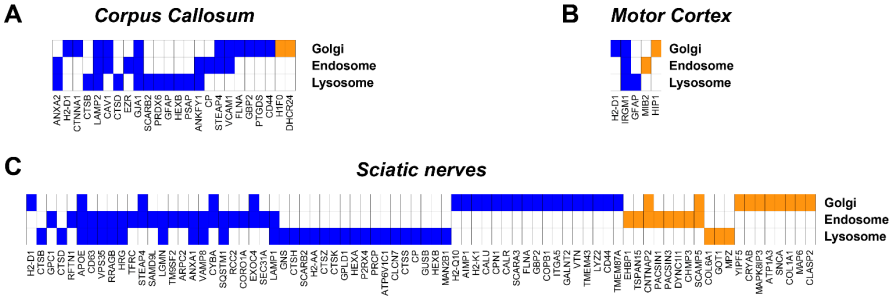


**Figure 5.9.** $G_0$-Cellular component analysis. List of deregulated protein groups that are localized on Golgi apparatus, endosomes and lysosomes for the corpus callosum **(A)**, motor cortex **(B)**, and sciatic nerves **(C)** datasets. Blue and orange indicate protein groups that are significantly up- and down-regulated in TWI mice, respectively.

### 5.2.6 Validation by western blot analysis

A set of the differentially expressed proteins, including proteins related to lysosomes, autophagy and PSY synthesis, were selected for validation by western blot analysis. These validation experiments were performed using sciatic nerve extracts. Figure 5.10 shows the western blots of the seven selected proteins. The relative expression of all the proteins selected for validation by western blot analysis was in agreement with the LC-MS/MS data. ATG16L1 and UGT8 were down-regulated in the TWI mice. ATG16L1 belongs to the autophagy-related proteins and plays a crucial role in the

autophagy pathway as part of a complex with autophagy proteins ATG5 and ATG12.[395] Down-regulation of ATG16L1 may indicate a reduced efficiency of autophagosome assembly. UGT8 (or CTG) is the enzyme that catalyzes the synthesis of psychosine.[135] The down-regulation of UGT8 in the TWI mice may indicate a homeostatic response of the cell to the accumulation of psychosine. LAMP1, HEXB, CTSB and VAMP8 are lysosomal proteins that were up-regulated in the TWI mice. Deregulation of the lysosomal pathway is a general hallmark of all LSD's, including KD.[396,396] p62 (also known SQTM1) is an autophagy substrate and a marker used to study autophagic flux (See Section 5 for details about p62).[397] p62 was detected at higher levels in the TWI mice, in accordance with data showed in Section 5.3.[41]

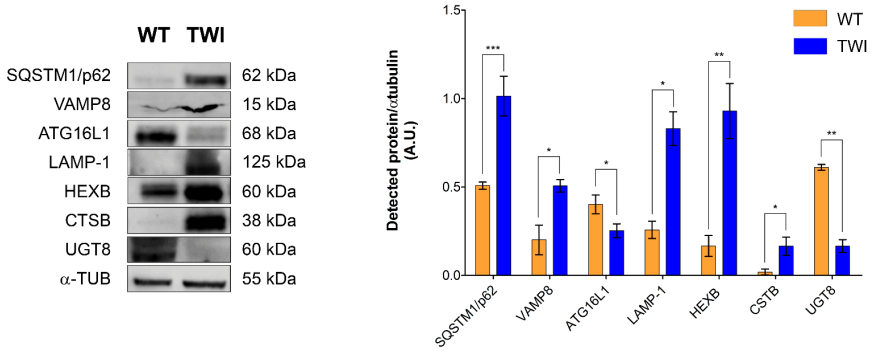


**Figure 5.10.** Western blots showing the expression levels of SQSTM1, VAMP8, ATG16L1, LAMP-1, HEXB, CTSB and UGT8 in the sciatic nerve extracts of WT mice compared to TWI mice. Results were normalized to α-tubulin. The WT mice pooled sample and the TWI mice pooled sample were prepared by combining the sciatic nerves extracts of three WT and three TWI mice, respectively. The western blot analysis was performed in technical triplicate on the pooled samples. *** = P < 0.001, ** = P < 0.01, * P = < 0.05; Student's *t*-test. Blue and orange bars indicate TWI and WT mice, respectively. Error bars indicate standard deviation.

### 5.2.7 Concluding remarks

This work represents the first mass spectrometry-based in-depth characterization of the TWI mouse proteome to study changes associated with KD. 10-plex TMT experiments were used to compare the proteomes of the corpus callosum, motor cortex and sciatic nerves of five TWI and five WT control mice. LCM was combined with a microproteomics approach[378] to focus the analysis on localized anatomical regions from individual animals; high pH fractionation[398] and multinotch MS3 was used to ensure high proteome coverage and higher relative quantitation precision[373,399], and together enabled the relative quantitation of 3000 to 4000 protein groups from the microdissected samples. Statistical analysis highlighted 75, 14 and 386 protein groups differentially expressed between TWI and WT mice in the corpus callosum, motor cortex and sciatic nerves, respectively. The expression levels of several proteins were further validated by western blot analysis of the sciatic nerve extracts. The roles of the differentially expressed proteins in the CNS and PNS of the TWI mouse are discussed below.

#### *Proteome changes in the Peripheral Nervous System of the Twitcher mouse*

The analysis of the sciatic nerve extracts showed an activation of inflammatory response in the TWI mouse. Gene ontology analysis, figure 5.8, revealed an up-regulation of several biological processes and pathways related to immune response, cytokines production, antigen processing and presentation pathway, complement and phagosome pathways, indicating a marked inflammation of the peripheral nervous system.

Seventeen proteins belonging to the complement pathway were up-regulated in the TWI mouse (A2M, C1QA, C1QB, C3, C8A, C8B, CFB, F2, FGA,

FGB, FGG, ITGAM, ITGB2, KNG1, PLG, SERPINF2, VTN). CD55, an inhibitor of complement activation, was also found to be significantly down-regulated in the TWI mouse, indicating an activation of the complement pathway. Moreover, the up-regulation of several macrophage markers (*e.g.* CSF1R, MPEG1, MSR1) suggests macrophage infiltration of the sciatic nerves. Complement activation has been shown to be involved in the initiation and/or progression of inflammation by attracting macrophages, stimulation of phagocytosis and tissue injury in diseases of both CNS and PNS, including Alzheimer's[400] and Gaucher disease[401]. The observed up-regulation of 18 proteins involved in phagocytosis (*e.g.* CORO1A, CALR and FCGR1) may be an effect of complement activation.

Neuroinflammation is a well-known feature of KD that was believed to be a consequence of demyelination.[402] Recent studies showed a neuroimmune activation in murine models of KD several weeks before symptoms onset, suggesting that neuroinflammation precedes demyelination.[84] The finding that complement proteins are up-regulated in TWI mice may be of interest since complement activation has been shown to be involved in progressive demyelination of the PNS in Guillain-Barré syndrome[403] and Miller Fisher syndrome[177], and to induce tissue inflammation in Gaucher disease.[401] In addition, 39 proteins associated with the PNS, axon development and neuron ensheathment (*e.g.* MAG, MPZ, MPZL1, JAM3, NEFL, NCAM2, STXBP1) were found to be down-regulated in the TWI mouse, indicating neuron damage and extensive demyelination.

Our data show a marked neuroinflammation, demyelination and complement up-regulation at the terminal stage of the disease (the mice were sacrificed at PND 30 and the mean lifespan of the TWI mouse is 35-40

days). Future work will focus on younger TWI mice in order to address the role of complement activation in the pathogenesis of KD. The lysosome pathway was found to be up-regulated in the TWI mouse (Fig. 5.8). Defective lysosomal function is a general hallmark of LSD's and leads to an accumulation of nondegraded macromolecules and metabolites.[135] We found 29 lysosomal proteins up-regulated in the TWI mouse (Fig. 5.9), including lysosome membrane proteins (*e.g.* LAMP1 and VAMP8), hydrolases (*e.g.* CTSB, CTSD) and vacuolar H+-ATPases (ATP6V1C1). A subset of lysosomal proteins associated with glycosaminoglycan (GAG) degradation were also up-regulated in the TWI mice, specifically four hydrolases (GUSB, HEXA, HEXB and GNS) that are involved in the degradation of hyaluronan, heparan sulfate, chondroitin sulfate and keratan sulfate.[404] GAGs are important constituents of the cell membrane and the extracellular matrix and play important roles not only in cell adhesion but also in inflammation, neurodevelopment and neuropathology.[177] GAGs have been shown to be involved in leukocyte transmigration at inflammatory sites and in the modulation of chemokines.[405] Accumulation and impaired degradation of specific GAGs in mucopolysaccharidosis disorder leads to cell death and a chronic inflammatory response resulting in neurodegeneration.[405] Our data indicate altered GAG degradation in TWI mice, which has not been reported previously. Further studies are needed to elucidate the potential role of GAG dysregulation in KD pathogenesis and/or progression.

The up-regulation of hydrolases suggests inefficient lysosomal degradation, while the up-regulation of lysosomal membrane proteins (e.g. LAMP1) may indicate a larger number of lysosomes in the TWI mouse.[406] An accumulation of lysosomes was already observed in induced neurons

derived from an adult onset KD patient.[102] The accumulation of lysosomes and lysosomal proteins may indicate a disruption of the autophagy pathway, which has previously been shown in several LSD's.[294,252] Here ATG16L1 was found to be down-regulated in the TWI mouse. ATG16L1 belongs to the autophagy related protein family and forms part of a large protein complex that is necessary for autophagy.[407] Specifically, ATG16L1 forms a complex with ATG12 and ATG5 that localizes to phagophores and pre-phagophore structures[283] and is essential for the proper elongation of the nascent autophagosome and for the lipidation of LC3.[408,409] Down-regulation of ATG16L1 may lead to a reduced rate of autophagosome assembly, and thus a reduced rate of autophagy.[410] A deregulation of the autophagic flux in TWI mice also explains the observed up-regulation of p62. The ubiquitin-binding protein p62 can bind to LC3 on the autophagosome membrane and be degraded by autophagy or target other proteins for degradation.[411] Accumulation of p62 and formation of p62 aggregates have been observed to occur upon autophagy inhibition and in several LSDs characterized by a disruption of the autophagy pathway, including mucopolysaccharidoses, mucolipidoses, Niemann-Pick C1, Pompe, Gaucher and Fabry diseases.[294] Thus, the accumulation of p62 is consistent with a reduced autophagic activity due to down-regulation of ATG16L1. Lysosomal protein accumulation could also be due to decreased autophagosome-lysosome fusion. A significant down-regulation of 28 proteins associated with microtubule cytoskeleton organization (*e.g.* MAP6, MAP7D2, CHMP3, CLASP2) were observed in TWI mice (Fig. 5.8 C), MAP6 and MAPK8IP3 have already been shown to be involved in the active transport of lysosomes.[412,413] The two kinesin motor proteins (KIF5C and KIF21A), which play an

active role in the anterograde transport of lysosomes[414], were also found to be down regulated in TWI mice. Moreover we observed a down-regulation of CHMP3, which is a protein that forms part of the ESCRT-III complex whose inactivation has been shown to induce autophagosome accumulation and autophagy disruption.[266] An accumulation of lysosomal proteins may also cause a destabilization of the lysosomal membrane that leads to lysosome membrane permeabilization (LMP)[415]. LMP have been shown to play a crucial role in lysosomal cell death (LCD) because of the release of lysosomal proteins in the cytosol. Cathepsins are believed to be the main mediators of LCD, even if they can also trigger LCD.[416] Among the lysosomal proteins that were found to be up-regulated in TWI mice there were 4 cathepsins: CTSB, CTSD, CTSS, CTSZ. In particular, CTSB and CTSD are involved not only in the triggering of LMP but also in cell death since they remain active at neutral pH, and so they remain active in the cytosol.[417] LMP may also be induced by ROS and apolipoproteins.[415,418] ROS production in KD disease has been linked to PSY accumulation, which activates secretory phospholipase A2 in oligodendrocytes MO3.13.[60] Here we found an up-regulation in TWI mice of PLAA (an activator of phospholipase A2) and 4 apolipoproteins (APOA1, APOB, APOD, APOE), supporting the hypothesis of LMP in the TWI mouse. APOE is a high density lipoprotein produced mostly by astrocytes in the CNS and secreted by macrophages at the site of injury in the PNS.[419] Accumulation of APOE has been shown to delay the regeneration of sciatic nerves, contributing to degeneration of the nervous system.[420] Moreover, APOE seems to impair autophagy in astrocytes leading to a reduced capacity of Aβ plaque clearance in the CNS of Alzheimer's disease patients.[420] Apolipoproteins have not previously been reported to

accumulate in the TWI mouse and future studies will be needed to establish their role in KD. Among the proteins down-regulated in the TWI mouse we also found UGT8, which is the enzyme that catalyzes the synthesis of PSY. This result is in agreement with previous studies that reported a down-regulation of UGT8 in the brain and spinal cord of the TWI mouse at a late stage of the disease.[421422110] The down-regulation of UGT8 in TWI mice is thought to be a homeostatic response of the cell to PSY accumulation.

### *Proteome changes in the Central Nervous System of the Twitcher mouse*

We characterized the CNS of the TWI mouse by analyzing the corpus callosum and motor cortex regions. The corpus callosum dataset contained a larger number of deregulated proteins than the motor cortex, consistent with the known mechanisms of KD in which the accumulation of PSY occurs mainly in myelinating cells (such as oligodendrocytes and Schwann cells), impairing remyelination and damaging the brain's white matter.[29]

The main biological processes up-regulated in the CNS of the TWI mouse are related to inflammatory and immune response and leukocyte infiltration (Fig. 5.8 A, B), as we found in the PNS. We found an up-regulation of the Complement and JAK/STAT pathways in both the corpus callosum and motor cortex, indicating neuroinflammation in the TWI mouse brain. The JAK/STAT pathway is essential for both innate and adaptive immunity and its aberrant activation has previously been reported in the neuroinflammatory diseases Multiple Sclerosis and Parkinson's Disease[423]. The use of JAK1 and JAK2 inhibitors in several murine models of Multiple Sclerosis has been shown to suppress clinical symptoms, reduce demyelination and suppress the production of pro inflammatory cytokines and chemokines[424]. The up-regulation of both STAT1 and STAT3 in the CNS

of the TWI mouse suggests that the JAK/STAT pathway may be a therapeutic target for KD treatment. We also found an up-regulation in the TWI mouse of GFAP and VIM, which are markers of reactive astrocytes and microglia activation.[425,426] GFAP and VIM up-regulation in the TWI mouse have been previously shown to occur before demyelination and in concomitance with macrophage infiltration, suggesting that CNS astrogliosis and inflammation may precede demyelination.[56,88]

Several lysosomal proteins were found up-regulated in the corpus callosum of the TWI mouse (Fig. 5.9 A, B), including HEXB, CTSB, CTSD and LAMP2. These results are in agreement with that found for the PNS of the TWI mouse, indicating that the accumulation of nondegraded material and the related biological alterations also occurs in the CNS of the TWI mouse.

Four proteins involved in membrane raft organization (ANXA2, CAV1, DOCK2 and PTPRC) were found to be up-regulated in the corpus callosum of the TWI mouse. Disruption of lipid raft domains have been shown to occur in sphingolipid storage disorders and KD as a consequence of undigested lipids and PSY accumulation.[58,427] Lipid rafts are involved in several signaling pathways and an alteration in raft composition can lead to altered membrane fluidity, and deregulation of cell signaling, influencing survival signals such as PKC, Akt and ERK.[59428]

Among the proteins down-regulated in the motor cortex of the TWI mouse we found UGT8, and which was also found to be down regulated in the sciatic nerve. This result is in agreement with previous studies, which reported a down-regulation of UGT8 at late stages of KD in both CNS and PNS.[421]

### 5.2.8 Material and methods

#### *Experimental design and statistical rationale*

We investigated the proteome changes associated with KD by comparing the proteomes extracted from the corpus callosum, motor cortex and sciatic nerves of littermate homozygous TWI and homozygous WT mice. We performed a TMT 10-plex experiment for each tissue region using independent biological replicates (N = 5) for each mouse type. The five TWI and five WT samples within each TMT 10-plex set were randomized using the Random.org list randomizer (www.random.org), and the expression levels of the confidently identified proteins compared using a two-sided Student's *t*-test with a permutation-based FDR cutoff (250 randomizations, FDR 0.01, S0 1).

#### *Materials*

Trypsin/LysC mix Mass Spec grade was purchased from Promega (Madison, WI). Tandem Mass Tags (TMT 10-plex) kits and microBCA protein assay kit were purchased from Thermo Fisher Scientific (Rockford, IL). Polyethylene naphthalate (PEN) membrane slides were purchased from Carl Zeiss (Carl Zeiss Microsystems GmbH, Göttingen, Germany). All other reagents and solvents were purchased from Sigma-Aldrich (St. Louis, MO).

#### *Mice*

Twitcher (strain B6.CE-Galctwi/J; Jackson Labs, Bar Harbor, Maine, USA) animals were bred at the Center for Experimental Biomedicine of CNR in Pisa, which is authorized for the use of animals for scientific purposes by the Ministry of Health (Authorization No. 114/2003-A of 16/9/2003). Animals were maintained under standard housing conditions and used

according to the protocols and ethical guidelines of the Italian (DLGS 26/2014; Permit Number: PT5.15, July 2015) and European Union (2010/63/EU) laws. Experiments were conducted in parallel on TWI-WT and littermate TWI-mutant homozygous mice (TWI), while TWI-mutant heterozygous mice (HET) for the TWI colony maintenance. Genomic DNA was extracted from the clipped tails of mice by Proteinase K digestion and subsequent genomic DNA extraction (EUROGOLD Tissue-DNA Mini kit, Euroclone) as previously described.[421,394] The genetic status of each mouse was determined from the genome analysis of the TWI mutation (Fig. 5.6), following the method reported by Sakai et al. (1996).[244]

Five WT (3 male and 2 female) and five TWI (4 male and 1 female) mice were sacrificed by cervical dislocation, dissected, and the brain extracted[429] and snap frozen in liquid nitrogen for 15 s. Sciatic nerves were dissected by making a 5 mm vertical incision along the thigh.[429] The muscles were split until the entire length of the sciatic nerve in the thigh region was exposed. The nerves were then gently lifted using forceps and removed by cutting at the proximal and distal ends. Brains and sciatic nerves were stored at -80°C until analysis.

### *Laser capture microdissection*

Consecutive coronal brain sections, 10 µm thick, were cut at 0.74-0.98 mm from Bregma using a cryostat (CM1950, Leica Microsystems Srl, Milan, Italy) and thaw mounted onto PEN membrane slides (previously conditioned in UV light for 30 minutes). After a light hematoxylin staining, small regions of 2.5 - 3.3 $mm^2$ were isolated from the corpus callosum and the motor cortex using a PALM microbeam laser capture microdissection system (Carl Zeiss MicroImaging, Munich, Germany). Microdissection was

performed using a x40 ocular lens and a 355 nm laser for cutting the tissue and catapulting the isolated regions of tissue into adhesive cap tubes (Carl Zeiss). Samples were stored at -80°C until analysis.

### *Protein extraction and digestion*

The isolated brain samples were dissolved in 20 µL of lysis buffer consisting of 50% trifluoroethanol (TFE), 0.5% sodium dodecyl sulfate (SDS), 2.5mM ethylenediaminetetraacetic acid (EDTA), 2.5 mM ethylene glycol-bis(β-aminoethyl ether)-N,N,N',N'-tetraacetic acid (EGTA), 10 mM 4-(2-hydroxyethyl)-1-piperazineethanesulfonic acid (HEPES) pH 8.5 and protease inhibitor (cOmpleteTM, Mini, EDTA-free Inhibitor Cocktail). The sciatic nerves were homogenized in 100 µL of the same lysis buffer. Proteins were extracted by sonication at 4°C using a Bioruptor Pico (Diagenode, Seraing, Belgium - 10 cycles of 30 s ON and 30 s OFF). Protein quantification was performed on a 1 µL aliquot of each sample using a modified microBCA assay.[378] Each anatomical region was compared using an identical amount of extracted protein, and which corresponded to the maximum amount that could be obtained from all ten animals, namely 1.5, 2.5 and 3 µg for the corpus callosum, motor cortex and sciatic nerves, respectively. Protein digestion was performed using a modified SP3 protocol.[378,379] The protein extracts were mixed with 20 µL of lysis buffer and 2 µL of paramagnetic beads [100 mg/mL solution of 50% Speedbeads A (GE45152105050250, Sigma) and 50% Speedbeads B (GE65152105050250, Sigma)] in 0.2 mL PCR tubes (Sarstedt). Briefly, proteins were denatured at 95°C for 5 min. Reduction (DTT 200 mM), alkylation (IAM 400 mM), protein purification and overnight trypsin/Lys-C digestion (1:25 enzyme/protein) steps were performed in the same tube.

### *TMT labelling*

The protein expression levels in the tissue samples from all ten animals were compared using 10-plex TMT isobaric labeling. After digestion the samples were vortexed and sonicated for 5 minutes with a Bioruptor Pico (5 cycles of 30 s ON and 30 s OFF). In-solution TMT labeling was performed using a 1:20 peptide/TMT proportion. Three TMT 10-plex reagents (0.8 mg) were dissolved in 26, 16, and 13 µL of ACN and used for the labeling of the peptides obtained from the corpus callosum, motor cortex and sciatic nerves, respectively (note the TMT solutions were made up using different volumes in order to ensure 2 µL of the TMT solutions provided the correct excess for each tissue extract). The TMT label was added in two equal steps of 1 µL, each followed by an incubation period of 30 min. TMT labeling was quenched by adding 2 µL of 4% hydroxylamine and incubating for 15 min. After TMT labeling, the samples were transferred to 0.5 mL LoBind tubes (Eppendorf) for peptide purification. Samples were rinsed with 100% ACN to promote peptide binding on the carboxylate coated beads. Peptides were washed twice with 70% ethanol and once with 100% ACN. The purified peptides were eluted from the beads with a 2% DMSO aqueous solution. The samples from the five WT and five TWI mice were each labeled with a different, randomized TMT label; the labeled peptides from the ten mice were then combined in a 1:1:1:1:1:1:1:1:1:1 ratio. An aliquot corresponding to 1.5 µg of total protein content was collected from each TMT set, diluted 1:1 with 10% formic acid and injected into a nanoLC system for the evaluation of the TMT labeling reaction efficiency. The remaining samples were dried down with a speedvac (Eppendorf) and stored at -20°C.

### *Automated high-pH fractionation*

High-pH fractionation was performed using an AssayMap Bravo robot (Agilent Technologies) using the fractionation protocol V1.0.[379] Peptide fractionation was performed using all of the sample remaining after TMT labeling, approximately 15, 25 and 30 µg for the corpus callosum, motor cortex and sciatic nerve extracts, respectively. Briefly, the dried samples were resuspended in 10 µL of 2% DMSO, mixed with 100 µL of 10 mM NH4OH (pH 10) and loaded on to reversed-phase (RP-S) cartridges. Peptides were isocratically eluted with 35 µL plugs of 12, 18, 24, 30, 36 and 80% ACN in 10 mM NH4OH (pH 10). The six fractions and the sample flow-through were transferred to 0.5 mL LoBind tubes (Eppendorf), dried down with a speedvac and stored at -20°C.

### *LC-MS3 analysis*

Peptides were resuspended in 10% formic acid and injected into an Easy-nLC1000 (Thermo Scientific) coupled to an Orbitrap Fusion (Thermo Scientific). Peptides were first trapped using a nanoviper trap column (2cm x 75 µm, C18, 3 µm, 100A; Thermo Scientific) and then separated using an EASY-SprayTM analytical column (ES803: 50 cm x 75 µm, C18, 2 µm, 100A; Thermo Scientific) using a flow rate of 300 nl/min and a 140 minutes gradient. Peptides were loaded at 800 bar followed by a non-linear gradient: 0-1 min, 8%B; t=105 min, 25%B; t=120 min, 35%B; t=130 min, 90%B; t=140 min, 90%B. Buffer A consisted of 0.1% FA and Buffer B of 99.9% ACN and 0.1% FA.

The Orbitrap Fusion was operated in a data dependent top-speed method using a 2 second maximum cycle time and multi-notch synchronous precursor selection (SPS) for MS3 based TMT quantification. The survey

scan was performed in the Orbitrap (*m/z* 375-1500, 120k resolution, AGC target 2e5, 50 ms maximum injection time). Monoisotopic precursor selection and a dynamic exclusion of 70s were adopted. Ions with charge states from 2+ to 7+ and intensity greater than 5e3 were selected for CID fragmentation (35% NCE) using an isolation window of 1.6 *m/z*.

MS2 spectra were recorded in the linear ion trap with a rapid scan rate, 5e3 AGC target and 125 ms maximum injection time. Following fragmentation, multinotch (synchronous) precursor selection was performed to select the 8 most abundant fragment ions for HCD-MS3 (50% NCE). MS3 scanning was performed in the Orbitrap at a resolution of 60K, with an AGC target of 1e5 and 150 ms maximum injection time.

### *Data analysis*

Raw data files were analyzed using Proteome Discoverer 2.1 (Thermo Scientific). For each tissue type the raw files from the 7 fractions were merged and searched with the SEQUEST HT[177] search engine against the Mus Musculus Swiss-Prot protein database (July 2016, 16,808 entries) supplemented with a common contaminant database (246 entries). Searches were performed using the TMT reagents (+229.163 Da, lysine and N-termini) and carbamidomethyl (+57.021 Da, cysteine) as static modifications, methionine oxidation (+15.995 Da) as a dynamic modification, 20 ppm precursor mass tolerance, 0.6 Da fragment mass tolerance, and 20 ppm reporter ion tolerance. The search was performed using fully tryptic peptides with a minimum length of 6 amino acids and up to 2 missed cleavages. The results were then filtered for a 1% false discovery rate (FDR) using the Percolator algorithm and additionally filtered for a minimum Xcorr score of 1.8. At least one unique peptide was

required for definitive protein identification. Protein intensities were calculated based on the label intensities of the 3 most abundant peptides with a co-isolation threshold of 50% taking into account unique peptides. Search results were exported as txt files and processed with Perseus 1.5.[430] For each TMT experiment the protein intensities were log2 transformed and subject to a median normalization. Data were filtered such that each protein was quantified in at least four TWI and four WT mice. Principal Component Analysis was performed on the normalized and filtered datasets. Significantly different protein levels between TWI and WT mice for the three TMT experiments were calculated using a two-sided Student's *t*-test using a permutation-based FDR cutoff (250 randomizations, FDR 0.01, S0 1). Proteins were considered as differentially regulated if their adjusted p-value corresponded to an FDR lower or equal to 0.01 and their fold change (expressed as log2 ratio) was <-1 or >+1.

Gene ontology was performed with WebGestalt[430] using the Overrepresentation Enrichment Analysis (ORA) method. For each TMT experiment the input protein list included the proteins significantly up or down regulated in the TWI mice. The reference protein list included all proteins identified in the TMT experiment. A Benjamini-Hochburg (BH) method for multiple test adjustment was used and the FDR was set at 0.05.

### *TMT labeling efficiency*

TMT labeling efficiency and over labeling rate were evaluated using 1.5µg aliquots of each TMT set. TMT labeling efficiency was evaluated by setting the TMT modification (+229.163 Da) at N-termini and lysine residues as dynamic and determining the percentage of labeled PSMs. TMT overlabeling was evaluated by setting the TMT modification at N-termini

and lysine residues as static, and TMT modification at serine, threonine, histidine and tyrosine as dynamic, and then determining the percentage of TMT-labeled serine, threonine, histidine and tyrosine.

### *Western blot analysis*

Western blot analysis was performed on the sciatic nerve extracts to validate the LC-MS/MS results of seven proteins that play important roles in the molecular mechanisms of KD. Proteins were extracted from the sciatic nerves and quantified identically as for the LC- MS/MS analysis (see *Protein extraction and digestion* section above). A WT mice pooled sample and a TWI mice pooled sample were prepared by combining the sciatic nerve extracts of three WT and three TWI mice, respectively. The western blot analysis was performed in technical triplicate on the two pooled samples. The samples were boiled in Laemli buffer containing b-mercaptoethanol (5% final concentration) for 5 minutes and centrifuged at RT. The supernatants were used for SDS-PAGE. Samples (25 µg) were resolved by SDS-PAGE using Gel Criterion XT-Precasted polyacrylamide gel 4–12% Bis-Tris (Bio-Rad, Hercules, CA) and subsequently transferred to nitrocellulose membranes.[342] Immunodetection was performed for ATG16L1 (Abcam, Cambridge, UK; catalog No. ab188642), VAMP8 (Abcam; catalog No. ab76021), UGT8 (Abcam; catalog No. ab170351), CTSB (Abcam; catalog No. ab58802), SQSTM1 (Abcam; catalog No. ab56416), HEXB (Santa Cruz Biotechnology, Dallas, Texas (USA); catalog No. sc-376781), LAMP1 (Santa Cruz Biotechnology, Dallas, Texas (USA); catalog No. sc-20011), and α-tubulin (Sigma Aldrich; catalog No. T6074). On the following day, the blots were incubated with the corresponding peroxidase-linked secondary antibodies and after incubation the membranes were developed with Clarity

enhanced chemiluminescent substrates (Bio-Rad). The chemiluminescent signal was acquired with an ImageQUANT LAS400 scanner (GE Healthcare Life Sciences, Uppsala, Sweden), and the density of immunoreactive bands quantified in ImageJ. The results were normalized to α-tubulin.

### *Data availability*

The mass spectrometry proteomics data have been deposited to the ProteomeXchange Consortium via the PRIDE[420] partner repository with the data set identifier PXD010594.

## 5.3 Capturing Metabolism-Dependent Solvent Dynamics in the Lumen of a Trafficking Lysosome.

*The experiments presented in this Section have been published after peer-reviewing on the journal ACS nano 13(2), 1670-1682. Co-authors of the work are: Begarani F, D'Autilia F, Signore G, Del Grosso A, Cecchini M, Gratton E, Beltram F, Cardarelli F. Role of authors: study concept and design: FBeg, FC. Performing of experiment: FBeg, FD, ADG. Analysis and interpretation of data: FBeg, FD, GS, FC. Drafting of the manuscript: All authors. Discussed data: FBeg, MC, FBel, EG, FC; Study supervision: FC. I, in particular, prepared samples with primary cells derived from both WT and TWI mice and contributed to the drafting of the related Material and Methods Section.*

### 5.3.1 Introduction

The eukaryotic cell is not a random mixture of proteins, lipids, nucleic acids, and other molecules freely diffusing and interacting. On the contrary, the cell contains distinct dynamic, membrane-enclosed subcompartments spanning over a broad spatial scale, from tens of nanometers (e.g., synaptic vesicles, caveolae, clathrin-coated pits) to hundreds of nanometers (e.g., endosomes, lysosomes, mitochondria, secretory granules) to several microns (e.g., Golgi apparatus, endoplasmic reticulum, nucleus) that are designed to concentrate specific sets of components and functions within confined cell regions.[431] This spatial organization determines a discontinuous landscape of the physicochemical properties of the intracellular solvent, in terms of its intrinsic polarity, viscosity, dynamics, etc.[432] These properties, in turn, play an active role in the regulation of the biochemical processes within each specific district.

In the last decades, a plethora of solvatochromic and fluorogenic dyes were developed as environment-sensitive probes tailored, in particular, for optical microscopy applications in living cells.[433] Yet, their exploitation to probe solvent physicochemical properties within subcellular compartments at the time scale relevant to molecular processes (i.e., micro-to-millisecond regime) is, at present, an unattained task. In fact, optical-microscopy-based analysis of subcellular structures is severely hindered by their continuous rapid movement in the three-dimensional (3D) cellular environment. State-of-the-art microscopy tools for delivering subcellular information at molecular resolution fail to subtract the 3D evolution of the entire system while preserving the temporal resolution required to successfully probing the local environment. Most classical approaches rely either on the use of fast cameras combined with customized modifications of the emission optics of the microscope to achieve sampling in the axial direction[434] or on the use of fast laser-scanning modules[435]. Still, these solutions are unavoidably time-consuming, and much time is spent to perform 3D sampling even far from the object of interest. Worthy of mentioning, recent improvements based on either the combination of stimulated emission depletion (STED) with electro-optical scanning[436] or the use of local excitation-intensity zeros for localizing emitters[437] pushed 3D localization experiments to high spatial (nanometer) and temporal (millisecond) resolutions. Still, the ability of such strategies to discriminate between the dynamics of the structure of interest and that of the biological processes occurring within the same structure has yet to be proven. This experimental bottleneck is tackled here by focusing an excitation light beam in a periodic orbit around the subcellular structure of interest. The recorded signal

(fluorescence) is used as feedback to track the structure of interest. As already demonstrated in preliminary applications in live cells[438–440], such strategy is able to subtract the natural movement of the subcellular reference system while preserving the required temporal resolution to study biological processes, that is, microseconds along the orbits and milliseconds between the orbits.

The lysosome is selected here as a paradigmatic subcellular target in light of its important role in metabolism, signaling, and cell-growth regulation.[441,442,136,443] Present knowledge suggests that the intraluminal solvent of lysosomes bears little resemblance to the surrounding cytoplasmic environment. First, the lysosome lumen is an extremely crowded aqueous environment, actually 50–500 times more viscous than the cytoplasm.[444,445] Second, the lysosome lumen is highly polydisperse, with constituent sizes spanning several orders of magnitude, from subnanometer (ions, metabolites) to nanometers (proteins) to tens/hundreds of nanometers (enzymatic complexes, membrane fragments, nano subcompartments).[446] Third, metabolic activities continuously drive the lysosome lumen far from thermodynamic equilibrium.[447] Thanks to these dynamic variations, the cell can reversibly shut down metabolism and respond to environmental cues.[102]

In order to probe the physicochemical properties of the lysosome lumen, we combined the feedback-based orbital tracking of single lysosomes with the use of the 6-acetyl-2-dimethylaminonaphthalene (ACDAN) molecule, synthesized by Gregorio Weber in 1979[448] and designed as a relaxation probe for various biological environments. ACDAN shows peculiar properties that are ideal for its application to the lysosome case.

Specifically, (i) it enters cells and partitions mostly into hydrophilic environments[449,450], while concomitantly becoming brighter within the most viscous/crowded ones (as demonstrated for other DAN probes)[451], such as the lysosome lumen; (ii) it has no ionizable groups and is thus not sensitive to pH changes in the range from 4 to 10[446] analogously to the other DAN probes[452]; and (iii) it shows exquisite sensitivity to solvent dipolar relaxation, displayed as red- or blue-shift in the emission spectrum[448–450]. Properties at points (i–ii) make ACDAN suitable for spontaneous and robust labeling of lysosomes in live cells. A property at point (iii), combined with feedback-based tracking, offers the opportunity to monitor the extent of solvent dipolar relaxation, in real time, in the lumen of a trafficking lysosome at a time resolution ranging from microseconds (sampling time along the orbit) to milliseconds (between orbits) and to several seconds (total time of tracking of a single lysosome).

Standard generalized polarization (GP) calculations[453] are used based on the ACDAN emission shift at any time point. Then, raster image correlation spectroscopy (RICS)[454] is performed to extract characteristic dissipation time of ACDAN GP fluctuations in the lysosome lumen, analogously to what was already done by others on membranes or within the cell cytoplasm using DAN probes.[449,450,455,456,457,458]. It is observed that intralysosomal ACDAN GP fluctuates with characteristic dissipation times in the micro-to-millisecond range. Control experiments demonstrate that GP fluctuations correlate with (acidic) lysosomal pH and metabolic energy in the form of ATP. Also, GP fluctuations are observed in live cells, but disappear upon cell fixation. Based on these findings, we argue that intralysosomal ACDAN GP fluctuates according to the ongoing lysosomal

metabolism. As a first test, we finally show that ACDAN GP fluctuations are altered both in amplitude and timing in the lysosomes of a cellular model of KD, a LSD in which the organelle metabolism is impaired by a specific enzymatic loss.

### 5.3.2 ACDAN Is a Stable Fluorescent Marker of the Lysosome Lumen

The lysosome is selected as a case study in light of its biological relevance. Thus far, classical localization-based approaches were successfully used to study lysosome 3D transport properties[458,459] but at the expense of molecular-level information. On the other hand, attempts to probe lysosome intraluminal properties (e.g., viscosity) in living cells were conducted by standard imaging approaches (e.g., fluorescence lifetime imaging, FLIM)[441], thus averaging on a time scale much longer than the time window of interest for molecular processes. Combined with the use of ACDAN as a solvent relaxation probe, the strategy adopted here makes it possible to probe hitherto hidden properties of the intralysosomal environment at micromillisecond temporal resolution. ACDAN subcellular localization in living HeLa cells is probed by standard confocal microscopy (Fig. 5.11). Upon administration to the cell medium at 5 μM, ACDAN spontaneously redistributes in few minutes into cells. In keeping with previous observations in yeast cells[446], ACDAN signal is characterized by a heterogeneous, punctuate-like intracellular distribution (Fig. 5.11 A). The localization within specific subcellular compartments is assessed by co-localization experiments with known fluorescent markers of subcellular structures. As discernible from the images in figure 5.11 A-C, a dominant contribution to ACDAN localization comes from lysosomes (labeled with

Red Lysotracker).

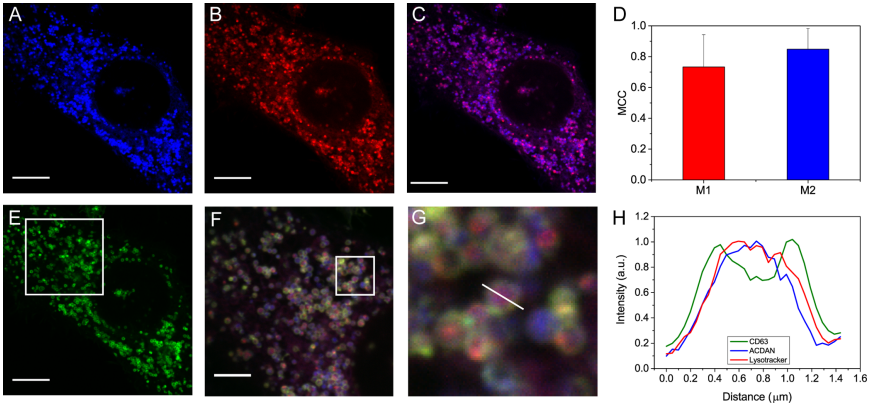


**Figure 5.11.** ACDAN-based staining of the lysosomal lumen in living cells. Confocal microscopy images of HeLa cells labeled with ACDAN **(A)** and LysoTracker **(B)** and the corresponding overlay of the two signals **(C).** Scale bars: 10 μm. **(D)** Quantitative analysis of the co-localization between ACDAN and LysoTracker signals by using the Fiji plugin for co-localization analysis and Manders' coefficients (M1 and M2). Values represent the mean ± SD for N = 10 cells. **(E)** The same HeLa cell is also expressing the lysosomal protein CD63-EGFP, which is localized to the organelle membrane. **(F)** Zoom of a cytoplasmic region showing several labeled lysosomes and the overlay of all the three signals recorded. Scale bar: 5 μm. **(G)** The area enclosed within the white square in **(F)** is enlarged here to show the details from single lysosomes. **(H)** Normalized intensity profile along the white line drawn in **(G)** on a single lysosome; the blue trace represents ACDAN intensity profile, green trace refers to CD63-EGFP signal, and red trace refers to Lysotracker.

This is quantitatively expressed by the two calculated Manders' overlap coefficients (MOCs: hereafter M1 and M2) for the two signals (Fig. 5.11 D). Worthy of mentioning, M2 (Lysotracker vs ACDAN) is slightly higher than M1 (ACDAN vs Lysotracker); this is not surprising, in light of the nonexclusive localization of ACDAN within lysosomes. In this regard, figure 5.12

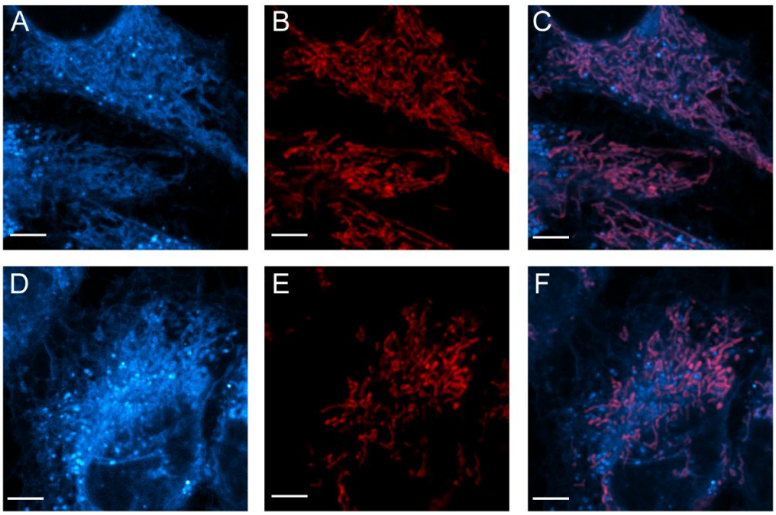


**Figure 5.12.** ACDAN localization within mitochondria in HeLa cells. Confocal microscopy images of HeLa cells labelled with ACDAN (**A, D**) and MitoTracker (**B, E**), and the corresponding overlay of the two signals (**C, F**). Punctuate-like signal from lysosomes has been saturated to better show the signal contribution from mitochondria. Scale bars: 5 μm.

shows that ACDAN is also present within mitochondria. The differential brightness of ACDAN within intracellular compartments (i.e., typically lysosomes > mitochondria > cytoplasm > nucleus, see exemplary fluorescence intensity analysis in Fig. 5.13) is consistent with previous reports on analogous probes[424] and may be linked to the environment viscosity (i.e., the higher the viscosity, the higher the brightness). The ACDAN molecule is known for being essentially insensitive to membrane-associated solvent dynamics, as it partitions to hydrophilic environments.[449,450] In order to verify that in our experiments ACDAN partitions to the lysosome lumen, we quantitatively compared ACDAN with specific markers of the lumen (i.e., Lysotracker) and membrane (i.e., EGFP-labeled CD63) (Fig. 5.11 A-G, see also additional examples in figure 5.14) of

this organelle.

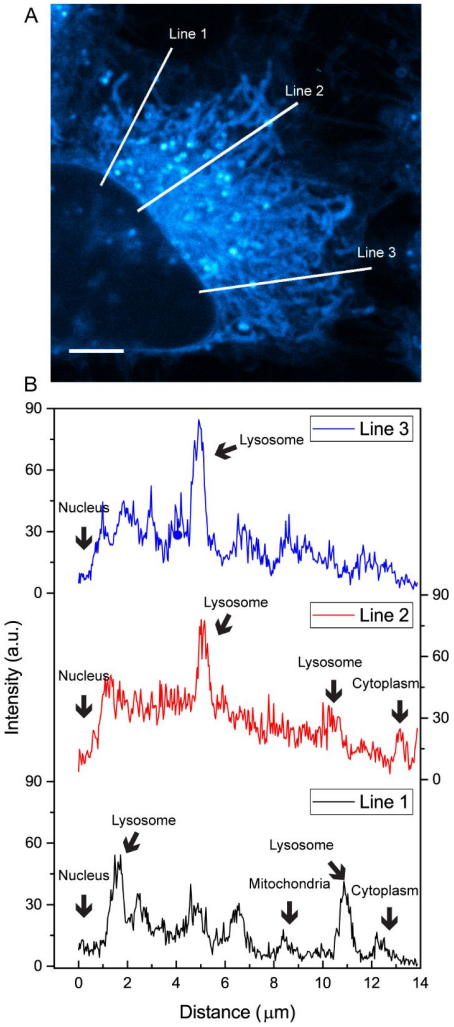


**Figure 5.13.** ACDAN distribution in HeLa cells. **(A)** Confocal microscopy images of a cell labelled with ACDAN. Scale bar: 2 μm. (**B**) Normalized intensity profiles along the white lines in

**(A)** showing the different brightness of ACDAN within different compartments. Typically, lysosomes>mitochondria>cytoplasm>nucleus.

The intensity profile of ACDAN superimposes to that of Lysotracker that shows a maximum corresponding to the center (lumen) of lysosome (Fig. 5.11 G-H, blue and red lines). By contrast, CD63-EGFP signal profile shows two maxima corresponding to the edges of the lysosome (membranes) and a minimum close to the center (lumen) (Fig. 5.11 G-H, green line).

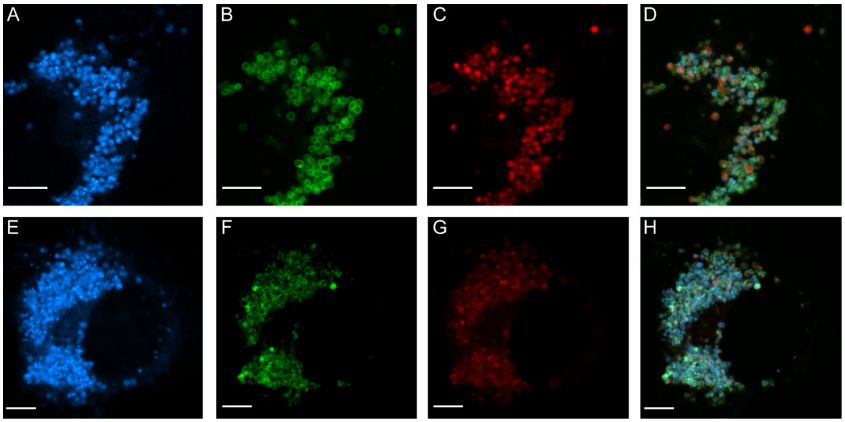


**Figure 5.14.** ACDAN colocalization with Lysotracker in the lumen of lysosomes in living HeLa cells. Confocal microscopy images of HeLa cells labelled with ACDAN **(A, E)**, CD63-GFP **(B, F)** and LysoTracker **(C, G)**, and the corresponding overlay of the three signals **(D, H)**. Scale bars: 5 µm. Please note that ACDAN better colocalizes with Lysotracker signal arising from the lysosome lumen as opposed to CD63-GFP that, instead, is clearly labeling the lysosome membrane.

### 5.3.3 Feedback-Based 3D Orbital Tracking and Fluctuation Spectroscopy on Single Lysosomes: Validation Tests

The ACDAN signal is used as feedback for the orbital-tracking algorithm. The scheme of a typical experiment is reported in figure 5.15 A. Cell staining with Red Lysotracker is used as reference to unequivocally select lysosomes

for the tracking experiment. Tracking experiments last 30–60 s each and are conducted at 1 ms temporal resolution per orbit (i.e., microsecond sampling along each orbit; see Methods section for more details). For each tracked lysosome, we obtain the 3D trajectory (Fig. 5.15 B) from which, in turn, we calculate the mean square displacement (MSD, Fig. 5.16) and the average

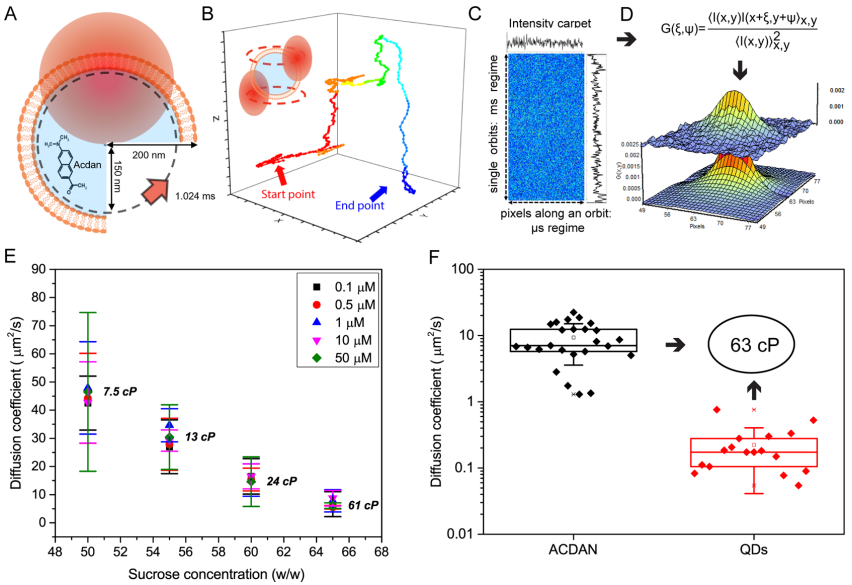


**Figure 5.15.** Orbital tracking of single lysosomes and circular-RICS analysis of ACDAN diffusion. **(A)** Scheme of a typical orbital tracking experiment. In red, the laser PSF; in orange, lysosomal membrane; and in light blue, the lysosome lumen; 200 nm is the average radius of lysosomes; 150 nm is the radius of the laser orbit, and 1.024 ms represents the time required for the laser to complete an entire orbit. The drawing is not to scale. **(B)** Example of a real single-lysosome trajectory originated from a 3D orbital tracking experiment. Ticks on axes represent pixels of 50 nm. This clearly shows that lysosomes on average move several nanometers in all directions during the measurements. On the top-left, a schematic representation of 3D-tracking configuration, showing a lysosome at the center and the scanning PSF creating two orbits separated along the vertical axis. **(C)** Exemplary ACDAN intensity carpet captured during the tracking experiment reported in **(B)**. **(D)** Circular-RICS general equation (eq 1) is reported here on the top. Circular-RICS autocorrelation curve (for experimental data acquired in **(B)**) and the corresponding Gaussian fit. **(E)** Average D values and SD (µm²/s) measured at different viscosities (i.e., different concentrations of Sucrose

dissolved in pure water). Different colors represent different ACDAN concentrations (see legend on the top right). **(F)** Plot of the diffusion coefficients of ACDAN (black) and QDs (red) measured inside lysosomes of HeLa cells. Each point corresponds to a single measurement on a single lysosome. Upper and lower edges of the boxes represent the 25 and 75 percentile of the distributions found, and the middle line shows the median value. Whiskers show standard deviations. 63 cP is the average viscosity value found using both QDs and ACDAN.

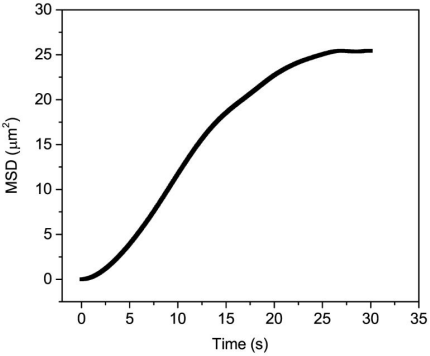


**Figure 5.16.** Average MSD curve recovered from feedback-based 3D tracking. This exemplary MSD, obtained by tracking a single lysosome, shows the contribution of directed motion at a short spatiotemporal scale (<5 s), and overall organelle confinement (or sub-diffusive behavior) at a larger spatiotemporal scale (>15 s).

diffusion coefficient (D, $\mu m^2/s$). Both the overall shape of the MSD and the retrieved D (0.009 ± 0.010 $\mu m^2/s$, mean ± SD) are in good agreement with previous results obtained with the iMSD approach on the same organelle.[460] It is worth mentioning that lysosomes typically move several microns in the x–y–z directions during the experiment (see, for instance, the exemplary trajectory in Fig. 5.15 B); this justifies the use of 3D orbital tracking means as compared to the 2D configuration. The fluorescence signal originated from ACDAN along each orbit (and used for the feedback-based tracking) is stored in an "intensity carpet" and used for fluctuation analysis (Fig. 5.15 C, D). In detail, we use classical RICS analysis[454,461] on ACDAN carpets (Fig. 5.15 D) (hereafter referred to as circular-RICS). Fitting

of the circular-RICS autocorrelation curves affords a quantitative estimate of ACDAN intralysosomal concentration and apparent diffusivity (hereafter indicated as 'D', $\mu m^2/s$). Concerning the former, the point extrapolated at zero-time lag of the autocorrelation curve (or G0) yields an estimated concentration of ACDAN within the lysosome of about 6 µM (see Fig. 5.17 for the $G_0$ calibration). Concerning the latter, we obtain an average D = 9.3 ± 5.7 $\mu m^2/s$ (mean ± SD, Fig. 5.15 F black points).

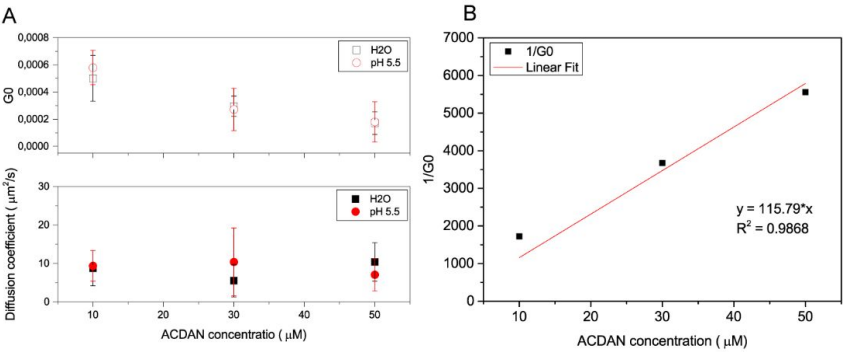


**Figure 5.17.** Calibration curves for concentration and viscosity analysis. **(A)** As expected, the G0 value decreases as ACDAN concentration increases in aqueous solution of 66% sucrose both at neutral (black) and acidic (red) pH (top panel). Diffusion coefficients instead remain constant (lower panel). **(B)** Calibration of 1/G0 in 66% sucrose solution at pH=5.5.

ACDAN diffusivity can be in principle used to estimate lysosome viscosity, thus further validating the proposed experimental strategy. To this end, we set out to preliminarily estimate ACDAN hydrodynamic radius by means of circular-RICS measurements performed in cuvette, using ACDAN aqueous solutions at different concentrations of sucrose (i.e., 50, 55, 60, and 65% w/w), to obtain different viscosities. As reported in figure 5.15 E, the measured D decreases with increasing sucrose concentration, as expected. By means of the Stokes–Einstein relation (eq 3 in the Methods

section) an apparent hydro-dynamic radius of the ACDAN molecule of approximately 0.43 nm is derived. This, in turn, combined with the average D and eq 3, affords an apparent viscosity of the lysosome lumen of about 63 cP (ranging from a minimum of 40 cP to a maximum of 148 cP, Fig. 5.15 and Tab. 5.3), a value that nicely matches previous FLIM-based estimates obtained using molecular rotors.[462] As reported in figure 5.18, this result is further validated by similar experiments conducted with quantum dots (QDs). First, the QDs hydrodynamic radius is estimated on the basis of in cuvette measurements performed both in solution and within synthetic lipid vesicles (Fig. 5.18 A).

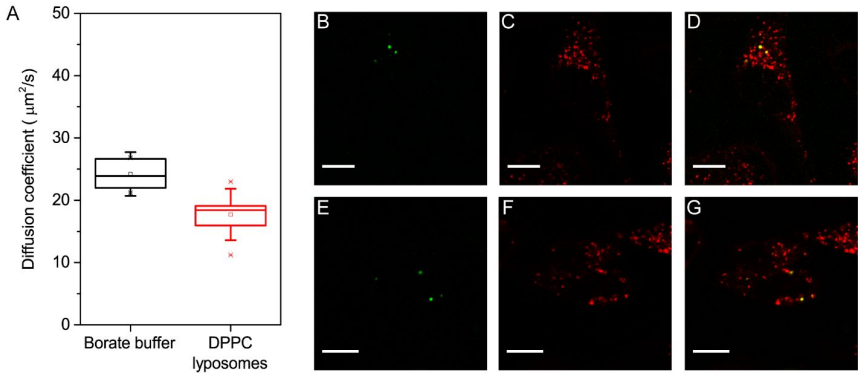


**Figure 5.18.** QDs in calibration solutions and in HeLa cells. **(A)** Diffusion coefficients of QDs in Borate buffer and in DPPC liposomes suspended in Borate buffer. These values were used for the calibration of QDs hydrodynamic radius, as described in the Methods section. **(B-G)** Confocal microscopy images of QDs **(B, E)** within lysosomes labelled with Lysotracker (**C, F**), and the corresponding overlay of the two signals **(D, G)**. Scale bar: 10 μm.

Upon administration to the culture medium, a fraction of QDs spontaneously enters cells and is trapped within lysosomes (Fig. 5.18 B–G). The stable signal of QDs can be exploited to track lysosome position while performing fluctuation analysis to study the intralysosomal diffusivity of

QDs (D = 0.22 ± 0.18 μm²/s, mean ± SD, Fig. 5.15 F red points). Combined with QD hydrodynamic radius, this result yields the same intralysosomal viscosity obtained using ACDAN as a probe. As a final control, analogous experiments are performed within the nucleus: As expected, these measurements reveal a less viscous environment, with a slightly larger distribution of D values (Fig. 5.19 and Tab. 5.3), in keeping with available literature.[463]

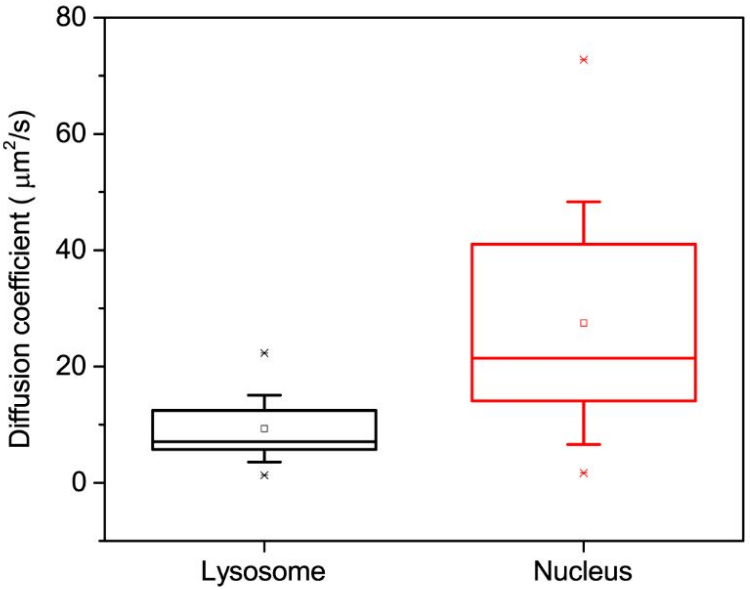


**Figure 5.19.** Diffusion coefficient of ACDAN within lysosomes (black) and nuclei (red) of HeLa cells. Upper and lower edges of the boxes represent the 25 and 75 percentile of the distributions, respectively; the middle line indicates the median value; the squares inside the boxes are the mean values; whiskers show standard deviations.

| | | Lysosome | | | | | Nucleus | Solution |
|---|---|---|---|---|---|---|---|---|
| | | Physiol. cond. | Sodium azide | Chloroquine | Osmotic shock | PFA | Physiol. cond. | |
| **RISC od ACDAN Diffusion viscosity (cP)** | mean | 63 | 58 | 57 | 48 | ND | 19 | 60 |
| | range | 40-148 | 34-161 | 34-148 | 29-130 | ND | 11-83 | 40-90 |
| **RISC od ACDAN GP τ range (s)** | fast | 2.5 x $10^{-5}$-6.6 x $10^{-3}$ | 4.8 x $10^{-5}$-2x$10^{-3}$ | 4.3 x $10^{-5}$-5x$10^{-3}$ | 3.7 x $10^{-5}$-3.2x$10^{-3}$ | - | 1.1 x $10^{-5}$-13x$10^{-3}$ | - |
| | slow | 0.5-28 | 0.7-29.2 | 0.27-28.7 | 0.31-29 | 4.6-24.6 | 0.48-37 | - |
| **Fractional population** | fast | 89 | 15 | 18 | 44 | 0 | 70 | ND |
| | slow | 11 | 85 | 82 | 56 | 100 | 30 | ND |
| **3D Feedback-Based ACDAN Imaging** | mean | 0.042 | 0.046 | 0.043 | 0.049 | 0.128 | 0.036 | 0.71 |
| | SD | 0.022 | 0.027 | 0.019 | 0.027 | 0.037 | 0.012 | 0.004 |

**Table 5.3.** Summary of Results on HeLa Cells. The upper part of the table shows the results from RICS analysis of ACDAN diffusion in all the tested experimental conditions. Viscosity estimates are derived by eq 3 (Methods section), using the diffusion coefficients reported in figure 5.15 F. The middle part shows the results from RICS analysis of ACDAN GP. For both the "fast" and "slow" populations, the range of characteristic GP fluctuation times ( $\tau$ ) and the fractional population contributions are reported. Finally, in the lower part, the average GP values retrieved from 3D feedback-based ACDAN imaging of single lysosomes are reported for all tested conditions. ND stands for not determined.

### 5.3.4 ACDAN GP Fluctuations in the Lumen of a Trafficking Lysosome

A distinguishing feature of ACDAN is its exquisite sensitivity to the extent of dipolar relaxation of intracellular solvent. This information can be quantitatively extracted through the GP analysis of ACDAN fluorescence emission (see calibration tests using protic and aprotic solvents in Fig. 5.20). For experiments in cells, the ACDAN signal can be split into two channels (CH1: 400–470 nm and CH2: 475–545 nm) that are then combined into the GP image (by applying eq 4 of Section 5.3.6).

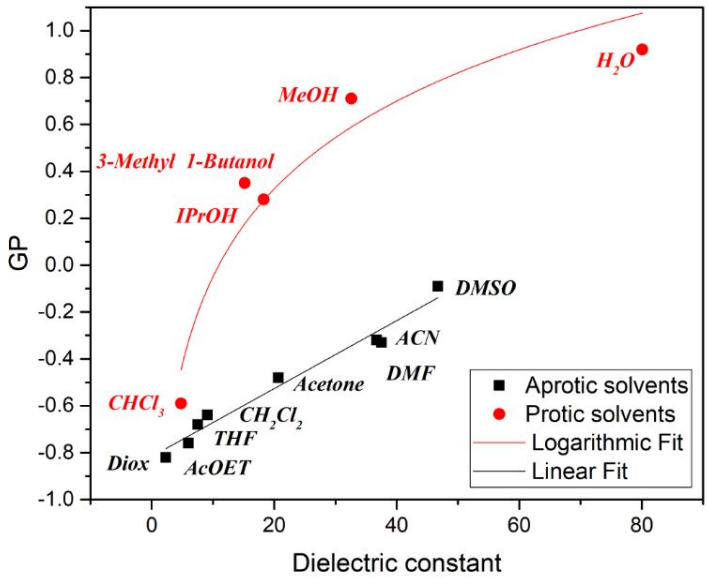


**Figure 5.20.** Dependence of ACDAN GP from the dielectric constant of the solvent. Plot of ACDAN GP as a function of the solvent dielectric constant, collected by using both protic (red dots) and aprotic (black squares) solvents.

A typical GP imaging experiment performed on a whole cell is reported in figure 5.22 A–C (additional examples are collected in Fig. 5.21). In more detail, from the zoom in of a portion of the cytoplasm (Fig. 5.22 D), it can be appreciated that most of the lysosomes show a similar average GP (namely, GP = 0.04, as reported in Tab. 5.3, feedback-based GP imaging) with few exceptions typically yielding higher GP average values (as can be noted in the example of Fig. 5.22 D).

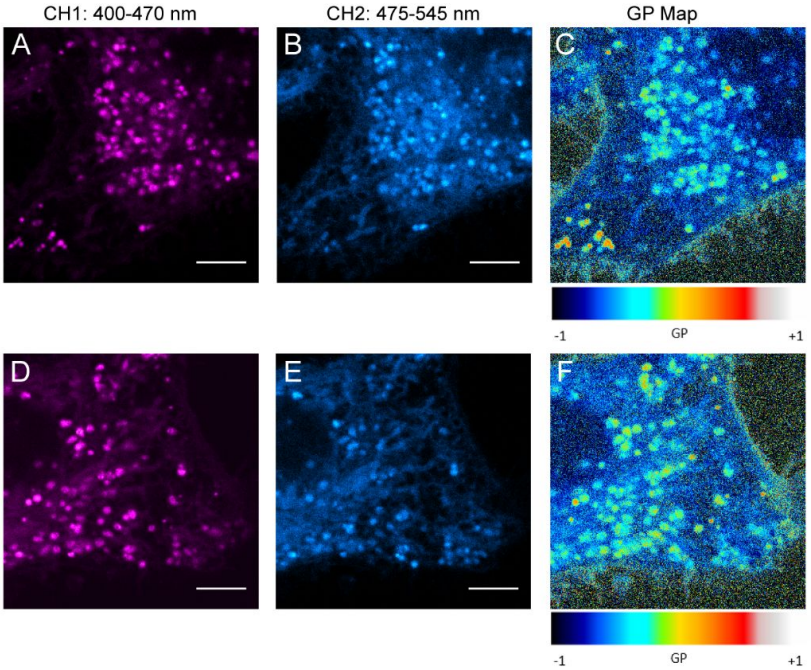


**Figure 5.21.** Imaging of ACDAN GP inside HeLa cells. Confocal microscopy images of HeLa cells labelled with ACDAN. Channel 1 (**A** and **D**, collection range: 400-470 nm) and Channel 2 (**B** and **E**, collection range: 475-545 nm) are used to quantitatively produce the GP map (**C** and **F**), as described in the Methods section. GP values are color-coded according to the LUT reported on the bottom.

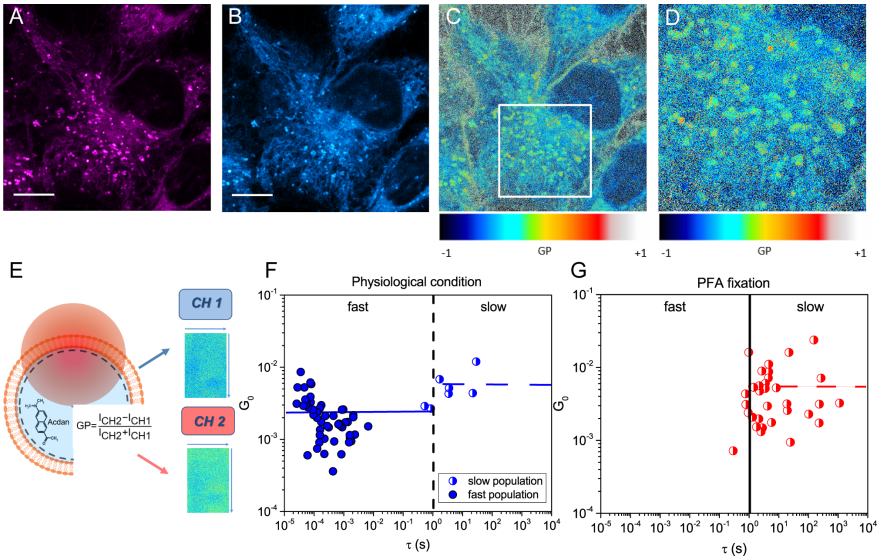


**Figure 5.22.** Imaging and circular-RICS analysis of ACDAN GP in lysosomes. **(A–C)** Confocal microscopy images of HeLa cells labeled with ACDAN. **(A)** CH1 collection range: 400–470 nm. **(B)** CH2 collection range: 475–545 nm. **(C)** GP image obtained by applying eq 4 to images in **(A)** and **(B)**. LUT of GP values is reported on the bottom. **(D)** The area enclosed within the white square in **(C)** is enlarged here to better show the GP map details from different intracellular organelles. LUT of GP values is reported on the bottom. **(E)** Scheme of the orbital tracking setup for GP acquisitions (with GP equation). CH1 and CH2 denote the two different acquisition ranges (400–470 nm for CH1 and 475–545 nm for CH2) and thus the two different fluorescence carpets acquired. (F,G) G0 vs τ plot showing the results of the GP analysis performed on HeLa cells cultured under physiological conditions (blue dots in F) and on HeLa cells fixed with PFA (red dots in E), respectively. The continuous black line in **(G)** shows the limit threshold identified by means of the statistical analysis of data from fixed cells (placed at τ = mean − SD). Such threshold helps identifying two regions of the G0 vs τ plot which are mostly populated by slow fluctuations ("slow" region) and fast fluctuations ("fast" region), respectively. It is used as a reference in all plots.

At this point, the orbital tracking approach is used to probe the GP evolution in time, in single lysosomes identified by the Lysotracker signal (see scheme in Fig. 5.22 E and, more in detail, in Fig. 5.23). GP is calculated pixel-by-pixel along the orbit and organized in a "GP carpet" that is finally processed by fluctuation spectroscopy (the complete workflow is reported

in Fig. 5.24). Circular-RICS analysis highlights the occurrence of GP fluctuations in the lumen of trafficking lysosomes. Figure 5.22 F shows the characteristic dissipation times (τ, equation 5) and the amplitudes (G0) of such fluctuations for lysosomes measured in HeLa cells under physiological conditions (blue dots; each dot represents the parameters extracted from a single lysosome, typically 2–5 lysosomes are measured in each cell). GP fluctuations measured among different lysosomes exhibit a broad distribution of characteristic dissipation times, with two main populations easily discernible: one in the micro-to-milliseconds time window, hereafter referred to as "fast" (Fig. 5.22 F, full dots), and the other in the seconds time window, hereafter referred to as "slow" (Fig. 5.22 F, half-full dots). Concerning the characteristic amplitude of the GP fluctuations, G0 values are typically distributed around an average value of about 10−3, an order of magnitude comparable to that previously measured in the cytoplasm of yeast cells by ACDAN GP analysis, even if on a different time scale (i.e., seconds).[449,450] Worthy of noting, we detect an overall increase in the GP fluctuation amplitude, on the average, in the "slow" population as compared to the "fast" one (see dashed blue lines in Fig. 5.22 F).

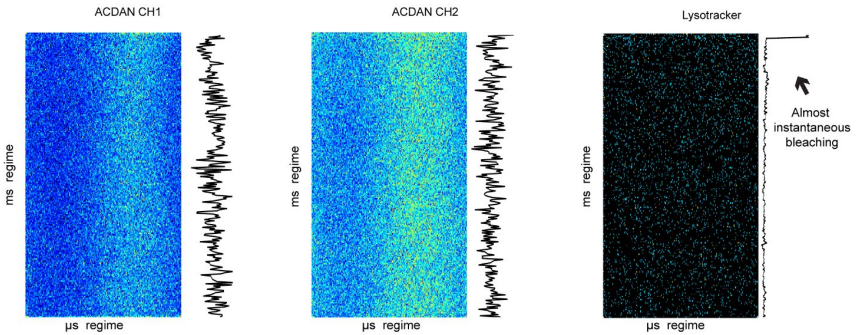


**Figure 5.23.** Comparison of ACDAN and Lysotracker carpets acquired by 3D feedback-based tracking. The carpet on the left corresponds to the signal of the first acquisition channel (CH1, collection range: 400-470 nm); the carpet in the middle represents the signal of the second acquisition channel (CH2, collection range: 475-545 nm); the carpet on the right corresponds to Lysotracker signal. It is worth noting that Lysotracker was used to localize the lysosomes to be tracked and then ACDAN signal was used as feedback source for tracking in light of its photophysical stability. Lysotracker signal, by contrast, was photobleached after few milliseconds from the beginning of the tracking experiment, as showed by the fluorescence intensity analysis associated with the carpet. Average intensities are reported both on the horizontal and vertical axes of each carpet.

We also anticipate here that a similar result is reported in all the conditions tested, as summarized in figure 5.25, and discernible from all G0 vs τ plots. At this point, several control experiments are performed to assess the nature of the ACDAN GP fluctuations observed in the lysosome lumen. A first control is performed in cuvette, using a 6 µM ACDAN aqueous solutions. While ACDAN diffusivity is correctly extracted from the intensity carpets, as expected, no detectable GP fluctuations are present in absence of cellular components (data included as '–' in Tab. 5.3).

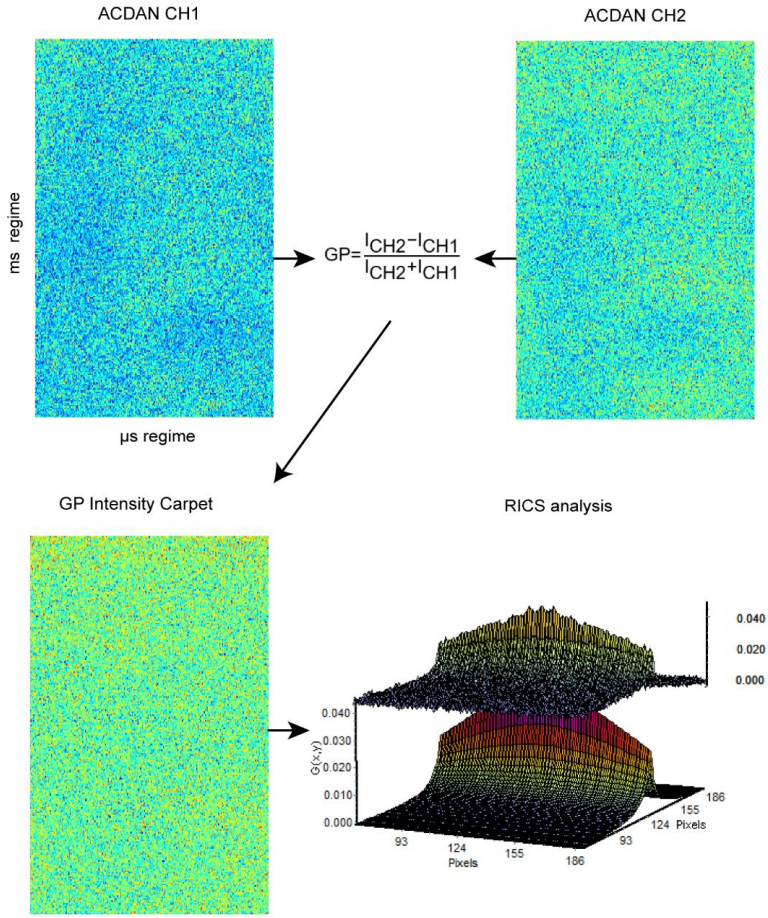


**Figure 5.24. Schematic representation of GP analysis workflow.** The two carpets of ACDAN corresponding to Channel 1 (CH1, range: 400-470 nm, top left) and Channel 2 (CH2, range: 475-545 nm, top right) are combined using Eq. 4 to obtain the GP carpet (bottom left). This carpet is then analyzed using RICS (bottom right).

A second control measurement is performed on PFA-fixed cells, a condition that preserves lysosome structural identity while physically preventing all dynamic biochemical processes. In this condition, fast ACDAN

GP fluctuations in the micro-to-millisecond regime are completely absent, and circular-RICS analysis highlights a clear shift of the experimental points toward slow fluctuations, in the second regime (half-full dots, Fig. 5.22 G). These experiments show that ACDAN GP fluctuations in the micro-to-millisecond range are characteristic of living cells only. Data from fixed-cell data are exploited to define a threshold ($\tau \sim 1$ s, at mean − SD, continuous black line) above which the method probes phenomena that are of no interest for the present analysis. It is worth noting that ACDAN GP fluctuates, under physiological conditions, mostly on the same time scale ($10^{-6}$–$10^{-3}$ s) that is known to be relevant for enzyme action (i.e., conformational changes, catalytic activity, etc.) and for the complementary, simultaneous, reorganization of the protein solvent proximity.[464] This suggests that intralysosomal GP fluctuates in space and time as a result of the complex molecular processes occurring in live cells and their spatiotemporal regulation. In other words ACDAN, in light of its exquisite solvatochromism, may be reporting on the spatiotemporally fluctuating concentrations (i.e., dynamics) of all the molecular species (e.g., proteins, lipids, metabolites, water) which participate in metabolism within the organelle. The observed variability in the characteristic time of GP fluctuation among different lysosomes might reflect the well-known intrinsic heterogeneity in lysosome function/metabolic activity depending, for instance, on their position within the cell and/or their luminal pH.[465,466] In fact, during the pixel-dwell time (i.e., 4 μs) ACDAN molecules explore several nanometers within the lysosome lumen (and across the observation spot): This represents the limit "resolution" of the spatial probing of the present scheme.

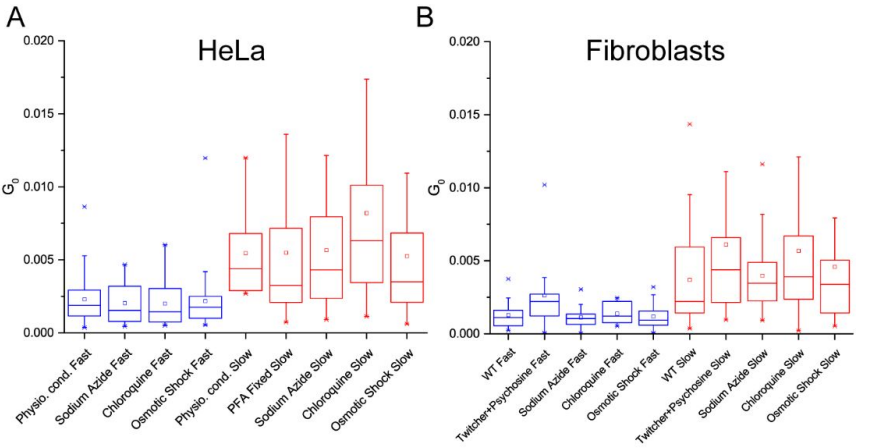


**Figure 5.25.** $G_0$ analysis for all the experimental conditions tested. Plot of the $G_0$ values of ACDAN measured inside lysosomes of HeLa cells **(A)** and fibroblasts **(B)**. $G_0$ values of the fast population are reported in blue while those of the slow population are shown in red, for all the experimental conditions tested. Upper and lower edges of the boxes represent the 25 and 75 percentile of the distributions, respectively; the middle line indicates the median value; the square inside the box shows the mean value; whiskers are standard deviations.

### 5.3.5 ACDAN GP Fluctuations Depend on Ongoing Metabolic Activity

In the following, we shall provide evidence that ACDAN GP fluctuations mirror the metabolic activity ongoing in the lysosome lumen. As a first experiment, we treat cells with sodium azide, a well-known blocker of ATP production (Fig. 5.26 A, upper panel, and Tab. 5.3). ACDAN and Lysotracker prove to be markers of the lysosome also under these conditions. Upon energy depletion, fast GP fluctuations almost completely disappear: ~85% of the retrieved values now fall within the slow region of the $G_0$ vs $\tau$ plot, the one characteristic of fixed cells (Fig. 5.26 A, upper panel, half-full green dots).

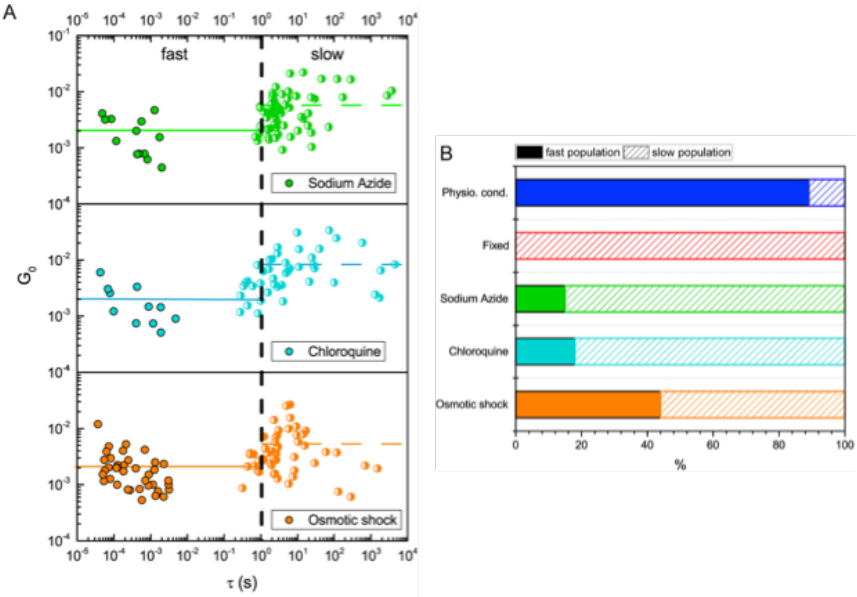


**Figure 5.26.** Circular-RICS analysis of ACDAN GP in lysosomes under different experimental conditions. **(A)** G vs τ plot of the GP0 fluctuation results obtained in HeLa cells treated with sodium azide (green dots), chloroquine (cyan dots), and osmotic shock (orange dots). The dashed black line indicates the limit threshold (mean – SD) already presented in figure 5.22 F,G. **(B)** Plot summarizing the fractions of experimental points retrieved within the "fast" region (filled histogram) and "slow" region (dashed histogram) of the $G_0$ vs τ plot for all the tested conditions.

Quantification of the fractional contribution of the "fast" and "slow" populations is reported in figure 5.26 B, green histogram. If ATP depletion is a generic treatment that inhibits all active processes within the cell, then chloroquine is a molecule that specifically affects lysosomal metabolism. In fact, it inhibits lysosomal enzymes (mostly hydrolases) by raising the intraluminal pH.40 Results obtained in the presence of 50 μM chloroquine nicely mirror those reported upon ATP removal (Fig. 5.26 A, middle panel, and Tab. 5.3). The fraction of fast GP fluctuations drops to ~18% (Fig. 5.26 B, cyan histogram). A third experiment is performed under osmotic shock

conditions (Fig. 5.26 A, lower panel, and Tab. 5.3). Here, the addition of pure water to the cell medium reflects an increased amount of water within the lysosome lumen. We report, as a direct consequence, an increase of the average size of lysosomes (i.e., for optimal tracking an increase of the orbit radius was needed, from 150 to 200 nm) and a ~ 20% increase of the average GP value as compared to the physiological condition (Tab. 5.3). Still, this is not intended as an experimental condition able to directly affect lysosomal activity and metabolism (at least not to the same extent of previous control experiments). Consistently with this, the fraction of fast GP fluctuations is almost double (44%, as showed in Fig. 5.26 B, orange histogram) as compared to ATP removal and lysosome basification, thus highlighting the continued presence of a significant lysosomal activity. It is worth noting that the average absolute value of ACDAN GP is quite similar among all the different conditions tested except for the osmotic shock (see Tab. 5.3).

### 5.3.6 ACDAN GP Fluctuations Are Altered in a Cellular Model of LSD

In this section, we present data from a murine cell model of KD. As described in detail in the Methods section, primary fibroblasts are extracted from ears of WT and TWI mice, the latter being a recognized naturally occurring animal model for the study of KD.[467,393] WT fibroblasts are cultured under normal conditions, while TWI fibroblasts are exposed to 100 μM PSY for 24 hours before imaging in order to exacerbate and better reproduce the KD phenotype. This latter treatment, indeed, mimics in the fibroblast model the toxicity typically elicited by the abnormal accumulation of PSY in the glial cells of the nervous system (considered to be the primarily

responsible for the pathogenesis).[64] In both cell preparations, ACDAN (and Lysotracker) proves to be a suitable marker of the lysosome, as reported by imaging in figure 5.27 A–H. First, the fluorescence signal originated from ACDAN within lysosomes is exploited to perform feedback-based 3D orbital tracking and fluctuation analysis. Fitting of the circular-RICS autocorrelation curves yields an ACDAN intralysosomal apparent D of 9.4 ± 4.2 $\mu m^2/s$ in WT cells and 6.9 ± 2.9 $\mu m^2/s$ in TWI cells treated with PSY. These values combined with eq 3 (Section 5.3.6) and the apparent hydrodynamic radius of ACDAN afford an estimate of the apparent viscosity of the lysosome lumen: 54 cP in WT cells (ranging from a minimum of 37 cP to a maximum of 98 cP, Fig. 5.27 I and Tab. 5.4) and 73 cP in TWI cells (ranging from a minimum of 51 cP to a maximum of 123 cP, Fig. 5.27 I and Tab. 5.4). The observed increase in lysosome viscosity in TWI cells as compared to WT ones (~35%) is consistent with the idea that the lysosome lumen is becoming more crowded owing to the accumulation of undigested lipids in TWI cells and well agrees with recent results on lysosome viscosity in a different LSD, as measured by subcellular nanorheology.[444] Worthy of mentioning, treatment of WT fibroblasts with sodium azide, chloroquine, and osmotic shock recapitulates results obtained in HeLa cells (see Fig. 5.28). At this point, the orbital tracking approach is used to probe the GP evolution in time, in single lysosomes.

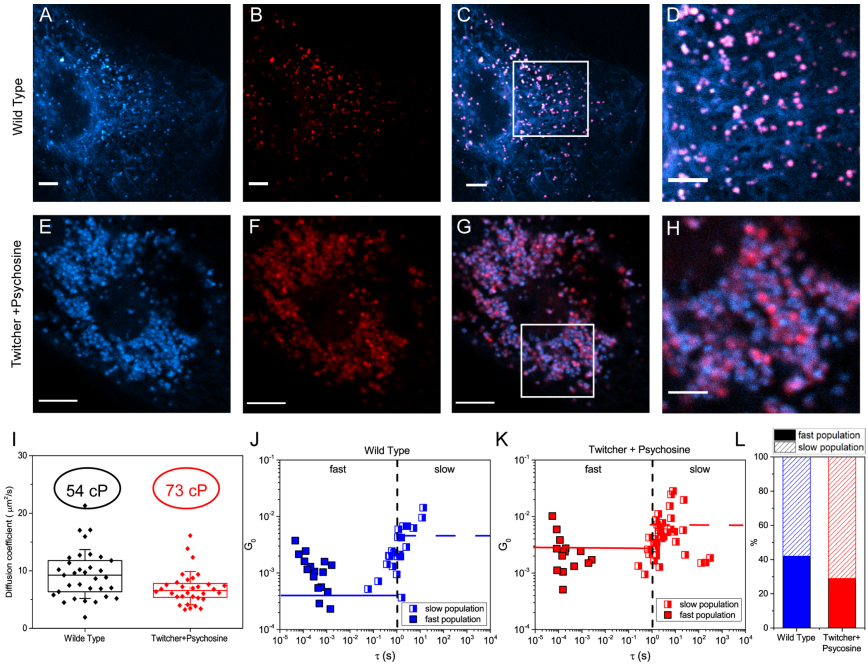


**Figure 5.27.** Circular-RICS analysis of ACDAN GP in a cellular model of LSD. Confocal microscopy images of WT primary fibroblasts labeled with ACDAN **(A)** and LysoTracker **(B)** and the corresponding overlay of the two signals **(C)**. Scale bar 5 μm. **(D)** Zoom of a cytoplasmic region (white square in Fig. 5C) shows labeled lysosomes and the overlay of the two signals recorded. Scale bar: 2 μm. **(E–H)** Analogously to WT fibroblasts, confocal microscopy images of psychosine-treated primary fibroblasts from Twitcher mice, labeled with ACDAN **(E)** and LysoTracker **(F)**, with the corresponding overlay of the two signals **(G)** (scale bar: 5 μm) and zoom from a cytoplasmic region **(H)** (scale bar: 2 μm). **(I)** Plot of the diffusion coefficients of ACDAN measured within lysosome lumen of both WT (black dots) and Twitcher (red dots) cells. Each point corresponds to a single measurement on a single lysosome. Upper and lower edges of the boxes represent the 25 and 75 percentile of the distributions, respectively; the middle line indicates the median value; whiskers are standard deviations. As highlighted in the graph, 54 cP (values ranging from 37 cP to 98 cP) is the average viscosity in lysosomes of WT fibroblasts, and 73 cP (values ranging from 51 cP to 123 cP) is the average viscosity in psychosine-treated Twitcher fibroblasts. **(J, K)** G0 vs τ plot showing the results of the GP analysis performed on WT fibroblasts (blue squares) and psychosine-treated Twitcher fibroblasts (red squares), respectively. **(L)** Plot summarizing the fractions of experimental points retrieved within the "fast" region (filled histogram) and "slow" region (dashed histogram) of the G0 vs τ plot for the two tested conditions.

| | | Wild-type | Twitcher+psychosine |
|---|---|---|---|
| | | Physiol. cond. | 24 h treatment |
| **RICS of ACDAN diffusion viscosity (cP)** | mean | 54 | 73 |
| | range | 37-98 | 51-123 |
| **RISC od ACDAN GP τ range (s)** | fast | $4.52 \times 10^{-5}$-$1.6 \times 10^{-3}$ | $5.44 \times 10^{-5}$-$3.4 \times 10^{-3}$ |
| | slow | 0.6-13.5 | 0.26-304 |
| **Fractional population** | mean | 43 | 30 |
| | range | 57 | 70 |
| **3D Feedback-Based ACDAN Imaging** | mean | 0.051 | 0.039 |
| | SD | 0.016 | 0.016 |

**Table 5.4.** Summary of Results on Primary Fibroblasts. As in Table 1, the upper part of the table shows the results from RICS analysis of ACDAN diffusion both in wild-type and Twitcher fibroblasts. Viscosity estimates are derived by eq 3 (Section 5.3.6), using the diffusion coefficients reported in figure 5.27 The middle part shows the results from RICS analysis of ACDAN GP. For both the "fast" and "slow" populations, the range of characteristic GP fluctuation times ( $\tau$ ) and the fractional population contributions are reported. Finally, in the lower part, the average GP values retrieved from 3D feedback-based ACDAN imaging of single lysosomes are reported.

As expected, circular-RICS analysis yields a broad distribution of characteristic GP dissipation times in the lumen of trafficking lysosomes in WT fibroblasts, from microseconds to seconds (Fig. 5.27 J), although slightly imbalanced in favor of the "slow" fluctuations in the seconds time window (57% of the total), contrary to what observed in HeLa cells (compare statistics reported in Tab. 5.3 and 5.4). Worthy of noting, in TWI fibroblasts, the fractional contribution of the "slow" GP fluctuations increases as compared to WT cells, reaching 70% of the total data collected (57% in WT cells). Based on the results collected so far, this effect can be interpreted as caused by the lysosome metabolism being impaired in TWI cells as compared to WT ones and by the lysosome lumen being more crowded in TWI cells than in WT ones (as testified also by the average GP value retrieved from orbital tracking measurements, see Tab. 5.4). Concerning the characteristic amplitude of the GP fluctuations, $G_0$ values are distributed similarly to those previously measured in HeLa (see Fig. 5.25). However, it is

found that TWI cells have a substantially higher amplitude of the GP fluctuation as compared to WT cells (see dashed lines in Fig. 5.27 J, K).

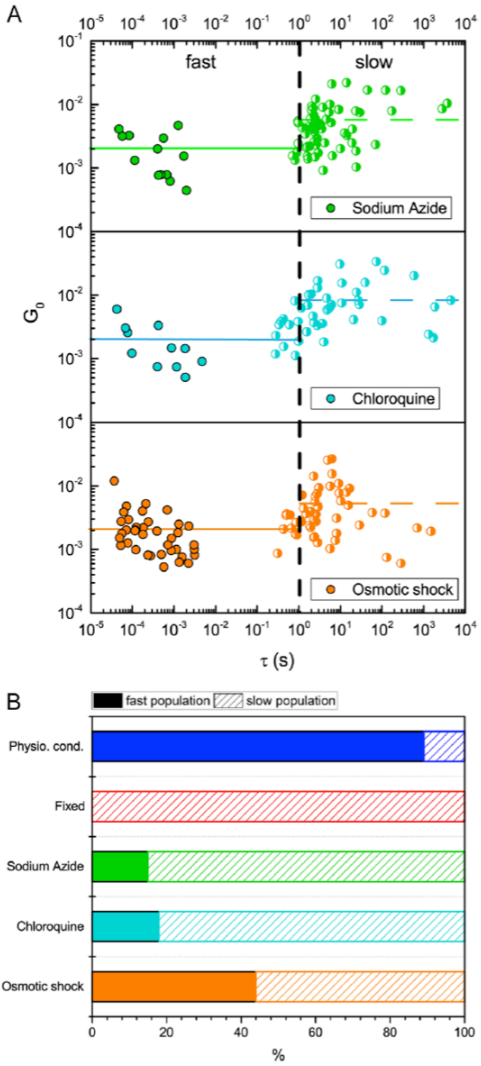


**Figure 5.28.** Circular-RICS analysis of ACDAN GP in fibroblasts. **(A)** G0-*vs*-τ plots showing the

results of the GP analysis performed on WT fibroblasts treated with Sodium Azide (green squares), Chloroquine (cyan squares) and osmotic shock (orange squares). In all plots, the dashed black line shows the limit threshold (Mean - SD) identified by the experiment on fixed HeLa cells, as explained in figure 5.22. **(B)** Graph showing the fraction of experimental points classified as 'fast' fluctuations (filled portion of the histogram) and 'slow' (dashed portion) for all the conditions analyzed. Refer to Table 2 for a complete summary of the results obtained using WT and TWI (+PSY) fibroblasts.

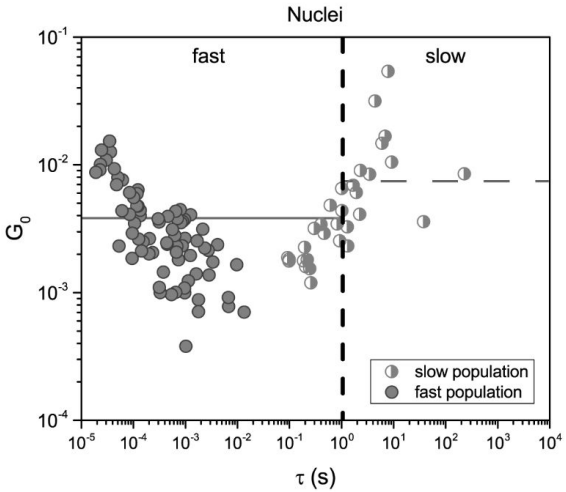


**Figure 5.29.** GP fluctuations of ACDAN in nuclei of HeLa cells. $G_0$-*vs*-$\tau$ plot showing the results of the GP analysis performed in the nuclei of HeLa cells under physiological conditions. Black dashed line corresponds to the Mean – SD from fixed cells, as explained in figure 5.22 G.

### 5.3.7 Concluding remarks

At this point, it is useful to discuss the molecular mechanisms driving the measured ACDAN GP fluctuations derived through our RICS analysis. As originally defined by Parasassi and co-workers, the GP function is sensitive to dipolar relaxation phenomena occurring in the DAN probe surroundings. Using Laurdan as the DAN probe and gel-to-liquid phase transitions in membranes under controlled conditions of water penetration, the authors successfully linked DAN dipolar relaxation to the presence of water

molecules with restricted mobility (restricted with respect to bulk-phase water) in the bilayer region where the probe was located.[468] A similar mechanistic interpretation was adopted by Thoke and co-workers to explain ACDAN GP fluctuations in the cytoplasm of Saccharomyces cerevisiae during glycolysis, although on a different time scale. Specifically, GP fluctuations were interpreted as fluctuations in the dynamics of intracellular water and the mechanism validated by replacing $H_2O$ by $D_2O$ in the cells.[449,450] Such interpretative framework can be transferred to the present data on the lysosome lumen. Given the rather constant chemical/molecular identity of the organelle during the measurement (few seconds), the dynamics of solvent dipolar relaxation extracted by correlation spectroscopy must be linked to the dynamics of the intraluminal molecular components, water being a ubiquitous, major constituent of the latter. In this picture, the GP fluctuation amplitude depends on the characteristic size of the fluctuating domain, analogously to what already proposed by others when measuring Laurdan GP fluctuations due to lipid domains diffusing on the cell membrane.[457] If we consider also the time dependence, small domains are expected to produce fast fluctuations with low amplitude (e.g., the "fast" GP fluctuation population), and large domains slow fluctuations with large amplitude (e.g., the "slow" GP fluctuation population). The measured GP fluctuation therefore probes the local modifications of the physicochemical properties of the milieu that are driven by the metabolic activity; these can be expected to occur in the whole cell albeit with different characteristic spatial and temporal scales. In fact, a preliminary analysis conducted here within the nucleus (see Fig. 5.29) highlights fluctuations of solvent dipolar relaxation in this compartment, although with slightly different

characteristic timing and amplitude compared to the lysosome. More in general, compelling evidence from the available literature supports the idea that a variety of mesoscale organizational levels do exist within the cell, in addition to the canonical membrane-bound organelles, and contribute to the spatiotemporal regulation of molecular processes. For instance, the cytoplasm is now seen as a highly heterogeneous environment, where solutes (proteins) are likely bound to scaffold structures (e.g., membranes, cytoskeleton) rather than freely diffusing and colliding, thus leaving complementary nanoscopic "pools" of solvent (i.e., water) with bulk-like properties.[469] Interestingly, a similar organization has been theoretically postulated for the prokaryotic cytoplasm.[470] Here, in absence of internal membranes and scaffold structures, the hydrophobic effect would act as master regulator, dividing the cytoplasm into dynamically crowded macromolecular regions and topologically complementary pools of solvent (i.e., water) with bulk-like properties.[471,472] In this regard, Parry and co-workers, based on SPT measurements conducted on foreign particles of different sizes, proposed that the bacterial cytoplasm displays properties of glass-forming liquids and that cellular metabolism fluidizes the cytoplasm, allowing larger components to escape their local environment and explore larger regions of the cytoplasm.[473–475] Finally, a growing body of data was collected on intracellular organelles that do not have an enclosing membrane yet remain coherent structures with a peculiar molecular identity. Examples include assemblies in the nucleus such as the nucleolus, Cajal bodies, nuclear speckles, and also cytoplasmic structures such as stress granules, P-bodies, and germ granules. Cuvette experiments using selected purified components support the idea that such membrane-less assemblies

are formed through phase separation, achieved either through nuclear polymerization of one (or more) component that acts as a seed to form solid/crystalline assemblies[472,473] or through liquid–liquid phase transition[448,473,476] resulting in liquid droplet formation that can eventually "age" into gels or glass. These processes create compartments that are enriched in pools of active biomolecules, while others are depleted[477], thus actively participating to the regulation of intracellular processes. Further investigations are certainly needed to uncover possible mechanistic links between the physical properties of the intracellular environment and metabolism. In this regard, Thoke and co-workers[449,450], building on a previous theoretical background[478], suggested a possible determining role for ATP and its energy-storing derivatives. In this view, ATP acts on metabolic processes through an "inductive effect" upon binding to intracellular proteins and, in turn, modulating their conformational state, their ion-binding properties, and the physicochemical properties of their environment (e.g., the dynamic state of water in the protein proximity). Its action can span over large spatial (from organelles to the entire cell) and temporal (from the microsecond time scale observed here to the second/min time scale of ATP production by glycolysis) scales as well as across the phylogenetic tree (from prokaryotes to eukaryotes), thus ideally enclosing all the observations collected so far.

### 5.3.8 Material and methods

#### *Cell Culture and Treatments.*

HeLa cells (CCL-2 ATCC) were cultured in DMEM without phenol red (Gibco), supplemented with 10% FBS (Gibco), 100 U/mL of penicillin, and

100 µg/mL of streptomycin in a humidified incubator at 37 °C and 5% $CO_2$. Cells were seeded on 22 mm glass bottom dishes (WillCo Wells) and allowed to adhere overnight in a 37 °C and 5% $CO_2$ cell culture incubator. For a typical experiment of lysosome imaging, cells were labeled by using both ACDAN and Lysotracker. ACDAN (Sigma-Aldrich) was dissolved from the stock solution to the desired concentration of 5 µM directly in the cell-culture medium. Cells were washed once with PBS and incubated for 20 minutes with the ACDAN-containing medium. Just before the experiment, the ACDAN-containing medium was removed, cells washed once with normal medium, and LysoTracker Red DND-99 (Invitrogen) added to the desired final concentration of 60 nM in the growth medium. To alter lysosome pH, chloroquine (Sigma-Aldrich) from the stock was solubilized at a concentration of 1 mM in PBS and then diluted to 50 µM in the cell-culture medium. Cells, after incubation with ACDAN, were washed once with medium and then incubated with chloroquine- containing medium (with Lysotracker added at 60 nM). For ATP depletion experiments, cells already treated with ACDAN were washed with medium and incubated in glucose-free DMEM (Gibco) containing 10% FBS, 100 U/mL penicillin, 100 µg/mL streptomycin, 10 mM sodium azide, and 6 mM 2-deoxy-D-glucose (and 60 nM Lysotracker). For swelling experiments, a hypotonic solution was prepared by mixing 50% of normal cell medium with 50% of deionized water. Cells were incubated for 20 minutes with the hypotonic solution (and ACDAN), then washed once with hypotonic solution, and incubated with solution and Lysotracker. For cell fixation, cells were rinsed three times with PBS and fixed in 4% PFA for 10 minutes at RT. After fixation, the cells were washed three times in PBS and incubated for 20 minutes with ACDAN and

Lysotracker. For lysosome labeling by transient transfection, the CD63-pEGFP C2 plasmid (Addgene plasmid # 62964) was introduced into cells by electroporation using the Neon Transfection System 10 µL Kit (Invitrogen). In detail, cells were trypsinized, pelleted, and resuspended in resuspension buffer R. DNA (0.1 µg/µL) was added to 5 × $10^5$ cells in 10 µL buffer, followed by electroporation using the Neon Transfection System (Invitrogen) operating at a voltage of 1005 V and width of 35 ms. The cells were then seeded and cultured in DMEM containing 10% FBS and supplements without antibiotics and used for imaging experiments 24 hours later. For experiments with Lysotracker and QDs, cells were washed 3 times with PBS, and then for each 22 mm glass bottom dish, 5 µL of QD stock solution (Qdot 545 ITK Amino PEG, Thermo Fisher Scientific) was suspended in 1 mL of growth medium without serum. The suspension was then sonicated for at least 5 min. The 1 mL of medium and QDs was then poured in the glass- bottom dish containing cells. After 3 hours of incubation, glass-bottom dishes were washed 3 times with PBS containing $Mg2^+$ and $Ca^{2+}$ (in order to avoid cell detachment) and then incubated again with FBS-containing medium. The day after, cells were washed three times with PBS containing $Mg^{2+}$ and $Ca^{2+}$ and then incubated with medium containing FBS and Red Lysotracker at a concentration of 60 nM, as described above. After 20 min, cells were ready for microscope analysis. Primary WT and TWI fibroblast were extracted from the ears of WT and TWI mice. TWI heterozygous mice (TWI± C57BL6 mice; Jackson Laboratories) were used as breeder pairs to generate homozygous Twitcher mice (TWI−/−). Animals were maintained under standard housing conditions and used according to the protocols and ethical guidelines

approved by the Ministry of Health (permit number: CBS-not. 0517; approved the 4/1/2018). The genetic status of each mouse was determined from the genome analysis of the TWI mutation, as previously done by some of us.[479] Briefly, after anesthesia, mice ears were extracted, washed with sterile water, and cut into small pieces. All pieces were than collected in an eppendorf tube and added with collagenase XI (C7657–100 mg; Sigma-Aldrich) diluted 1:1 in high glucose DMEM supplemented with 10% of heat-inactivated FCS, 2 mM L-glutamine, and 1% penicillin/streptomycin (all products were from GIBCO-Life Technologies). After 2 hours of incubation at 37 °C, the Eppendorf tube was centrifuged for 5 minutes at 200 g, the supernantant was discarded, and the pellet was washed with 2 mL of PBS and centrifuged again discarding the supernatant. Trypsin-EDTA 0,05% (Thermo Fisher Scientific) was then added to the tube and left 45 minutes at 37 °C. The tube was then centrifuged, and the pellet was resuspended in the complete DMEM described above. Obtained cells were thus divided pipetting up and down with a syringe, plated in a 60 mm cell plate (Falcon), and maintained at 37 °C in a humidified atmosphere containing 5% $CO_2$. The next day, cells were washed, and media was replaced. After reaching confluence (approximately 3–4 days), cells were washed with 1 mL of PBS and split with a ratio of 1:2. For the imaging experiments, WT and TWI cells were plated in 12 mm Willco dishes (~7 × 104 cells/dish), and 6 hours later TWI cells were exposed to 100-μM PSY. PSY was dissolved in DMSO, and control cultures received the same quantity of vehicle, which never exceeded 0.6% v/v. All imaging experiments were performed 24 hours after plating.

*Live-Cell Imaging and Co-Localization Experiments.*

Live-cell imaging for co-localization assays were carried out on a Zeiss LSM 880 raster scan confocal microscope equipped with three detectors (two GaAsP and one Airyscan) using a 63× NA 1.40 oil immersion objective. ACDAN was excited with laser light at 405 nm, while its emission was collected in the 410–480 nm range. CD63-EGFP was excited at 488 nm and collected in the 490–550 nm range. Lysotracker was excited at 561 nm and collected in the 570–650 nm range. For the three-channel experiment described in figure 5.15 A–G, the signals from ACDAN, EGFP, and Lysostracker where acquired in "sequential mode" operating on lines, that is, the system records the three signals sequentially switching-on only one laser per channel (with the other two switched off), and it repeats the operation for each image line. This imaging mode reduces cross-talk between channels to a minimum, while maintaining high temporal resolution (the three channels are acquired in approximately 0.5 s). Co-localization of the signals was assessed by calculating the Manders' coefficients. Manders' coefficients values range from 0 to 1, with '1' indicating the maximum co-localization of the two signals.[480]

### *Orbital Tracking Setup and Experiments.*

Orbital tracking measurements were carried out adopting the ISS Orbital Tracking System, analogous to that previously described[481], and embedded in an Olympus FluoView 1000-ASW-2.0 confocal laser microscope. During tracking, the ISS system sends two π/2-phase-shifted sine wave voltage signals to the scanning mirrors of the microscope in order to generate a laser circular orbit; the offset values of the sine wave signals determine instead the scanning center. In tracking mode, the position of the center of the orbit is updated at each tracking cycle (every 4 orbits in our

case) in accordance to an algorithm based on fast Fourier transform (FFT) of the collected reference signal.[482] From the FFT of the fluorescence signal, one can get the continuous (or "DC") component (i.e., the zeroth term of the Fourier series) and its "AC" component as the first harmonic term of the Fourier series. Having the "DC' and "AC" components allows to determine the distance of a tracked object from the center of the orbit using the modulation of the signal (defined a modulation = AC/DC) and the angular coordinate by the phase of the AC term. The tracking system changes the sine wave signals in such a way to keep the modulation at its minimum, thus keeping the particle at the center of the orbit. In our experiments, the fluorescence signal was collected on 256 pixels around a 150 nm-radius orbit with a period of 1024 ms (thus using a pixel dwell time of 4 μs derived from 1024 ms/ 256 px = 4 μs), and the orbit position was updated every 4-orbit period (defined as a "cycle", approximately 4 ms).

For experiments on the diffusivity of ACDAN, the simultaneous excitation of ACDAN and Lysotracker was achieved by two-photon Ti:sapphire laser (Chameleon Vision, Coherent) tuned at 780 nm. Fluorophore emission was collected by using a 60× planApo water immersion objective (NA = 1.2). ACDAN emission was measured in the 430–530 nm range (CH1), while Lysotracker signal was collected in the 570–650 nm range (CH2). For experiments on the GP of ACDAN, Ti:sapphire laser (Chameleon Vision, Coherent) tuned at 780 nm was used to excite both ACDAN and Lysotracker. In this case, three channels were activated, the first two to split ACDAN signal for GP reconstruction (400–470 nm, CH1, and 475–545 nm, CH2, respectively), the last to collect Lysotracker emission (570–650 nm, CH3). Please note that this latter setup was used also for GP

imaging at the whole cell level (i.e., to get GP spatial maps, see Fig. 5.22 A-D) with the microscope system operating in standard raster-scan mode.

For experiments on the diffusivity of QDs "545" within lysosomes, the simultaneous excitation of QDs and Lysotracker was obtained by using a 515 nm argon laser line. Fluorophore emission was collected by using a 60× planApo water immersion objective (NA = 1.2). QDs emission was collected in the 530−550 nm range (CH1), while Lysotracker signal was collected in the 570−650 nm range (CH2).

Worthy of mentioning, in all the experiments described in this work, Lysotracker signal was used to identify the target organelle for the tracking experiment. Both in the cases of two-photon excitation at 780 nm and one-photon excitation at 515 nm, Lysotracker signal vanished after few milliseconds of laser irradiation (i.e., few orbits) due to extensive photobleaching (Fig. 5.23). By contrast, ACDAN signal proved to be stable under the same experimental conditions. By the way, the very first orbits from ACDAN intensity carpet(s) were not considered for fluctuation analysis (see below).

### *Circular-RICS Analysis along the Orbit.*

As mentioned, the fluorescence intensity signal collected during the orbital tracking measurements was stored in intensity carpets where each column represents a pixel along the orbit and each row reports each orbit collected, as previously described.[439] Adjacent columns represent adjacent pixels along the orbit, while adjacent rows correspond to consecutive orbits during the acquisition (Fig. 5.15 C). Spatial correlation was calculated on intensity carpets using the following equation:

$$G\ (\xi,\psi) = \frac{\langle I(x,y)I(x+\xi,y+\psi)\rangle_{x,y}}{\langle I(x,y)\rangle^2_{x,y}} \quad (1)$$

where I is the intensity of the pixel at the coordinates x (horizontal axis of the carpet) and y (vertical axis), and ξ and φ are the spatial increments in the x and y direction, respectively. Square brackets indicate the average operation over all spatial coordinates (i.e., x and y). Spatial correlation curves were obtained from experimental carpets, and, later, these curves were fitted using the spatial correlation equation for circular scanning[483]:

$$\frac{\gamma}{N}\left\{1+\frac{4D(\tau_p\xi+\tau_l\psi)}{w_0^2}\right\}^{-1}\times\left\{1+\frac{4D(\tau_p\xi+\tau_l\psi)}{w_z^2}\right\}^{-1/2}\times\exp\left\{\frac{-\frac{1}{2}\left[\left(\frac{2\xi\delta r}{w_0}\right)^2\right]}{1+\frac{4D\,(\tau_p\xi+\tau_l\psi)}{w_0^2}}\right\} \quad (2)$$

where D is the diffusion coefficient, and $w_0$ and $w_z$ are, respectively, the planar and axial waists of the laser beam profile. Also, $\tau_p$ is the pixel dwell time and $\tau_l$ is the time between lines in the intensity carpet (which, in this case, corresponds to the orbit time). The fitting of the experimental curve with eq 2 (Fig. 5.15 D bottom) allowed us to find the diffusion coefficient (D) of the molecules studied (i.e., ACDAN or QDs). All this analysis was conducted using SimFCS software (www.lfd.uci.edu, University of California Irvine) that contained the above-described functionalities. The Stokes–Einstein equation below was used to derive either the hydrodynamic radius or the solvent viscosity from diffusion measurements:

$$D = \frac{K_bT}{6\pi\eta r} \quad (3)$$

Here, diffusion coefficient (D) is directly proportional to temperature (T) through the Boltzmann constant ($k_B$) and inversely proportional to hydrodynamic radius (r) and solvent viscosity (η).

*ACDAN GP Analysis and Fluorescence Correlation Spectros- copy.*

Data acquired with the Orbital Tracking System were analyzed with simFCS software (www.lfd.uci.edu, University of California Irvine) in two different ways: (i) circular-RICS analysis on intensity carpets (described above) and (ii) circular-RICS analysis on GP carpets. To perform circular-RICS analysis on the GP carpet, the independent traces originated from the split collection of the emission of ACDAN fluorescence (CH1 and CH2) were processed using the following GP equation:

$$GP = \frac{CH2-CH1}{CH2+CH1} \quad (4)$$

If applied pixel-by-pixel, eq 4 generates a GP "carpet" (Fig. 5.18). GP carpets are then analyzed using the same circular-RICS tool mentioned above. Thus, D and $G_0$ values were obtained by fitting the correlation curves. The D value, in this specific case, was linked to the characteristic average duration ($\tau$) of the GP fluctuations contained in the carpet by using the relation represented in eq 5:

$$\tau = \frac{W_0^2}{4D} \quad (5)$$

where $w_0$ is the radial waist of the laser beam profile (in this case 0.3 μm).

*Fluorescence Spectrum Acquisition and GP Evaluation.*

ACDAN was dissolved in different solvents at a concentration of 2.5 μM. Each solvent is characterized by a different dielectric constant (data not shown). The fluorescence emission spectrum of each solution was collected using a Varian Cary Eclipse Fluorescence Spectrophotometer in the 400−545 nm range. To evaluate the characteristic GP value of each solution, ACDAN spectrum was split into two regions, similarly to what performed at the microscope. The first (CH1) was computed by integrating the spectrum

intensities in the 400−470 nm range, while the second (CH2) by integrating the emission in the 475−545 nm range. GP values were then obtained by using eq 4.

### *Synthetic Vesicles with QDs.*

The lipid 1,2-dipalmitoyl-sn-glycero-3-phosphocholine (DPPC, 10 mg/mL in chloroform) was purchased from Avanti Polar Lipids (Alabaster, AL, USA). Low gelling temperature agarose BioReagent was purchased from Sigma-Aldrich (St. Louis, MO, USA). Liposomes of DPPC were prepared using the standard method.[484] A thin film of lipid was obtained by evaporating 100 μL of chloroform solution containing 1 mg of DPPC by placing the sample in a centrifugal evaporator under vacuum for 2 hours. The lipid film was hydrated by adding 245 μL PBS at pH 7.45 and 5 μL of the stock solution of QDs at 50 °C. The final DPPC concentration was 5 mM. The vescicles were frozen in liquid nitrogen and then thawed at 50°C in a water bath. The freeze-thaw cycle was repeated five times.[483] Agarose gel was used to immobilized liposomes as described previously.[485] Agarose was dissolved in PBS at a concentration of 1% w/v. Liposomes were mixed in gel, while the agarose was in the fluid state. After mixing, the solution was placed on a glass bottom Petri dish and was left at RT for jellification. Following jellification, lipid vesicles containing QDs were analyzed using Orbital tracking system. Fluorescence signal was collected and analyzed as described above (Circular-RICS Analysis along the Orbit section). Inserting the average value of D found in this case and the well-known viscosity of water (i.e., 0.894 cP) in eq 3 allowed us to find the hydrodynamic radius of QDs. The value of the radius derived was then averaged with the value

obtained for QDs in suspension and used to evaluate the viscosity of lysosomes containing QDs (eq 3), as described above for ACDAN.

### *Preparation of Sucrose Solutions.*

Solutions with different concentration of sucrose 50%, 55%, 60%, and 66% w/w were prepared by warming up the solution with the appropriate amount of sucrose and water/buffer pH 5. In each sample, ACDAN was added to obtain the desired concentrations, namely: 0.1, 0.5, 1, 10, 30, and 50 μM.

### *Calibration of Hydrodynamic Radius of QDs in Buffer Solution.*

For calibration of hydrodynamic radius of QDs, we suspended 5 μL of QD stock solution in 250 μL of 50 mM borate buffer. The suspension was then poured in a 22 mm glass bottom dish for cell culture and analyzed under the Orbital tracking system. The fluorescence signal was collected and analyzed as described above for ACDAN (Circular-RICS Analysis along the Orbit section). Through eq 3, the average hydrodynamic radius was evaluated and averaged with the value obtained from vesicles with QDs. The result was then used to compute the viscosity of lysosomes when analyzed with QDs.

### *Statistical Analysis.*

Diffusion coefficients (and viscosities, derived by eq 3) are normally distributed in each experiment. Thus, their values are reported throughout the text as mean ± SD and compared among different experiments using the Student's t test. By contrast, GP fluctuation values are not normally distributed. Their values are reported in the text using the minimum-maximum range. In this case, distributions from different experiments were

compared using the Mann–Whitney test. Each analysis was conducted using OriginPro 9. Differences were considered significant for $P < 0.05$.

# Chapter 6: Conclusions and future perspectives

During my PhD I worked on Krabbe disease (KD), a rare neurodegenerative disease without any cure currently available. KD is caused by a deficiency of the lysosomal enzyme GALC, which is essential for the metabolism of galactosylsphingolipids of the nervous system. However, differently from other LSDs, the supply of the therapeutic enzyme in the systemic circulation is not an effective strategy because of the presence of the BBB. Furthermore, despite it is known that GALC deficiency is responsible for PSY-tissue accumulation and consequent demyelination and neurodegeneration, KD pathogenesis is not exhaustively known yet.

In this scenario, the final aims of this thesis were: **(i)** to set up and test a new nanomedicine-based ERT for KD; **(ii)** to investigate the involvement of the autophagy pathway in the molecular pathogenesis of KD and to consider autophagy modulation as a possible therapeutic strategy. Moreover, Chapter 5 allows adding some knowledge on KD pathogenesis thanks to the usage of two innovative research methods: quantitative microproteomics and 3D orbital tracking microscopy.

Regarding aim **(i)**, I developed a new nanomedicine-based approach for ERT in KD. The nanovector, which was developed in collaboration with the group of Dr. Giovanni Signore of the Italian Institute Technology, was based on *cross-linked enzyme aggregates* (CLEAs) of recombinant GALC, which were encapsulated into PLGA NPs functionalized with one of the following BBB targeting ligands: Ang2, g7 or Tf2. Functionalized GALC-NPs (GALC-Ang2-NPs; GALC-g7-NPs and GALC-Tf2-NPs) were first preliminary characterized, revealing to maintain low hydrodynamic dimension (< 200 nm), a rather uniform z-potential and good encapsulation efficiency (40-

75%). Then, the three different formulations were tested for ERT *in vitro*, in both primary murine and human KD fibroblasts. All the formulations were able to deliver functional GALC into cells lysosomes, significantly increasing intracellular enzymatic activity in a dose and time-dependent manner up to the level of the wild type cells. Subsequently, we tested the formulations in the Twitcher mouse, the naturally occurring mouse model for KD. We demonstrated that, after 4 hours from a single intraperitoneal injection of the drug, GALC enzymatic activity in the brain of the affected mice can be recovered up to the level of the heterozygous carrier mice. It is an exciting result if considering that heterozygous mice, as also happen in the case of human carriers, present a healthy phenotype. As expected, GALC activity was found also in accumulation organs like liver and kidneys, confirming that NPs are correctly metabolized from the body without losing enzymatic activity. Interestingly, instead, GALC recovery was not achieved in the PNS. This suggests the need of a specific protocol for the treatment of the PNS, as a different treatment time or differential NP functionalization. Further studies to address this point will be necessary, being the deterioration of PNS performances a typical feature of KD along with CNS involvement.

Thus, given the established ability of our developed drug to pass the BBB and release the active enzyme, future experiments to continue the work have currently been planned. First, an accurate pharmacokinetic and pharmacodynamic characterization of the drug will be carried out. This will allow choosing the more appropriate dose and time for drug administration in view of a repeated and prolonged treatment. Later, mice will be treated with the selected modality of administration, and the phenotypic recovery

will be evaluated [mice survival, motor behavior, biochemical (especially PSY content) and morphological characterization of CNS and PNS].

As reported in the literature, however, the recovering of GALC activity may not be sufficient to completely rescue the KD phenotype, suggesting that pathways not yet taken into account could be implicated in KD pathogenesis. From this perspective, I started to investigate the possible contribution of autophagy dysregulation in the molecular pathogenesis of KD **(ii)**. Autophagy is a vital lysosomal pathway that allows the recycling of cellular constituents and that has been found altered in many neurodegenerative conditions and LSDs. However, almost nothing was known about autophagy in KD when I started my PhD program. Specifically, I studied autophagy in two KD cellular models, demonstrating the presence of a dysregulation at the level of some fundamental autophagic markers, such as LC3, p62 and Beclin-1. I also showed that autophagy is dysregulated in the Twitcher mouse, proving for the first time *in vivo* that autophagy might concur in the pathogenesis of the disease. Finally, I demonstrated that autophagy activation [by both m-TOR dependent (Lithium) and m-TOR independent (Rapamycin) pathways] has positive effects on cell viability and on protein aggregates accumulation *in vitro*, laying the foundations for pre-clinical testing of autophagy activators in the TWI mouse. Ongoing and future experiments will include a systematic pre-clinical test in Twitcher mice of both Lithium and Rapamycin, alone or in combination. Also in this case, behavioral features will be monitored during treatments, as well as biochemical and morphological parameters. Most importantly, in case of positive results this therapy will be readily applicable to humans for clinical

trials, given that Lithium and Rapamycin are already available as pharmaceutical preparations.

Additionally, a help in the understanding of the pathogenesis of KD also arises from the two studies I made in strict collaboration with the groups of Dr. Liam Mc Donnel of the Fondazione Pisana per la Scienza Onlus and Prof. Francesco Cardarelli of our institute. In particular, thanks to the first collaboration we demonstrated by quantitative microproteomics the dysregulation of multiple molecular pathways in both CNS and PNS of the Twitcher mice, including autophagy, inflammatory response and cell adhesion. Numerous up or down-expressed proteins which have been individuated deserves to be deeper investigated. The second collaboration, instead, thanks to the usage of an advanced 3D orbital tracking imaging method, allowed demonstrating the presence of altered solvent viscosity and dynamics in the lumen of trafficking KD lysosomes. Next steps plan to repeat these experiments in more representative cellular types for KD, as primary oligodendrocytes, astrocytes and neurons. Both works add a little piece to the complex and incomplete puzzle of the KD pathogenesis.

Studies conducted in this thesis, in conclusion, support the emerging idea that, due to the complexity of KD, a combination therapy could be a reliable way to try to find an effective cure for this disease. In a forward-looking vision, in fact, autophagy modulation and/or other complementary therapeutic strategies could be used in combination with a main GALC-deficiency correcting therapy (as our developed nanomedicine-based ERT and/or gene therapy) to help in achieving the complete KD phenotype rescue.

# List of abbreviations

3D: three dimensions
AAV: adeno associated virus
ACD-ase: acid ceramidase
ACDAN : 6-acetyl-2-dimethylaminonaphthalene
AD: Alzheimer disease
AJ: adherent junctions
ASL: amyotrophic lateral sclerosis
ATG: autophagy related
ATTC: american type culture collection
AY: activity yeld
BBB: blood brain barrier
BH: Benjamini-Hochburg
Bif-1: endophilin B1
BMT: bone marrow transplantation
BOB: blood ocular barrier
BSA: bovine serum albumine
CGT: UDP-galactose ceramide galactosyl transferase
CLEAs: cross-linked enzyme aggregates
CNS: central nervous system
CSF: cerebrospinal fluid
D: diffusion coefficient
DCF: 2',7'-dichlorofluorescein
DCM: methylene chloride
DE: double emulsion
DMEM: Dulbecco's modified eagle medium
DMSO: Dimethylsulfoxide
DPPC: 1,2-dipalmitoyl-sn-glycero-3-phosphocholine
DRPLA: dentatorubral-pallidoluysian atrophy
DTT: DL-dithiothreitol
EA: enzyme aggregates
EDTA: ethylenediaminetetraacetic acid
EE: encapsulation efficiency
ER: endoplasmic reticulum
ERT: enzyme replacement therapy
ESCRT: endosomal sorting complexes required for transport
FBS: fetal bovine serum
FCS: fetal calf serum
FD: Fabry disease
FDA: food and drug administration
FDR: false discovery rate
FFT: fast Fourier transform

FLIM: fluorescence lifetime imaging
FPS: fondazione pisana per la scienza
FSC: forward scatter
GAA: α-glucosidase
GAG: glycosaminoglycan
Gal-cer: galactosylceramide
GALC: galactosylceramidase
GD: Gaucher disease
GO: gene ontology
GFAP: glial fibrillary acidic protein
GLD: globoid cell leukodistrophy
GLUT-1: Glucose transporter 1
GP: generalized polarization
GSD: glycogen storage disease
GSK-3b: glycogen synthase kinase 3 beta
GT: gene therapy
HD: Huntington's disease (Section 4)
HD: hydrodynamic diameter (Section 3)
HEPES: 4-(2-hydroxyethyl)-1-piperazineethanesulfonic acid
HET: heterozygous
HGMD: human gene mutation database
HLA: human leukocite antigen
HOPS: homotypic fusion and vacuole protein sorting
HPLC/MS: high-pressure liquid chromatography/ tandem mass spectrometry
HSCT: hematopoietic stem cell transplantation
IC: intracerebral
ICAM-1: intracellular adhesion molecule 1
IDS: iduronate 2-sulfatase
IGF-II: insulin like growth factor 2
IL-2: interleukin-2
IMPase: inositol monophosphates
IP: intraperitoneal
IT: intrathecal
KD: Krabbe disease
Ki quenching assay
KI: potassium iodide
KSV: Stern-Volmer quenching constant
LAMP-2: lysosomal associated membrane protein-2
LAT-1: large neutral amino acid transporter
LB: Luria Bertani
LC3: light chain 3
LCD:lysosomal cell death
LCM: laser capture microdissection

LCM: laser capture microdissection
Li: lithium
LMP: lysosome membrane permeabilization
LRP-1: lipophorin receptor 1
LSD: lysosomal storage disorder
LV: lentiviral
M6PR: mannose 6 phosphate receptor
MBP: myelin binding protein
MOCs: Manders' overlap coefficients
MPS: mucopolysaccharidosis
MSD: mean square displacement
MSD: multiple sulphatase deficiency
mTOR: mammalian target of rapamycin
MVB: multivesicular bodies
N,N-DMS: N,N-dimethylsphingosine
NA: numerical aperture
NAC: N-acetylcysteine
NBR1: neighbor of *BRCA1* gene 1
NCL1: neuronal Ceroid Lipofuscinosis 1
NCLs: neuronal Ceroid Lipofuscinosis
ND: neurodegenrrative disorders
NP: nanoparticles
NSC: neural Stem Cell
ORA: overrepresentation enrichment analysis
PBS: phosphate buffered saline
PCD: protein conformational disorders
PD: Parkinson's disease
PE: phosphoethanolamine
PEI: prolyl endopeptidase inhibitor 2
PFA: paraformaldehyde
PI: propidium iodide
PI3K: phosphoinositide 3-kinase
PKC: protein kinase C
PLA2: phospholipase A2
PLGA-PEG: poly(lactic acid) and poly(ethylene glycol)
PLGA: poly-(lactide-co-glycolide)
PND: post natal day
PNS: peripheral nervous system
PPT1: palmitoyl protein thioesterase 1
PCA: principal component analysis
PSMs: peptide spectral matches
PSY: psychosine
R-CLEAs: reduced CLEAs

RAP: receptor associated protein (Section 3)
RAP: rapamycin (Section 4)
RESV: Resveratrol
RICS: raster image correlation spectroscopy
RIPA: radioimmunoprecipitation assay
ROI: region of interest
ROS: reactive oxigene species
RP-S: reversed-phase
SA: specific activity
SActr: specific activity of the unaltered enzyme
SAs: activity of the sample
SBMA: spinobulbar muscular atrophy
SCAs: spinocerebellar ataxias
SEM: standard error of the mean
SNAREs: endosomal sorting complexes required for transport
SOD1: copper/zinc superoxide dismutase 1
SPS: synchronous precursor selection
SRT: substrate reduction therapy
SSC: side-scatter
STED: stimulated emission depletion
TEA: triethylamine
TFE: trifluoroethanol
TGFβ: transforming growth factor-β
TJ: tight junctions
TLR2: toll-like receptor 2
TMT: tandem mass tags
TWI: twitcher
U: units
UCB: umbilical cord blood
ULK1: UNC-51-like kinase 1
*U*U: unit of enzyme
hVps34: mammalian vacuolar protein sorting 34 homologue
UVRAG: UV irradiation resistance-associated gene
WT: wilde type
ZP: zeta potential
α GLU: α glucosidase
β GLU: β glucosidase

# List of publications

In chronological order:

- Del Grosso, A., Antonini, S., Tonazzini, I., Signore, G., & Cecchini, M. (2015). Galactosylceramidase (GALC) enzymatic activity and psychosine accumulation in central and peripheral nervous system cells and tissues from wild-type and Twitcher mice: T05-10B. *Glia*, *63*.

- Del Grosso, A., Antonini, S., Angella, L., Tonazzini, I., Signore, G., & Cecchini, M. (2016). Lithium improves cell viability in psychosine-treated MO3. 13 human oligodendrocyte cell line via autophagy activation. *Journal of neuroscience research*, *94*(11), 1246-1260.

- Parenti, N., Del Grosso, A., Antoni, C., Cecchini, M., Corradetti, R., Pavone, F. S., & Calamai, M. (2017). Direct imaging of APP proteolysis in living cells. *PeerJ*, *5*, e3086.

- Galliani, M., Santi, M., Del Grosso, A., Cecchettini, A., Santorelli, F. M., Hofmann, S. L., Lu, J. Y., Angella, L., Cecchini, M., & Signore, G. (2018). Cross-Linked Enzyme Aggregates as Versatile Tool for Enzyme Delivery: Application to Polymeric Nanoparticles. *Bioconjugate chemistry*, *29*(7), 2225-2231.

- Pellegrini, D., Del Grosso, A., Angella, L., Giordano, N., Dilillo, M., Tonazzini, I., Caleo, M., Cecchini, M., & McDonnell, L. A. (2019). Quantitative Microproteomics Based Characterization of the Central and Peripheral Nervous System of a Mouse Model of Krabbe Disease. *Molecular & Cellular Proteomics*, *18*(6), 1227-1241.

- Begarani, F., D'Autilia, F., Signore, G., Del Grosso, A., Cecchini, M., Gratton, E., Beltram, F., & Cardarelli, F. (2019). Capturing Metabolism-Dependent Solvent Dynamics in the Lumen of a Trafficking Lysosome. *ACS nano*, *13*(2), 1670-1682.

- Del Grosso, A., Angella, L., Tonazzini, I., Moscardini, A., Giordano, N., Caleo, M., Rocchiccioli, S., & Cecchini, M. (2019). Dysregulated autophagy as a new aspect of the molecular pathogenesis of Krabbe disease. *Neurobiology of disease*, *129*, 195-207.

- Del Grosso, A. and Galliani, M., Angella, L., Santi, M., Tonazzini, I., Parlanti, G., Signore, G., & Cecchini, M. (2019). Brain-targeted enzyme loaded nanoparticles: a breach through the blood brain barrier for enzyme replacement therapy in Krabbe disease. In press on Science Advances. DOI: 10.1126/sciadv.aax7462.
-

# Bibliography


1. Wenger, D. A. Krabbe disease. *Pagon, R.A., Adam, M.P., Ardinger, H.H., al. (Eds.), GeneReviews® [Internet]. Univ. Washington, Seattle (Jun 19 [Updated 2011 Mar 31],* Pagon, R.A., Adam, M.P., Ardinger, H.H., et al. (E (2000).
2. Suzuki, K. Twenty five years of the 'Psychosine Hypothesis': A personal perspective of its history and present status. *Neurochem. Res.* **23**, 251–259 (1998).
3. Suzuki, K. Evolving perspective of the pathogenesis of globoid cell leukodystrophy (Krabbe disease). *Proc. Jpn. Acad.* **79**, 1–8 (2003).
4. Sakai, N. Pathogenesis of leukodystrophy for Krabbe disease: Molecular mechanism and clinical treatment. *Brain Dev.* **31**, 485–487 (2009).
5. Bruni, S., Loschi, L., Incerti, C., Gabrielli, O. & Coppa, G. V. Update on treatment of lysosomal storage diseases. *Acta Myol.* **26**, 87–92 (2007).
6. Sun, A. Lysosomal storage disease overview. *Ann. Transl. Med.* **6**, 476.-476. (2018).
7. Walkley, S. U. Pathogenic cascades in lysosomal disease—why so complex?. *J. Inherit. Metab. Dis.* **32**, 181–189 (2009).
8. Wenger, D. A., Coppola, S. & Liu, S. L. Insights into the diagnosis and treatment of lysosomal storage diseases. *Arch. Neurol.* **60**, 322–328 (2003).
9. Zlotogora, J., Chakraborty, S., Knowlton, R. G. & Wenger, D. A. Krabbe disease locus mapped to chromosome 14 by genetic linkage. *Am. J. Hum. Genet.* **47**, 37–44 (1990).
10. Chen, Y. Q., & Wenger, D. A. Galactocerebrosidase from human urine: purification and partial characterization. *Biochim. Biophys. Acta (BBA)-Lipids Lipid Metab.* **1170**, 53–61 (1993).
11. Sakai, N., Inui, K., Fujii, N., Fukushima, H., Nishimoto, J., Yanagihara, I., ... & Okada, S. Krabbe disease: isolation and characterization of a full-length cDNA for human galactocerebrosidase. *Biochem. Biophys. Res. Commun.* **198**, 485–491 (1994).
12. Won, J. S., Singh, A. K., & Singh, I. Biochemical, cell biological, pathological, and therapeutic aspects of Krabbe's disease. *J. Neurosci. Res.* **94**, 990–1006 (2016).
13. Luzi, P., Rafi, M. A., & Wenger, D. A. Characterization of the large deletion in the GALC gene found in patients with Krabbe disease. *Hum. Mol. Genet.* **4**, 2335–2338 (1995).
14. Wenger, D. A., Rafi, M. A. & Luzi, P. Molecular genetics of krabbe disease (Globoid cell Leukodystrophy): Diagnostic and clinical implications. *Hum. Mutat.* **10**, 268–279 (1997).
15. Lee, W. C. *et al.* Molecular characterization of mutations that cause globoid cell leukodystrophy and pharmacological rescue using small molecule chemical chaperones. *J. Neurosci.* **30**, 5489–5497 (2010).
16. Nagano, S. *et al.* Expression and processing of recombinant human galactosylceramidase. *Clin. Chim. Acta* **276**, 53–61 (1998).
17. Deane, J. E. *et al.* Insights into Krabbe disease from structures of galactocerebrosidase. *Proc. Natl. Acad. Sci. U. S. A.* **108**, 15169–15173 (2011).
18. Kornfeld, S. Trafficking of lysosomal enzymes in normal and disease states. *J. Clin. Invest.* **77**, 1–6 (1986).
19. Muro, S. New biotechnological and nanomedicine strategies for treatment of lysosomal storage disorders. *Wiley Interdiscip. Rev. Nanomedicine andNanobiotechnology* **2**, 189–204 (2010).
20. Lefebvre, S., Vartanian, T. *Disorders of Myelin in the Central and Peripheral Nervous Systems. From Molecular basis of myelin Butterworth Heinemann. Chapter 2.* (2002).
21. Wenger, D. A. Galactosyl-ceramide lipidosis: globoid cell leukodystrophy (Krabbe disease). *Metab. Mol. bases Inherit. Dis.* (2001).

22. Wenger, D. A. Murine, canine and non-human primate models of Krabbe disease. *Mol. Med. Today* **6**, 449–451 (2000).
23. HAGBERG, B., SOURANDER, P. & SVENNERHOLM, L. Diagnosis of Krabbe's infantile leucodystrophy. *J. Neurol. Neurosurg. Psychiatry* **26**, 195–198 (1963).
24. Wenger, D. A., Rafi, M. A., & Luzi, P. Krabbe disease: One Hundred years from the bedside to the bench to the bedside. *J. Neurosci. Res.* **94**, 982–989 (2016).
25. Lyon, G., Hagberg, B., Evrard, P. H., Allaire, C., Pavone, L., & Vanier, M. Symptomatology of late onset Krabbe's leukodystrophy: the European experience. *Dev. Neurosci.* **13**, 240–244 (1991).
26. Jacob, J. C., Kutty, K. M., Islam, M., Dominic, R. G., & Dawson, G. (1973). Krabbe's Disease: globoid cell leukodystrophy. Canadian Medical Association Journal, 108(11), 1398. *Jacob, J. C., Kutty, K. M., Islam. M., Dominic, R. G., Dawson, G.* **108**, 1398 (1973).
27. Suzuki, K. Globoid cell leukodystrophy (Krabbe's disease): update. *J. Child Neurol.* **18**, 595–603 (2003).
28. Starr, C., Taggart, R., & Evers, C. *Volume 5-Animal Structure & Function. Cengage Learning.* (2012).
29. Graziano, A. C. E. & Cardile, V. History, genetic, and recent advances on Krabbe disease. *Gene* **555**, 2–13 (2015).
30. Parlanti, P. *et al.* Size and specimen-dependent strategy for x-ray micro-ct and tem correlative analysis of nervous system samples. *Sci. Rep.* **7**, 2858 (2017).
31. Spassieva, S. & Bieberich, E. Lysosphingolipids and sphingolipidoses: Psychosine in Krabbe's disease. *J. Neurosci. Res.* **94**, 974–981 (2016).
32. Svennerholm, L., Vanier, M. T. & Mansson, J. E. Krabbe disease: A galactosylsphingosine (psychosine) lipidosis. *J. Lipid Res.* **21**, 53–64 (1980).
33. Vanier, M. & Svennerholm, L. Chemical pathology of Krabbe disease: the occurrence of psychosine and other neutral sphingoglycolipids. *Adv. Exp. Med. Biol.* **68**, 115–126 (1976).
34. Tanaka, K., Nagara, H., Kobayashi, T., & Goto, I. The twitcher mouse: accumulation of galactosylsphingosine and pathology of the sciatic nerve. *Brain Res.* **454**, 340–346 (1988).
35. Tanaka, K., & Webster, H. D. Effects of psychosine (galactosylsphingosine) on the survival and the fine structure of cultured Schwann cells. *J. Neuropathol. Exp. Neurol.* **52**, 490–498 (1993).
36. Inamura, N. *et al.* Developmental defects and aberrant accumulation of endogenous psychosine in oligodendrocytes in a murine model of Krabbe disease. *Neurobiol. Dis.* **120**, 51–62 (2018).
37. Bongarzone, E. R., Escolar, M. L., Gray, S. J., Kafri, T., Vite, C. H., & Sands, M. S. Insights into the Pathogenesis and Treatment of Krabbe Disease. *Pediatr. Endocrinol. Rev. PER.* **13**, 689–696 (2016).
38. Belleri, M. & Presta, M. Endothelial cell dysfunction in globoid cell leukodystrophy. *J. Neurosci. Res.* **94**, 1359–1367 (2016).
39. Del Grosso, A. *et al.* Lithium improves cell viability in psychosine-treated MO3.13 human oligodendrocyte cell line via autophagy activation. *J. Neurosci. Res.* **94**, 1246–1260 (2016).
40. Pellegrini, D., del Grosso, A., Angella, L., Giordano, N., Dilillo, M., Tonazzini, I., ... & McDonnell, L. A. Quantitative Microproteomics Based Characterization of the Central and Peripheral Nervous System of a Mouse Model of Krabbe Disease. , . *Mol. Cell. Proteomics* **mcp-RA118**, (2019).
41. Del Grosso, A. *et al.* Dysregulated autophagy as a new aspect of the molecular

pathogenesis of Krabbe disease. *Neurobiol. Dis.* **129**, 195–207 (2019).
42. Kose, M., Demir, S. A., Akinci, G., Eraslan, C., Yilmaz, U., Ceylaner, S., ... & Seyrantepe, V. The second case of saposin a deficiency and altered autophagy. *JIMD Rep.* **44**, 43–54 (2019).
43. Ribbens, J. J., Moser, A. B., Hubbard, W. C., Bongarzone, E. R. & Maegawa, G. H. B. Characterization and application of a disease-cell model for a neurodegenerative lysosomal disease. *Mol. Genet. Metab.* **111**, 172–183 (2014).
44. Smith, B. R., Santos, M. B., Marshall, M. S., Cantuti-Castelvetri, L., Lopez-Rosas, A., Li, G., ... & Crocker, S. J. Neuronal inclusions of α-synuclein contribute to the pathogenesis of Krabbe disease. *J. Pathol.* **232**, 509–521 (2014).
45. Cantuti Castelvetri, L. *et al.* The Sphingolipid Psychosine Inhibits Fast Axonal Transport in Krabbe Disease by Activation of GSK3β and Deregulation of Molecular Motors. *J. Neurosci.* **33**, 10048 LP – 10056 (2013).
46. Marshall, M. S., & Bongarzone, E. R. (2016). Beyond Krabbe's disease: The potential contribution of galactosylceramidase deficiency to neuronal vulnerability in late-onset synucleinopathies. Journal of neuroscience research, 94(11), 1328-1332. *J. Neurosci. Res.* **94**, 1328–1332 (2016).
47. Voccoli, V., Tonazzini, I., Signore, G., Caleo, M., & Cecchini, M. Role of extracellular calcium and mitochondrial oxygen species in psychosine-induced oligodendrocyte cell death. *Cell Death Dis.* **5**, e1529 (2014).
48. Nicaise, A. M., Bongarzone, E. R. & Crocker, S. J. A microglial hypothesis of globoid cell leukodystrophy pathology. *J. Neurosci. Res.* **94**, 1049–1061 (2016).
49. Miyatake, T., & Suzuki, K. Globoid cell leukodystrophy: additional deficiency of psychosine galactosidase. *Biochem. Biophys. Res. Commun.* **48**, 538–543 (1972).
50. Kennedy, P. The Enzymatic Synthesis of Psychosine *. **235**, (1960).
51. Li, Y. *et al.* Genetic ablation of acid ceramidase in Krabbe disease confirms the psychosine hypothesis and identifies a new therapeutic target. *Proc. Natl. Acad. Sci.* **116**, 20097–20103 (2019).
52. Knaap MSvd, V. J. *Magnetic Resonance of Myelination and Myelin Disorders. New York: Springer* (2005).
53. Schaeren-Wiemers, N., P. Van Der Bijl, and M. E. S. The UDP-galactose: ceramide galactosyltransferase: Expression pattern in oligodendrocytes and Schwann cells during myelination and substrate preference for hydroxyceramide. *J. Neurochem.* **65**, 2267–2278 (1995).
54. Pernber, Z., Molander-Melin, M., Berthold, C. H., Hansson, E., & Fredman, P. Expression of the myelin and oligodendrocyte progenitor marker sulfatide in neurons and astrocytes of adult rat brain. *J. Neurosci. Res.* **69**, 86–93 (2002).
55. Castelvetri, L. C., Givogri, M. I., Zhu, H., Smith, B., Lopez-Rosas, A., Qiu, X., ... & Bongarzone, E. R. Axonopathy is a compounding factor in the pathogenesis of Krabbe disease. *Acta Neuropathol.* **122**, 35–48 (2011).
56. Nagara, H., Ogawa, H., Sato, Y., Kobayashi, T., & Suzuki, K. The twitcher mouse: degeneration of oligodendrocytes in vitro. *Dev. Brain Res.* **26**, 79–84 (1986).
57. Ida, H., Kawame, F., Kim, S. U., & Eto, Y. Abnormality in cultured oligodendrocytes and Schwann cells isolated from the twitcher mouse. ,. *Mol. Chem. Neuropathol.* **13**, 195–204 (1990).
58. White, A. B. *et al.* Psychosine accumulates in membrane microdomains in the brain of Krabbe patients, disrupting the raft architecture. *J. Neurosci.* **29**, 6068–6077 (2009).
59. D'auria, L. *et al.* Psychosine enhances the shedding of membrane microvesicles: Implications in demyelination in Krabbe's disease. *PLoS One* **12**, 1–19 (2017).

60. Giri, S., Khan, M., Rattan, R., Singh, I. & Singh, A. K. Krabbe disease: Psychosine-mediated activation of phospholipase A2 in oligodendrocyte cell death. *J. Lipid Res.* **47**, 1478–1492 (2006).
61. Misslin, C., Velasco-Estevez, M., Albert, M., O'Sullivan, S. A. & Dev, K. K. Phospholipase A2 is involved in galactosylsphingosine-induced astrocyte toxicity, neuronal damage and demyelination. *PLoS One* **12**, 1–19 (2017).
62. Marshall, M. S. *et al.* Analysis of age-related changes in psychosine metabolism in the human brain. *PLoS One* **13**, 1–20 (2018).
63. Abdelkarim, H. *et al.* α-Synuclein interacts directly but reversibly with psychosine: implications for α-synucleinopathies. *Sci. Rep.* **8**, 1–19 (2018).
64. Hawkins-Salsbury, J. A. *et al.* Psychosine, the cytotoxic sphingolipid that accumulates in globoid cell leukodystrophy, alters membrane architecture. *J. Lipid Res.* **54**, 3303–3311 (2013).
65. Zulueta Díaz, Y. de las M., Caby, S., Bongarzone, E. R. & Fanani, M. L. Psychosine remodels model lipid membranes at neutral pH. *Biochim. Biophys. Acta - Biomembr.* **1860**, 2515–2526 (2018).
66. Abbandonato, G. *et al.* Lipid-Conjugated Rigidochromic Probe Discloses Membrane Alteration in Model Cells of Krabbe Disease. *Biophys. J.* **116**, 477–486 (2019).
67. Hamanoue M, Yoshioka A, Ohashi T, Eto Y, T. K. NF-kappaB prevents TNF-alpha-induced apoptosis in an oligodendrocyte cell line. 2004; 29(8):1571–1576. [PubMed: 15260136]. *Neurochem. Res.* **29**, 1571–1576 (2004).
68. Zaka, M., Rafi, M. A., Rao, H. Z., Luzi, P. & Wenger, D. A. Insulin-like growth factor-1 provides protection against psychosine-induced apoptosis in cultured mouse oligodendrocyte progenitor cells using primarily the PI3K/Akt pathway. *Mol. Cell. Neurosci.* **30**, 398–407 (2005).
69. Won, J. S., Kim, J., Paintlia, M. K., Singh, I., & Singh, A. K. Role of endogenous psychosine accumulation in oligodendrocyte differentiation and survival: implication for Krabbe disease. *Brain Res.* 44–52 (2013).
70. Haq E, Giri S, Singh I, S. A. Molecular mechanism of psychosine-induced cell death in human oligodendrocyte cell line. *J. Neurochem.* **86**, 1428–1440 (2003).
71. Smith, B. *et al.* Peripheral neuropathy in the Twitcher mouse involves the activation of axonal Caspase 3. *ASN Neuro* **3**, 213–222 (2011).
72. Graziano, A. C. E., Parenti, R., Avola, R. & Cardile, V. Krabbe disease: Involvement of connexin43 in the apoptotic effects of sphingolipid psychosine on mouse oligodendrocyte precursors. *Apoptosis* **21**, 25–35 (2016).
73. Kobayashi, S., Chiu, F. C., Katayama, M., Sacchi, R. S., Suzuki, K., & Suzuki, K. Expression of glial fibrillary acidic protein in the CNS and PNS of murine globoid cell leukodystrophy, the twitcher. *Am. J. Pathol.* **125**, 227 (1986).
74. Jesionek-Kupnicka D, Majchrowska A, Krawczyk J, Wendorff J, Barcikowska M, Lukaszek S, L. P. Krabbe disease: an ultrastructural study of globoid cells and reactive astrocytes at the brain and optic nerves. *Folia Neuropathol.* **35**, 155–162 (1997).
75. Mohri, I., Taniike, M., Taniguchi, H., Kanekiyo, T., Aritake, K., Inui, T., ... & Kanaoka, Y. Prostaglandin D2-mediated microglia/astrocyte interaction enhances astrogliosis and demyelination in twitcher. *J. Neurosci.* **26**, 4383–4393 (2006).
76. Hawkins-Salsbury, J. A., Qin, E. Y., Reddy, A. S., Vogler, C. A. & Sands, M. S. Oxidative stress as a therapeutic target in globoid cell leukodystrophy. *Exp. Neurol.* **237**, 444–452 (2012).
77. Ijichi K, Brown GD, Moore CS, Lee JP, Winokur PN, Pagarigan R, Snyder EY, Bongarzone ER, C. S. MMP-3 mediates psychosine-induced globoid cell formation:

implications for leukodystrophy pathology. *Glia* **61**, 765–777 (2013).
78. Claycomb KI, Winokur PN, Johnson KM, Nicaise AM, Giampetruzzi AW, Sacino AV, Snyder EY, Barbarese E, Bongarzone ER, C. S. Aberrant production of tenascin-C in globoid cell leukodystrophy alters psychosine-induced microglial functions. *J. Neuropathol. Exp. Neurol.* **73**, 964–974 (2014).
79. Wu YP, Matsuda J, Kubota A, Suzuki K, S. K. Infiltration of hematogenous lineage cells into the demyelinating central nervous system of twitcher mice. *J. Neuropathol. Exp. Neurol.* **59**, 628–639 (2000).
80. Kondo Y, Adams JM, Vanier MT, D. I. Macrophages counteract demyelination in a mouse model of globoid cell leukodystrophy. *J. Neurosci. Off. J. Soc. Neurosci.* **31**, 3610–3624 (2011).
81. LeVine SM, B. D. IL-6 and TNFalpha expression in brains of twitcher, quaking and normal mice. *J. Neuroimmunol.* **73**, 47–56 (1997).
82. Ransohoff RM, B. M. Innate immunity in the central nervous system. *J. Clin. Invest.* **122**, 1164–1171 (2012).
83. Ohno, M., Komiyama, A., Martin, P. M., & Suzuki, K. MHC class II antigen expression and T-cell infiltration in the demyelinating CNS and PNS of the twitcher mouse. *Brain Res.* **652**, 186–196 (1993).
84. Snook, E. R., Fisher-Perkins, J. M., Sansing, H. A., Lee, K. M., Alvarez, X., MacLean, A. G., ... & Bunnell, B. A. Innate immune activation in the pathogenesis of a murine model of globoid cell leukodystrophy. *Am. J. Pathol.* **184**, 382–396 (2014).
85. Bashir, A., & Haq, E. Effect of psychosine on inducible nitric-oxide synthase expression under different culture conditions: implications for Krabbe disease. *Eur Rev Med Pharmacol Sci* **15**, 1282–7 (2011).
86. Giri, S., Jatana, M., Rattan, R., Won, J. S., Singh, I., & SINGH, A. K. Galactosylsphingosine (psychosine)-induced expression of cytokine-mediated inducible nitric oxide synthases via AP-1 and C/EBP: implications for Krabbe disease. *FASEB J.* **16**, 661–672 (2002).
87. Wu YP, McMahon EJ, Matsuda J, Suzuki K, Matsushima GK, S. K. Expression of immune-related molecules is downregulated in twitcher mice following bone marrow transplantation. *J. Neuropathol. Exp. Neurol.* **60**, 1062–1074 (2001).
88. Potter, G. B. *et al.* Missense mutation in mouse GALC mimics human gene defect and offers new insights into Krabbe disease. **22**, 3397–3414 (2013).
89. Galbiati F, Basso V, Cantuti L, Givogri MI, Lopez-Rosas A, Perez N, Vasu C, Cao H, van Breemen R, Mondino A, B. E. Autonomic denervation of lymphoid organs leads to epigenetic immune atrophy in a mouse model of Krabbe disease. *J. Neurosci. Off. J. Soc. Neurosci.* **27**, 13730–13738 (2007).
90. Formichi P, Radi E, Battisti C, Pasqui A, Pompella G, Lazzerini PE, Laghi-Pasini F, Leonini A, Di Stefano A, F. A. Psychosine-induced apoptosis and cytokine activation in immune peripheral cells of Krabbe patients. *J. Cell. Physiol.* **212**, 737–743 (2007).
91. Visigalli I, Ungari S, Martino S, Park H, Cesani M, Gentner B, Sergi Sergi L, Orlacchio A, Naldini L, B. A. The galactocerebrosidase enzyme contributes to the maintenance of a functional hematopoietic stem cell niche. *Blood.* **116**, 1857–1866 (2010).
92. Giri, S., Khan, M., Nath, N., Singh, I. & Singh, A. K. The role of AMPK in psychosine mediated effects on oligodendrocytes and astrocytes: Implication for Krabbe disease. *J. Neurochem.* **105**, 1820–1833 (2008).
93. Khan M, Haq E, Giri S, Singh I, S. A. Peroxisomal participation in psychosine-mediated toxicity: implications for Krabbe's disease. *J. Neurosci. Res.* **80**, 845–854 (2005).
94. Borda JT, Alvarez X, Mohan M, Ratterree MS, Phillippi-Falkenstein K, Lackner AA, B. B.

Clinical and immunopathologic alterations in rhesus macaques affected with globoid cell leukodystrophy. *Am J Pathol.* **172**, 98–11 (2008).
95. Abdelkarim, H. *et al.* α-Synuclein interacts directly but reversibly with psychosine: implications for α-synucleinopathies. *Sci. Rep.* **8**, 12462 (2018).
96. Haq E, Contreras MA, Giri S, Singh I, S. A. Dysfunction of peroxisomes in twitcher mice brain: a possible mechanism of psychosine-induced disease. *Biochem. Biophys. Res. Commun.* **343**, 229–238 (2006).
97. Irahara-Miyana, K., Otomo, T., Kondo, H., Hossain, M. A., Ozono, K., & Sakai, N. Unfolded protein response is activated in Krabbe disease in a manner dependent on the mutation type. *J. Hum. Genet.* **63**, 699 (2018).
98. Begarani, F. *et al.* Capturing Metabolism-Dependent Solvent Dynamics in the Lumen of a Trafficking Lysosome. *ACS Nano* **13**, 1670–1682 (2019).
99. Folts, C. J., Scott-Hewitt, N., Pröschel, C., Mayer-Pröschel, M. & Noble, M. Lysosomal Re-acidification Prevents Lysosphingolipid-Induced Lysosomal Impairment and Cellular Toxicity. *PLoS Biol.* **14**, 1–39 (2016).
100. Marjanovic B, Cvetkovic D, Dozic S, Todorovic S, D. M. Association of Krabbe leukodystrophy and congenital fiber type disproportion. *Pediatr. Neurol.* **15**, 79–82 (1996).
101. Cantuti-Castelvetri L, Zhu H, Givogri MI, Chidavaenzi RL, Lopez-Rosas A, B. E. Psychosine induces the dephosphorylation of neurofilaments by deregulation of PP1 and PP2A phosphatases. *Neurobiol. Dis.* **46**, 325–335 (2012).
102. Lim, C. Y. & Zoncu, R. The lysosome as a command-and-control center for cellular metabolism. **214**, 653–664 (2016).
103. Cantuti-Castelvetri, L. *et al.* Mechanism of neuromuscular dysfunction in Krabbe disease. *J. Neurosci.* **35**, 1606–1616 (2015).
104. Dolcetta, D., Amadio, S., Guerrini, U., Givogri, M. I., Perani, L., Galbiati, F., ... & Bongarzone, E. Myelin deterioration in Twitcher mice: motor evoked potentials and magnetic resonance imaging as in vivo monitoring tools. , 81(4), 597-604. *J. Neurosci. Res.* **81**, 597–604 (2005).
105. Cantuti Castelvetri, L. *et al.* The sphingolipid psychosine inhibits fast axonal transport in krabbe disease by activation of GSK3β and deregulation of molecular motors. *J. Neurosci.* **33**, 10048–10056 (2013).
106. Dehkharghani F, Sarnat HB, Brewster MA, R. S. Congenital muscle fiber-type disproportion in Krabbe's leukodystrophy. *Arch. Neurol.* **38**, 585–587 (1981).
107. Kondo A, S. K. The blood brain barrier in human leukodystrophies and allied diseases. Ultrastructural and morphometric studies on the capillaries in brain biopsies. *Clin Neuropathol.* **12**, 169–174 (1993).
108. Belleri M, Ronca R, Coltrini D, Nico B, Ribatti D, Poliani PL, Giacomini A, Alessi P, Marchesini S, Santos MB, Bongarzone ER, P. M. Inhibition of angiogenesis by beta-galactosylceramidase deficiency in globoid cell leukodystrophy. *Brain* **136**, 2859–2875 (2013).
109. Giacomini A, Ackermann M, Belleri M, Coltrini D, Nico B, Ribatti D, Konerding MA, Presta M, R. M. Brain angioarchitecture and intussusceptive microvascular growth in a murine model of Krabbe disease. *Angiogenesis* **18**, 499–510 (2015).
110. Suzuki, K., & Suzuki, K. The twitcher mouse: a model for Krabbe disease and for experimental therapies. *Brain Pathol.* **5**, 249–258 (1995).
111. Olmstead, C. E. Neurological and neurobehavioral development of the mutant 'twitcher'mouse. , 25(2), 143-153. *Behav. Brain Res.* **25**, 143–153 (1987).
112. Suzuki, K., & Suzuki, K. Myelin Pathology in the Twitcher Mouse. *Ann. N. Y. Acad. Sci.*

**605**, 313–324 (1990).
113. Ricca, A. & Gritti, A. Perspective on innovative therapies for globoid cell leukodystrophy. *J. Neurosci. Res.* **94**, 1304–1317 (2016).
114. Krivit, W., Shapiro, E. G., Peters, C., Wagner, J. E., Cornu, G., Kurtzberg, J., ... & Dusenbery, K. H E M ATO P O I ET I C ST E M - C E L L T R A N S P L A N TAT I O N I N G LO B O I D - C E L L L E U KO DYST RO P H Y. *N. Engl. J. Med.* **338**, 1119–1126 (1998).
115. Mikulka, C. R. & Sands, M. S. Treatment for Krabbe's disease: Finding the combination. *J. Neurosci. Res.* **94**, 1126–1137 (2016).
116. Caniglia, M. *et al.* Allogeneic bone marrow transplantation for infantile globoid-cell leukodystrophy (Krabbe's disease). *Pediatr. Transplant.* **6**, 427–431 (2002).
117. Escolar, M. L., Poe, M. D., Provenzale, J. M., Richards, K. C., Allison, J., Wood, S., ... & Morse, R. Transplantation of umbilical-cord blood in babies with infantile Krabbe's disease. , 352(20), . *N. Engl. J. Med.* **352**, 2069–2081 (2005).
118. Lee, W. C., Courtenay, A., Troendle, F. J., Stallings-Mann, M. L., Dickey, C. A., DeLucia, M. W., ... & Eckman, C. B. Enzyme replacement therapy results in substantial improvements in early clinical phenotype in a mouse model of globoid cell leukodystrophy. *FASEB J.* **19**, 1549–1551 (2005).
119. Matthes, F. *et al.* Enzyme replacement therapy of a novel humanized mouse model of globoid cell leukodystrophy. *Exp. Neurol.* **271**, 36–45 (2015).
120. Zhang, X. Y., Dinh, A., Cronin, J., Li, S. C. & Reiser, J. Cellular uptake and lysosomal delivery of galactocerebrosidase tagged with the HIV Tat protein transduction domain. *J. Neurochem.* **104**, 1055–1064 (2008).
121. Lee, W. C., Tsoi, Y. K., Troendle, F. J., DeLucia, M. W., Ahmed, Z., Dicky, C. A., ... & Eckman, C. B. Single-dose intracerebroventricular administration of galactocerebrosidase improves survival in a mouse model of globoid cell leukodystrophy. *FASEB J.* **21**, 2520–2527 (2007).
122. Parenti, G., Andria, G., & Ballabio, A. Lysosomal storage diseases: from pathophysiology to therapy. , 66, 471-486. *Annu. Rev. Med.* **66**, 471–486 (2015).
123. Sundaram KS, L. M. Inhibition of sphingolipid synthesis by cycloserine in vitro and in vivo. *J Neurochem.* **42**, 577–81 (1984).
124. LeVine, S. M., Pedchenko, T. V., Bronshteyn, I. G., & Pinson, D. M. L-cycloserine slows the clinical and pathological course in mice with globoid cell leukodystrophy (twitcher mice). *J. Neurosci. Res.* **231–236**, (2AD).
125. Asokan, A., Schaffer, D. V. & Samulski, R. J. The AAV vector toolkit: Poised at the clinical crossroads. *Mol. Ther.* **20**, 699–708 (2012).
126. Shen, J. S., Watabe, K., Ohashi, T. & Eto, Y. Intraventricular administration of recombinant adenovirus to neonatal twitcher mouse leads to clinicopathological improvements. *Gene Ther.* **8**, 1081–1087 (2001).
127. Rafi, M. A. *et al.* AAV-Mediated expression of galactocerebrosidase in brain results in attenuated symptoms and extended life span in murine models of globoid cell leukodystrophy. *Mol. Ther.* **11**, 734–744 (2005).
128. Lin, D. *et al.* AAV2/5 vector expressing galactocerebrosidase ameliorates CNS disease in the murine model of globoid-cell leukodystrophy more efficiently than AAV2. *Mol. Ther.* **12**, 422–430 (2005).
129. Rafi, M. A., Rao, H. Z., Luzi, P., Curtis, M. T. & Wenger, D. A. Extended normal life after AAVrh10-mediated gene therapy in the mouse model of krabbe disease. *Mol. Ther.* **20**, 2031–2042 (2012).
130. Lattanzi, A. *et al.* Therapeutic benefit of lentiviral-mediated neonatal intracerebral gene therapy in a mouse model of globoid cell leukodystrophy. *Hum. Mol. Genet.* **23**,

3250–3268 (2014).
131. Ricca, A. *et al.* Combined gene/cell therapies provide long-term and pervasive rescue of multiple pathological symptoms in a murine model of globoid cell leukodystrophy. *Hum. Mol. Genet.* **24**, 3372–3389 (2015).
132. Hawkins-Salsbury, J. A. *et al.* Mechanism-based combination treatment dramatically increases therapeutic efficacy in murine globoid cell leukodystrophy. *J. Neurosci.* **35**, 6495–6505 (2015).
133. Estelle, M. & Kelley, D. R. Mol Cell Proteomics Papers in Press. Published on March 27, 2019 as Manuscript RA119.001378. 1–35 (2019).
134. Marshall, M. S. *et al.* Long-Term Improvement of Neurological Signs and Metabolic Dysfunction in a Mouse Model of Krabbe's Disease after Global Gene Therapy. *Mol. Ther.* **26**, 874–889 (2018).
135. Platt, F. M., Boland, B. & Spoel, A. C. Van Der. Lysosomal storage disorders : The cellular impact of lysosomal dysfunction. **199**, 723–734 (2012).
136. Settembre, C., Fraldi, A., Medina, D. L. & Ballabio, A. Signals from the lysosome: a control centre for cellular clearance and energy metabolism. *Nat. Rev. Mol. Cell Biol.* **14**, 283–296 (2013).
137. Luzi, P. *et al.* Effects of treatments on inflammatory and apoptotic markers in the CNS of mice with globoid cell leukodystrophy. *Brain Res.* (2009) doi:10.1016/j.brainres.2009.09.017.
138. Teixeira, C. A. *et al.* Early axonal loss accompanied by impaired endocytosis, abnormal axonal transport, and decreased microtubule stability occur in the model of Krabbe's disease. *Neurobiol. Dis.* **66**, 92–103 (2014).
139. Raben, N. *et al.* Suppression of autophagy permits successful enzyme replacement therapy in a lysosomal storage disorder - Murine Pompe disease. *Autophagy* **6**, 1078–1089 (2010).
140. Medina, D. L. *et al.* Transcriptional activation of lysosomal exocytosis promotes cellular clearance. *Dev. Cell* **21**, 421–430 (2011).
141. Spampanato, C. *et al.* Transcription factor EB (TFEB) is a new therapeutic target for Pompe disease. *EMBO Mol. Med.* **5**, 691–706 (2013).
142. Usmani, S. S. *et al.* THPdb: Database of FDA-approved peptide and protein therapeutics. *PLoS One* **12**, 1–12 (2017).
143. Mitragotri, S., Burke, P. A. & Langer, R. Overcoming the challenges in administering biopharmaceuticals: Formulation and delivery strategies. *Nat. Rev. Drug Discov.* **13**, 655–672 (2014).
144. Leader, B., Baca, Q. J. & Golan, D. E. Protein therapeutics: A summary and pharmacological classification. *Nat. Rev. Drug Discov.* **7**, 21–39 (2008).
145. Morales, L. E. General Medicine GAUCHER ' S DISEASE : A REVIEW. *Ann Pharmacother* **30**, 381–388 (1996).
146. Niederau, C., & Häussinger, D. Gaucher's disease: a review for the internist and hepatologist. *Hepatogastroenterology.* **47**, 984–997 (2000).
147. Grabowski, G. A. *et al.* Enzyme therapy in type 1 Gaucher disease: Comparative efficacy of mannose- terminated glucocerebrosidase from natural and recombinant sources. *Ann. Intern. Med.* **122**, 33–39 (1995).
148. Engelberg, A. B., Kesselheim, A. S., & Avorn, J. (Balancing innovation, access, and profits—market exclusivity for biologics. *N. Engl. J. Med.* **361**, 1917–1919 (2009).
149. Lachmann, R. H. Enzyme replacement therapy for lysosomal storage diseases. Current opinion in pediatrics, 23(6), 588-593. **23**, 588–593 (2011).
150. Sirrs, S. & Alfadhel, M. Enzyme replacement therapy for Fabry disease: some answers

but more questions. *Ther. Clin. Risk Manag.* 69 (2011) doi:10.2147/tcrm.s11987.
151. Giugliani, R. *et al.* Mucopolysaccharidosis I, II, and VI: Brief review and guidelines for treatment. *Genet. Mol. Biol.* **33**, 589–604 (2010).
152. LeBowitz, J. H., Grubb, J. H., Maga, J. A., Schmiel, D. H., Vogler, C., & Sly, W. S. Glycosylation-independent targeting enhances enzyme delivery to lysosomes and decreases storage in mucopolysaccharidosis type VII mice. *Proc. Natl. Acad. Sci.* **101**, 3083–3088 (2004).
153. Yogalingam, G., Luu, A. R., Prill, H., Lo, M. J., Yip, B., Holtzinger, J., ... & LeBowitz, J. H. BMN 250, a fusion of lysosomal alpha-N-acetylglucosaminidase with IGF2, exhibits different patterns of cellular uptake into critical cell types of Sanfilippo syndrome B disease pathogenesis. *PLoS One* **14**, e0207836 (2019).
154. Prince, W. S., McCormick, L. M., Wendt, D. J., Fitzpatrick, P. A., Schwartz, K. L., Aguilera, A. I., ... & Lemontt, J. F. Lipoprotein receptor binding, cellular uptake, and lysosomal delivery of fusions between the receptor-associated protein (RAP) and α-L-iduronidase or acid α-glucosidase. *J. Biol. Chem.* **279**, 35037–35046 (2004).
155. Lee, K. O., Luu, N., Kaneski, C. R., Schiffmann, R., Brady, R. O., & Murray, G. J. Improved intracellular delivery of glucocerebrosidase mediated by the HIV-1 TAT protein transduction domain. *Biochem. Biophys. Res. Commun.* **337**, 701–707 (2005).
156. Vaags, A. K., Campbell, T. N., & Choy, F. Y. HIV TAT variants differentially influence the production of glucocerebrosidase in Sf9 cells. *Genet Mol Res* **4**, 491–495 (2005).
157. Xia, H., Mao, Q., & Davidson, B. L. The HIV Tat protein transduction domain improves the biodistribution of β-glucuronidase expressed from recombinant viral vectors. *Nat. Biotechnol.* **19**, 640 (2001).
158. Young, S. W. S., Stenzel, M., & Jia-Lin, Y. (). Nanoparticle-siRNA: a potential cancer therapy?. , 98, 159-169. *Crit. Rev. Oncol. Hematol.* **98**, 159–169 (2016).
159. Rathor, S., Bhatt, D. C., Aamir, S., Singh, S. K., & Kumar, V. A Comprehensive Review on Role of Nanoparticles in Therapeutic Delivery of Medicine. , 5(4), 263-275. *Pharm. Nanotechnol.* **5**, 263–275 (2017).
160. Park, J., Wrzesinski, S. H., Stern, E., Look, M., Criscione, J., Ragheb, R., ... & Ferrandino, A. F. Combination delivery of TGF-β inhibitor and IL-2 by nanoscale liposomal polymeric gels enhances tumour immunotherapy. *Nat. Mater.* **11**, 895 (2012).
161. Safary, A., Khiavi, M. A., Mousavi, R., Barar, J., & Rafi, M. A. Enzyme replacement therapies: what is the best option? *BioImpacts BI* **8**, 153 (2018).
162. Schuh, R. S., Baldo, G., & Teixeira, H. F. Nanotechnology applied to treatment of mucopolysaccharidoses. *Expert Opin. Drug Deliv.* **13**, 1709–1718 (2016).
163. Brunella, T., Giovanni, T., Barbara, B., Diego, D., Alessandro, M., Eleonora, D. M., ... & Angela, V. M. Use of polylactide-co-glycolide-nanoparticles for lysosomal delivery of a therapeutic enzyme in glycogenosis type II fibroblasts. *J. Nanosci. Nanotechnol.* **15**, 2657–2666 (2015).
164. Galliani, M. *et al.* Cross-Linked Enzyme Aggregates as Versatile Tool for Enzyme Delivery: Application to Polymeric Nanoparticles. *Bioconjug. Chem.* **29**, 2225–2231 (2018).
165. Kelly, J. M., Gross, A. L., Martin, D. R., & Byrne, M. E. Polyethylene glycol-b-poly (lactic acid) polymersomes as vehicles for enzyme replacement therapy. *Nanomedicine* **12**, 2591–2606 (2017).
166. Daneman, R. & Prat, A. The Blood Brain Barrier (BBB). *Cold Spring Harb. Perspect. Biol.* **10**, 1–24 (2015).
167. Serlin, Y., Shelef, I., Knyazer, B. & Friedman, A. Seminars in Cell & Developmental Biology Anatomy and physiology of the blood – brain barrier. *Semin. Cell Dev. Biol.* **38**,

2–6 (2015).
168. Zhang, T. T., Li, W., Meng, G., Wang, P., & Liao, W. Strategies for transporting nanoparticles across the blood–brain barrier. *Biomater. Sci.* **4**, 219–229 (2016).
169. Kamalinia, G. *et al.* Cationic Albumin-Conjugated Chelating Agent as a Novel Brain Drug Delivery System in Neurodegeneration. *Chem. Biol. Drug Des.* **86**, 1203–1214 (2015).
170. William M Pardridge. The bloo-brain barrier: bottleneck in brain drug development. *NeuroRx* **2**, 3–14 (2005).
171. del Amo, E. M., Urtti, A. & Yliperttula, M. Pharmacokinetic role of L-type amino acid transporters LAT1 and LAT2. *Eur. J. Pharm. Sci.* **35**, 161–174 (2008).
172. Huwyler, J., Drewe, J. & Krähenbühl, S. Tumor targeting using liposomal antineoplastic drugs. *Int. J. Nanomedicine* **3**, 21–29 (2008).
173. Teleanu, D. M., Negut, I., Grumezescu, V., Grumezescu, A. M. & Teleanu, R. I. Nanomaterials for drug delivery to the central nervous system. *Nanomaterials* **9**, 1–18 (2019).
174. Bellettato, C. M. & Scarpa, M. Possible strategies to cross the blood-brain barrier. *Ital. J. Pediatr.* **44**, 131 (2018).
175. Jones, S. A. *et al.* A phase 1/2 study of intrathecal heparan-N-sulfatase in patients with mucopolysaccharidosis IIIA. *Mol. Genet. Metab.* **118**, 198–205 (2016).
176. Muenzer, J. *et al.* A phase I/II study of intrathecal idursulfase-IT in children with severe mucopolysaccharidosis II. *Genet. Med.* **18**, 73–81 (2016).
177. Lu, C. T. *et al.* Current approaches to enhance CNS delivery of drugs across the brain barriers. *Int. J. Nanomedicine* **9**, 2241–2257 (2014).
178. Pardridge, W. M. Blood–brain barrier drug delivery of IgG fusion proteins with a transferrin receptor monoclonal antibody. *Expert Opin. Drug Deliv.* **12**, 207–222 (2015).
179. Kalmouni, M., Al-Hosani, S. & Magzoub, M. Cancer targeting peptides. *Cell. Mol. Life Sci.* **76**, 2171–2183 (2019).
180. Mathew, A., Maekawa, T., & Sakthikumar, D. Aptamers in targeted nanotherapy. *Curr. Top. Med. Chem.* **15**, 1102–1114 (2015).
181. Duskey, J. T., Belletti, D., Pederzoli, F., Vandelli, M. A., Forni, F., Ruozi, B., & Tosi, G. Current strategies for the delivery of therapeutic proteins and enzymes to treat brain disorders. *Int. Rev. Neurobiol.* **137**, 1–28 (2017).
182. Vilella, A. *et al.* Endocytosis of nanomedicines: The case of glycopeptide engineered PLGA nanoparticles. *Pharmaceutics* **7**, 74–89 (2015).
183. Salvalaio, M. *et al.* Targeted polymeric nanoparticles for brain delivery of high molecular weight molecules in lysosomal storage disorders. *PLoS One* **11**, 1–17 (2016).
184. Rigon, L. *et al.* Targeting brain disease in MPSII: Preclinical evaluation of IDS-loaded PLGA nanoparticles. *Int. J. Mol. Sci.* **20**, 1–15 (2019).
185. Kanda, T. Biology of the blood–nerve barrier and its alteration in immune mediated neuropathies. *J Neurol Neurosurg Psychiatry* **84.2 (2013**, (2013).
186. Langert, K. A. & Brey, E. M. Strategies for targeted delivery to the peripheral nerve. *Front. Neurosci.* **12**, 1–10 (2018).
187. Madduri, Srinivas, and B. G. Growth factor delivery systems and repair strategies for damaged peripheral nerves. *J. Control. Release* **161.2 (201**, (2012).
188. Lee, S., Ashizawa, A. T., Kim, K. S., Falk, D. J. & Notterpek, L. Liposomes to target peripheral neurons and Schwann cells. *PLoS One* **8**, (2013).
189. Luisa Corvo, M. *et al.* Superoxide dismutase entrapped in long-circulating liposomes:

Formulation design and therapeutic activity in rat adjuvant arthritis. *Biochim. Biophys. Acta - Biomembr.* **1564**, 227–236 (2002).
190. Stadler, B. *et al.* A microreactor with thousands of subcompartments: Enzyme-loaded liposomes within polymer capsules. *Angew. Chemie - Int. Ed.* **48**, 4359–4362 (2009).
191. Liu, W. *et al.* Behaviour of liposomes loaded with bovine serum albumin during in vitro digestion. *Food Chem.* **175**, 16–24 (2015).
192. Manuela Gaspar, M., Blanco, D., Cruz, M. E. M. & José Alonso, M. Formulation of L-asparaginase-loaded poly(lactide-co-glycolide) nanoparticles: Influence of polymer properties on enzyme loading, activity and in vitro release. *J. Control. Release* **52**, 53–62 (1998).
193. Martins, M. B. F., Simoes, S. I. D., Cruz, M. E. M., & Gaspar, R. Development of enzyme-loaded nanoparticles: Effect of pH. *J. Mater. Sci. Mater. Med.* **7**, 413–414 (1996).
194. Kokai, L. E. *et al.* Protein bioactivity and polymer orientation is affected by stabilizer incorporation for double-walled microspheres. *J. Control. Release* **141**, 168–176 (2010).
195. Rietscher, R. *et al.* Impact of PEG and PEG-b-PAGE modified PLGA on nanoparticle formation, protein loading and release. *Int. J. Pharm.* **500**, 187–195 (2016).
196. Danhier, F. *et al.* PLGA-based nanoparticles: An overview of biomedical applications. *J. Control. Release* **161**, 505–522 (2012).
197. Fonte, P. *et al.* Co-encapsulation of lyoprotectants improves the stability of protein-loaded PLGA nanoparticles upon lyophilization. *Int. J. Pharm.* **496**, 850–862 (2015).
198. Bilati, U., Allémann, E. & Doelker, E. Development of a nanoprecipitation method intended for the entrapment of hydrophilic drugs into nanoparticles. *Eur. J. Pharm. Sci.* **24**, 67–75 (2005).
199. Morales-Cruz, M. *et al.* Two-step nanoprecipitation for the production of protein-loaded PLGA nanospheres. *Results Pharma Sci.* **2**, 79–85 (2012).
200. Swed, A., Cordonnier, T., Fleury, F., & Boury, F. Protein encapsulation into plga nanoparticles by a novel phase separation method using non-toxic solvents. *J Nanomed Nanotechnol* **5**, 241 (2014).
201. Zhu, X. *et al.* Polymeric Nanoparticles Amenable to Simultaneous Installation of Exterior Targeting and Interior Therapeutic Proteins. *Angew. Chemie - Int. Ed.* **55**, 3309–3312 (2016).
202. Wu, J. *et al.* Development of multinuclear polymeric nanoparticles as robust protein nanocarriers. *Angew. Chemie - Int. Ed.* **53**, 8975–8979 (2014).
203. Cao, L., van Rantwijk, F., & Sheldon, R. A. Cross-linked enzyme aggregates: a simple and effective method for the immobilization of penicillin acylase. *Org. Lett.* **2**, 1361–1364 (2000).
204. Lopez-Serrano, P., Cao, L., Van Rantwijk, F., & Sheldon, R. A. Cross-linked enzyme aggregates with enhanced activity: application to lipases. *Biotechnol. Lett.* **24**, 1379–1383 (2002).
205. Schoevaart, R. *et al.* Preparation, optimization, and structures, of cross-linked enzyme aggregates (CLEAs). *Biotechnol. Bioeng.* **87**, 754–762 (2004).
206. Ali, H., Weigmann, B., Collnot, E. M., Khan, S. A., Windbergs, M., & Lehr, C. M. Budesonide loaded PLGA nanoparticles for targeting the inflamed intestinal mucosa—pharmaceutical characterization and fluorescence imaging. *Pharm. Res.* **33**, 1085–1092 (2016).
207. Zolnik, B. S. & Burgess, D. J. Effect of acidic pH on PLGA microsphere degradation and release. *J. Control. Release* **122**, 338–344 (2007).
208. Kolte, A., Patil, S., Lesimple, P., Hanrahan, J. W. & Misra, A. PEGylated composite

nanoparticles of PLGA and polyethylenimine for safe and efficient delivery of pDNA to lungs. *Int. J. Pharm.* **524**, 382–396 (2017).
209. Ding, S., Cargill, A. A., Medintz, I. L., & Claussen, J. C. Increasing the activity of immobilized enzymes with nanoparticle conjugation. *Curr. Opin. Biotechnol.* **34**, 242–250 (2015).
210. Welsch, N., Wittemann, A., & Ballauff, M. Enhanced activity of enzymes immobilized in thermoresponsive core– shell microgels. *J. Phys. Chem. B* **113**, 16039–16045 (2009).
211. Borch, R. F., Bernstein, M. D. & Durst, H. D. The Cyanohydridoborate Anion as a Selective Reducing Agent. *J. Am. Chem. Soc.* **93**, 2897–2904 (1971).
212. Hermans, M. M. P., Kroos, M. A., Van Beeumen, J., Oostra, B. A. & Reuser, A. J. J. Human lysosomal α-glucosidase: Characterization of the catalytic site. *J. Biol. Chem.* **266**, 13507–13512 (1991).
213. Lyly, A. *et al.* Glycosylation, transport, and complex formation of palmitoyl protein thioesterase 1 (PPT1) - Distinct characteristics in neurons. *BMC Cell Biol.* **8**, (2007).
214. Santi, M. *et al.* Rational Design of a Transferrin-Binding Peptide Sequence Tailored to Targeted Nanoparticle Internalization. *Bioconjug. Chem.* **28**, 471–480 (2017).
215. Lu, J. Y., Hu, J. & Hofmann, S. L. Human recombinant palmitoyl-protein thioesterase-1 (PPT1) for preclinical evaluation of enzyme replacement therapy for infantile neuronal ceroid lipofuscinosis. *Mol. Genet. Metab.* **99**, 374–378 (2010).
216. Starcher, B. A ninhydrin-based assay to quantitate the total protein content of tissue samples. *Anal. Biochem.* **292**, 125–129 (2001).
217. Van Diggelen, O. P. *et al.* A rapid fluorogenic palmitoyl-protein thioesterase assay: Pre- and postnatal diagnosis of INCL. *Mol. Genet. Metab.* **66**, 240–244 (1999).
218. Sharma, G., Sharma, A. R., Lee, S. S., Bhattacharya, M., Nam, J. S., & Chakraborty, C. Advances in nanocarriers enabled brain targeted drug delivery across blood brain barrier. *Int. J. Pharm.* (2019).
219. M. Demeule, J. Currie, Y. Bertrand, C. Ché, T. Nguyen, A. Régina, R. Gabathuler, J. Castaigne, R. B. Involvement of the low-density lipoprotein receptor-related protein in the transcytosis of the brain delivery vector Angiopep-2. *J. Neurochem.* **106**, 1534–1544 (2008).
220. Tosi, G., Fano, R. A., Bondioli, L., Badiali, L., Benassi, R., Rivasi, F., ... & Vandelli, M. A. Investigation on mechanisms of glycopeptide nanoparticles for drug delivery across the blood–brain barrier. *Nanomedicine* **6**, 423–436 (2011).
221. Kamaly, N., Fredman, G., Subramanian, M., Gadde, S., Pesic, A., Cheung, L., ... & Farokhzad, O. C. Development and in vivo efficacy of targeted polymeric inflammation-resolving nanoparticles. *gs Natl. Acad. Sci.* **110**, 6506–6511 (2013).
222. Meng, X. L., Eto, Y., Schiffmann, R. & Shen, J. S. HIV tat domain improves cross-correction of human galactocerebrosidase in a gene- And flanking sequence-dependent manner. *Mol. Ther. - Nucleic Acids* **2**, e130 (2013).
223. Wu, Y. *et al.* Theranostics Chimeric peptide supramolecular nanoparticles for plectin-1 targeted miRNA-9 delivery in pancreatic cancer. **10**, (2020).
224. Mirshafiee, V., Mahmoudi, M., Lou, K., Cheng, J., & Kraft, M. L. Protein corona significantly reduces active targeting yield. *Chem. Commun.* **49**, 2557–2559 (2013).
225. Kobayashi, T., Yamanaka, T., Jacobs, J. M., Teixeira, F., & Suzuki, K. The Twitcher mouse: an enzymatically authentic model of human globoid cell leukodystrophy (Krabbe disease). *Brain Res.* **202**, 479–483 (1980).
226. Regina, A., Demeule, M., Che, C., Lavallee, I., Poirier, J., Gabathuler, R., ... & Castaigne, J. P. Antitumour activity of ANG1005, a conjugate between paclitaxel and the new brain delivery vector Angiopep-2. *Br. J. Pharmacol.* **155**, 185–197 (2008).

227. Xin, H., Jiang, X., Gu, J., Sha, X., Chen, L., Law, K., ... & Fang, X. Angiopep-conjugated poly (ethylene glycol)-co-poly (ε-caprolactone) nanoparticles as dual-targeting drug delivery system for brain glioma. *Biomaterials* **32**, 4293–4305 (2011).
228. Hickey, J. W., Santos, J. L., Williford, J. M., & Mao, H. Q. Control of polymeric nanoparticle size to improve therapeutic delivery. *J. Control. Release* **219**, 536–547 (2015).
229. Galliani, M., Tremolanti, C., & Signore, G. Nanocarriers for Protein Delivery to the Cytosol: Assessing the Endosomal Escape of Poly (Lactide-co-Glycolide)-Poly (Ethylene Imine) Nanoparticles. *Nanomaterials* **9**, 652 (2019).
230. Mühlstein, A., Gelperina, S., & Kreuter, J. Development of nanoparticle-bound arylsulfatase B for enzyme replacement therapy of mucopolysaccharidosis VI. *Die Pharm. Int. J. Pharm. Sci.* **68**, 549–554 (2013).
231. Raucher, D., Dragojevic, S., & Ryu, J. Macromolecular Drug Carriers for Targeted Glioblastoma Therapy: Preclinical Studies, Challenges and Future Perspectives. *Front. Oncol.* **8**, 624 (2018).
232. Turner, P. V., Brabb, T., Pekow, C. & Vasbinder, M. A. Administration of substances to laboratory animals: Routes of administration and factors to consider. *J. Am. Assoc. Lab. Anim. Sci.* **50**, 600–613 (2011).
233. Umezawa, F., Eto, Y., Tokoro, T., Ito, F., & Maekawa, K. Enzyme replacement with liposomes containing beta-galactosidase from Charonia lumpas in murine globoid cell leukodystrophy (twitcher). *Biochem. Biophys. Res. Commun.* **127**, 663–667 (1985).
234. Boado, R. J., Zhang, Y., Zhang, Y., Xia, C. F., Wang, Y., & Pardridge, W. M. Genetic engineering of a lysosomal enzyme fusion protein for targeted delivery across the human blood-brain barrier. *Biotechnol. Bioeng.* **99**, 475–484 (2008).
235. Kelly, J. M., Bradbury, A., Martin, D. R., & Byrne, M. E. . Emerging therapies for neuropathic lysosomal storage disorders. *Prog. Neurobiol.* **152**, **166–1**, (2017).
236. Tschetter, T. H., Klassen, A. C., Resch, J. A. & Meyer, M. W. Blood flow in the central and peripheral nervous system of dogs using a particle distribution method. *Stroke* **1**, 370–374 (1970).
237. Smythies, John R. and Bradly, R. J. International Review of Neurobiology. *Acad. Press* **31**, (1990).
238. Maeki, M. Microfluidics for Pharmaceutical. in *Applications, Micro and Nano Technologies. H. A. Santos, D. Liu, H. Zhang, Eds. (William Andrew Publishing, 2019)* 101–119. (2019).
239. Serpooshan, V., Sheibani, S., Pushparaj, P., Wojcik, M., Jang, A. Y., Santoso, M. R., ... & Nejadnik, H. Effect of cell sex on uptake of nanoparticles: the overlooked factor at the nanobio interface. *ACS Nano* **12**, 2253–2266 (2018).
240. Tappino, B., Biancheri, R., Mort, M., Regis, S., Corsolini, F., Rossi, A., ... & Di Rocco, M. Identification and characterization of 15 novel GALC gene mutations causing Krabbe disease. *Hum. Mutat.* **31**, E1894–E1914 (2010).
241. Yamazaki, N., Kosuga, M., Kida, K., Takei, G., Fukuhara, Y., Matsumoto, H., ... & Yabe, H. Early enzyme replacement therapy enables a successful hematopoietic stem cell transplantation in mucopolysaccharidosis type IH: Divergent clinical outcomes in two Japanese siblings. *Brain Dev.* **41**, 546–550 (2019).
242. Mahmoudi, M. Debugging nano–bio interfaces: systematic strategies to accelerate clinical translation of nanotechnologies. *Trends Biotechnol.* **36**, 755–769 (2018).
243. Wiederschain, G., Srinivasa, R., & Kolodny, E. Characterization of 6-hexadecanoylamino-4-methylumbelliferyl-β-D-galactopyranoside as fluorogenic substrate of galactocerebrosidase for the diagnosis of Krabbe disease. *Clin. Chim. acta*

**205**, 87–96 (1992).
244. Sakai, N., Inui, K., Tatsumi, N., Fukushima, H., Nishigaki, T., Taniike, M., ... & Okada, S. Molecular cloning and expression of cDNA for murine galactocerebrosidase and mutation analysis of the twitcher mouse, a model of Krabbe's disease. *J. Neurochem.* **66**, 1118–1124 (1996).
245. Zhou, P., An, T., Zhao, C., Li, Y., Li, R., Yang, R., ... & Gao, X. Lactosylated PLGA nanoparticles containing ϵ-polylysine for the sustained release and liver-targeted delivery of the negatively charged proteins. ,. *Int. J. Pharm.* **478**, 633–643 (2015).
246. Hamasaki, M. *et al.* Autophagosomes form at ER–mitochondria contact sites. *Nature* **495**, 389 (2013).
247. Hayashi-Nishino, M. *et al.* A subdomain of the endoplasmic reticulum forms a cradle for autophagosome formation. *Nat. Cell Biol.* **11**, 1433–1437 (2009).
248. Ravikumar, B., Moreau, K., Jahreiss, L., Puri, C. & Rubinsztein, D. C. Plasma membrane contributes to the formation of pre-autophagosomal structures. *Nat. Cell Biol.* **12**, 747–757 (2010).
249. Hailey, D. W. *et al.* Mitochondria Supply Membranes for Autophagosome Biogenesis during Starvation. *Cell* **141**, 656–667 (2010).
250. Berg, T. O., Fengsrud, M., Strømhaug, P. E., Berg, T. & Seglen, P. O. Isolation and characterization of rat liver amphisomes: Evidence for fusion of autophagosomes with both early and late endosomes. *J. Biol. Chem.* **273**, 21883–21892 (1998).
251. Sarkar, S. Regulation of autophagy by mTOR-dependent and mTOR-independent pathways: autophagy dysfunction in neurodegenerative diseases and therapeutic application of autophagy enhancers. *Biochem. Soc. Trans.* **41**, 1103–1130 (2013).
252. Sarkar, S. *et al.* Impaired autophagy in the lipid-storage disorder niemann-pick type c1 disease. *Cell Rep.* **5**, 1302–1315 (2013).
253. Tanida, I. *et al.* HsAtg4B/HsApg4B/autophagin-1 cleaves the carboxyl termini of three human Atg8 homologues and delipidates microtubule-associated protein light chain 3- and GABAA receptor-associated protein-phospholipid conjugates. *J. Biol. Chem.* **279**, 36268–36276 (2004).
254. Petiot, A., Ogier-Denis, E., Blommaart, E. F. C., Meijer, A. J. & Codogno, P. Erratum: Distinct classes of phosphatidylinositol 3'-kinases are involved in signaling pathways that control macro-autophagy in HT-29 cells (Journal of Biological Chemistry (2000) 275 (992-998)). *J. Biol. Chem.* **275**, 12360 (2000).
255. Axe, E. L. *et al.* Autophagosome formation from membrane compartments enriched in phosphatidylinositol 3-phosphate and dynamically connected to the endoplasmic reticulum. *J. Cell Biol.* **182**, 685–701 (2008).
256. Itakura, E., Kishi, C., Inoue, K., & Mizushima, N. Beclin 1 forms two distinct phosphatidylinositol 3-kinase complexes with mammalian Atg14 and UVRAG. , 19(12), . *Mol. Biol. Cell* **19**, 5360–5372 (2008).
257. Kihara, A., Kabeya, Y., Ohsumi, Y. & Yoshimori, T. Beclin-PI3K complex functions at the trans -Golgi network. **2**, 330–335 (2001).
258. Matsunaga, K. *et al.* Two Beclin 1-binding proteins, Atg14L and Rubicon, reciprocally regulate autophagy at different stages. *Nat. Cell Biol.* **11**, 385–396 (2009).
259. He, C. & Levine, B. The Beclin 1 interactome. *Curr. Opin. Cell Biol.* **22**, 140–149 (2010).
260. Ravikumar, B., Imarisio, S., Sarkar, S., O'Kane, C. J. & Rubinsztein, D. C. Rab5 modulates aggregation and toxicity of mutant huntingtin through macroautophagy in cell and fly models of Huntington disease. *J. Cell Sci.* **121**, 1649–1660 (2008).
261. Mizushima, N., Yoshimori, T. & Levine, B. Methods in Mammalian Autophagy Research. *Cell* **140**, 313–326 (2010).

262. Jahreiss, L., Menzies, F. M. & Rubinsztein, D. C. The itinerary of autophagosomes: From peripheral formation to kiss-and-run fusion with lysosomes. *Traffic* **9**, 574–587 (2008).
263. Kimura, S., Noda, T. & Yoshimori, T. Dynein-dependent movement of autophagosomes mediates efficient encounters with lysosomes. *Cell Struct. Funct.* **33**, 109–122 (2008).
264. Jäger, S. *et al.* Role for Rab7 in maturation of late autophagic vacuoles. *J. Cell Sci.* **117**, 4837–4848 (2004).
265. Filimonenko, M. *et al.* Functional multivesicular bodies are required for autophagic clearance of protein aggregates associated with neurodegenerative disease. *J. Cell Biol.* **179**, 485–500 (2007).
266. Lee, J. A., Beigneux, A., Ahmad, S. T., Young, S. G. & Gao, F. B. ESCRT-III Dysfunction Causes Autophagosome Accumulation and Neurodegeneration. *Curr. Biol.* **17**, 1561–1567 (2007).
267. Rusten, T. E. & Simonsen, A. ESCRT functions in autophagy and associated disease. *Cell Cycle* **7**, 1166–1172 (2008).
268. Renna, M. *et al.* Autophagic substrate clearance requires activity of the syntaxin-5 SNARE complex. *J. Cell Sci.* **124**, 469–482 (2011).
269. Bjørkøy, G. *et al.* p62/SQSTM1 forms protein aggregates degraded by autophagy and has a protective effect on huntingtin-induced cell death. *J. Cell Biol.* **171**, 603–614 (2005).
270. Pankiv, S. *et al.* p62/SQSTM1 binds directly to Atg8/LC3 to facilitate degradation of ubiquitinated protein aggregates by autophagy*[S]. *J. Biol. Chem.* **282**, 24131–24145 (2007).
271. Singh, R. *et al.* Autophagy regulates lipid metabolism. *Nature* **458**, 1131–1135 (2009).
272. Youle, R. J. & Narendra, D. P. Mechanisms of mitophagy. *Nat. Rev. Mol. Cell Biol.* **12**, 9–14 (2011).
273. Levy, J. M. M., Towers, C. G. & Thorburn, A. Targeting autophagy in cancer. *Nat. Rev. Cancer* **17**, 528 (2017).
274. Rubinsztein, D. C., Mariño, G. & Kroemer, G. Autophagy and aging. *Cell* **146**, 682–695 (2011).
275. Towers, C. G. & Thorburn, A. Therapeutic Targeting of Autophagy. *EBioMedicine* **14**, 15–23 (2016).
276. Ross, C. A. & Poirier, M. A. Protein aggregation and neurodegenerative disease. *Nat. Med.* **10**, S10–S17 (2004).
277. Zoghbi, H. Y., & Orr, H. T. Glutamine repeats and neurodegeneration. *Annu. Rev. Neurosci.* **23**, 217–247 (2000).
278. Lansbury, P. T. & Lashuel, H. A. A century-old debate on protein aggregation and neurodegeneration enters the clinic. *Nature* **443**, 774–779 (2006).
279. Watanabe, Y. *et al.* p62/SQSTM1-Dependent Autophagy of Lewy Body-Like α-Synuclein Inclusions. *PLoS One* **7**, 1–12 (2012).
280. Kuusisto, E., Salminen, A., & Alafuzoff, I. Ubiquitin-binding protein p62 is present in neuronal and glial inclusions in human tauopathies and synucleinopathies. *Neuroreport* **12**, 2085–2090 (2001).
281. Komatsu, M. *et al.* Homeostatic Levels of p62 Control Cytoplasmic Inclusion Body Formation in Autophagy-Deficient Mice. *Cell* **131**, 1149–1163 (2007).
282. Sarkar, S., Ravikumar, B., & Rubinsztein, D. C. Autophagic clearance of aggregate-prone proteins associated with neurodegeneration. *Methods Enzymol.* **453**, 83–110 (2009).
283. Rubinsztein, D. C., Codogno, P. & Levine, B. Autophagy modulation as a potential therapeutic target for diverse diseases. *Nat. Rev. Drug Discov.* **11**, 709–730 (2012).

284. Fleming, A., Noda, T., Yoshimori, T. & Rubinsztein, D. C. Chemical modulators of autophagy as biological probes and potential therapeutics. *Nat. Chem. Biol.* **7**, 9–17 (2011).
285. Ravikumar, B. *et al.* Inhibition of mTOR induces autophagy and reduces toxicity of polyglutamine expansions in fly and mouse models of Huntington disease. *Nat. Genet.* **36**, 585–595 (2004).
286. Pan, T., Kondo, S., Zhu, W., Xie, W., Jankovic, J., & Le, W. Neuroprotection of rapamycin in lactacystin-induced neurodegeneration via autophagy enhancement. *Neurobiol. Dis.* **32**, 16–25 (2008).
287. Wang, T., Lao, U. & Edgar, B. A. TOR-mediated autophagy regulates cell death in Drosophila neurodegenerative disease. *J. Cell Biol.* **186**, 703–711 (2009).
288. Mandrioli, J. *et al.* Rapamycin treatment for amyotrophic lateral sclerosis protocol for a phase II randomized, double-blind, placebo-controlled, multicenter, clinical trial (RAP-ALS trial). *Med. (United States)* **97**, (2018).
289. Ghaiad, H. R., Nooh, M. M., El-Sawalhi, M. M. & Shaheen, A. A. Resveratrol Promotes Remyelination in Cuprizone Model of Multiple Sclerosis: Biochemical and Histological Study. *Mol. Neurobiol.* **54**, 3219–3229 (2017).
290. Williams, R. S. B., Eames, M., Ryves, W. J., Viggars, J. & Harwood, A. J. Loss of a prolyl oligopeptidase confers resistance to lithium by elevation of inositol (1,4,5) trisphosphate. *EMBO J.* **18**, 2734–2745 (1999).
291. Cloughesy, T. F., Yoshimoto, K., Nghiemphu, P., Brown, K., Dang, J., Zhu, S., ... & Liau, L. Antitumor activity of rapamycin in a Phase I trial for patients with recurrent PTEN-deficient glioblastoma. *PLoS Med.* **5**, e8 (2008).
292. Majumder, S., Richardson, A., Strong, R., & Oddo, S. Inducing autophagy by rapamycin before, but not after, the formation of plaques and tangles ameliorates cognitive deficits. *PLoS One* **6**, e25416 (2011).
293. Sarkar, S., Krishna, G., Imarisio, S., Saiki, S., O'Kane, C. J., & Rubinsztein, D. C. A rational mechanism for combination treatment of Huntington's disease using lithium and rapamycin. *Hum. Mol. Genet.* **17**, 170–178 (2007).
294. Lieberman, A. P. *et al.* Autophagy in lysosomal storage disorders. *Autophagy* **8**, 719–730 (2012).
295. Tanaka Y., Guhde G., Suter A., Eskelinen E. L., Hartmann D, Lüllmann-Rauch R., Janssen P. M. L., B. J. & von Figura K. & Saftig P. Accumulation of autophagic vacuoles and cardiomyopathy in LAMP-2-deficient mice. *Nature* **406**, 902–906 (2000).
296. Koike M., Shibata M., W. S. et al. Participation of autophagy in storage of lysosomes in neurons from mouse models of neuronal ceroid-lipofuscinoses (Batten disease). *Am. J. Pathol.* **167**, 1713–1728 (2005).
297. Cao Y., Espinola J. A., Fossale E., Massey A. C., Cuervo A. M., MacDonald M. E., & C. S. L. . Autophagy is disrupted in a knock-in mouse model of juvenile neuronal ceroid lipofuscinosis. *J. Biol. Chem.* **281**, 20483–20493 (2006).
298. Jennings, J. J., Zhu, J. H., Rbaibi, Y., Luo, X., Chu, C. T., & Kiselyov, K. Mitochondrial aberrations in mucolipidosis Type IV. *J. Biol. Chem.* **281**, 39041–39050 (2006).
299. Fukuda T., Roberts A., Ahearn M., Zaal K., Ralston E., Plotz P. H., & R. N. Autophagy and lysosomes in Pompe disease. *Autophagy* **2**, 318–320 (2006).
300. Takamura A., Higaki K., Kajimaki K., Otsuka S., Ninomiya H., Matsuda J., Ohno K., S. Y. & N. E. Enhanced autophagy and mitochondrial aberrations in murine G M1-gangliosidosis. *Biophys. Res. Commun.* **367**, 616–622 (2008).
301. Settembre, C. *et al.* A block of autophagy in lysosomal storage disorders. *Hum. Mol. Genet.* **17**, 119–129 (2008).

302. Settembre, C., Fraldi, A., Rubinsztein, D. C. & Ballabio, A. Lysosomal storage diseases as disorders of autophagy. *Autophagy* **4**, 113–114 (2008).
303. Ballabio, A. & Gieselmann, V. Lysosomal disorders: From storage to cellular damage. *Biochim. Biophys. Acta - Mol. Cell Res.* **1793**, 684–696 (2009).
304. Ward, C. *et al.* Autophagy, lipophagy and lysosomal lipid storage disorders. *Biochim. Biophys. Acta - Mol. Cell Biol. Lipids* **1861**, 269–284 (2016).
305. Seranova, E. *et al.* Dysregulation of autophagy as a common mechanism in lysosomal storage diseases. *Essays Biochem.* **61**, 733–749 (2017).
306. Ashe, K., Taylor, K. M., Chu, Q., Meyers, E., Ellis, A., Jingozyan, V., ... & Marshall, J. Inhibition of Glycogen Biosynthesis via mTORC1 Suppression as an Adjunct Therapy for Pompe Disease. *Clin. Ther.* **33**, S31 (2011).
307. Blommaart, E.F.C., Luiken, J.J.F.P., Blommaart, P.J.E., van Woerkom, G.M. and Meijer, A. J. Phosphorylation of ribosomal protein S6 is inhibitory for autophagy in isolated rat hepatocytes. *J. Biol. Chem.* **270**, 2320–2326 (1995).
308. Maetzel, D. *et al.* Genetic and chemical correction of cholesterol accumulation and impaired autophagy in hepatic and neural cells derived from niemann-pick type C patient-specific iPS cells. *Stem Cell Reports* **2**, 866–880 (2014).
309. Canonico, B., Cesarini, E., Salucci, S., Luchetti, F., Falcieri, E., Di Sario, G. et al. Defective autophagy, mitochondrial clearance and lipophagy in Niemann-Pick Type B lymphocytes. *PLoS One 11* **e0165780**, (2016).
310. Nascimbeni, A. C., Fanin, M., Masiero, E., Angelini, C. & Sandri, M. The role of autophagy in the pathogenesis of glycogen storage disease type II (GSDII). *Cell Death Differ.* **19**, 1698–1708 (2012).
311. Kinghorn, K. J. *et al.* A Drosophila model of neuronopathic gaucher disease demonstrates lysosomal-autophagic defects and altered mTOR signalling and is functionally rescued by rapamycin. *J. Neurosci.* **36**, 11654–11670 (2016).
312. Sarkar, S., Davies, J. E., Huang, Z., Tunnacliffe, A. & Rubinsztein, D. C. Trehalose, a novel mTOR-independent autophagy enhancer, accelerates the clearance of mutant huntingtin and α-synuclein. *J. Biol. Chem.* **282**, 5641–5652 (2007).
313. DeBosch, B. J. *et al.* Trehalose inhibits solute carrier 2A (SLC2A) proteins to induce autophagy and prevent hepatic steatosis. *Sci. Signal.* **9**, (2016).
314. Palmieri, M. *et al.* mTORC1-independent TFEB activation via Akt inhibition promotes cellular clearance in neurodegenerative storage diseases. *Nat. Commun.* **8**, 14338 (2017).
315. Maetzel, D., Sarkar, S., Wang, H., Abi-Mosleh, L., Xu, P., Cheng, A. W. et al. Genetic and chemical correction of cholesterol accumulation and impaired autophagy in hepatic and neural cells derived from Niemann-Pick Type C patient-specific iPS cells. *Stem Cell Rep.* **2**, 866–880 (2014).
316. Sarkar, S. *et al.* Lithium induces autophagy by inhibiting inositol monophosphatase. *J. Cell Biol.* **170**, 1101–1111 (2005).
317. Chang, J.-W., Choi, H., Cotman, S.L. and Jung, Y.-K. Lithium rescues the impaired autophagy process in CbCln3_ex7/8/_ex7/8 cerebellar cells and reduces neuronal vulnerability to cell death via IMPase inhibition. *J. Neurochem.* **116**, 659–668 (2011).
318. Williams, A. *et al.* Novel targets for Huntington's disease in an mTOR-independent autophagy pathway. *Nat. Chem. Biol.* **4**, 295–305 (2008).
319. Kuo, S. Y. *et al.* Small-molecule enhancers of autophagy modulate cellular disease phenotypes suggested by human genetics. *Proc. Natl. Acad. Sci. U. S. A.* **112**, E4281–E4287 (2015).
320. Proikas-Cezanne, T., Ruckerbauer, S., Stierhof, Y. D., Berg, C., & Nordheim, A. Human

WIPI-1 puncta-formation: a novel assay to assess mammalian autophagy. *FEBS Lett.* **581**, 3396–3404 (2007).
321. Travassos, L. H. *et al.* Nod1 and Nod2 direct autophagy by recruiting ATG16L1 to the plasma membrane at the site of bacterial entry. *Nat. Immunol.* **11**, 55–62 (2010).
322. Heiseke, A., Aguib, Y., Riemer, C., Baier, M. & Schätzl, H. M. Lithium induces clearance of protease resistant prion protein in prion-infected cells by induction of autophagy. *J. Neurochem.* **109**, 25–34 (2009).
323. Mizushima, N. & Yoshimori, T. How to interpret LC3 immunoblotting. *Autophagy* **3**, 542–545 (2007).
324. Rubinsztein, D. C. *et al.* In search of an 'autophagomometer'. *Autophagy* **5**, 585–589 (2009).
325. Bampton, E. T. W., Goemans, C. G., Niranjan, D., Mizushima, N. & Tolkovsky, A. M. The dynamics of autophagy visualized in live cells: from autophagosome formation to fusion with endo/lysosomes. *Autophagy* **1**, 23–36 (2005).
326. Motoi, Y., Shimada, K., Ishiguro, K. & Hattori, N. Lithium and autophagy. *ACS Chem. Neurosci.* **5**, 434–442 (2014).
327. Malhi, G.S., Tanious M., Das P., Coulston C.M., & B. M. Potential mechanisms of action of Li in bipolar disorder. *Curr Understanding. CNS Drugs* **27**, 135-153. (2013).
328. Dwivedi, T. & Zhang, H. Lithium-induced neuroprotection is associated with epigenetic modification of specific BDNF gene promoter and altered expression of apoptotic-regulatory proteins. *Front. Neurosci.* **9**, 1–8 (2015).
329. Haq, E., Giri, S., Singh, I. & Singh, A. K. Molecular mechanism of psychosine-induced cell death in human oligodendrocyte cell line. *J. Neurochem.* **86**, 1428–1440 (2003).
330. Ju, J. S., Varadhachary, A. S., Miller, S. E., & Weihl, C. C. Quantitation of" autophagic flux" in mature skeletal muscle. *Autophagy* **6**, 929–935 (2010).
331. Puissant, A., Fenouille, N. & Auberger, P. When autophagy meets cancer through p62/SQSTM1. *Am. J. Cancer Res.* **2**, 397–413 (2012).
332. Xie, X., White, E. P. & Mehnert, J. M. Coordinate Autophagy and mTOR Pathway Inhibition Enhances Cell Death in Melanoma. *PLoS One* **8**, 1–11 (2013).
333. Decressac, M. *et al.* TFEB-mediated autophagy rescues midbrain dopamine neurons from α-synuclein toxicity. *Proc. Natl. Acad. Sci. U. S. A.* **110**, (2013).
334. Hu, G. *et al.* Triptolide Promotes the Clearance of α-Synuclein by Enhancing Autophagy in Neuronal Cells. *Mol. Neurobiol.* **54**, 2361–2372 (2017).
335. Tian, T. *et al.* Acupuncture promotes mTOR-independent autophagic clearance of aggregation-prone proteins in mouse brain. *Sci. Rep.* **6**, 19714 (2016).
336. Tommasino, C., Marconi, M., Ciarlo, L., Matarrese, P. & Malorni, W. Autophagic flux and autophagosome morphogenesis require the participation of sphingolipids. *Apoptosis* **20**, 645–657 (2015).
337. Lingwood, D. & Simons, K. Lipid rafts as a membrane-organizing principle. *Science (80-. ).* **327**, 46–50 (2010).
338. Sorice, M. *et al.* Dynamics of mitochondrial raft-like microdomains in cell life and death. *Commun. Integr. Biol.* **5**, 217–219 (2012).
339. Fantini, J., Carlus, D. & Yahi, N. The fusogenic tilted peptide (67-78) of α-synuclein is a cholesterol binding domain. *Biochim. Biophys. Acta - Biomembr.* **1808**, 2343–2351 (2011).
340. Shi, C.-S. *et al.* Activation of autophagy by inflammatory signals limits IL-1β production by targeting ubiquitinated inflammasomes for destruction. *Nat. Immunol.* **13**, 255–263 (2012).
341. Masiero, E. *et al.* Autophagy Is Required to Maintain Muscle Mass. *Cell Metab.* **10**, 507–

515 (2009).
342. Tonazzini, I., Meucci, S., Van Woerden, G. M., Elgersma, Y., & Cecchini, M. Impaired Neurite Contact Guidance in Ubiquitin Ligase E3a (Ube3a)-Deficient Hippocampal Neurons on Nanostructured Substrates. *Adv. Healthc. Mater.* **5**, 850–862 (2016).
343. Vazquez-Martin, A., Oliveras-Ferraros, C. & Menendez, J. A. Autophagy facilitates the development of breast cancer resistance to the anti-HER2 monoclonal antibody trastuzumab. *PLoS One* **4**, (2009).
344. Ramírez-Peinado, S. *et al.* Glucose-starved cells do not engage in prosurvival autophagy. *J. Biol. Chem.* **288**, 30387–30398 (2013).
345. Nelson, C. M. *et al.* Stat3 defines three populations of müller glia and is required for initiating maximal müller glia proliferation in the regenerating zebrafish retina. *J. Comp. Neurol.* **520**, 4294–4311 (2012).
346. Tresse, E. *et al.* VCP/p97 is essential for maturation of ubiquitin-containing autophagosomes and this function is impaired by mutations that cause IBMPFD. *Autophagy* **6**, 217–227 (2010).
347. Eruslanov, E., & Kusmartsev, S. Identification of ROS using oxidized DCFDA and flow-cytometry. *Adv. Protoc. oxidative Stress II* 57–72 (2010).
348. Gusel'Nikova, V. V., & Korzhevskiy, D. E. NeuN as a neuronal nuclear antigen and neuron differentiation marker. *Acta Naturae (англоязычная версия)* **7**, 25 (2015).
349. Barbarese, E., Barry, C., Chou, C. H. J., Goldstein, D. J., Nakos, G. A., Hyde-DeRuyscher, R., ... & Carson, J. H. (1988). Expression and localization of myelin basic protein in oligodendrocytes and transfected fibroblasts. , 51(6), 1737-1745. *J. Neurochem.* **51**, 1737–1745 (1988).
350. Singh, B., & Bhaskar, S. Methods for Detection of Autophagy in Mammalian Cells. *Methods Mol. Biol.* **2045.**, (2017).
351. Li, F. *et al.* Beclin1 restricts RNA virus infection in plants through suppression and degradation of the viral polymerase. *Nat. Commun.* **9**, 1268 (2018).
352. Guha, S., Baltazar, G. C., Coffey, E. E., Tu, L. A., Lim, J. C., Beckel, J. M., ... & Laties, A. M. Lysosomal alkalinization, lipid oxidation, and reduced phagosome clearance triggered by activation of the P2X7 receptor. *FASEB J.* **27**, 4500–4509 (2013).
353. Graziano, A. C. E., & Cardile, V. History, genetic, and recent advances on Krabbe disease. *Gene* **555**, 2–13 (2015).
354. Boland, B. *et al.* Macroautophagy is not directly involved in the metabolism of amyloid precursor protein. *J. Biol. Chem.* **285**, 37415–37426 (2010).
355. Seidel, K. *et al.* On the distribution of intranuclear and cytoplasmic aggregates in the brainstem of patients with spinocerebellar ataxia type 2 and 3. *Brain Pathol.* **27**, 345–355 (2017).
356. Micsenyi, M. C., Sikora, J., Stephney, G., Dobrenis, K. & Walkley, S. U. Lysosomal membrane permeability stimulates protein aggregate formation in neurons of a lysosomal disease. *J. Neurosci.* **33**, 10815–10827 (2013).
357. Pierzynowska, K. *et al.* Autophagy stimulation as a promising approach in treatment of neurodegenerative diseases. *Metab. Brain Dis.* **33**, 989–1008 (2018).
358. Ravikumar, B. Aggregate-prone proteins with polyglutamine and polyalanine expansions are degraded by autophagy. *Hum. Mol. Genet.* **11**, 1107–1117 (2002).
359. Sarkar, S. & Rubinsztein, D. C. Huntington's disease: Degradation of mutant huntingtin by autophagy. *FEBS J.* **275**, 4263–4270 (2008).
360. Webb, J. L., Ravikumar, B., Atkins, J., Skepper, J. N. & Rubinsztein, D. C. α-synuclein Is Degraded by Both Autophagy and the Proteasome. *J. Biol. Chem.* **278**, 25009–25013 (2003).

361. Rafi, M. A., Rao, H. Z., Luzi, P. & Wenger, D. A. Long-term improvements in lifespan and pathology in CNS and PNS after BMT plus one intravenous injection of AAVrh10-GALC in twitcher mice. *Mol. Ther.* **23**, 1681–1690 (2015).
362. de Vito, G., Tonazzini, I., Cecchini, M. & Piazza, V. RP-CARS: label-free optical readout of the myelin intrinsic healthiness. *Opt. Express* **22**, 13733 (2014).
363. Fu, R. *et al.* Low-dose ethanol excites lateral habenula neurons projecting to VTA, RMTg, and raphe. *Int. J. Physiol. Pathophysiol. Pharmacol.* **9**, 217–230 (2017).
364. Lu, Y., Lin, B., & Zhong, J. The therapeutic effect of dexmedetomidine on rat diabetic neuropathy pain and the mechanism. *Biol. Pharm. Bull.* **b17**, 00224 (2017).
365. Spalletti, C. *et al.* Combining robotic training and inactivation of the healthy hemisphere restores pre-stroke motor patterns in mice. *Elife* **6**, 1–31 (2017).
366. Floden, A. M., & Combs, C. K. Microglia demonstrate age-dependent interaction with amyloid-β fibrils. *J. Alzheimer's Dis.* **25**, 279–293 (2011).
367. Zanfini, A., Dreassi, E., Berardi, A., Governini, L., Corbini, G., Costantino-Ceccarini, E., ... & Luddi, A. Quantification of psychosine in the serum of twitcher mouse by LC–ESI-tandem-MS analysis. *J. Pharm. Biomed. Anal.* **80**, 44–49 (2013).
368. Esch, S. W., Williams, T. D., Biswas, S., Chakrabarty, A., & Levine, S. M. (). Sphingolipid profile in the CNS of the twitcher (globoid cell leukodystrophy) mouse: a lipidomics approach. , 49(5), . *Cell. Mol. Biol. (Noisy-le-grand).* **49**, 779–787 (2003).
369. Zanfini, A., Dreassi, E., Berardi, A., Piomboni, P., Costantino-Ceccarini, E., & Luddi, A. GC-EI-MS analysis of fatty acid composition in brain and serum of twitcher mouse. *Lipids* **49**, 1115–1125 (2014).
370. Meisingset, T. W., Ricca, A., Neri, M., Sonnewald, U. & Gritti, A. Region- and age-dependent alterations of glial-neuronal metabolic interactions correlate with CNS pathology in a mouse model of globoid cell leukodystrophy. *J. Cereb. Blood Flow Metab.* **33**, 1127–1137 (2013).
371. Weinstock, N. I., Wrabetz, L., Feltri, M. L., & Shin, D. Metabolic profiling reveals biochemical pathways and potential biomarkers associated with the pathogenesis of K rabbe disease. *J. Neurosci. Res.* **94**, 1094–1107.
372. Aebersold, R. & Mann, M. Mass spectrometry-based proteomics. *Nature* **422**, 198–207 (2003).
373. Altelaar, A. F. M., Munoz, J. & Heck, A. J. R. Next-generation proteomics: towards an integrative view of proteome dynamics. *Nat. Rev. Genet.* **14**, 35–48 (2013).
374. Cravatt, B. F., Simon, G. M. & Yates III, J. R. The biological impact of mass-spectrometry-based proteomics. *Nature* **450**, 991–1000 (2007).
375. Clair, G. *et al.* Spatially-Resolved Proteomics: Rapid Quantitative Analysis of Laser Capture Microdissected Alveolar Tissue Samples. *Sci. Rep.* **6**, 39223 (2016).
376. Liu, N. Q. *et al.* Quantitative proteomic analysis of microdissected breast cancer tissues: Comparison of label-free and SILAC-based quantification with shotgun, directed, and targeted MS approaches. *J. Proteome Res.* **12**, 4627–4641 (2013).
377. Gutstein, H. B., Morris, J. S., Annangudi, S. P., & Sweedler, J. V. Microproteomics: analysis of protein diversity in small samples. *Mass Spectrom. Rev.* **27**, 316–330 (2008).
378. De Graaf, E. L., Pellegrini, D. & McDonnell, L. A. Set of Novel Automated Quantitative Microproteomics Protocols for Small Sample Amounts and Its Application to Kidney Tissue Substructures. *J. Proteome Res.* **15**, 4722–4730 (2016).
379. Hughes, C. S. *et al.* Ultrasensitive proteome analysis using paramagnetic bead technology. *Mol. Syst. Biol.* **10**, 757 (2014).
380. Wiśniewski, J. R., Zougman, A., Nagaraj, N. & Mann, M. Universal sample preparation

method for proteome analysis. *Nat. Methods* **6**, 359–362 (2009).
381. Cologna, S. M. *et al.* Quantitative Proteomic Analysis of Niemann-Pick Disease, Type C1 Cerebellum Identifies Protein Biomarkers and Provides Pathological Insight. *PLoS One* **7**, (2012).
382. Sleat, D. E., Wiseman, J. A., Sohar, I., El–Banna, M., Zheng, H., Moore, D. F., & Lobel, P. Proteomic analysis of mouse models of N iemann-P ick C disease reveals alterations in the steady-state levels of lysosomal proteins within the brain. *Proteomics* **12**, 3499–3509 (2012).
383. Rauniyar, N. *et al.* Quantitative proteomics of human fibroblasts with I1061T mutation in niemann-Pick C1 (NPC1) protein provides insights into the disease pathogenesis. *Mol. Cell. Proteomics* **14**, 1734–1749 (2015).
384. Jones, E. E. *et al.* Tissue Localization of Glycosphingolipid Accumulation in a Gaucher Disease Mouse Brain by LC-ESI-MS/MS and High-Resolution MALDI Imaging Mass Spectrometry. *SLAS Discov.* **22**, 1218–1228 (2017).
385. Vissers, J. P. C., Langridge, J. I. & Aerts, J. M. F. G. Analysis and quantification of diagnostic serum markers and protein signaturs for Gaucher disease. *Mol. Cell. Proteomics* **6**, 755–766 (2007).
386. Moore, D. F. *et al.* Proteomics of specific treatment-related alterations in Fabry disease: A strategy to identify biological abnormalities. *Proc. Natl. Acad. Sci. U. S. A.* **104**, 2873–2878 (2007).
387. Manwaring, V. *et al.* The identification of new biomarkers for identifying and monitoring kidney disease and their translation into a rapid mass spectrometry-based test: Evidence of presymptomatic kidney disease in pediatric fabry and type-I diabetic patients. *J. Proteome Res.* **12**, 2013–2021 (2013).
388. Whitfield, P. D., Sharp, P. C., Taylor, R. & Meikle, P. Quantification of galactosylsphingosine in the twitcher mouse using electrospray ionization-tandem mass spectrometry. *J. Lipid Res.* **42**, 2092–2095 (2001).
389. Escolar, M. L., Kiely, B. T., Shawgo, E., Hong, X., Gelb, M. H., Orsini, J. J., ... & Poe, M. D. Psychosine, a marker of Krabbe phenotype and treatment effect. *Mol. Genet. Metab.* **121**, 271–278 (2017).
390. Fagan, N., Alexander, A., Irani, N., Saade, C., & Naffaa, L. Magnetic resonance imaging findings of central nervous system in lysosomal storage diseases: A pictorial review. *J. Med. Imaging Radiat. Oncol.* **61**, 344–352 (2017).
391. Abdelhalim, A. N., Alberico, R. A., Barczykowski, A. L., & Duffner, P. K. Patterns of magnetic resonance imaging abnormalities in symptomatic patients with Krabbe disease correspond to phenotype. *Pediatr. Neurol.* **50**, 127–134 (2014).
392. Zarifi, M. K., Tzika, A. A., Astrakas, L. G., Young Poussaint, T., Anthony, D. C., & Darras, B. T. Magnetic resonance spectroscopy and magnetic resonance imaging findings in Krabbe's disease. *J. Child Neurol.* **16**, 522–526 (2001).
393. Cappello, V. *et al.* Ultrastructural Characterization of the Lower Motor System in a Mouse Model of Krabbe Disease. *Sci. Rep.* **6**, 1 (2016).
394. de Vito, G., Cappello, V., Tonazzini, I., Cecchini, M., & Piazza, V. RP-CARS reveals molecular spatial order anomalies in myelin of an animal model of Krabbe disease. *J. Biophotonics* **10**, 385–393 (2017).
395. Rogov, V., Dötsch, V., Johansen, T., & Kirkin, V. Interactions between autophagy receptors and ubiquitin-like proteins form the molecular basis for selective autophagy. *Mol. Cell* **53**, 167–178 (2014).
396. Futerman, A. H. & van Meer, G. The cell biology of lysosomal storage disorders. *Nat. Rev. Mol. Cell Biol.* **5**, 554–565 (2004).

397. Liu, W. J. *et al.* p62 links the autophagy pathway and the ubiqutin–proteasome system upon ubiquitinated protein degradation. *Cell. Mol. Biol. Lett.* **21**, 29 (2016).
398. Manadas, B., Mendes, V. M., English, J., & Dunn, M. J. Peptide fractionation in proteomics approaches. *Expert Rev. Proteomics* **7**, 655–663 (2010).
399. Mcalister, G. C. *et al.* MultiNotch MS3 Enables Accurate, Sensitive, and Multiplexed Detection of Di ff erential Expression across Cancer Cell Line Proteomes. (2014) doi:10.1021/ac502040v.
400. Crehan, H., Hardy, J. & Pocock, J. Microglia , Alzheimer ' s Disease , and Complement. **2012**, (2012).
401. Pandey, M. K. *et al.* Complement drives glucosylceramide accumulation and tissue inflammation in Gaucher disease. *Nature* **543**, 108 (2017).
402. Potter, G. B., & Petryniak, M. A. Neuroimmune mechanisms in K rabbe's disease. , 94(11), 1341-1348. *J. Neurosci. Res.* **94**, 1341–1348 (2016).
403. Kaida, K., and Kusunoki, S. Guillain–Barré syndrome: update on immunobiology and treatment. *Expert Rev. Neurother.* **9**, 1307–1319 (2009).
404. Freeze, H. H. Genetic disorders of glycan degradation. In Essentials of Glycobiology. *2nd Ed. Cold Spring Harb. Lab. Press.* (2009).
405. Parish, C. R. The role of heparan sulphate in inflammation. *Nat. Rev. Immunol.* **6**, 633–643 (2006).
406. Gowrishankar, S. *et al.* Massive accumulation of luminal protease-deficient axonal lysosomes at Alzheimer ' s disease amyloid plaques. (2015) doi:10.1073/pnas.1510329112.
407. Behrends, C., Sowa, M. E., Gygi, S. P. & Harper, J. W. Network organization of the human autophagy system. *Nature* **466**, 68–76 (2010).
408. Mizushima, N., Yoshimori, T., & Ohsumi, Y. The role of Atg proteins in autophagosome formation. *Annu. Rev. Cell Dev. Biol.* **27**, 107–132 (2011).
409. Cadwell, K. *et al.* A key role for autophagy and the autophagy gene Atg16l1 in mouse and human intestinal Paneth cells. *Nature* **456**, 259–263 (2008).
410. Nakamura, S. & Yoshimori, T. New insights into autophagosome – lysosome fusion. 1209–1216 (2017) doi:10.1242/jcs.196352.
411. Watanabe, Y. & Tanaka, M. p62 / SQSTM1 in autophagic clearance of a non-ubiquitylated substrate. 2692–2701 (2011) doi:10.1242/jcs.081232.
412. Schwenk, B. M. *et al.* The FTLD risk factor TMEM 106B and MAP6 control dendritic trafficking of lysosomes. **33**, (2014).
413. Drerup, C. M. & Nechiporuk, A. V. JNK-Interacting Protein 3 Mediates the Retrograde Transport of Activated c-Jun N-Terminal Kinase and Lysosomes. **9**, (2013).
414. Pu, J., Guardia, C. M., Keren-kaplan, T. & Bonifacino, J. S. Mechanisms and functions of lysosome positioning. 4329–4339 (2016) doi:10.1242/jcs.196287.
415. Mrschtik, M., & Ryan, K. M. Lysosomal proteins in cell death and autophagy. *FEBS J.* **282**, 1858–1870 (2015).
416. Aits, S. & Ja, M. Lysosomal cell death at a glance. (2013) doi:10.1242/jcs.091181.
417. Boya, P. & Kroemer, G. Lysosomal membrane permeabilization in cell death. *Oncogene* **27**, 6434 (2008).
418. Ji, Z. *et al.* Reactivity of Apolipoprotein E4 and Amyloid $_{NL}$ Peptide. **281**, 2683–2692 (2006).
419. Comley, L. H. *et al.* ApoE isoform-specific regulation of regeneration in the peripheral nervous system. **22**, 2406–2421 (2011).
420. Vizca, J. A. *et al.* 2016 update of the PRIDE database and its related tools. **44**, 447–456 (2016).

421. Taniike, M., Marcus, J. R., Nishigaki, T., Fujita, N., Popko, B., Suzuki, K., & Suzuki, K. Suppressed UDP-galactose: Ceramide galactosyltransferase and myelin protein mRNA in twitcher mouse brain. *J. Neurosci. Res.* **51**, 536–540 (1998).
422. Kodama, S., Igisu, H., Siegel, D. A., & Suzuki, K. Glycosylceramide synthesis in the developing spinal cord and kidney of the twitcher mouse, an enzymatically authentic model of human Krabbe disease. *J. Neurochem.* **39**, 1314–1318 (1982).
423. Yan, Z., Gibson, S. A., Buckley, J. A., Qin, H., & Benveniste, E. N. Role of the JAK/STAT signaling pathway in regulation of innate immunity in neuroinflammatory diseases. , 189, 4-13. *Clin. Immunol.* **189**, 4–13 (2018).
424. Liu, T. *et al.* Quantitatively Mapping Cellular Viscosity with Detailed Organelle Information via a Designed PET Fluorescent Probe. *Sci. Rep.* **4**, 5418 (2014).
425. Pekny, M., & Nilsson, M. Astrocyte activation and reactive gliosis. Glia, 50(4), 427-434. *Glia* **50**, 427–434 (2005).
426. Pekny, M., Wilhelmsson, U., & Pekna, M. The dual role of astrocyte activation and reactive gliosis. , 565, 30-38. *Neurosci. Lett.* **565**, 30–38 (2014).
427. White, A. B., Galbiati, F., Givogri, M. I., Lopez Rosas, A., Qiu, X., Van Breemen, R., & Bongarzone, E. R. Persistence of psychosine in brain lipid rafts is a limiting factor in the therapeutic recovery of a mouse model for Krabbe disease. , 89(3), 352-364. *J. Neurosci. Res.* **89**, 352–364 (2011).
428. Sural-Fehr, T., & Bongarzone, E. R. How membrane dysfunction influences neuronal survival pathways in sphingolipid storage disorders. *J. Neurosci. Res.* **94**, 1042–1048 (2016).
429. Soueid, J., Nokkari, A., and Makoukji, J. *Techniques and Methods of Animal Brain Surgery, in Brain Neurotrauma: Molecular, Neuropsychological, and Rehabilitation Aspects., 1st ed., CRC Press/Taylor & Francis, Boca Raton (FL).* (2015).
430. Tyanova, S., Temu, T., Sinitcyn, P., Carlson, A., Hein, M. Y., Geiger, T., ... & Cox, J. The Perseus computational platform for comprehensive analysis of (prote) omics data. *Nat. Methods* **13**, 731 (2016).
431. Alberts, B., Bray, D., Johnson, A., Lewis, J., Raff, M., Roberts, K., ... & Latchman, D. S. Essential Cell Biology: An Introduction to the Molecular Biology of the Cell. *Trends Biochem. Sci.* **23**, 268–268 (1998).
432. Theillet, F. *et al.* Physicochemical Properties of Cells and Their E ff ects on Intrinsically Disordered Proteins ( IDPs ). doi:10.1021/cr400695p.
433. Klymchenko, A. S. Solvatochromic and Fluorogenic Dyes as Environment-Sensitive Probes : Design and Biological Applications. (2017) doi:10.1021/acs.accounts.6b00517.
434. Pavani, S. R.; Thompson, M. A.; Biteen, J. S.; Lord, S. J.; Liu, N. . & Twieg, R. J.; Piestun, R.; Moerner, W. E. Three-Dimensional, Single- Molecule Fluorescence Imaging Beyond the Diffraction Limit by Using a Double-Helix Point Spread Function. *Proc. Natl. Acad. Sci. U. S. A.* **106**, 2995–2999 (2009).
435. Ruthardt, N.; Lamb, D. C.; Brauchle, C. Single-Particle Tracking as a Quantitative Microscopy-Based Approach to Unravel Cell Entry Mechanisms of Viruses and Pharmaceutical Nanoparticles. *Mol. Ther.* **19**, 1199–1211 (2011).
436. Schneider, J. *et al.* Ultrafast, temporally stochastic STED nanoscopy of millisecond dynamics. *Nat. Methods* **12**, 827 (2015).
437. Balzarotti, F. *et al.* with minimal photon fluxes. **612**, 606–612 (2017).
438. Lanzano, L.; Digman, M. A.; Fwu, P.; Giral, H.; Levi, M. . G. & E. Nanometer-Scale Imaging by the Modulation Tracking Method. *J. Biophotonics* **4**, 415–424 (2011).
439. Cardarelli, F.; Lanzano, L.; Gratton, E. Capturing Directed Molecular Motion in the

Nuclear Pore Complex of Live Cells. *Proc. Natl. Acad. Sci. U. S. A.* **109**, 9863–9868 (2012).
440. Cardarelli, F.; Lanzano, L.; Gratton, E. Fluorescence Correlation Spectroscopy of Intact Nuclear Pore Complexes. *Biophys. J.* **101**, L27-29 (2011).
441. Appelqvist, H. & Wa, P. The lysosome : from waste bag to potential therapeutic target. 214–226 (2013).
442. Ballabio, A. The awesome lysosome. **8**, 73–76 (2016).
443. Giovannantonio, L. G.; Nusco, E.; Platt, N.; Guida, A. . O., M. H.; Lanfrancone, L.; Perera, R. M.; Zoncu, R.; Pelicci, P. G. . & Settembre, C.; Ballabio, A. Di Malta, C.; Siciliano, D.; Calcagni, A.; Monfregola, J.; Punzi, S.; Pastore, N.; Eastes, A. N.; Davis, O.; De Cegli, R.; Zampelli, A.; Di Transcriptional Activation of RagD GTPase Controls mTORC1 and Promotes Cancer Growth. *Science (80-. ).* **356**, 1188–1192 (2017).
444. Devany, J.; Chakraborty, K.; Krishnan, Y. Subcellular Nanorheology Reveals Lysosomal Viscosity as a Reporter for Lysosomal Storage Diseases. *Nano Lett.* **18**, 1351–1359 (2018).
445. Wang, L.; Xiao, Y.; Tian, W.; Deng, L. Activatable Rotor for Quantifying Lysosomal Viscosity in Living Cells. *J. Am. Chem. Soc.* **135**, 2903–2906 (2013).
446. Lübke, T., Lobel, P., & Sleat, D. E. Proteomics of the lysosome. *Biochim. Biophys. Acta (BBA)-Molecular Cell Res.* **1793**, 625–635 (2009).
447. Xu, H., & Ren, D. (. Lysosomal physiology. *Annu. Rev. Physiol.* **77**, 55–80 (2015).
448. Weber, G.; Farris, F. J. Synthesis and Spectral Properties of a Hydrophobic Fluorescent Probe: 6-Propionyl-2-(dimethylamino)- naphthalene. *Biochemistry* **18**, 3075–3078 (1979).
449. Thoke, H. S., Tobiesen, A., Brewer, J. & Hansen, P. L. Tight Coupling of Metabolic Oscillations and Intracellular Water Dynamics in Saccharomyces cerevisiae. 1–16 (2015) doi:10.1371/journal.pone.0117308.
450. Thoke, H. S., Thorsteinsson, S., Stock, R. P., Bagatolli, L. A. & Olsen, L. F. The dynamics of intracellular water constrains glycolytic oscillations in Saccharomyces cerevisiae. *Sci. Rep.* **7**, 16250 (2017).
451. Parasassi, T.; De Stasio, G.; Ravagnan, G.; Rusch, R. M. . G. & E. Quantitation of Lipid Phases in Phospholipid Vesicles by the Generalized Polarization of Laurdan. *Biophys. J.* **60**, 179–189 (1991).
452. Parasassi, T., Krasnowska, E. K., Bagatolli, L. & Gratton, E. Laurdan and Prodan as Polarity-Sensitive Fluorescent Membrane Probes. **8**, 365–373 (1998).
453. Parasassi, T., & Gratton, E. Membrane lipid domains and dynamics as detected by Laurdan fluorescence. *J. Fluoresc.* **5**, 59–69 (1995).
454. Digman, M. A.; Brown, C. M.; Sengupta, P.; Wiseman, P. W. . & Horwitz, A. R.; Gratton, E. Measuring Fast Dynamics in Solutions and Cells with a Laser Scanning Microscope. *Biophys. J.* **89**, 1317– 1327 (2005).
455. Celli, A.; Gratton, E. Dynamics of Lipid Domain Formation: Fluctuation Analysis. Biochim. Biophys. Acta, Biomembr. **1798**, 1368–1376 (2010).
456. Celli, A.; Beretta, S.; Gratton, E. Phase Fluctuations on the Micron-Submicron Scale in GUVs Composed of a Binary Lipid 94, 104–116. *Mix. Biophys. J.* **94**, 104–116 (2008).
457. Sanchez, S. A., Tricerri, M. A. & Gratton, E. Laurdan generalized polarization fluctuations measures membrane packing micro-heterogeneity in vivo. **109**, (2012).
458. Balint, S.; Verdeny Vilanova, I.; Sandoval Alvarez, A. . & Lakadamyali, M. Correlative Live-Cell and Superresolution Microscopy Reveals Cargo Transport Dynamics at Microtubule Intersections. 2013, 110, 3375–3380. *Proc. Natl. Acad. Sci. U. S. A.* **110**, 3375–3380 (2013).

459. Cordonnier, M. N., Dauzonne, D., Louvard, D., & Coudrier, E. Actin filaments and myosin I alpha cooperate with microtubules for the movement of lysosomes. *Mol. Biol. Cell* **12**, 4013–4029 (2001).
460. Digiacomo, L. *et al.* Dynamic fingerprinting of sub-cellular nanostructures by image mean square displacement analysis. *Sci. Rep.* **7**, 14836 (2017).
461. Digman, M. A.; Sengupta, P.; Wiseman, P. W.; Brown, C. M. . & Horwitz, A. R.; Gratton, E. Fluctuation Correlation Spectroscopy with a Laser-Scanning Microscope: Exploiting the Hidden Time Structure. *Biophys. J.* **88**, L33-36 (2005).
462. Wang, L., Xiao, Y., Tian, W. & Deng, L. Activatable Rotor for Quantifying Lysosomal Viscosity in Living Cells. (2013) doi:10.1021/ja311688g.
463. Dross, N.; Spriet, C.; Zwerger, M.; Muller, G.; Waldeck, W. . & Langowski, J. Mapping eGFP Oligomer Mobility in Living Cell Nuclei. *PLoS One* **4**, No. e5041 (2009).
464. Careri, G., Fasella, P., Gratton, E., & Jencks, W. P. Statistical time events in enzymes: a physical assessmen. *CRC Crit. Rev. Biochem.* **3**, 141–164 (1975).
465. Johnson, D. E.; Ostrowski, P.; Jaumouille, V.; Grinstein, S. The Position of Lysosomes Within the Cell Determines Their Luminal pH. *J. Cell Biol.* **212**, 677–692 (2016).
466. Nilsson, E.; Ghassemifar, R.; Brunk, U. T. ysosomal Heterogeneity Between and Within Cells with Respect to Resistance Against Oxidative Stress. *Histochem. J.* **29**, 857–865 (1997).
467. Duchen, L. W.; Eicher, E. M.; Jacobs, J. M.; Scaravilli, F. . T. & F. Hereditary Leucodystrophy in the Mouse: the New Mutant Twitcher. *Brain* **103**, 695–710 (1980).
468. Parasassi, T.; De Stasio, G.; Ravagnan, G.; Rusch, R. M. . G. & E. Quantitation of Lipid Phases in Phospholipid Vesicles by the Generalized Polarization of Laurdan Fluorescence. *Biophys. J.* **60**, 179–189 (1991).
469. Di Rienzo, C., Piazza, V., Gratton, E., Beltram, F. & Cardarelli, F. Probing short-range protein Brownian motion in the cytoplasm of living cells. *Nat. Commun.* **5**, 5891 (2014).
470. Spitzer, J. From Water and Ions to Crowded Biomacromolecules: in Vivo Structuring of a Prokaryotic Cell. *Microbiol Mol. Biol. Rev.* **75**, 491–506 (2011).
471. Rabouille, C.; Alberti, S. Cell Adaptation Upon Stress: the Emerging Role of Membrane-less Compartments. *Curr. Opin. Cell Biol.* **47**, 34–42 (2017).
472. Munder, M. C. *et al.* A pH-driven transition of the cytoplasm from a fluid- to a solid-like state promotes entry into dormancy. 1–30 (2016) doi:10.7554/eLife.09347.
473. Hyman, A. A. & Simons, K. Phase Transitions in Cells. **337**, 1047–1050 (2012).
474. Hyman, A. A.; Simons, K. Cell Biology. Beyond Oil and Water– Phase Transitions in Cells. *Science (80-. ).* **337**, 1047–1049 (2012).
475. Milovanovic, D.; Wu, Y.; Bian, X.; De Camilli, P. A. Liquid Phase of Synapsin and Lipid Vesicles. *Science (80-. ).* **361**, 604–607 (2018).
476. Milovanovic, D., Wu, Y., Bian, X. & Camilli, P. De. A liquid phase of synapsin and lipid vesicles. **607**, 604–607 (2018).
477. Su, X.; Ditlev, J. A.; Hui, E.; Xing, W.; Banjade, S.; Okrut, J. . K. & D. S.; Taunton, J.; Rosen, M. K.; Vale, R. D. Phase Separation of Signaling Molecules Promotes T Cell Receptor Signal Transduction. *Science (80-. ).* **352**, 595–599 (2016).
478. Ling, G. N. *Physical theory of the living state.* (1962).
479. Parlanti, P., Cappello, V., Brun, F., Tromba, G., Rigolio, R., Tonazzini, I., ... & Gemmi, M. Size and specimen-dependent strategy for x-ray micro-ct and tem correlative analysis of nervous system samples. *Sci. Rep.* **7**, 2858 (2017).
480. Manders, E. M. M., Stap, J., Brakenhoff, G. J., Driel, R. V. A. N. & Aten, J. A. Dynamics of three-dimensional replication patterns during the S-phase , analysed by double

labelling of DNA and confocal microscopy. **862**, 857–862 (1992).
481. Levi, V.; Ruan, Q.; Gratton, E. 3-D Particle Tracking in a Two- Photon Microscope: Application to the Study of Molecular Dynamics in Cells. *Biophys. J.* **88**, 2919–2928 (2005).
482. Kis-Petikova, K.; Gratton, E. Distance Measurement by Circular Scanning of the Excitation Beam in the Two-Photon Microscope. *Microsc. Res. Tech.* **63**, 34–49 (2004).
483. Mayer, L. D.; Hope, M. J.; Cullis, P. R.; Janoff, A. S. Solute Distributions and Trapping Efficiencies Observed in Freeze-Thawed Multilamellar Vesicles. Biochim. 1985, 817, 193–196. *Biophys. Acta, Biomembr.* **817**, 193–196 (1985).
484. Bangham, A. D., Standish, M. M., & Weissmann, G. The action of steroids and streptolysin S on the permeability of phospholipid structures to cations. *J. Mol. Biol.* **13**, 253-IN28 (1965).
485. Lira, R. B., Steinkühler, J., Knorr, R. L., Dimova, R. & Riske, K. A. Posing for a picture: vesicle immobilization in agarose gel. *Sci. Rep.* **6**, 25254 (2016).

# Acknowledgements

Non li volevo fare… no dai, questa volta li faccio. Però in italiano :)
Vorrei ringraziare tutte le persone con cui ho interagito durante questo percorso. Tutte mi hanno aiutato, in modi diversi, a portare a termine questo lavoro di tesi.
Un grazie particolare a Marco, che ha sempre creduto in questo progetto e mi ha trasmesso il suo entusiasmo anche nei momenti più difficili. Perché… "cosa succede quando iniettiamo le nanoparticelle nel topo non lo vuoi vedere???" Grazie perché è stato sempre disponibile per qualsiasi cosa, e perché ha sempre lasciato spazio anche alle mie idee. Grazie poi a Luci, l'altra metà del mio cervello per 5 anni in lab. Sei stata una fortuna immensa, non riesco a pensare a come sarebbero stati questi anni senza aver potuto condividere ogni "dubbio amletico" con te… e il mio cervello non riesce ancora ad accettare il fatto che non sei più al NEST! Grazie poi a Ila, che mi ha insegnato a "correre" (per leggere i blot), ad arrangiarmi, ed a saper sempre cavare il meglio da ogni situazione…. senza arrendersi mai! resistere… and fill the gender gap!
Grazie poi a Sandro, che con pazienza si è sorbito le mie presentazioni e le mie ansie, e che mi è sempre stato vicino ❤
Grazie ovviamente a mamma e papi, che mi hanno sostenuta in questo percorso e che sono sempre stati curiosi di sapere cosa faccio in quei laboratori…… e "se ho scoperto qualcosa" :))). Grazie a sisters Marty e Michi, per tutte le volte che mi hanno ascoltato e dato consigli sinceri. Grazie a nonna e Katia per gli incoraggiamenti! Grazie a Beux, un punto fermo in my life, nonostante la mia migrazione nel pisano :)

Insomma, grazie a tutti!

